Key concepts for implementing SoC-Holter

Hao Ding

N° d'ordre : 2166

EDSPIC: 534

UNIVERSITÉ BLAISE PASCAL - CLERMONT II

ÉCOLE DOCTORALE DE

SCIENCES POUR L'INGÉNIEUR DE CLERMONT-FERRAND

Thèse

Présentée par

Hao DING

Pour obtenir le grade de

DOCTEUR D'UNIVERSITÉ

Spécialité: INFORMATIQUE

Key Concepts for Implementing SoC-Holter

Soutenue publiquement le 13 octobre 2011 devant le jury :

Madame	Edwige PISSALOUX
Monsieur	Didier LE RUYET
Monsieur	Xin Chen ZHANG
Monsieur	Dan Yan LUO
Monsieur	Kun Mean HOU
Madame	Hong SUN

Acknowledgements

As a Sino-French Joint PhD student, I wish to express my sincere appreciation to my thesis advisors, Prof. Hong Sun and Prof. Kun-Mean Hou for their encouragement, guidance and support during this effort. It has been a great pleasure to learn from them during the process of my research.

I want to express my deep gratitude to Prof. Xin Xu, for his support and inspiring guidance for the years I spent in Wuhan University. Much thanks go to Dr. Wen Yang, Dr. Chu He, Mrs. Li Su for their help and encouragement.

I also like to express my gratefulness to Dr. Jian-Jin Li, for her continuous encouragements help during my PhD study period in the LIMOS laboratory of Blaise Pascal University.

I am thankful to my collaborator, Jacques Lecoq for his insightful discussions and valuable suggestions for supporting the chip design.

I am thankful to my classmates of Wuhan University, especially Xin Lu for her encouragement. I would like to thank Ge Xu, Hang Dong and Jiayu Chen. To all other PhD students of signal processing and modern communication laboratory (SPMC).

I would also like to thank all colleagues and friends of the LIMOS laboratory. Especially thanks to Hongling SHI for his valuable suggestion and Yibo Chen for his assistance. It also has been a great working with my lab-mates in LIMOS. Much thanks go to Messaoud Kara, Dr. Xunxing Diao, Christophe de Vaulx, Abdelaziz Amamra, Aurélien Jacquot, Xing Liu, Tao Su and Gil De Sousa for all support and encouragements.

Special thanks to my family, especially my Mom and Dad, for their support and encouragements over the years. And I am thankful to my sister and her husband for their support and encouragements.

Résumé

En dépit du développement rapide de la médecine, les maladies cardiovasculaires restent la première cause de mortalité dans le monde. En France, chaque année, plus de 50 000 personnes meurent subitement en raison d'arythmies cardiaques. L'identification des patients à risque élevé de décès soudain est toujours un défi. Pour détecter les arythmies cardiaques, actuellement Holter est généralement utilisé pour enregistrer les signaux électrocardiogramme (ECG) à 1~3 dérivations pendant 24h à 72h. Cependant l'utilisation de Holter est limitée parmi la population en raison de son encombrement (pas convivial) et de son coût. Un Holter mono puce portable nommé SoC-Holter qui permet d'enregistrer 1 à 4 dérivations est introduit. Le déploiement d'un réseau de capteurs sans fil exige que chaque SoC-Holter soit peu encombrant et peu cher, et consomme peu d'énergie.

Afin de minimiser la consommation d'énergie et le coût du système, la technologie Complementary Metal Oxide Semiconductor (CMOS) (0.35µm) est utilisée pour la première implémentation de SoC-Holter. Puis une nouvelle méthode de détection basée sur Acquisition Comprimée (CS) est introduite pour résoudre les problèmes de consommation d'énergie et de capacité de stockage de SoC-Holter. Le principe premier de cette plate-forme est d'échantillonner les signaux ECG sous la fréquence de Nyquist 'sub-Nyquist' et par la suite de classer directement les mesures compressées en états normal et anormal. Minimiser le nombre de fils qui relient les électrodes à la plate-forme peut rendre l'utilisateur de SoC-Holter plus confortable, car deux électrodes sont très proche sur la surface du corps. La différence ECG enregistrée est analysée à l'aide de Vectocardiogramme (VCG).

Les résultats expérimentaux montrent qu'une approche intégrée, à faible coût et de faible encombrement (SoC-Holter) est faisable. Le SoC-Holter consomme moins de 10mW en fonctionnement. L'estimation des paramètres du signal acquis est effectuée directement à partir de mesures compressés, éliminant ainsi l'étape de la reconstruction et réduisant la complexité et le volume des calculs. En outre, le système fournit les signaux ECG compressés sans perte d'information, de ce fait il réduit significativement la consommation d'énergie pour l'envoi de message et l'espace de stockage mémoire. L'effet de placement des électrodes est évalué sur la QRS complexe lorsqu'il a enregistré avec deux électrodes adjacentes. La méthode est basée sur l'algorithme de 'QRS-VCG loop alignment', La méthode moindre carré est utilisée pour estimer la corrélation entre une boucle VCG observée et une boucle de référence en respectant les transformations de rotation et la synchronisation du temps. Les emplacements d'électrodes les moins sensibles aux interférences sont étudiés.

Mots-clés— Électrocardiographie (ECG), Complementary Metal Oxide Semiconductor (CMOS), Acquisition Comprimée (CS), arythmies cardiaques, Vectocardiographie (VCG)

Abstract

According to the figures released by World Health Organization (WHO), cardiovascular disease is the number one cause of death in the world. In France every year more than 50,000 people die suddenly due cardiac arrhythmias. Identification of high risk sudden death patients is still a challenge. To detect cardiac arrhythmias, currently Holter is generally used to record 1~4 leads electrocardiogram (ECG) signals during 24h to 72h. However the use of Holter is limited among the population due to its form factor (not user-friendly) and cost. An integrated single chip wearable Holter named SoC-Holter that enables to record 1 to 4 leads ECG is introduced. Deployment of wireless sensor network requires each SoC-Holter with less power consumption, low-cost charging system and less die area.

To minimize energy consumption and system cost, Complementary Metal Oxide Semiconductor (CMOS) technology (0.35µm) is used to prototype the first implementation of SoC-Holter. Then a novel method based on Compressed Sensing (CS) technique is introduced for solving the problems of power consumption and storage capacity of SoC-Holter. The main principle underlying this framework is to sample analog signals at sub-Nyquist rate and to classify directly compressed measurement into normal and abnormal state. Minimizing the wire connected electrodes to the platform can make the carrier more comfortable because two electrodes are attached closely on the surface of the body. Recording difference ECG is analyzed using Vectorcardiogram (VCG) theory.

Experimental results show that an integrated, low cost, and user-friendly SoC-Holter is feasible. SoC-Holter consumes less than 10mW while the device is operating. It takes advantage of estimating parameters directly from compressed measurements, thereby eliminating the reconstruction stage and reducing the computational complexity on the platform. In addition, the framework provides compressed ECG signals without loss of information, reducing significantly the power consumption for message sending and memory storage space. The effect of electrode placement is evaluated by estimating QRS complex in recorded ECG signals by two adjacent electrodes. The method is based on the QRS-VCG loop alignment algorithm that estimates Least Square (LS) between an observed VCG loop and a reference loop with respect to the transformations of rotation and time synchronization. The electrode location with less sensitive to interference is investigated.

Index Terms— Electrocardiography (ECG), Complementary Metal Oxide Semiconductor (CMOS), Compressed Sensing (CS), Cardiac arrhythmias, Vectorcardiography (VCG).

Contents

Résumé ii
Abstract iii
List of Tables ix
List of Figures x
List of Acronyms xiv
Introduction 1
Chapter 1 Overview and Objective of the Wireless Sensor Network for Telemedical Application 3
1.1. Wireless Sensor Network: Concept 3
1.2. Architecture of Pervasive Cardiac Care (PCC) 4
Chapter 2 Real-time Hardware Platform for ECG monitoring 9
2.1. State of the Art 10
2.1.1. Continuous Recorders 10
2.1.2. Intermittent Recorders 11
2.2. Background on Hardware Platform for Wireless Sensor Network 15
2.2.1. MOS Characteristics 16
2.3. Amplifier 19
2.3.1. Common-mode Input 20
2.3.2. Full Differential Operational Amplifier 22
2.3.3. Common Mode Feedback (CMFB) 22
2.3.4. Current Mirror 23
2.3.5. Shunt-shunt Feedback 24
2.3.6. Two Stages Operational Amplifier 26
2.3.7. Simulation Tests 29
2.3.7.1. Output Signal Swing. 30
2.3.7.2. Gain 31

2.3.7.3. Common-mode Rejection Ratio 32
2.3.7.4. GBW and Phase Margin 32
2.3.7.5. Total Power Consumption 33
2.4. Filter based on Operational Transconductance Amplifier (OTA) 33
2.4.1. Input stage 34
2.4.2. Current Divisor 36
2.4.3. Degeneration 36
2.4.4. Common Mode Feedback 38
2.4.5. Current Source 39
2.4.6. Active Filter Design 40
2.5. 12-bit ADC 43
2.5.1. Ramp 43
2.5.2. Input Front-end of Comparator 45
2.5.3. Comparator 46
2.5.4. Simulation Results 47
2.6. Oscillator 48
2.7. Mixer 50
2.8. Layout and Experimental Measurements 51
2.9. Nano-controller 53
2.10. Conclusion 55
Chapter 3 Implementation of Compressed Sensing for Telecardiology Sensor Network 57
3.1. Introduction of Electrocardiogram (ECG) 57
3.1.1. Action Potentials in the Heart 57
3.1.2. Interferences and Noise 60
3.1.3. Cardiac Arrhythmias 62
3.1.4. Computational-based Algorithm for ECG Signals 69
3.1.4.1. Algorithm based on Amplitude 69
3.1.4.2. Algorithm based on Derivative 70
3.1.4.3. Algorithm based on Digital Filter 70

3.1.4.4. Algorithm based on Artificial Neural Network 71
3.1.4.5. Algorithm based on Other Analysis Techniques 72
3.2. Direct Cardiac Arrhythmias via Compressed Measurements 72
3.2.1. Introduction 72
3.2.2. Cardiac signal model 76
3.2.2.1. Wavelet Transform for Cardiac Signal 76
3.2.2.2. Multiresolution Analysis 78
3.2.2.3. The DWT Matrix Representation 82
3.2.3. Compressed Sensing 85
3.2.4. Bayesian Compressed Sensing 90
3.2.5. Anomaly Detection using BCS 92
3.3. Simulation 93
3.3.1. Energy Estimation of QRS Complex 94
3.3.2. Detection of QRS Complex with BCS 96
3.3.3. Analysis of Reconstruction (1) 98
3.3.4. Analysis of Reconstruction (2) 102
3.3.5. Experiments in Cardiac Arrhythmias 103
3.4. Conclusion 122
Chapter 4 Distortion Effect of Electrode Location 123
4.1. Introduction 123
4.1.1. Theoretical Analysis of Volume Source 124
4.1.2. Lead Vector 124
4.2. Vectorcardiographic lead system 126
4.2.1. Bipolar Limb Leads 129
4.2.2. Unipolar Limb Leads 129
4.2.3. Augmented Unipolar Limb Leads 130
4.2.4. Unipolar Chest Leads 131
4.2.5. 12-lead ECG relationship 131
4.3. Signal model 134
4.3.1. VCG Alignment Algorithm 140

4.4. Simulation 144
4.4.1. Experimental Model 146
4.4.2. Vector Lead Model 149
4.4.3. QRS Detection 150
4.4.4. Vector Lead Model of V_1 151
4.4.5. Vector Lead Model of V_5 157
4.5. Conclusion 162
Chapter 5 Conclusion and Ongoing Work 165
Bibliography 167

List of Tables

Table 3.1 A cycle of normal beat consists of waves, segments and intervals [36] 61
Table 3.2 Type comparison inverse transform 99
Table 4.1 Deviation from transverse plane 139
Table 4.2 Performance of estimation form signals difference around V_1 157
Table 4.3 Performance of estimation form signals difference around V_5 162

List of Figures

Figure 2.1 Wireless sensor work for medical application. 13
Figure 2.2 Block diagram of WES (a) and SoC-Holter (b). 14
Figure 2.3 The actual connection provided through p-substrate is depicted. 16
Figure 2.4 Drain current versus drain source voltage. 17
Figure 2.5 Complementary differential pair common mode input range. 20
Figure 2.6 Complementary differential pair transconductance versus common mode input. 21
Figure 2.7 Schematic of current mirror. 23
Figure 2.8 Current mirror simulation result. 24
Figure 2.9 Full differential op-amp configuration. 25
Figure 2.10 Signal flow graph for Figure 2.9. 26
Figure 2.11 Two stage operational amplifier 27
Figure 2.12 Schematic of two stages full differential amplifier. 28
Figure 2.13 Preamplifier circuit diagram. 30
Figure 2.14 Input and output signals for transient analysis of preamplifier. 30
Figure 2.15 Bode plots of loop gain of the amplifier. 31
Figure 2.16 Schematic of input stage. 35
Figure 2.17 Schematic of current divisor. 36
Figure 2.18 Reduction technique: source degeneration. 37
Figure 2.19 Schematic of the degeneration block. 38
Figure 2.20 Schematic of the Common Mode Feedback block. 39
Figure 2.21 Schematic of the current source. 40
Figure 2.22 Architecture of the band-pass filter that is constructed with 1^{rst} order low-pass filter and 1^{rst} order high-pass filter. 41
Figure 2.23 Simulation results of the 1^{rst} order low-pass filter. 41
Figure 2.24 Simulation results of the 1^{rst} order band-pass filter. 42
Figure 2.25 Bandwidth of the 1^{rst} order band-pass filter. 42
Figure 2.26 Simulation results of the 1^{rst} order band-pass filter. 43
Figure 2.27 Bloc diagram of the A/D processing stage. 44
Figure 2.28 Schematic of the ramp. 44
Figure 2.29 Schematic of the input stage. 45
Figure 2.30 Schematic of the comparator. 46
Figure 2.31 Simulation results of ramp. 47
Figure 2.32 Transient response of ADC. 48
Figure 2.33 Schematic of the oscillator. 48
Figure 2.34 AC response of the oscillator. 49
Figure 2.35 FFT of transient output waveform of the oscillator. 49
Figure 2.36 Schematic of the mixer. 50
Figure 2.37 Transient response of the mixer versus time. 51
Figure 2.38 Layout of final preamplifier. 51
Figure 2.39 Layout of the 1^{rst} order band-pass filter. 52
Figure 2.40 Circuit of the different analog blocks of SoC-Holter. 52
Figure 2.41 Actual oscilloscope traces of ECG signal near V_5 electrode. 53
Figure 2.42 Bloc diagram of the nano-controller. 54
Figure 2.43 Transient response of the mixer versus time. 55

Figure 3.1 The original formulation of these processes was produced by Hodgkin and Huxley, so the model is known as the Hodgkin-Huxley model. 58
Figure 3.2 Schematic diagram of a typical ECG tracing in normal sinus rhythm. 60
Figure 3.3 Normal Sinus Rhythm. 63
Figure 3.4 Sinus Bradycardia. 63
Figure 3.5 Ventricular Bradycardia. 64
Figure 3.6 Ventricular Tachycardia. 65
Figure 3.7 Atrial Bigeminy. 65
Figure 3.8 Ventricular Bigeminy. 66
Figure 3.9 Atrial Flutter. 67
Figure 3.10 Atrial Fibrillation 68
Figure 3.11 Supraventricular Tachyarrhythmia. 68
Figure 3.12 Wireless ECG Sensor continuously monitoring the patients suffering from cardiac arrhythmia. 74
Figure 3.13 Comparison of traditional and CS ADC.. 75
Figure 3.14 WES compressed samples analog ECG signals according to CS theory. 77
Figure 3.15 Pyramid algorithm or sub-band coding and a 3 level filter bank. 80
Figure 3.16 Orthonormal decomposition of ECG signal. 81
Figure 3.17 Two channel filter bank. 82
Figure 3.18 Compressed sensing of ECG.. 85
Figure 3.19 Statistical characteristic of irregular peak values of ECG signals.. 95
Figure 3.20 Statistical characteristic of irregular distance between the peaks of ECG Signals. 96
Figure 3.21 Comparison of signal reconstruction on irregular value case.. 97
Figure 3.22 Comparison of sparse expansion.. 97
Figure 3.23 Comparison of signal reconstruction on irregular distance case. 98
Figure 3.24 Comparison of sparse expansion.. 98
Figure 3.25 Number of measurements versus construction performance, Comparison directly detection of QRS complex and entire signal. 100
Figure 3.26 The sparse exponents of signal on different wavelet transform. 101
Figure 3.27 Comparison of reconstruction performance on different wavelet transform and compression ratio.. 101
Figure 3.28 Heart Rate, storage, performance and power consumption for Compressive Sensing versus original sampling. 103
Figure 3.29 Comparison of signal reconstruction in normal sinus rhythm.. 104
Figure 3.30 Statistical characteristic of ECG Signals in normal sinus rhythm. 105
Figure 3.31 Comparison of sparse expansion.. 105
Figure 3.32 Comparison of signal reconstruction in sinus bradycardia.. 106
Figure 3.33 Statistical characteristic of ECG Signals in sinus bradycardia.. 107
Figure 3.34 Comparison of sparse expansion.. 107
Figure 3.35 Comparison of signal reconstruction in ventricular bradycardia.. 108
Figure 3.36 Statistical characteristic of ECG Signals in ventricular bradycardia.. 109
Figure 3.37 Comparison of sparse expansion.. 110
Figure 3.38 Comparison of signal reconstruction in ventricular tachycardia.. 110
Figure 3.39 Statistical characteristic of ECG Signals in ventricular tachycardia. 111
Figure 3.40 Comparison of sparse expansion.. 111
Figure 3.41 Comparison of signal reconstruction in atrial bigeminy.. 112
Figure 3.42 Statistical characteristic of ECG Signals in atrial bigeminy.. 113

Figure 3.43 Comparison of sparse expansion.. 113
Figure 3.44 Comparison of signal reconstruction in atrial flutter.. 114
Figure 3.45 Statistical characteristic of ECG Signals in atrial flutter..... 115
Figure 3.46 Comparison of sparse expansion.. 115
Figure 3.47 Comparison of signal reconstruction in atrial fibrillation.. 116
Figure 3.48 Statistical characteristic of ECG Signals in atrial fibrillation.. 117
Figure 3.49 Comparison of sparse expansion.. 117
Figure 3.50 Comparison of signal reconstruction in ventricular bigeminy.. 118
Figure 3.51 Statistical characteristic of ECG Signals in ventricular bigeminy.. 119
Figure 3.52 Comparison of sparse expansion.. 119
Figure 3.53 Comparison of signal reconstruction in supraventricular tachyarrhythmia.. 120
Figure 3.54 Statistical characteristic of ECG Signals in supraventricular tachyarrhythmia.. 121
Figure 3.55 Comparison of sparse expansion.. 121
Figure 4.1 Determination of the point 3 on the surface of body corresponding to an image space point located between V_1 and V_2. 125
Figure 4.2 The basic of Vectorcardiography is illustrated the human body by three orthogonal leads and projected on the various planes from [86]. 128
Figure 4.3 The lead vectors in a finite, homogeneous torso model calculated from the model of Hyttinen. 135
Figure 4.4 The three VCG leads X, Y and Z, The graphical recording of these body surface potentials as a function of time, V_1, V_2, V_4 and V_5 136
Figure 4.5 QRS loop based on the ECG signals of V_1, V_2, V_4 and V_5.. 136
Figure 4.6 The normal sequence of ventricular depolarization. 137
Figure 4.7 Derivation of the ECG signals of V_1 and V_4 from the transverse plane loop. Dots are several key points. 140
Figure 4.8 Morphologic variability..... 143
Figure 4.9 Example of estimated rotation angles angles $\widehat{\emptyset}_x$, $\widehat{\emptyset}_y$ and $\widehat{\emptyset}_z$ using QRS-VCG loop alignment algorithm. 144
Figure 4.10 (top-left) The volunteer with ECG recording and WES, (top right) ECG electrode, (bottom-left) A wearable ECG sensor with real time measurement and wireless medium (Bluetooth), (bottom-right) Real time display of measurements of the electrocardiogram. 145
Figure 4.11 (1) Standard ECG signals of V_1, (2) Standard ECG signals of V_1', (3) Standard ECG signals of V_1'', (4) Detailed description of QRS complex of standard ECG signals, (5) Difference ECG signals between V_1' and V_1, (6) Difference ECG signals between V_1'' and V_1, (7) Detailed description of the part of difference ECG signals in the same interval of QRS complex of standard ECG signals. 146
Figure 4.12 (top) The voltage between the neck and right leg, (bottom) The voltage between the standard position V_1 and right leg. 147
Figure 4.13 The difference of V_1 and V_{neck}, the voltage is recorded between the standard position V_1 and the neck. 148
Figure 4.14 (top) The voltage is recorded between the standard position V_1 and the closed electrode, (bottom) The blue line is the difference between the voltage of V_1 and the voltage of its neighbor, and the red line is the reverse difference. 148
Figure 4.15 (top) The voltage is recorded of the standard position V_1 and its closed electrodes V_1' and V_1'', (bottom) The voltage of V_1 and the result of the disposal. 149

Figure 4.16 *QRS* complex detection algorithm processing steps for the actual recorded ECG signals of volunteer (25 years old, male).. 151
Figure 4.17 Morphologic variability shown of these three ECG signals.. 153
Figure 4.18 (top) The standard ECG signals of V_1, (center) The difference signal between V_1' and V_1, (bottom) The difference signal between V_1'' and V_1. 153
Figure 4.19 Detailed description of QRS loop of the standard ECG signal and signal differences.. 154
Figure 4.20 (top) RR interval, (bottom) Heart rate. 154
Figure 4.21 (top) The standard ECG signals of V_1, (center) The estimated signal $\widehat{V_1'}$ from the difference signal between V_1' and V_1, (bottom) The estimated signal $\widehat{V_1''}$ from the difference signal between V_1'' and V_1. 155
Figure 4.22 Detailed description of QRS loop of the standard ECG signal and its estimations. . 156
Figure 4.23 From the top to the bottom are the duration and amplitude of RS wave. 156
Figure 4.24 Morphologic variability shown of these three ECG signals.. 158
Figure 4.25 (top) The standard ECG signals of V_5, (center) The difference signal between V_1' and V_5, (bottom) The difference signal between V_5'' and V_5. 159
Figure 4.26 Detailed description of QRS loop of the standard ECG signal and signal differences.. 159
Figure 4.27 (top) RR interval, (bottom) Heart rate. 160
Figure 4.28 (top) The standard ECG signals of V_5, (center) The estimated signal $\widehat{V_5'}$ from the difference signal between V_5' and V_5, (bottom) The estimated signal $\widehat{V_5''}$ from the difference signal between V_5'' and V_5. 161
Figure 4.29 Detailed description of QRS loop of the standard ECG signal and its estimations... 161
Figure 4.30 From the top to the bottom are the duration and amplitude of RS wave.. 162
Figure 4.31 VCG loop of QRS complex.. 163
Figure 4.32 VCG loops of continuous several circles.. 163

List of Acronyms

AC	Alternating Current
ADC	Analog-to-Digital Converter
AG	Available Gain
AHA	American Heart Association
ANN	Artificial Neural Network
AV	Atrioventricular
BME	Biomedical Engineering
BPM	Beats Per Minute
CM	Common Mode
CMOS	Complementary Metal Oxide Semi-conductor
CMFB	Common Mode Feedback
CMRR	Common-Mode Rejection Ratio
COTS	Commercial Off-The-Shelf
CS	Compressed Sensing
CSD	Cardiac Sudden Death
CWT	Continuous Wavelet Transform
DC	Direct Current
DWT	Discrete Wavelet Transform
ECG	Electrocardiography
HP	Horizontal Plane
HR	Heart Rate
HRV	Heart Rate Variability
ICD	Implantable Cardioverter-Defibrillator
IF	Intermediate Frequency
LA	Left Arm
LL	Left Leg
LS	Least Square
LO	Local Oscillator
MEMS	Micro-Electro-Mechanical Systems
MI	Medical Informatics
MMC	Multimedia flash Memory Card
OP-AMP	Operational amplifier
OTA	Operational Transconductance Amplifier
PEM	Personal ECG monitor
PHC	Pervasive Healthcare
PM	Phase Margin
PCC	Pervasive Cardiac Care
PPG	Photoplethysmogram
PVC	Premature Ventricular
RA	Right Qrm
RF	Radio Frequency
RISC	Reduced instruction set computer
RR	R wave to R wave interval
RVM	Relevance Vector Machine

SA	Sinoatrial
SHM	Structural Health Monitoring
SIO_2	Silicon dioxide
SMS	Short Message Service
SoC	System-on-Chip
SoC-Holter	System-on-Chip Holter
SVEC	Stereovectorelectrocardiography
TG	Transducer Gain
T/H	Track and Hold
UbiComp	Ubiquitous Computing
UGB	Unit Gain Bandwidth
VCG	Vectorcardiography
VF	Ventricular Fibrillation
VLP	Ventricular Late Potentials
VT	Ventricular Tachycardia
WAP	Wireless Application Protocol
WBSN	Wireless Body Sensor Network
WCT	Wilson Central Terminal
WES	Wireless ECG Sensor
WHO	World Health Organization
WLAN	Wireless Local Area Network
WSN	Wireless Sensor Network

Introduction

As WHO claims that the proportion of the world's elderly population continues to increase. Thus that leads to high demand for telemedical care in which telemonitoring is essential. WHO claims that estimated 17.1 million people died from cardiovascular disease in 2004, presenting 29% of all global deaths. Cardiovascular disease is the leading cause of death worldwide, especially to the elderly. By 2025, the world's aging population over the age of 65 is reaching 761 million. More than 80% elderly people have chronic diseases and more than 30% of them suffer from two or more types of chronic diseases. The urgent reality drives a new healthcare system that consumes fewer financial and human resources. Pervasive Healthcare (PHC) is a new healthcare model that includes several characteristics, such as patient mobility, continuous health monitoring and timely detection of anomalies. A specialized PHC system that focuses on providing long-term continuous monitoring of patients or elderly people suffering from cardiovascular diseases not only inside the hospital environment is Pervasive Cardiac Monitoring (PCC). It can record the physical data and related information that could reflect any changes in patient status. PCC can monitor people without any supervision, driven by new technologies such as wireless biomedical sensor network and microelectronics technology. The key technologies of PCC system model and service provision could include low power consumption sensor, signal processing with less resource and the lower cost. PCC has a wide range of applications not only in developed countries but also those emerging countries. PCC composed of ECG sensor nodes and multi-hop networking capability can be deployed to provide long-term and continuous healthcare monitoring for the patients or elderly people who have cardiovascular diseases.

The first part introduces Wireless Sensor Network (WSN) hardware platform that is to support real-time cardiac arrhythmias detection and diagnosis. The main challenge arises from the shortage of power and storage resources of wireless sensor for remotely monitoring. It is necessary to transmit a huge amount of life-critical data over a communication link to a remote server for large-scale analysis and diagnosis. The architecture of a wearable system-on-chip (SoC) to record ECG signal is introduced in this chapter.

The next chapter introduces a new concept Compressed Sensing (CS) that provides the equipment with more power savings and minor impact to signal quality. The design and implementation of compressed sensing in WSN for telecardiology is studied in this chapter. The performances of compressed sensing employing onto different wavelet basis where ECG signal is sparse are compared. This paradigm for WSN exhibits the advantages of a meaningful reduction of data acquisition and a decrease of data transmission.

The last chapter introduces the effect of electrode location. The proper ECG signal is recorded from ECG electrodes that must be placed at several special positions. ECG signal is usually to be detected by electrodes attached to specified positions on the body (chest, arms and legs) and reference electrode which is placed far away from the heart to provide reference potential (i.e. left leg). We try to investigate the effect of electrode placement on the QRS-complex when ECG signal is recorded from precordial leads.

Chapter 1
Overview and Objective of the Wireless Sensor Network for Telemedical Application

1.1. Wireless Sensor Network: Concept

Wireless sensor network is a paradigm consisting of distributed sensors with self-organization capabilities to interact with the outside environment. WSN is mainly dedicated to monitor physical parameters, such as temperature, soil moisture, vibration pressure or motion. WSN may be used in many application areas, including industrial monitoring and control, healthcare applications, environment monitoring and traffic control. WSN has the potential to use in medical care. The cardiologist can collect the biological data from sensors and analyze these data online or offline. Patients outfitted with wearable wireless sensors would allow the cardiologist to monitor their status continuously in real-time. In a case of cardiac arrhythmias, the cardiologist needs to accumulate the long term ECG data to improve the efficiency of patient treatment and the accurate diagnosis of this disease, consequently possible to make a timely treatment. Despite an unprecedented improvements in this area, there still exists the technical disparity between the existing wireless sensor network and the requirements of medical care [1].

In a typical architecture of WSN, a wireless sensor network consists of sensor node, which collects information of interest from the outside environment, and sink node, which behaves as an interface between sensor network and exterior network, like the Internet. It is envisioned that some neighboring sensor nodes locate within the communication range of the sink node accumulating all the gathered information, and of the Internet which becomes more feasible to establish global information sharing.

Each sensor node includes several functions: 1) sensing the physical parameter from the outside environment, 2) manipulating the raw data by using some signal processing, 3) transmitting the information to the sink node through wireless access medium.

There are some enabling technologies in the hardware basis of WSN. Firstly, System-on-Chip (SoC) technology is able to integrate all components of a sensor on a single chip. A SoC sensor node consists of both the hardware (e.g. embedded processor and peripheral devices) and the software which controls the hardware. The SoC design aims to develop the hardware and software in parallel to minimize energy consumption, form factor and cost. Several sensor nodes have been implemented such as UC Berkeley's motes, MIT's uMAPS-1 and LIMOS [2].

Finally, Micro-Electro-Mechanical Systems (MEMS) technology is available to integrate some functions and components of sensors onto the same CMOS chip. The integration of multiple local sensors such as acoustic and thermal sensors, barometric pressure detectors, optical transducers, chemical and biological transducers, and accelerometers is currently feasible.

Health monitoring is mainly used in smart nursing-home and in-home assistance that uses pervasive networks to assist habitants and their caregivers appears with the developments in microelectronic technology, wireless networks and medical fields. Structural Health Monitoring (SHM) implements a damage detection and characterization strategy. University of Southern California develops two software systems: Wisden and NET-SHM, for facilitating continuous data acquisition over a self-configuring multi-hop WSN [3]. Other researchers develop an automated wayfinding system devoted to continuous healthcare monitoring for degenerative diseases like cognitive impairments [4]. Harvard sensor network lab is working on the applications of WSN technology to a range of medical applications, including pre-hospital and in-hospital emergency care, disaster response of Parkinson's disease [5]. They also develop a wearable sensor network platform for high-fidelity motion analysis [6].

A sensor node with different types of sensors can be used in various applications, including motion tracking with GPS receiver or cardiac arrhythmias detection with ECG sensor [7]. Another key technology is to require signal processing algorithms for improving the flexibility and capability of WSN in various applications. While the raw data collected by sensor nodes are properly processed locally, only useful information is of importance and needs to be sent to the sink node. Since the computation of sensor node is much more power efficient than wireless communication, it is therefore for consideration that avoids sending large volumes of raw data in order to reduce power consumption. An outline of the envisioned impression for wireless sensor is given in the above description. The application of WSN can be categorized into two classes: data gathering application with limited signal processing requirements and computation intensive application with complex signal processing. Furthermore the emergence of WSN is to promote a research topic in health monitoring for patients. Large amounts of data gathered make it unnecessary to be transported. Thus, it becomes imperative to transmit only useful information rather than the obtained raw data so increasing the system lifetime.

1.2. Architecture of Pervasive Cardiac Care (PCC)

Healthcare application requires a relatively large amount of data and reliable communication by contrast to most WSN, which focus on data collection at the relatively low data rate. Pervasive Healthcare (PHC) is a new healthcare model that enables patient mobility, continuous health monitoring and timely detection of anomalies. PHC may be defined from two perspectives: 1) the application of pervasive computing technologies for healthcare and 2) making healthcare arbitrarily available.

The aging of the population will put a pressure on the social health insurance system. The burden of chronic disease and age-related illness significantly is increasing at the expense of

consumption of financial and human resources. The World Health Organization 'WHO' reports that France provides the "best overall health care" but spending 11.2% of GDP on health care. China takes up 22% of world population, among which around 685 million people live in rural areas. However most of expensive resources, such as health information technology and specialist have been concentrated in urban areas. China is undertaking a reform on imbalance in the present health care system. Therefore driven by quality and cost issues, the demand of health care service is prominent in China [8].

PHC is related to biomedical engineering (BME), medical informatics (MI), and ubiquitous computing (UbiComp). BME is the application of engineering principles and techniques to the medical and biology field. BME combines the knowledge in medical and biological science with particular skills of engineering to improve the patient's quality of life. MI is a cross discipline including information science, medicine and health care. MI is to introduce information technology into the biomedicine and achieve the optimization of the acquisition, storage, retrieval and use of information in health care. One of the main features of UbiComp system is expected to be their ability to large deployment of sensitized systems. Pervasive sensing in healthcare may be defined as a patient monitoring system including the following two aspects: 1) automatic and continuously monitoring of the internal and external environmental parameters of the body, 2) reliable converting the sensed data into high-level application. Pervasive cardiac care (PCC) is an example of pervasive sensing that continuously senses electrocardiography (ECG) data for estimating physical activity from heart rate and activity of users[9]. The main challenge of a wearable sensor design is the tradeoff between reliability and robustness of hardware design and patients comfort. It can be gained by the implantation of ECG electrodes into clothes that provide a high level of comfort with generated noninvasive data, while differentiating between abnormal patient states and corrupted data. In comparison invasive ECG electrodes, a non-invasive continuous monitoring system is to provide a signal of high quality without inducing skin irritation. With regards to the tradeoff between long-term portability of patient and reliable signal quality, these difficult requirements necessitate carefully design of wearable sensor, as well as intelligent data interpretation and innovative post-processing of sensor data. Post-processing of sensor data is one common approach to detect and compensate artifacts that are relatively weak signals and have low signal quality. The post-processing of sensor data has provides the improvements in sensor usability. However reliable data interpretation is still in the early stage of development. Some real-time detection algorithms are necessary to reduce high rates of false alarms and to improve data interpretation. A simple threshold to measure artifacts can lead to a false alarm since original data is corrupted and thereby looks like plausible. This will cause problems associated with the interpretation of the data. Hence, it is very useful to indicate that the signal quality has a positive impact on data interpretation and medical decision in clinical settings. In many clinical cases unreliable artifacts removal from ECG signals can lead to misdiagnosis in humans when the actual detection of cardiac arrhythmia uses the long-term continuous noninvasive ECG data to be proposed to these novel algorithms. It requires further improvements in SoC-Holter hardware and software in order to fully exploit the widespread benefits of wearable ambulatory monitoring system. There are several mature wearable sensors in various technologies, which measure cardiopulmonary symptoms as heart rate, respiratory rate, arterial blood pressure, temperature and cardiac signals. Holter and related fields of ECG monitoring have supplied one wearable

electrophysiological monitoring system in the diagnosis of cardiac arrhythmias. It is now possible to extract cardiac output from medical equipment worn by patients, record and analyze in these medical devices, lastly transmit data concerning patient's health symptoms continuously. Most existing solutions employ portable equipment that requires the patient to remain still during measurements and provides only discrete waveforms.

According to the cardiac monitoring applications, the prototypes can be divided into various requirements: 1) periodic transmission of routine heart beating signal and real-time alarm signals when vital signs cross the threshold, or device battery must be recharged; 2) wearable ECG sensor for patient comfortable; 3) accommodating the diversity amongst patients; 4) reliable access to wireless infrastructure; 5) access to diagnosis database on the Internet network; 6) the transmission of variable information needs to be reliable and effective. For example, in some medical cases, some patients with low risk require the device to transmit the vital signal every few minutes, and in some others it is necessary to transmit data every few seconds. However, in any case a sudden change of signal or detection of specific pathological symptoms should be transmitted immediately.

An existing mobile telecardiology system has the architecture that transmits the data recorded from the patient to a remote server through the network. The European EPI-MEDICS project uses an intelligent personal ECG monitor (PEM) having the capabilities of recording professional quality ECG signal for an early detection of cardiac arrhythmia. The PEM analyzes the successive ECG signal of patient and stores all the necessary information into storage device of the PEM. The device can generate three different levels of alarms based on ECG measurement and the medical history of patient. The working process of PEM for healthcare monitoring is actually divided into several steps. At first, it is necessary to transmit a real-time alarm message generated by PEM including the actual ECG signal and the patient's personal health record to the nearest emergency server. Then a short message service (SMS) produced by the server is sent to an attending cardiologist or a real-time diagnostic tool to evaluate the risk of cardiac arrhythmias in patients. Today the progress of wireless communication technology, including high capacity for data transmission and miniaturization of medical telemetry equipments, has set forth the rapid advancement in mobile telecardiology. A wireless monitoring system for hospital clinical care using PDA operates inside the hospital. Micropaq wireless patient monitoring system measures several physiological parameters of cardiac patient such as ECG signal, heart rate and blood pressure. The acquired data is transmitted to a monitoring provide by using the hospital WLAN. Another surveillance system of Medtronic [10] supports patient monitoring at home with storing an ECG at the time of an episode. Later a cardiologist will analyze the stored information and determine if the episode was caused by abnormal cardiac arrhythmias. Others systems such as CardioNet and Biotronik, provide health care of patients at home in the period of 1 or 2 weeks. A new surveillance system for outdoor mobile monitoring with continuous collecting and transmitting vital signs by wireless network such as WLAN, mobile phone network, satellite network is designed. For example, a system for out-of-hospital monitoring of patient with chronic heart disease is depicted in [11]. The telemedicine system based on wireless application protocol (WAP) is provided to remote surveillance. The patients using this telemedicine system can carry a mobile phone or other portable recording equipments that provide the services of ECG data transmission and WAP. There are also

some typical PHC systems for elderly people such as Gator Tech Smart Room, perception Room, and the elite care [12].

Heart disease is the major cause of early disability and premature death of elderly people and of middle-aged person in long-term sub-health state. It is responsible for almost two thirds of cardiac death occurs outside the hospital. Clinical experience suggests that it is more potential to reduce cardiac sudden death (CSD) by earlier detecting the cardiac abnormalities in time. New strategies are thus needed to design pervasive cardiac care (PCC) which is different from the traditional healthcare system. By introducing ubiquitous computing into traditional healthcare, the PCC system has the network architecture for telehealthcare that will open up a new method for providing continuous medical monitoring of assisted patients that are suffering from cardiac diseases. Unobtrusive and wearable sensors that combine wearable devices are used to estimate and evaluate the physiological state of patients in different circumstances such as outdoor, in-home and clinical care.

Chapter 1. Overview and Objective of the WSN for Telemedical Application

Chapter 2
Real-time Hardware Platform for ECG monitoring

In spite of the rapid development of medicine, cardiovascular disease is still the number one cause of death in the world. In many cases, cardiovascular disease causes cardiac arrest, and most cardiac arrests occur following myocardial infarction (heart attack). Most of them are sudden deaths, of which are mainly due to cardiac arrhythmias. There are mainly caused by two cases: a slow signal from the sinus node called as bradycardia makes 20% of sudden cardiac arrhythmias deaths and a fast signal generated in the ventricles of the heart called as ventricular fibrillation (VF) that frequently initiated by ventricular tachycardia (VT) causes 80% of sudden cardiac arrhythmias deaths [2]. Most sudden deaths are caused by cardiac arrhythmias. The most effective prevention and treatment of this serious disease is to provide early detection and early treatment in people who have had heart attack. Cardiovascular disease does not result from any one condition. It is not possible to list all symptoms, because each condition might have many different symptoms. There are many symptoms of heart disease that include chest discomfort, unexplained pains, shortness of breath and faster heartbeats etc. In most cases, early detection and diagnosis of these unusual symptoms help the cardiologist save valuable time in attending to the patients who need an efficient treatment to play a critical role in heart attack prevention.

An implantable cardioverter-defibrillator (ICD) is a usual device that prevents sudden cardiac death due to ventricular fibrillation and ventricular tachycardia. ICD has been extended to atrial and ventricular arrhythmias. ICD has several disadvantages limiting wider use such as the expensive implantation and complex surgical procedures. Thus it is important to develop a new noninvasive, thus wearable technology that enables to detect efficiently, accurately and early cardiac arrhythmias.

Holter monitor is an appropriate portable device to detect cardiac arrhythmias that records 1~3 leads ECG signal during 24h to 72h. However the current available preventive techniques are not fully efficient due to their cost and discomfort. The patient equipped with a Holter feels uncomfortable due to its form factor. Therefore it is necessary to develop a new cardiac monitoring device such as System-on-Chip Holter (SoC-Holter), which enables to identify precisely patients to face the high risk of sudden death. This new device should be user-friendly, cost-effective and risk-free for patients without much interference with their daily life.

This chapter gives an overview of our previous works on cardiac monitoring system and specifies some interesting technical details.

2.1. State of the Art

An ambulatory electrocardiogram records the electrical activity of a patient's heart with no concrete interference with patient's usual activities. There are many ambulatory monitors to detect cardiac arrhythmias including ambulatory electrocardiogram, ambulatory ECG,

HOLTER is medical device that can be used as monitoring system and cardiac event monitoring. As cardiac arrhythmias may be infrequent, HOLTER provides a continuous 24-72 hours recording of ECG heart to detect any abnormality in heartbeat that occur during the activities such as exercise, stress or even sleeping.

There are two basic categories of ambulatory ECG: continuous recorder and intermittent recorders.

2.1.1. Continuous Recorders

The most commonly used continuous recorder of extended ECG recording is Holter monitor that it enables to record 1~3 leads ECG signals during 24h to 72h. Holter is in general to record the electrical signals in the heart which might reasonably be expected to occur within that time frame i.e. frequency, or at least once a day. Holter monitor has several electrodes that are placed onto the patient's chest and connected to the small lightweight device with the wires. In order to facilitate patients carrying, they can wear the recorder round the waist by using a belt. ECG signals are measured by electrodes. Acquired information is saved in the storage of Holter monitor for reviewing later.

The recorded ECG signals of Holter monitoring system are processed by specific software (offline). It is necessary to generate a diagnostic report to help cardiologists for further analysis. Holter is a medical device that records the heart's electrical activity. However, it is largely insufficient to use Holter for a long-term prediction. Because the occurrence of events represented critical cardiac arrhythmias does not necessarily equate with the lifetime of Holter during these 72h [13] and [14].

A brief period includes 40 to 50 heartbeats generated by standard ECG monitors. The devices can continuous record about 100,000 heartbeats in 24 hours. It is possible to detect any abnormal heartbeats as long as they happen with the patient's activity. The patient can store a diary of symptoms and records over time intervals according to the Holter clock. It can detect cardiac arrhythmia events that may not appear during a test at the doctor's office. Every ECG beat is available to be viewed as long as they do occur during the recorded time over Holter report which is a digital format including some useful information for evaluating. However, the short-term detection may also miss some infrequent arrhythmias. Thus it is not suitable to analyze real-time ECG for preventing the real-time heart attack. ECG signals stored on the Holter monitor are processed later with dedicated software developed by programmer that gives a Holter pilot report to the cardiologist for further analysis. Comparing to conventional ambulatory ECG in detecting episodes of cardiac arrhythmias, there are some continuous recorders which can be implanted under the skin of the chest without any wires or chest sensors. These implanted recorders allow to record electrical signals of the heart for a

longer time than the others. In some cases the lifetime extends even to one year so that they provide enough recorded data for diagnosis of cardiac diseases.

There are no contraindications for holding Holter recorder which doesn't interfere with the normal daily life of the patients. The patients can do normal activities while they are wearing the Holter recorder, except taking a bath or shower.

Holter monitoring is not an appropriate diagnostic recorder for intermittent palpitations which usually behave infrequent symptoms of an abnormal heart rhythm. Therefore intermittent recorder is useful for this kind of ambulatory ECG. The longer recording period of intermittent recorders is almost the main reason which implies a higher diagnostic yield than a continuous recorder.

2.1.2. Intermittent Recorders

Intermittent recorders are further divided into loop recorders and event monitors.

- **Loop Recorder**

A loop recorder is a portable device which enables to record ECG signals continuously for an extended period of time. Unlike Holter, not all ECG signals are recorded, but only a sequence of ECG signals will be saved when the patient notes or feels a cardiac arrhythmia symptom. The information may be sent to cardiologists or saved locally. Loop recorder is implantable for long monitoring period (18 months) [15].

A loop recorder can record the heartbeats continuously. When the patient feels the occurrence of symptoms, the patient can record the state of the heart by pressing a button on the recorder. Though the loop recorder works as alike as the event recorder in operation, it is different as the event recorder only stores a brief recording ECG signal. It is also configured to record and erase automatically a sequence of ECG signals after the recorder detects the abnormality defined by cardiologists. In order to retain the important information for cardiologists' diagnosis, the ECG signals before 1 to 4 minutes and after 30 to 60 seconds of abnormality are all gathered in the device. When the button is pressed, a small amount of information of the heartbeat is saved in the loop recorder before the occurrence of symptoms. This function is especially useful and avoids the defect that the ECG signals cannot be recorded when the patient is unconscious or asleep while the heart problems occur. Newer loop recorders can transmit the recording ECG signals via telephone/3G mobile/internet to a remote surveillance for cardiologists to analyze.

Cardiologists set the function of recorder by relying on the different application scenarios and requirements, and by taking into account the patient's physical status and medium access with available bandwidth for wireless network. Since the recorder is not a continuous monitoring, ECG signals will not be analyzed immediately, but be stored on the recorder for a detailed process analysis in the future. It can be not used for real-time monitoring of the patient with the gravity of the symptoms. These intermittent episodes are more reliably detected when the ECG signals are recorded continuously over a long-term period because some transitory changes of symptoms may easily be missed due to the relatively short time period.

The R.TEST is a one lead cardiac event recorder which can long term record a sequence of ECG signals, when the patient notes an arrhythmia symptom. Furthermore, R.TEST may be configured to record automatically cardiac arrhythmias up to 8 days. The recorded ECG signals would be sent through MODEM/Email communication to a remote server to be analyzed and diagnosed either by a cardiac technician or by a cardiologist [14].

Note that loop recorder and R.TEST enable to monitor an extended period of time and the patient can manually save the ECG signals, but cardiac arrhythmias are often asymptomatic.

- **Event Recorder**

Ambulatory Event recorder can provide longer periods of monitoring because it stores only a brief recording of ECG signals while the electrical activity of the heart in response of symptoms of the heart problem are perceived by patients. This recorder is suitable for long-term monitoring toward the patient who has a lower risk of sudden death because it works only when symptoms of cardiac arrhythmias appeared. Note that cardiologists cannot seek a cardiac etiology of the patient's symptoms without the observed abnormality on ECG signals.

Since the event recorder is carried by the patient over a longer period of days or weeks to record cardiac arrhythmias that occur infrequently, it should be very small in order not to disturb the wearer daily life. The event recorder is very easy to carry for the patient. The patient can wear the event recorder on the wrist like a watch or carry it in his purse or pocket. In the first case, the patient can record ECG signals by only typing a button on the recorder when symptoms occur. But in the later case, it is a little complicated for the patient who needs to press the back of the recorder against the chest and then press the button on the recorder to start recording when the symptoms of the heart diseases are felt. The back of the device has small metal discs that have the same function as electrodes in other monitoring devices. Since the ECG signals are recorded only when symptoms happened, we can obtain a relationship between these symptoms and the underlying cardiac arrhythmias. The event recorder is only activated by the patient when symptoms occur and stored several minutes of ECG signals, so this recorder also has a shortcoming for the real-time application like Holter monitoring. Furthermore, it is too dependent on the subjective feeling of the patient. This subjective judgment is always credible to influence the performance of Holter.

The recorded data of an intermittent recorder can be sent over wireless network technology in the patient's home or mobile phone network to the office of cardiologists, clinic or hospital.

Figure 2.1 illustrates a simple presentation of an example of wireless sensor network, where wireless sensors are used to capture ECG signals and send them to an external (remote) server. Subsequently the remote server aggregates all the ECG signals. This system integrates the advanced wireless technology and the distributed embedded real-time intelligent sensors communication over the internet. It consists of two subsystems: a local subsystem and a remote subsystem. The local subsystem contains a wireless sensor or a wearable device and a local server. And the remote subsystem includes a remote server accessed to the internet and a remote diagnosis and surveillance system. There are two main operating modes of the system: online and offline. In online mode, the sensors are placed on the user's bodies to gather ECG signals which are then transmitted to a local server at home or in the hospital, depending on a wireless medium such as WiFi, Bluetooth and ZigBee. In offline mode, ECG signals are

converted to digital data and stored into a Multimedia flash Memory Card (MMC) without any analysis and diagnosis. Obviously the lifetime of the system in this mode is relative to the specifics of the device: the storage capacity of the MMC, the sampling rate of the device and the number of ECG leads.

In fact, we have implemented a platform dedicated to telemedicine applications in LIMOS previous work. The system has the ability to perform real-time cardiac arrhythmias tele-assistance and monitoring [14]. The system is composed of wireless ECG sensor (WES), local access unit, remote center server and remote surveillance terminal [16] and [17]. These 4 configurable elements are combined to perform complex applications in cardiac arrhythmias. The platform was used to evaluate 30 patients of the cardiology department at the CHRU of Gabriel Montpied's hospital (Clermont-Ferrand, France). Each patient was equipped with the WES and with the HP's telemetry device. In real-time this platform provides the same results as the HP's telemetry devices. Note that the quality of the ECG signal of LIMOS platform is better than the HP's telemetry device because the sample frequency of the WES is higher (1 KHz). Moreover, note that the WES electrical features response the last AHA (American Heart Association) recommendations [18].

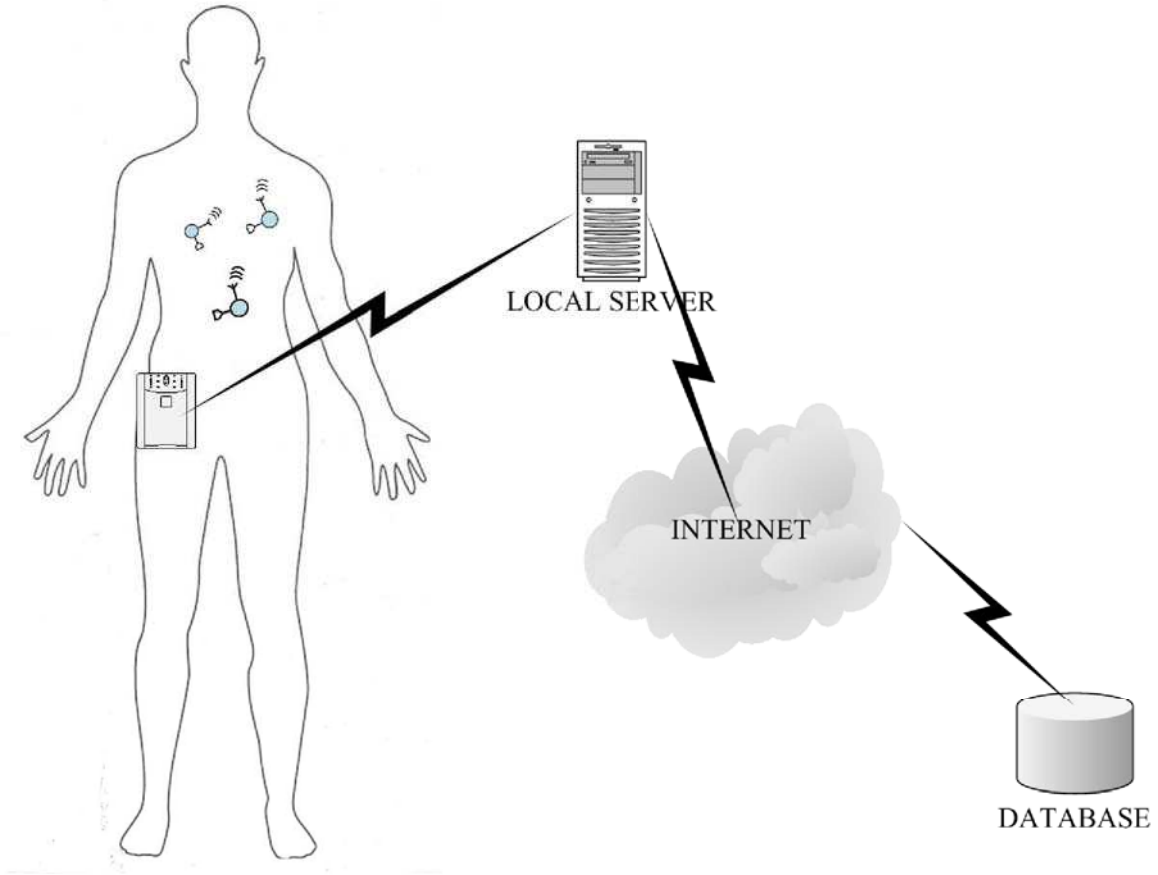

Figure 2.1 Wireless sensor work for medical application.

There are several application modes and operation modes of the WES. It is configured merely as an ECG surveillance equipment to monitor the heart states of patients. The recorded data of ECG signals are stored into the internal memory in the WES. It is not very convenient for patients because they need to periodically go to the hospital to submit the ECG records to cardiologists for further diagnoses. The cardiologists analyze and diagnose these ECG signals

of WES, which works like the Holter [19]. In another application mode, patients and cardiologists in the local area can directly exchange the ECG records by sharing the local network infrastructure. The ECG signals acquired by the WES will be compressed and sent via local wireless mediums. Note that the diagnostic procedure is not implemented in the WES but on local or remote server, thus reduce the required resource in the WES. In this mode, our system works as a telemetry arrhythmia recording system, as shown in the Agilent telemetry system [2]. If the patient is far from the cardiologist, the connection is established via the existent network infrastructure, for example the wide wireless technology.

The telemedicine system using LIMOS platform offers three operation modes over the different application schemas but can be configured by the cardiologist in order to evaluate the patient's heart status. The first also the highest alarm mode provides the real-time continuous ECG signals for online diagnosing by cardiologists. This operation mode has some limitations due to the restricted network bandwidth, system resources and human resources. In the second operation mode, the system stores and sends only a sequence of ECG signals, which consist of the two side data of cardiac arrhythmias events. This mode avoids generating huge data and network traffics. This operation mode is suitable for lower-risk heart disease population, who are needed to reduce data for monitoring the presence of heart disease. In the third mode, a short emergency message is sent to the cardiologist including the symptom of the cardiac arrhythmia.

Thanks to LIMOS previous works and experiment results, we think that one of the key issues to prevent sudden death is to develop an effective device such as SoC-Holter for early detection and early treatment, which should be user-friendly, cost-effective and more expedient to use for a large number of populations. In the next section we focus on the implementation of SoC-Holter and present all hardware components.

The previous WES is built by using commercial off-the-shelf (COTS) components and it has the following functions: signal conditioner and pre-amplifier, low-pass and high-pass filters, MSP430 microcontroller (low power 16-bit RISC processor) [20] and wireless access medium module Figure 2.2(a).

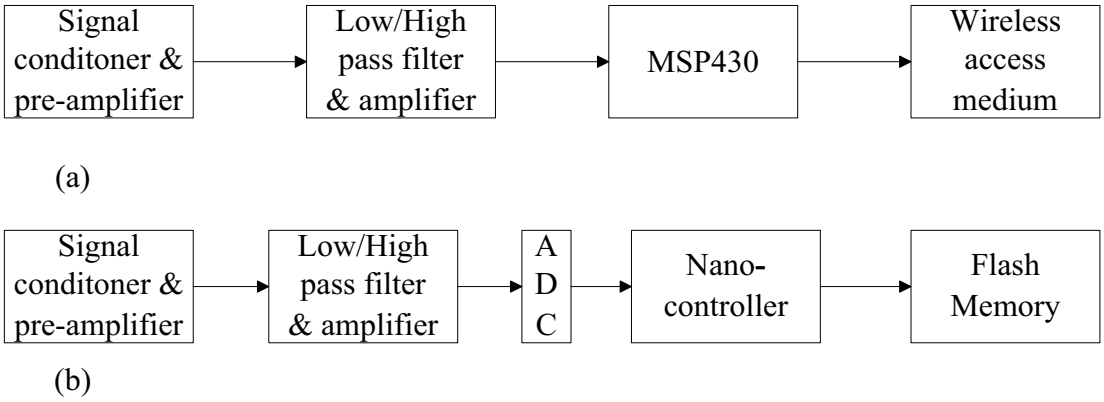

Figure 2.2 Block diagram of WES (a) and SoC-Holter (b).

The previous versions of WES prototype is implemented on procedures recommended by the AHA (American Heart Association) [18]. The WES prototype (Figure 2.1) contains a wireless embedded sensor (size=70*100mm) that are useful for real-time monitoring and a

highly portable. The device is designed on the MSP430 which is an ultra low power microcontroller family and provided from Texas Instruments [14].

A dedicated SoC-Holter integrates as much functionalities as possible into a single chip and miniaturizes the die area, which enables to decrease power consumption. Its architecture is shown in Figure 2.2(b). Integrated Nano-controller means that SoC-Holter allows signal processing in chip and increases the system performance. The entire system also becomes more flexible. ECG signals can be transmitted immediately for real-time application or saved in memory for offline mode. The latter mode avoids consuming much energy in sending large volume of raw data, suitable for the patients without serious illness. The technical features of SoC-Holter are: (i) Gain: 500; (ii) Minimum Common Mode Rejection Ratio (CMRR): 110dB; (iii) 3 dB Bandwidth: 140Hz; (iv) Programmable sampling frequency: from 500 up to 1000Hz; (v) Resolution of Analog to digital converter (ADC): 12 bits; (vi) Leakage current: 10μA.

2.2. Background on Hardware Platform for Wireless Sensor Network

Portable medical equipments are designed to monitor the body status of the patients or the athletes via transformation of biophysical signals into electrical signals. The application of ECG signals is critical due to the low amplitude of the signals recorded by the sensors and corrupted with the presence of many sources of noise (e.g. motion artifact). ECG signals are measured in the sensor range from a 1mv (400μv) to 5mv that the frequency extending from 0.05 Hz to 130 Hz. When the recorded ECG signal is amplified, the noise is amplified too, and often stains the original ECG signal. Luckily, the noise is usually generated by electromagnetic interference. Differential amplifier where the sensed ECG signals are distributed into two equal signals but opposite phases has been considered. However the noise of a higher frequency can be reduced by low-pass filtering.

Another reason for using differential amplifier is to obtain ECG signals as the difference in voltage between two nearby points on the skin. The differential amplifier basically amplifies the difference of voltage subtracting from input voltages. Certainly the common mode voltage of two differential signals is placed in center potential between both input signals. The common reference is typically chosen to be far away from the heart, so an ideal choice is at the location on the right leg of the patient. When we choose the symmetric structure of differential amplifier, noise affects a couple of output signals by equal amount. Moreover thanks to the symmetric structure the peak to peak output swing is equal to two times of single-ended counterparts. It may seem the differential circuit occupies twice as much area as single-ended one, the advantages of differential amplifier counteract far beyond the drawback of the possible increase in the circuit area.

2.2.1. MOS Characteristics

Complementary Metal-Oxide-Semiconductor (CMOS) is the most widely used electrical transistor for implementing integrated circuits, which is utilized in microprocessors, microcontrollers and other digital logic circuits [21]. CMOS devices offer the feature like high noise immunity over a wide range of power supply. Another important characteristic of CMOS devices is to exhibit lower static power consumption to provide the feasibility of high density in electronic design. Shown in Figure 2.3 is a cross section of two CMOS transistors with a gate tie. As in the case of N-well CMOS process, four terminals of one device are gate (G), source (S), body (B) and drain (D). A single crystal silicon wafer fabricated on a p-type substrate is also called the body. The device consists of two heavily doped n-type regions, which are the source and the drain regions, and a heavily doped piece of polysilicon operating as the gate. A thin layer of silicon dioxide (SiO_2) is insulating between the source and the drain.

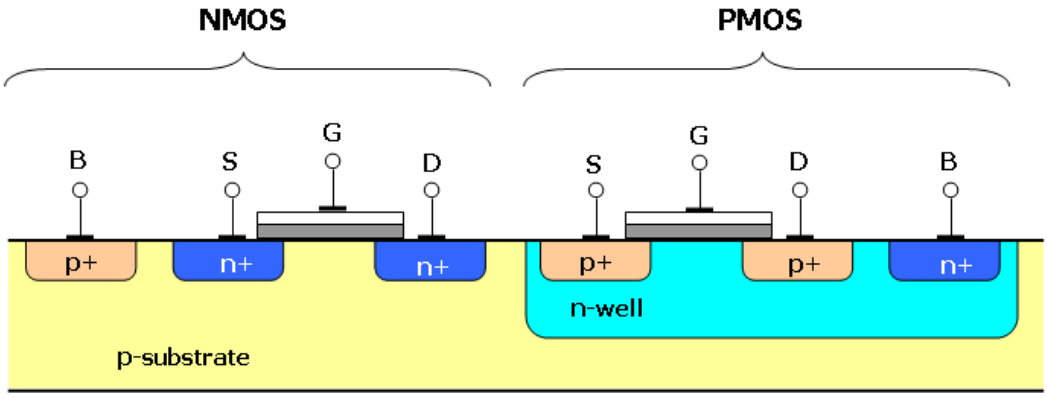

Figure 2.3 The actual connection provided through p-substrate.

In order to design a differential structure amplifier and obtain the relationship between the current and the voltage, we make some derivation of I/V characteristics of CMOS devices. As shown in Figure 2.4, in the beginning of the parabolas, there is approximate a straight line in deep triode region. Then the drain current becomes relatively constant when this CMOS device operates in the saturation region.

Figure 2.4 shows a typical set of current-voltage characteristics for different values of V_{gs}, indicating that the increase of the current of the device follows certain rules. It could be classified three regions of operation according to some relationship of the voltage of various terminals.

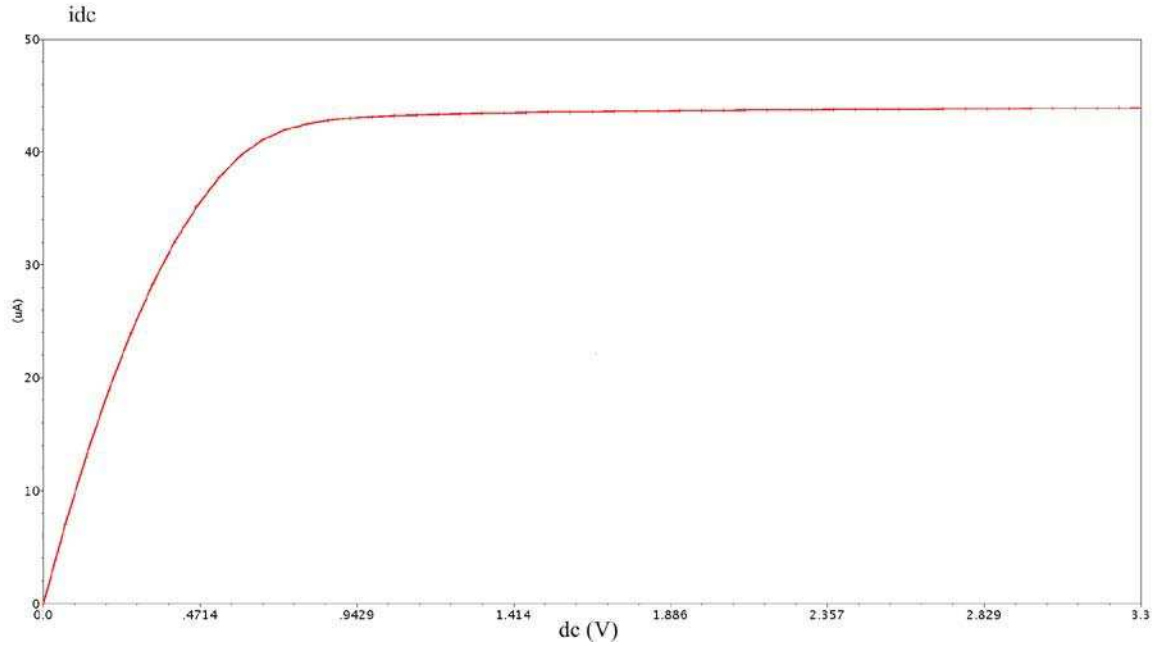

Figure 2.4 Drain current versus drain source voltage.

If the V_{gs} increases from zero, the MOS is off and no current crosses the device. So $V_{gs} < V_{th}$ (V_{th} is the threshold voltage) means the transistor is in the region of cut-off operation, where no channel effect and no current are present.

If $V_{gs} > V_{th}$ and $V_{gs} - V_{ds} > V_{th}$, the terminal S and terminal D are connected and the electrons in the channel are flowed. Since current is constant along the channel, we can get an equation as

$$I_d = \mu_n C_{ox} \frac{W}{L}\left[(V_{gs} - V_{th})V_{ds} - \frac{1}{2}V_{ds}^2\right] \tag{2-1}$$

L is the effective channel length and W is the effective channel width, μ_n represents the mobility of electrons of the transistor, C_{ox} is the gate oxide capacitance per unit area. The transistor operates like a resistor expressing the characteristic of transition from the exponential subthreshold region to the triode region.

The current of the device reaches the peak at $V_{ds} = V_{gs} - V_{th}$, this current is

$$I_{d,max} = \frac{1}{2}\mu_n C_{OX} \frac{W}{L}(V_{gs} - V_{th})^2 \tag{2-2}$$

$V_{gs} - V_{th}$ is the overdrive voltage and W/L is the aspect ratio, if $V_{ds} \leq V_{gs} - V_{th}$, the device operates in the triode region, also called the linear region.

Back in Equation (2-1), if V_{ds} is much less than $2(V_{gs} - V_{th})$. The drain current is regarded as a linear function of V_{ds}.

$$I_d \approx \mu_n C_{OX} \frac{W}{L}(V_{gs} - V_{th})V_{ds} \tag{2-3}$$

This is evident as shown in Figure 2.4, each front part of the curves can be approximated by a straight line. This linear relationship implies that the connection of terminal S and terminal D can be represented by a given resistor

$$R_{on} = \frac{V_{ds}}{I_d} = \frac{1}{\mu_n C_{OX} \frac{W}{L}(V_{gs} - V_{th})} \tag{2-4}$$

The above equation is describing the dependence of current capability upon the constant of the technology $\mu_n C_{OX}$. Approximately $10\mu A/V^2$ for the standard NMOS process with $0.1\mu m$ oxide thickness. So the aspect ratio of W and L and drain potentials determine the current capability of the device.

For PMOS devices, the equations are respectively written as

$$I_d = -\mu_p C_{OX} \frac{W}{L}\left[(V_{gs} - V_{th})V_{ds} - \frac{1}{2}V_{ds}^2\right] \tag{2-5}$$

and the peak current is

$$I_{d,max} = -\frac{1}{2}\mu_p C_{OX} \frac{W}{L}(V_{gs} - V_{th})^2 \tag{2-6}$$

The negative sign means I_d flows from the source to the drain. Generally the current capacity of PMOS devices is about one-half to one-fourth of NMOS devices.

If $V_{ds} > V_{gs} - V_{th}$ and $V_{gs} > V_{th}$, the device operates in the saturation region and current I_d keeps relatively constant. I_d equals to the maximum of the parabola and relatively independent of V_{ds}. To understand this phenomenon, there is a principle which the local density if the inversion layer charge is proportional to $V_{gs} - V_{th} - V_1$. Where V_1 is the channel potential at position of 1. Thus, if the channel potential V_1 approaches $V_{gs} - V_{th}$, in other words, V_{ds} is slightly greater than $V_{gs} - V_{th}$, the inversion layer stops and the channel is pinched off. The current no longer depends on the voltage apply between terminal S and terminal D.

$$I_{d,sat} = \frac{1}{2}\mu_n C_{OX} \frac{W}{L}(V_{gs} - V_{th})^2 \tag{2-7}$$

Thus the device provides a constant current whose value is independent of the drain voltage V_{ds} and only determined by the gate voltage V_{gs}.

For PMOS devices equation (2-7) is written as

$$I_{d,sat} = -\frac{1}{2}\mu_p C_{OX} \frac{W}{L}(V_{gs} - V_{th})^2 \tag{2-8}$$

The negative sign means I_d flows from the source to the drain, in the opposite direction of NMOS devices. It is very useful to discuss the operation state of device in saturation, according to complete independence of V_{ds} and the corresponding infinite output resistance, the latter is an idealization because the change of V_{ds} has no effect to I_d when the channel is pinched off. However in practice, increasing V_{ds} affects the channel because the pinch-off point of the channel breaks off from the drain and moves toward the source with the increase of V_{ds}. The shift of pinch-off point causes the reduction of effective channel. This called

channel length modulation, which means the channel resistance proportional to the channel length. As a result, the drain current has a slight increase beyond the saturation level. The channel length modulation can be introduced with a mathematical formula as

$$I_{d,clm} = \frac{1}{2}\mu_n C_{OX}\frac{W}{L}\left(V_{gs} - V_{th}\right)^2(1 - \lambda V_{ds}) \tag{2-9}$$

λ is the channel length modulation parameter, generally range from 0.005 to 0.03.

The output resistance in saturation is written as

$$R_{out} = \frac{V_{ds}}{I_{d,clm}} \approx \frac{1}{\frac{1}{2}\mu_n C_{OX}\frac{W}{L}\left(V_{gs} - V_{th}\right)^2\lambda} = \frac{1}{\lambda I_d} \tag{2-10}$$

Thus the output resistance is inversely proportional to the current I_d.

In our circuit design, the output resistance is usually 1000Ω according the current CMOS technology using the 50Ω and 75Ω impedance system. Therefore in many cases the channel length modulation affects the performance very slightly. But we can use this relationship between resistance and current to adjust the parameters of the circuit and make the circuit operate in the correct bias point. In addition, the channel length modulation effect will also affect noise parameter of the MOS device.

The body effect is another important issue that needs to be taken into consideration. The body effect describes the change of V_{bs} because the different potential between the body and the source of the devices. Then as V_{gs} changes and V_{ds} follows, the potential difference between the source and the body makes the value of V_{th} change.

$$V_{th} = V_{th0} + v\left(\sqrt{|2\Phi_F + V_{sb}|} - \sqrt{|2\Phi_F|}\right) \tag{2-11}$$

where V_{th0} is zero bias threshold voltage, Φ_F is Fermi energy level, v is body effect parameter, typically equals to between 0.3 to 0.4 $V^{1/2}$.

The body and the source of the devices would be connected to minimize the body effect. On most transistors, the body is connected to the lowest or the highest potential within the circuit, depending on the transistor type. For example, the body and the source of NMOS transistor is connected to the ground, by this way, the effect of the body effect in the transistors is reduced. However, it is impossible to ignore the body effect in the actual design, because most of transistors in integrated circuits whose sources are not directly connected to the body terminal. Body effect is usually undesirable. The change in the threshold often complicates the design of the circuit. Fortunately the majority of transistors used in the circuit operating in the strong inversion region, which means V_{ds} and g_m often large and the threshold voltage V_{th} is not sensitive against V_{ds}.

2.3. Amplifier

Electrode V_5 is placed on the left side of the chest and has noisy output. From the measured ECG signal, the amplitude of a standard ECG circle can be deduced about 1mV. In fact to be able to extract ECG signals from noise, it is necessary to implement an appropriate

signal conditioner and preamplifier stage having at least 110dB of CMRR. The discussion about theoretical approach of the operational amplifier is as follows.

2.3.1. Common-mode Input

The simplest input of the operational amplifier is connecting PMOS or NMOS input transistor with NMOS and PMOS load transistor. To present a great range output dynamic range, the common mode input architecture is introduced. The transconductance of the differential pair, no matter what type they are, the value of transconductance holds unchanged over its range and drops to zero outside the range. The complementary differential pair has the configuration which simultaneously implements both NMOS and PMOS differential pairs as shown in Figure 2.5.

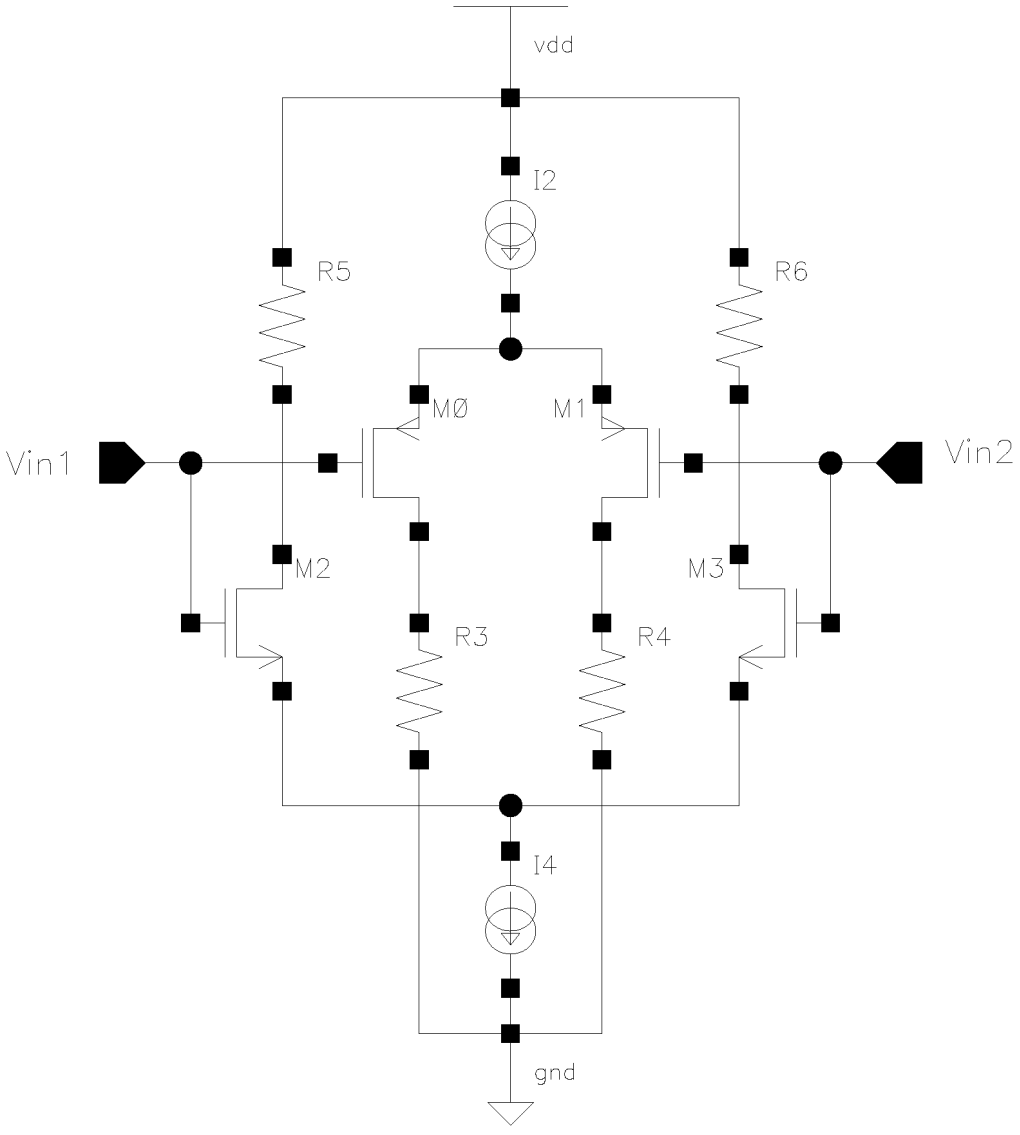

Figure 2.5 Complementary differential pair common mode input range.

If the input voltage is below threshold voltage V_{th}, the NMOS transistor is off, as V_{in} approaches $V_{th} + V_{1,sat}$, where $V_{1,sat}$ is minimum voltage needed to keep the current source in

saturation. Applying the same analysis as the NNOS differential pair, we will obtain the result of the PMOS differential pair as shown in Figure 2.6. If the input voltage ranges form $V_{gs} + V_{1,sat}$ to the positive supply or the negative supply. The fact that both NMOS and PMOS differential pairs are working makes the input voltage keep in the middle region of the figure. It is obvious that the transconductance of the complementary differential pair is higher than the case when only one sort of pair is used. And the transconductance of each pair when it operates over the common mode range has a constant value. But the transconductance drops dramatically when the device moves away this area of common mode.

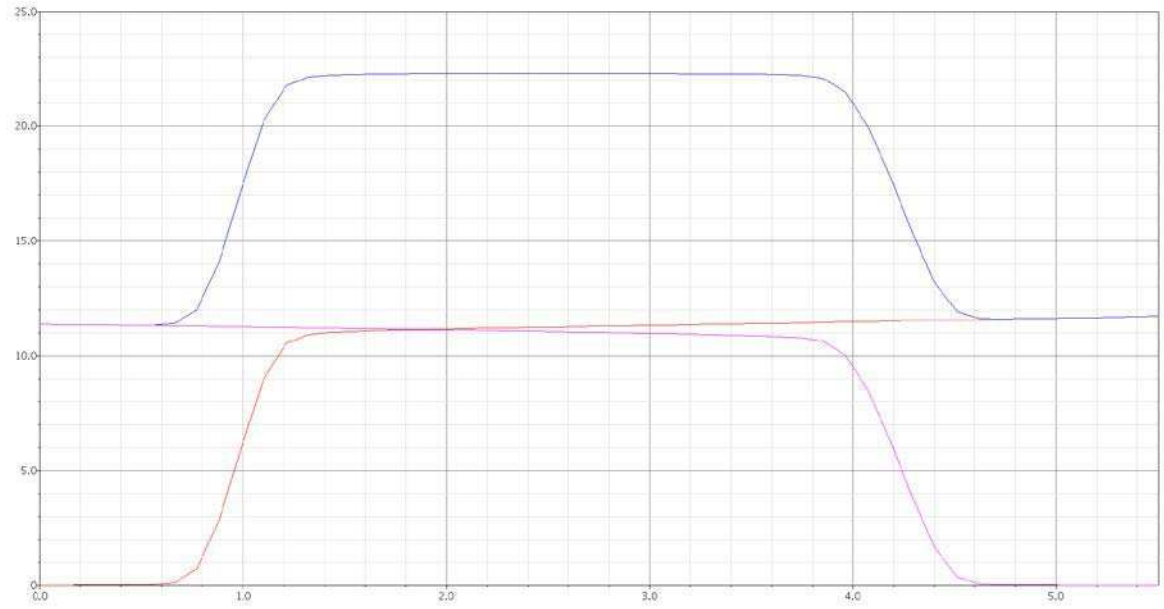

Figure 2.6 Complementary differential pair transconductance versus common mode input.

Thanks to all transistors that form both NMOS and PMOS differential pairs operate in the saturation region, the transconductance of the complementary differential input stage is given by:

$$g_{m,np} = g_{m,n} + g_{m,p} = \sqrt{\mu_n C_{OX} \frac{W_n}{L_n} I_n} + \sqrt{\mu_p C_{OX} \frac{W_p}{L_p} I_p} \tag{2-12}$$

We can control the transconductance by the tail current or the aspect ratio of both differential pair from the upper equation. As these transistors are operating in the saturation region, the Equation (2-12) is rewritten as

$$g_{m,np} = \sqrt{\mu_n C_{OX} \frac{W_n}{L_n} \frac{1}{2} \mu_n C_{OX} \frac{W_n}{L_n} \left(V_{gs,n} - V_{th,n}\right)^2} + \sqrt{\mu_n C_{OX} \frac{W_p}{L_p} \left(-\frac{1}{2} \mu_p C_{OX} \frac{W_p}{L_p} \left(V_{gs,p} - V_{th,p}\right)^2\right)} \tag{2-13}$$

and the negative sign inside the second radial only indicates the current direction. So

$$g_{m,np} = \frac{1}{\sqrt{2}}\mu_n C_{OX}\frac{W_n}{L_n}\left(V_{gs,n} - V_{th,n}\right) + \frac{1}{\sqrt{2}}\mu_p C_{OX}\frac{W_p}{L_p}\left(V_{gs,p} - V_{th,p}\right) \quad (2\text{-}14)$$

The transconductance can also be controlled by the effective voltage of the transistor as depicted from this equation.

The common-mode input is the first stage of the future structure. The disadvantage of this structure is unable to provide the required gain, because the output resistance can only reach 100KΩ. So the maximum gain provided by the common-mode input is around 40 dB.

2.3.2. Full Differential Operational Amplifier

Full differential amplifier has an obvious advantage that the output signal swing is two times than the counterpart of single ender amplifier. Because a single ended output operational amplifier (op-amp) has the maximum output voltage equaling to $V_{dd}/2$. However, the maximum output voltage of the full differential op-amp is V_{dd}, which equals to the difference between the output ends. The result is obvious to increase the dynamic range of circuits employing full differential signal paths.

The open loop gain of the full differential op-amp is given in terms of the inputs and outputs

$$A_o = \frac{V_{op} - V_{om}}{V_{ip} - V_{im}} \quad (2\text{-}15)$$

We should notice the open loop gain of the single ended op-amp is

$$A_o = \frac{V_o}{V_{ip} - V_{im}} \quad (2\text{-}16)$$

So a differential op-amp can be formed by two single ended topologies that work well at low frequency.

2.3.3. Common Mode Feedback (CMFB)

The CMFB is necessary to design high-gain differential op-amp. It is a simple realization of a single ended op-amp, where the DC level is relative to the current mirror. The output Common Mode (CM) level is quite sensitive to circuit properties. For a full differential op-amp, the output CM level is largely depending on the bias voltage of the current source. This means mismatch of the circuit that can lead op-amp to unstabilization. Thus the CMFB must be added to sense the CM level of the outputs and adjusted according to the bias current or the bias voltage.

In fact the foregoing depiction implies that the circuit could be unstable in the sense that a small deviation of the input common mode and the gain is dependent on the different bias voltage. Thus the introduction of CMFB can make the gain not so dependent on the input common mode.

One approach to design CMFB is to employ a resistive divider that is a continuous time approach, another corresponding approach is a switch capacitor approach using a capacitive divider. Our CMFB is described in Figure 2.12. It is composed of 2 parts that are the common mode level sensing and the comparator. The common mode level sensing is to sense the CM level and the comparator is to compare the CM level to a voltage reference and give negative feedback. Also it is noticed that the current in the first stage is controlled by CMFB. When the CM level is increased, the current is increased also that increases the current in the input branch flowing from the NMOS/PMOS load transistor. On the opposite case, the current is decreased that decreases the current in the input branch flowing from the NMOS/PMOS load transistor. Thus the output of the comparator corrects the current in the input stage and makes the circuit work stable.

2.3.4. Current Mirror

In the design of differential amplifiers current mirror acts as a large resistor without consuming excessive voltage headroom. Current mirror is useful in analog-to-digital convertors to provide current sources as well.

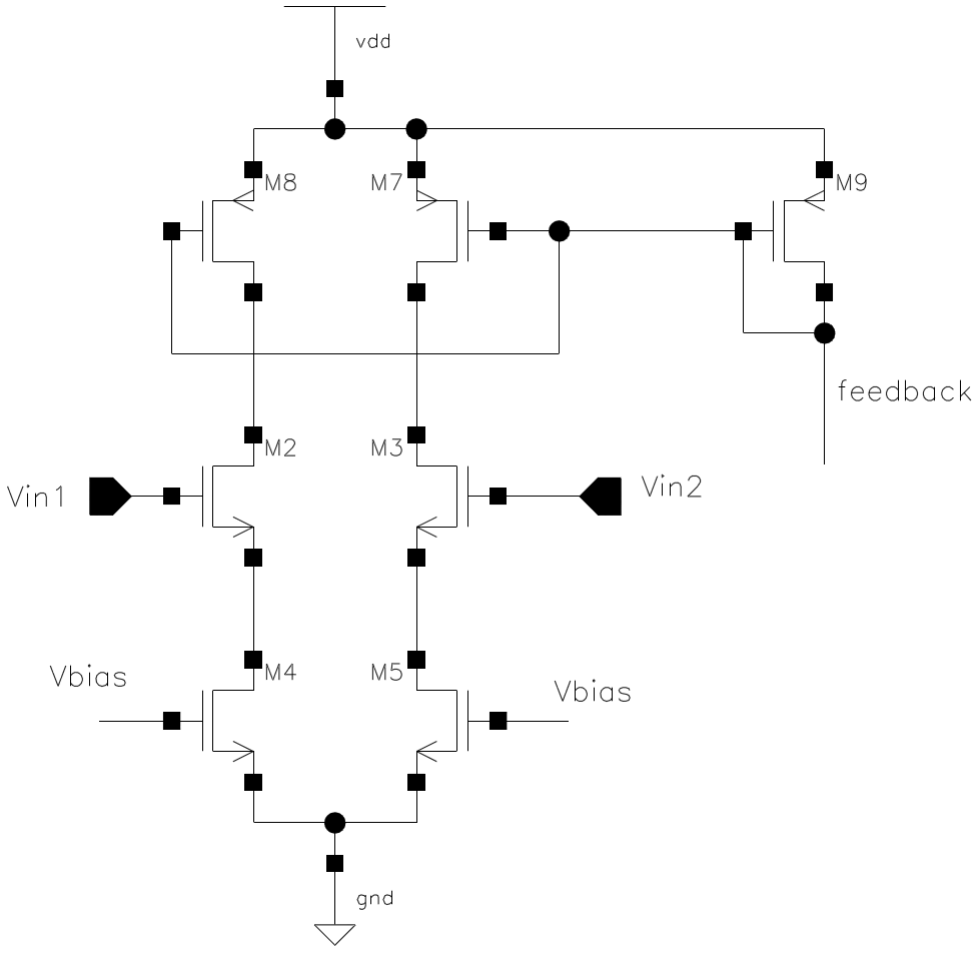

Figure 2.7 Schematic of current mirror.

The negative sign only means the direction of the current. Drain current is written as

$$I_{ref} = -\frac{1}{2}\mu_p C_{OX}\frac{W_{MP9}}{L_{MP9}}\left(V_{gs} - V_{th}\right)^2 \quad (2\text{-}17)$$

obtaining

$$I_d = \frac{\frac{W_{MP7,8}}{L_{MP7,8}}}{\frac{W_{MP9}}{L_{MP9}}} I_{ref} \quad (2\text{-}18)$$

The result in Figure 2.8 shows the property of the current mirror which allows precise copying of the current with independence on process and temperature, the repetition of the reference current is only related to the ratio of device dimensions. Another point we should remark that the stage is reliably biased only if a feedback loop force V_{out} to a known value.

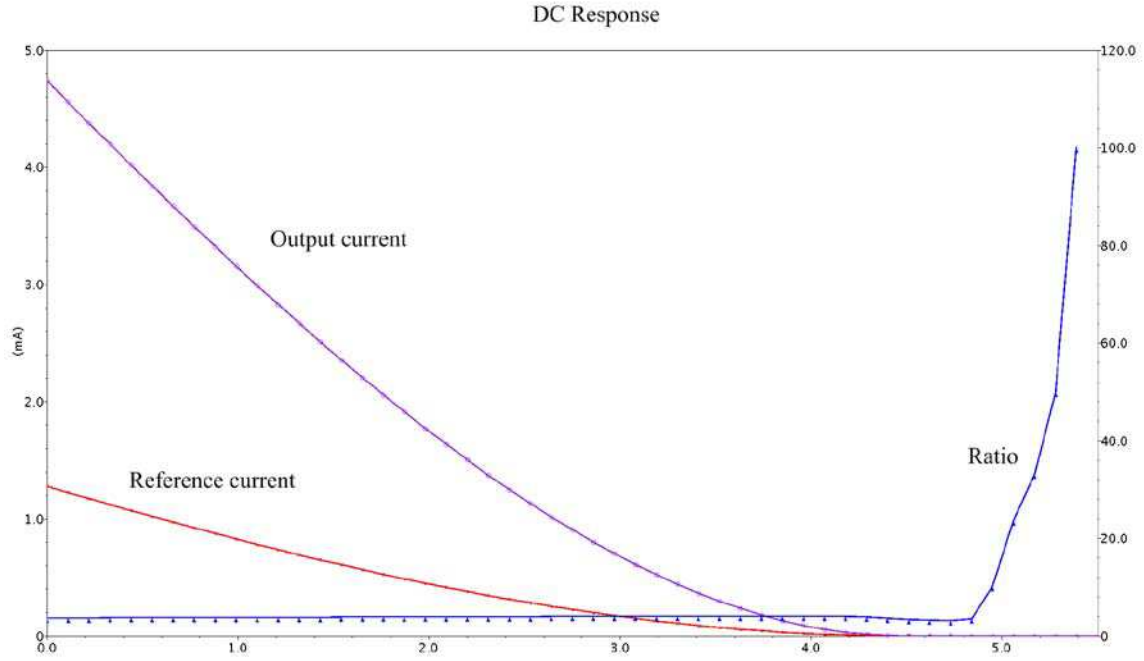

Figure 2.8 Current mirror simulation result.

2.3.5. Shunt-shunt Feedback

A negative feedback amplifier is an amplifier in which part of the output signal is looped back to the input to form the error signal to oppose the original signal. The amplifier uses negative feedback to obtain the constant bandwidth and improve gain stability, linearity and frequency response. The closed-loop gain is independent with parameter variation due to chip production and environment temperature. A shunt-shunt feedback amplifier is an inverting amplifier in which the input voltage signal is converted into a current [22]. Feedback system that shows a negative feedback system, where A_{OL} or A is called feedforward network and β is feedback factor.

$$\frac{V_{out}}{V_{in}} = \frac{-A}{1 + \beta A} \quad (2\text{-}19)$$

An operational amplifier consisting of a negative feedback network is shown in Figure 2.9. The input signal is connected through a resistor R_F to the inverting input. The resistor R_S is placed in series with input source for a converting function. The input current I_{in} and the feedback factor β are given by

$$I_{in} = \frac{V_{in}}{R_S} \tag{2-20}$$

and

$$\beta = \frac{1}{R_F} \tag{2-21}$$

The error current I_{err} is a piece which a fraction β of the output is subtracted from the input current, where

$$I_{err} = I_{in} + \beta V_{out} \tag{2-22}$$

noticing the shunt-shunt feedback amplifier is an inverting amplifier, thus V_{out} is negative comparing to I_{in}.

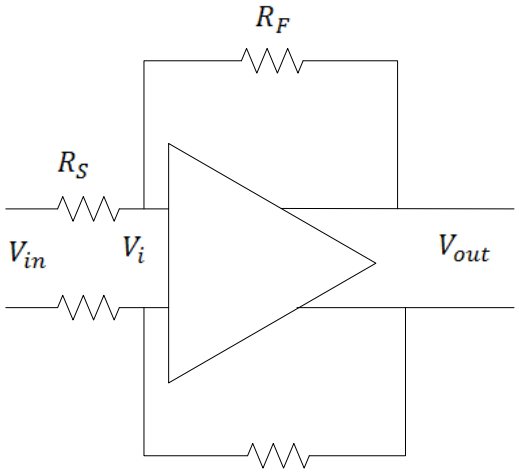

Figure 2.9 Full differential op-amp configuration.

Because the input is a current and the output is a voltage, the gain A represents by a resistance r_o. Note that the feedback connects to the same terminal as the input signal, we get

$$V_i = (I_{in} + \beta V_{out})R_1 = I_{err}R_1 \tag{2-23}$$

and

$$R_1 = R_S||R_F \tag{2-24}$$

$$R_2 = R_O||R_F \tag{2-25}$$

The circuit can be presented by the Mason signal flow graph [23]. Mason's formula can be used to find the transfer function of a given signal flow graph. The gain formula is as follows

$$G = \frac{1}{\Delta}\sum_k G_k \Delta_k \tag{2-26}$$

where G_k is the gain of the k^{th} forward path, the determinant of the graph is

$$\Delta = 1 - \sum L_i + \sum L_i L_j - \sum L_i L_j L_k + \cdots + (-1)^m \sum \cdots \tag{2-27}$$

where L_k is the loop gain of each closed loop in the system. So the determinant of Figure 2.10 is given by

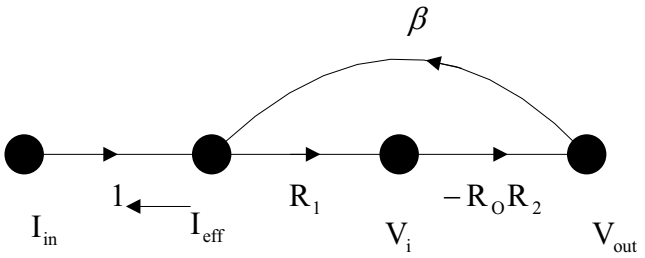

Figure 2.10 Signal flow graph for Figure 2.9.

$$\Delta = 1 - [R_1(-R_O R_2)\beta] = 1 + \beta R_O R_1 R_2 \tag{2-28}$$

from the flow graph, the transresistance gain is given by

$$\frac{V_{out}}{I_{in}} = \frac{1}{\Delta}(-R_O R_1 R_2) = \frac{-R_O R_1 R_2}{1 + \beta R_O R_1 R_2} = \frac{-A}{1 + \beta A} \tag{2-29}$$

and

$$A = R_O R_1 R_2 \tag{2-30}$$

The voltage gain of the original circuit in Figure 2.10 is

$$\frac{V_{out}}{V_{in}} = \frac{V_{out}}{I_{in}}\frac{I_{in}}{V_{in}} = \frac{-A}{1 + \beta A}\frac{1}{R_S} \cong \frac{-A}{\beta A}\frac{1}{R_S} = -\frac{R_F}{R_S} \tag{2-31}$$

Using negative feedback configuration has some properties to increase the performance of op-amp. 1) make the gain of the system less sensitive to variations of circuit components, such as variation caused by temperature, 2) make the system more linear that means the output proportional to the input with independent of signal level, 3) reduce the effects of unwanted electric signals generated by the circuit components and inference, 4) control the impedances by adjust feedback topology, 5) increase the amplifier bandwidth. These properties are obtained by reducing the gain of the system and increasing the instability.

2.3.6. Two Stages Operational Amplifier

In our design of preamplifier, we desire to obtain a high gain and large output swing. But this is too hard to implement by only one stage operational amplifier, which allows the gain to have the limitation due to the input pair transconductance and the output impedance. So we resort to two stage operational amplifier, with the first stage providing a high gain and the second with large swing [24].

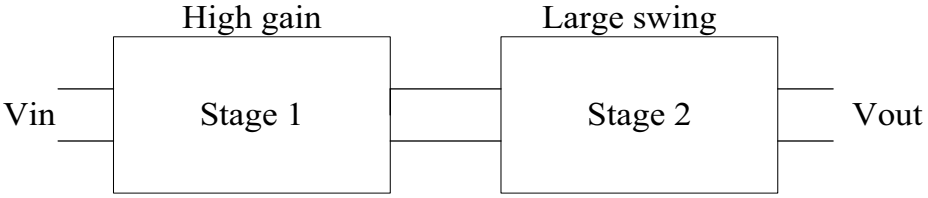

Figure 2.11 Two stage operational amplifier

The first stage is the complementary differential pair introduced in previous sections, and the second stage is typically configured as a common source stage so as it allows maximum output swings. Figure 2.12 shows the full schematic representations. The output stage is also the second stage of operational amplifier. Except providing large signal swings, we need to consider another important issue that provides the maximum available output signal to the load without loss of gain. In order to achieve this objective, the resistance of the amplifier needs to be as low as possible in the output stage. Figure 2.12 shows the schematic of a differential input stage with current mirror load, followed by a common emitter configuration with active load that provides most of the voltage gain. Furthermore the rail to rail configuration makes the input stage gain independent of the signal amplitude and achieves a high CMRR. This topology can provide a high voltage gain meeting the design requirements. In addition, this topology provides a good linearity due to the current mirror circuit connected. To solve the shortcoming that the operating point of the amplifier is shifting with a full symmetrical design, a simple way is taken by connecting the resistive common mode feedback with output stage of the amplifier. The negative feedback loop of the structure consists of a capacitor and a resistor, in which the resistor is important to the bandwidth of the amplifier and controls its input impedance.

The amplifier shown in Figure 2.12 can be segregated into four blocks: complementary differential input stage, biasing block, CMFB and output stage.

The behavior of complementary differential input pair is shown in Figure 2.12. It can be expressed as a function of the input differential voltage, where the circuit is symmetric and NMOS devices are saturated and $\lambda = 0$. The biasing circuit of the input pair is replaced by current source I_{SS}.

$$I_{ss} = I_{d1} + I_{d2} \tag{2-32}$$

According to the above equation, the point where the source of NMOS devices are connected can be considered as AC ground, if both sides of the amplifier perfectly matched. The body effect is neglected.

$$V_{in1} - V_{in2} = V_{gs1} + V_{gs2} \tag{2-33}$$

we have

$$V_{gs} = \sqrt{\frac{2I_d}{\mu_n C_{ox} \frac{W_n}{L_n}}} + V_{th} \tag{2-34}$$

following the above equations that

$$V_{in1} - V_{in2} = \sqrt{\frac{2I_{d1}}{\mu_n C_{ox}\frac{W_n}{L_n}}} - \sqrt{\frac{2I_{d2}}{\mu_n C_{ox}\frac{W_n}{L_n}}} \tag{2-35}$$

squaring the two sides of Equation (2-35) and $I_{ss} = I_{d1} + I_{d2}$ we obtain

$$(V_{in1} - V_{in2})^2 = \frac{2}{\mu_n C_{ox}\frac{W_n}{L_n}}(I_{ss} - 2\sqrt{I_{d1}I_{d2}}) \tag{2-36}$$

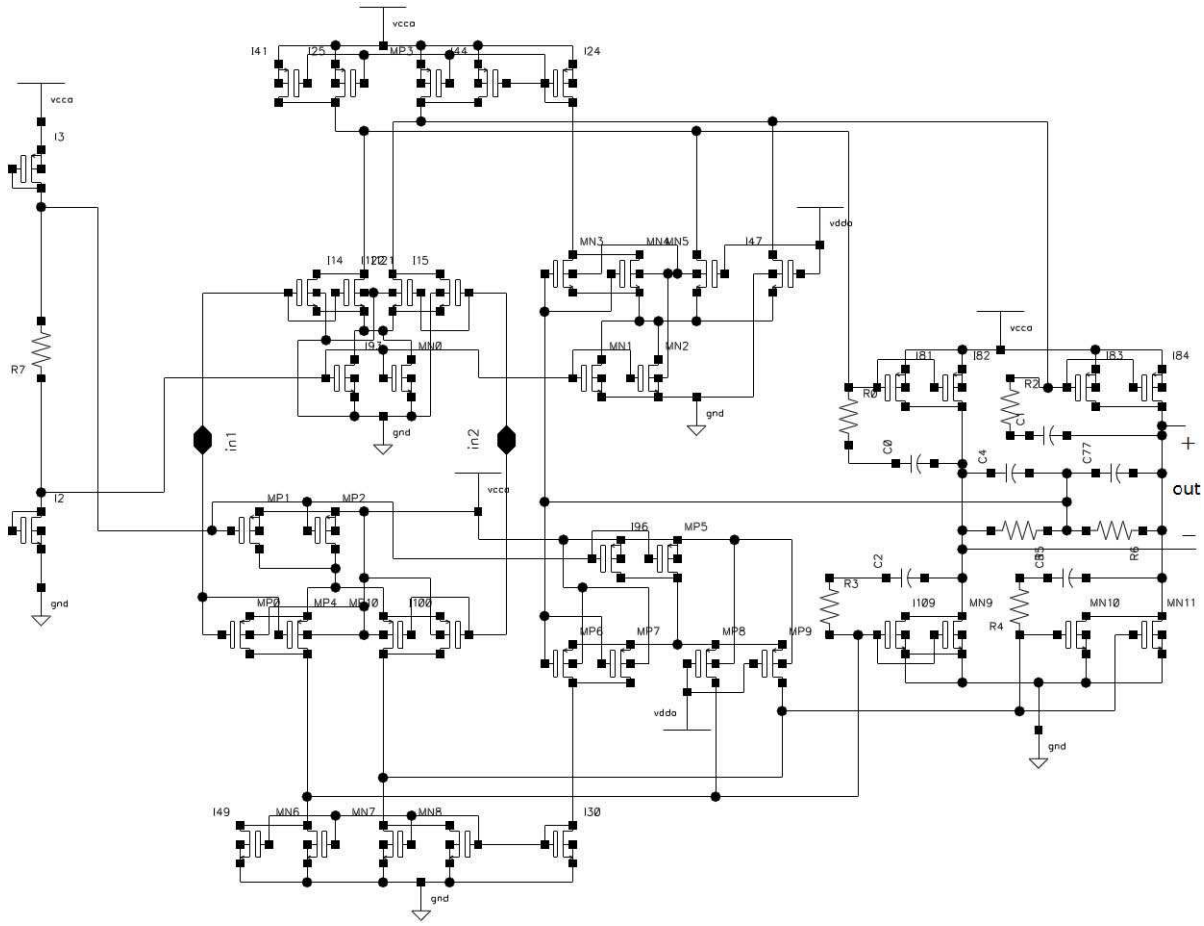

Figure 2.12 Schematic of two stages full differential amplifier.

changing the two sides of Equation (2-36)

$$I_{ss} - \frac{1}{2}\mu_n C_{ox}\frac{W_n}{L_n}(V_{in1} - V_{in2})^2 = 2\sqrt{I_{d1}I_{d2}} \tag{2-37}$$

and squaring the two sides of Equation (2-37) and

$$4I_{d1}I_{d2} = (I_{d1} + I_{d2})^2 - (I_{d1} - I_{d2})^2 \tag{2-38}$$

So we obtain

$$(I_{d1} - I_{d2})^2 = \mu_n C_{ox}\frac{W_n}{L_n}(V_{in1} - V_{in2})^2 I_{SS} - \frac{1}{4}\left(\mu_n C_{ox}\frac{W_n}{L_n}\right)^2 (V_{in1} - V_{in2})^4 \tag{2-39}$$

thus

$$I_{d1} - I_{d2} = \frac{1}{2}\mu_n C_{ox}\frac{W_n}{L_n}(V_{in1} - V_{in2})\sqrt{\frac{4I_{ss}}{\mu_n C_{ox}\frac{W_n}{L_n}} - (V_{in1} - V_{in2})^2} \tag{2-40}$$

denoting $I_{d1} - I_{d2}$ and $V_{in1} - V_{in2}$ by ΔI_d and ΔV_{in} respectively, we obtain that

$$\frac{\partial \Delta I_d}{\partial \Delta V_{in}} = \frac{1}{2}\mu_n C_{ox}\frac{W_n}{L_n}\frac{\frac{4I_{ss}}{\mu_n C_{ox}\frac{W_n}{L_n}} - 2\Delta V_{in}^2}{\sqrt{\frac{4I_{ss}}{\mu_n C_{ox}\frac{W_n}{L_n}} - \Delta V_{in}^2}} \tag{2-41}$$

Because the amplitude of signal is very small and differential input pair that $\Delta V_{in} = 0$, so

$$G_m = \sqrt{\mu_n C_{ox}\frac{W_n}{L_n} I_{ss}} \tag{2-42}$$

Now since NMOS devices are matched and PMOS devices are matched too, the sources of all devices are considered as one node and have the same potential. The same current I_{d1} also follows from the source to drain of PMOS.

$$I_{out1} = I_{d1} - (-I_{d1}) = 2I_{d1} \tag{2-43}$$

The output resistance can be written

$$r_{out1} = r_{n1}||r_{p1} \tag{2-44}$$

and

$$r_{out1} = r_{out2} = \frac{1}{2\lambda I_d} = \frac{1}{\lambda I_{ss}} \tag{2-45}$$

so

$$V_{out1} = I_{out1} r_{out1} \tag{2-46}$$

since

$$V_{out1} - V_{out2} = r_{out1}(2I_{d1} - 2I_{d2}) = 2r_{out1}G_m \Delta V_{in} \tag{2-47}$$

The differential voltage gain of the circuit in the equilibrium condition as

$$|A_V| = 2\sqrt{\mu_n C_{ox}\frac{W_n}{L_n} I_{ss}}(r_n||r_p) = 2\sqrt{\mu_n C_{ox}\frac{W_n}{L_n} I_{ss}}\frac{1}{\lambda I_{ss}} = 2\sqrt{\mu_n C_{ox}\frac{W_n}{L_n}\frac{1}{I_{ss}}}\frac{1}{\lambda} \tag{2-48}$$

2.3.7. Simulation Tests

The preamplifier contains three identical amplifiers with different negative feedback factor. The circuit diagram is shown in Figure 2.13. Where R_F is the feedback resistor and R_S

is the source resistor, the value of feedback loop is settled by the ratio of two resistors. The resistor of feedback R_F is set to 500 KΩ, so the gain can be adjusted by changing the source resistor R_S according to the upper formula.

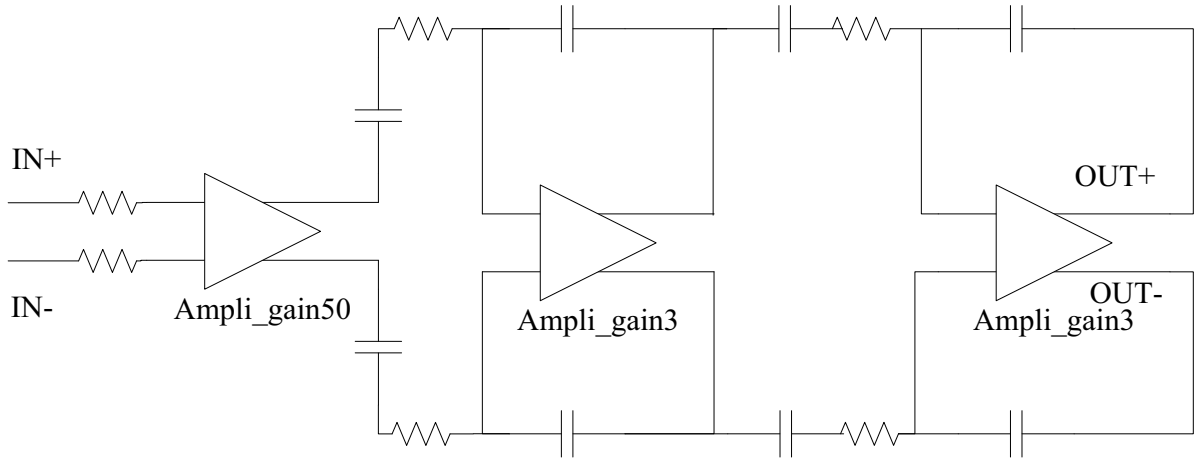

Figure 2.13 Preamplifier circuit diagram.

The first amplifier offers the gain of 55 by setting R_S to 9 KΩ, and the last two amplifiers supply the same gain of 3 by setting R_S to 166 KΩ, then the final gain is obtained up to 500, achieving a 110dB CMRR with low power supply (±2.5V, 5V peak to peak).

2.3.7.1. Output Signal Swing.

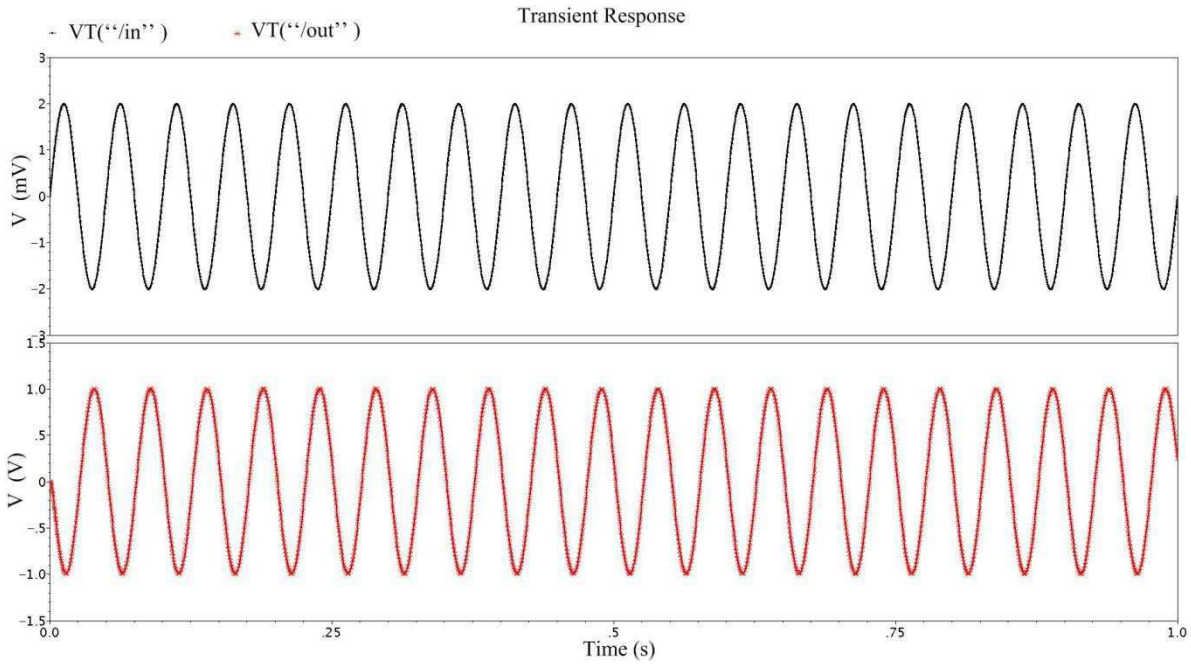

Figure 2.14 Input and output signals for transient analysis of preamplifier.

The transient analysis of the circuit is shown in Figure 2.14, with a resistance load of 100MΩ and input signal of 20Hz with a magnitude of 2mV. It can be seen from the output waveform that the final gain is about 500.

2.3.7.2. Gain

The gain is easily seen on the AC response also. The subplot of voltage gain in Figure 2.15 shows the voltage gain of the amplifier throughout the frequency band of 1Hz to 10MHz. The voltage gain is at its maximum at the low frequency band and drops to 0dB at the frequency of 5.8KHz. The voltage gain is about 54dB at the frequency band below to 100Hz.

$$A = 20\log_{10}(\frac{V_{out}}{V_{in}}) = 20\log_{10}(500) = 53.9dB \quad (2\text{-}49)$$

The subplot of phase in Figure 2.15 shows the phase margin (PM) of the open gain response which is a good quantitative way to measure the stability of a feedback circuit. Phase margin is the difference between the amount of phase shift a signal experiences through the operational amplifier and 180^o. The PM must be greater than 180^o for no oscillation to occur.

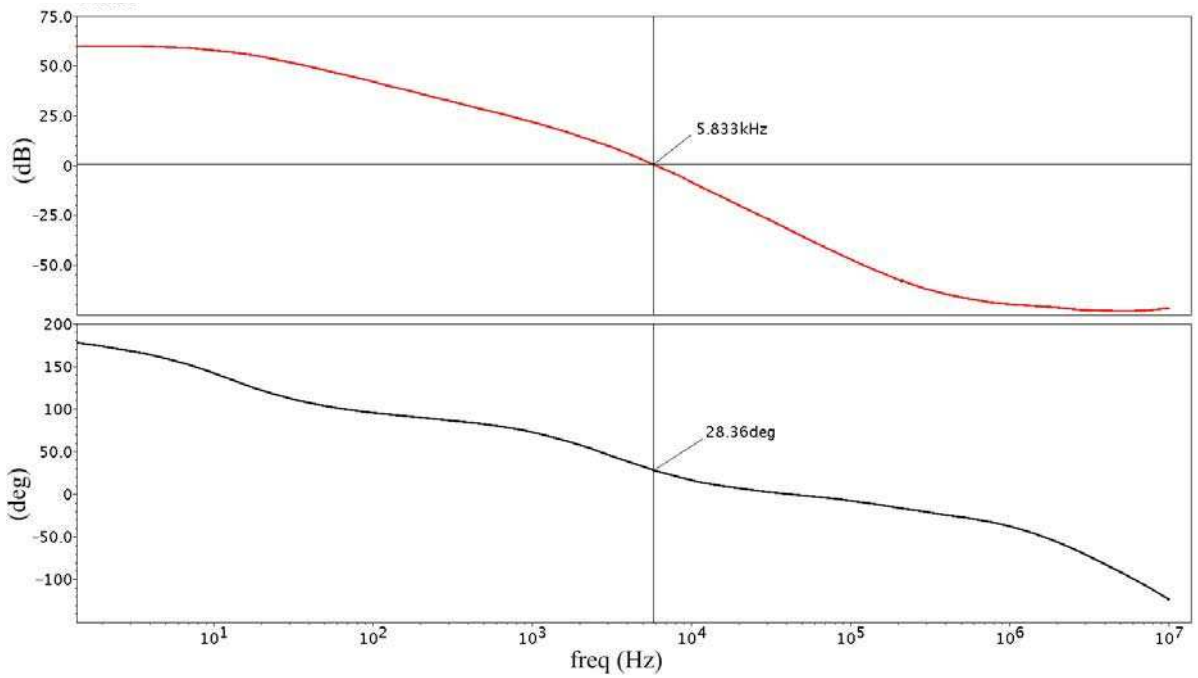

Figure 2.15 Bode plots of loop gain of the amplifier.

The transducer gain TG is close to 25dB and the available gain AG is about 54dB in the below 100Hz frequency domain. The gain is at its maximum at the lower frequency band, and drops to a minimum at the end of the band. These results satisfy the requirement and ensure the input signal of the mixer from the amplifier to be not overloaded. The AC gain is adjustable with the increasing frequency. By keeping the voltage fixed, the relationship between the AC gain and the frequency is measured. The AC gain is at its maximum at the lower frequency band, and drops to a minimum at the end of the band. These results satisfy

the requirement and ensure the input signal of the mixer from the amplifier to be not overloaded.

2.3.7.3. Common-mode Rejection Ratio

Common-mode rejection ratio (CMRR) is an important issue for the design of circuit that means the ratio of differential voltage amplification to common-mode voltage amplification. CMRR falls off following the increase of the frequency

$$CMRR = \frac{A_{diff}}{A_{com}} \tag{2-50}$$

The fact is that a change in input common-mode voltage will result in a change of input offset voltage. CMRR uses this ratio to measure the ability of the device to reject the difference between input signals.

2.3.7.4. GBW and Phase Margin

Phase margin (PM) is an important feature to design op-amp. Phase margin crosses -180^o before unity gain drops to unity means the op-amp has unstable in feedback configuration. The PM that is to measure the stability at the gain frequency is smaller, the system is more stable. PM is defined as

$$PM = 180^o + P_{\omega=\omega_c} \tag{2-51}$$

where ω_c is the gain crossover frequency, $P_{\omega=\omega_c}$ is the degree at this point.

It is obvious that the system is unstable while the PM is less than 0^o or is stable while the PM is between 20^o and 30^o.

The GBW of the circuit is 4.9KHz and the PM is 28^o. The feedback system becomes more stable but time response slows down when the PM increases greater.

Back to the open-loop transfer function of the two op-amps

$$A(s) = \frac{A_1 A_2 \omega_1 \omega_2}{(s+\omega_1)(s+\omega_2)} \tag{2-52}$$

and the magnitude and phase function is given by

$$|A(j\omega)| = \frac{A_1 A_2 \omega_1 \omega_2}{\sqrt{(\omega_1\omega_2 - \omega^2)^2 + (\omega_1\omega + \omega_2\omega)^2}} \tag{2-53}$$

and

$$P_\omega = -180 - arctan\left(\frac{\omega_1\omega + \omega_2\omega}{\omega_1\omega_2 + \omega^2}\right) \tag{2-54}$$

The frequency where the amplitude crosses 0dB point is the gain crossover and the frequency where the phase crosses 180^o is the phase crossover. The gain crossover point must occur before the phase crossover point takes place in a stable system. If the phase is

reduced that means the feedback is decreased, the magnitude is shifted down as shown in Figure 2.15. The gain point crosses over closer to the origin that makes the feedback system more stable. Unit gain bandwidth (UGB) is about 5 KHz derived from Figure 2.15.

2.3.7.5. Total Power Consumption

The total power consumption in the circuit is equal to the product of the total current flowing from V_{dd} to ground and supply voltage V_{dd}.

$$P_{tot} = I_{tot} * V_{dd} = 935.65\mu\text{A} * 5.5\text{V} = 5146\mu\text{W} \quad (2\text{-}55)$$

The full differential op-amp with feedback configuration can achieve the constant bandwidth but at the cost of a decreased loop gain and bandwidth because the feedback network consisting of the resistors with large values.

2.4. Filter based on Operational Transconductance Amplifier (OTA)

An active filter for medical application allows a signal which has a very low cut-off frequency passing through. The recommendation cut-off frequency of band-pass filter of 0.05 to 100 Hz for ECG signals [16]. The integrated circuit interested in ECG signal is expected to operate at the very low frequency, which useful signal bandwidth is around of the order of a few hertz. Typically, the active filter for ECG signal is below 100Hz pass filter. A low-pass filter could be designed to connect a feedback capacitor with an operational amplifier. This feedback structure has an advantage to decrease the frequency response in the field of high frequency via the Miller effect and prevent oscillation in the amplifier. But such low frequency of 100Hz implies large capacitor and low transconductance in the operational transconductance amplifier-capacitor filter implementation. Classical biquad filter with passive RC components needs large die size. Numerous techniques have been developed in order to minimize die size in case of large time constant circuit such as switched capacitor and continuous time. Thus we can design the low-pass filter for ECG application by decreasing the transconductance of operational amplifier, or using a very large capacitor on chip. Typically the value of this feedback capacitor is of the order of a few nanofarads (nf). The design technologies of the active low-pass filter with the low transconductance and smaller feedback capacitor are introduced considering in terms of these important factors such as energy consumption and die area. Differential design is chosen to improve the signal noise ratio as well as good voltage swing.

The OTA is an amplifier that produces an output current based on a fully differential input structure for enhanced dynamic range. Compared to a standard operational amplifier, the OTA has the same topology but higher impedance and a negative feedback. Because the OTA produces the output current, it is not used in the vast majority of the circuits that use standard op-amps. One of its principal uses is to implement electronically controlled application such as filters.

2.4.1. Input stage

As presented in Figure 2.16， the operational amplifier based on differential structure improves its performance over the single side counterpart. This operational amplifier consists of a differential pair and current mirror. The transconductance of the amplifier G_m is depending on the match situation, which means the circuit with completely symmetrical structure.

From the previous contents, we can write

$$\Delta I = \frac{1}{2}\mu_1 C_{ox}\frac{W_1}{L_1}(V_{in1} - V_{in2})\sqrt{\frac{4I_{ss}}{\mu_1 C_{ox}\frac{W_1}{L_1}} - (V_{in1} - V_{in2})^2} \tag{2-56}$$

$$\frac{\partial \Delta I}{\partial \Delta V} = \frac{1}{2}\mu_1 C_{ox}\frac{W_1}{L_1}(V_{in1} - V_{in2})\sqrt{\frac{4I_{ss}}{\mu_1 C_{ox}\frac{W_1}{L_1}} - (V_{in1} - V_{in2})^2} \tag{2-57}$$

$$G_{m0} = \frac{1}{2}\mu_1 C_{ox}\frac{W_1}{L_1}V_{in}\sqrt{\frac{4I_{ss}}{\mu_1 C_{ox}\frac{W_1}{L_1}} - V_{in}^2} \tag{2-58}$$

Where I_{ss} is the bias current delivered by PMOS transistor. The transconductance is only related to the parameter of the input differential pair $\mu_1 C_{ox}\frac{W_1}{L_1}$ and the bias current I_{ss}. $\mu_1 C_{ox}$ has been fixed by CMOS technology. Depending on the value of the small transconductance G_{m0}, the current levels of this structure should be extremely small. This may lead to the ratio of W_1 and L_1 of the order of 0.001 or less. The requirement of layout is a great challenge to match. If we set the width parameter W_1 too small that is difficult to achieve a satisfactory matching of input pair. But if we set the length parameter L_1 too large that results the same shortcoming and bigger die area. Based on these reasons to consider, reducing the bias current I_{ss} is an appropriate way to maintain input transistor in the saturation state.

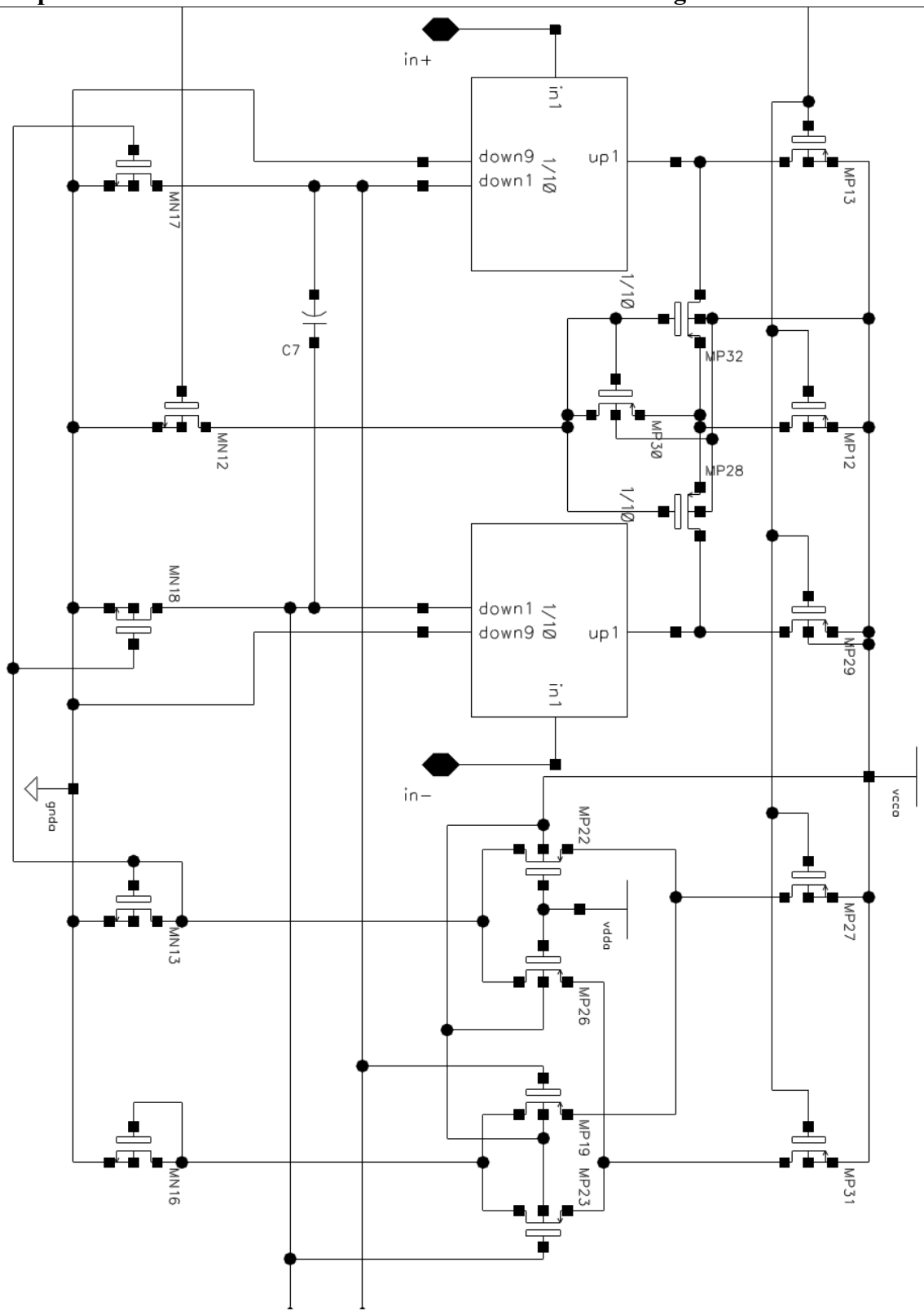

Figure 2.16 Schematic of input stage.

2.4.2. Current Divisor

The OTA contains the two current divisor blocks [25, 26] as depicted in Figure 2.17. In order to decrease the transconductance of the amplifier, one of the methods is to replace the input transistor by several equal transistors to divide the transconductance by the factor of the number of equal transistors which compose the composite transistor. Figure 2.17 illustrates that each input transistor is replaced by 10 equal transistors, thus the transconductance of the amplifier is then reduced by the factor of 10 because only one of the drain current of the composite transistor is outputted

$$G_m = \frac{G_{m0}}{10} \tag{2-59}$$

where G_{m0} is the transconductance of the amplifier without degeneration. The transconductance is defined by the parameters of the transistors and the bias current.

$$G_{m0} = \sqrt{2\mu C_{ox}\frac{W}{L}I_0}\sqrt{1-\frac{\mu C_{ox}\frac{W}{L}V_{in}^2}{8I_0}} \tag{2-60}$$

where I_0 is the bias current delivered by transistors MP8.

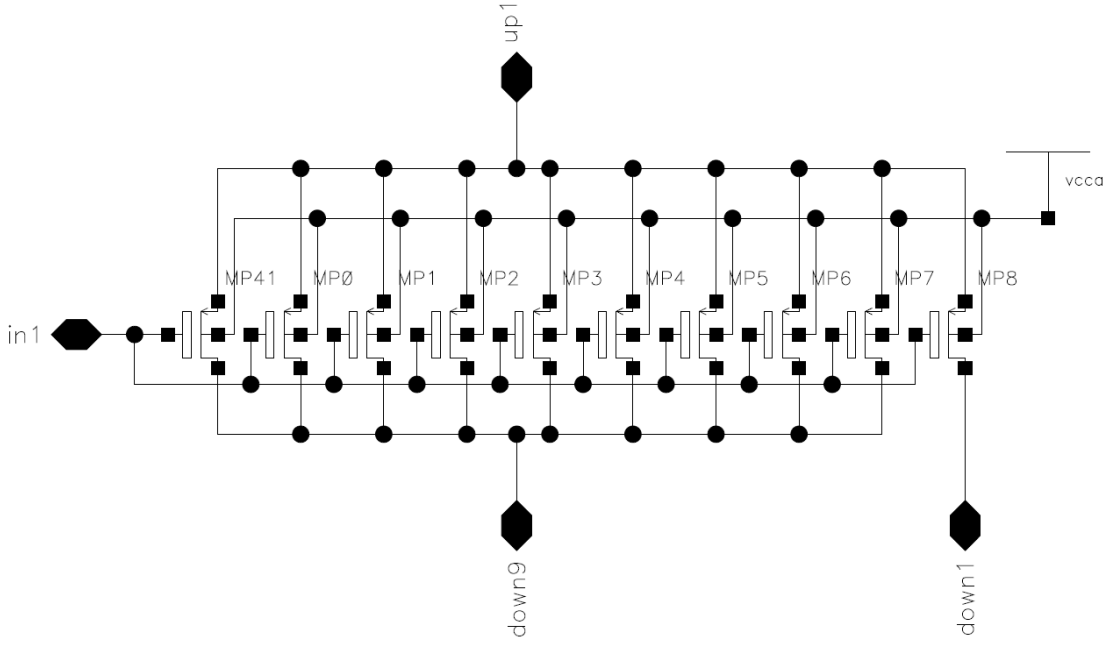

Figure 2.17 Schematic of current divisor.

2.4.3. Degeneration

The degeneration block is placed between the current source of the input stage to decrease the transconductance [27].

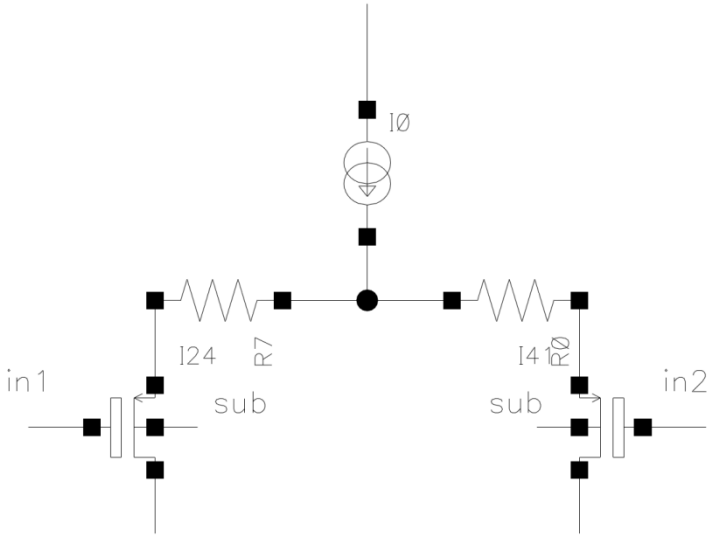

Figure 2.18 Reduction technique: source degeneration.

Figure 2.18 shows the principle behind source degeneration where effective G_m is given by

$$G_m = \frac{G_{m\_0}}{1 + G_{m\_0}R} \tag{2-61}$$

The effective transconduction degeneration is provided by the factor of $1 + G_{m\_0}R$. Replacing resistor R by the transistor which works in the triode region, the source degeneration is rewritten as represented in Figure 2.19.

The source degeneration resistor of transistor is

$$R = \frac{1}{g_m} \tag{2-62}$$

It can be controlled by resizing the transconductance of transistor MP30. The source degeneration increases linearity of the circuit and further reduces the transconductance given by Equation (2-62)

$$G_m = \frac{G_{m\_0}}{1 + \frac{MG_{m\_0}}{g_m}} \tag{2-63}$$

and

$$g_m = n\mu_p C_{ox} \frac{W_{32}}{L_{32}} (V_{gs} - |V_{th}|) \tag{2-64}$$

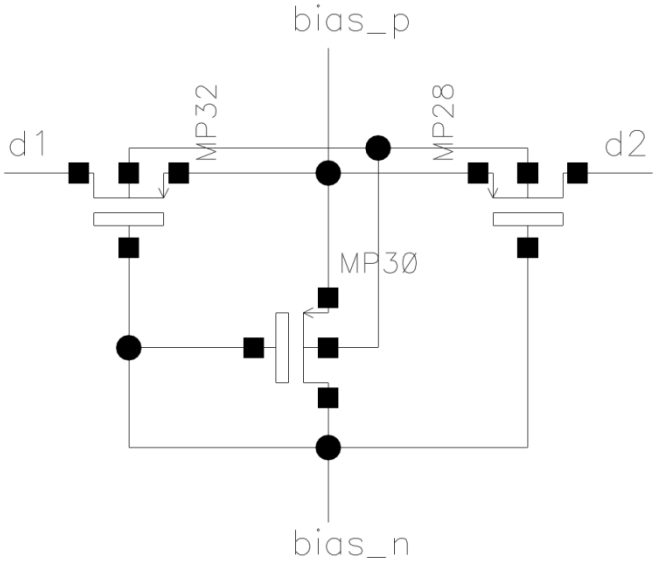

Figure 2.19 Schematic of the degeneration block.

Where G_{m_0} is the transconductance value of the amplifier without degeneration and g_m is the output transconductance of the input pair. The transistors can be biased in the triode region acting as source degeneration resistors. The purpose of MP8 is to control the V_{gs} of MP6 and thus the resistance, so rewriting Equation (2-64) as

$$g_m = n\mu_p C_{ox} \frac{W_{32}}{L_{32}} \sqrt{\frac{2I_{ss}}{n\mu_p C_{ox}} \frac{W_{30}}{L_{30}}} \tag{2-65}$$

so $M-1$ transistors result in a considerable portion of the bias current I_{ss} flowing through the gate of MP8, thus reducing G_m by the factor M.

As discussed earlier, the very small current is not easy to generate and control. For this reason, we use the current division scheme to reduce the bias current flowing through the input pair while maintaining very low transconductance.

2.4.4. Common Mode Feedback

A common mode feedback (CMFB) block is added to the operational amplifier to stabilize the common mode output voltage. The CMFB is shown in Figure 2.20 and this differential structure compares the output voltages of both branches to the desired common mode reference voltage.

If we consider the circuit composed of the bias current flowing through MP13 and the active loads made of transistors MN17 and MN18. The output current flows through the NMOS transistor MP27 and MP 31 of Figure 2.16 is given by

$$I_{\mathrm{MN17}} = I_{\mathrm{bias}} + 2g_{CM}\left[V_{CM} - \frac{V_{out1} - V_{out2}}{2}\right] \tag{2-66}$$

where g_{CM} is the transconductance of transistors MP22 and MP26, MP19 and MP23. I_{bias} is the bias current given by MP27 and MP31.

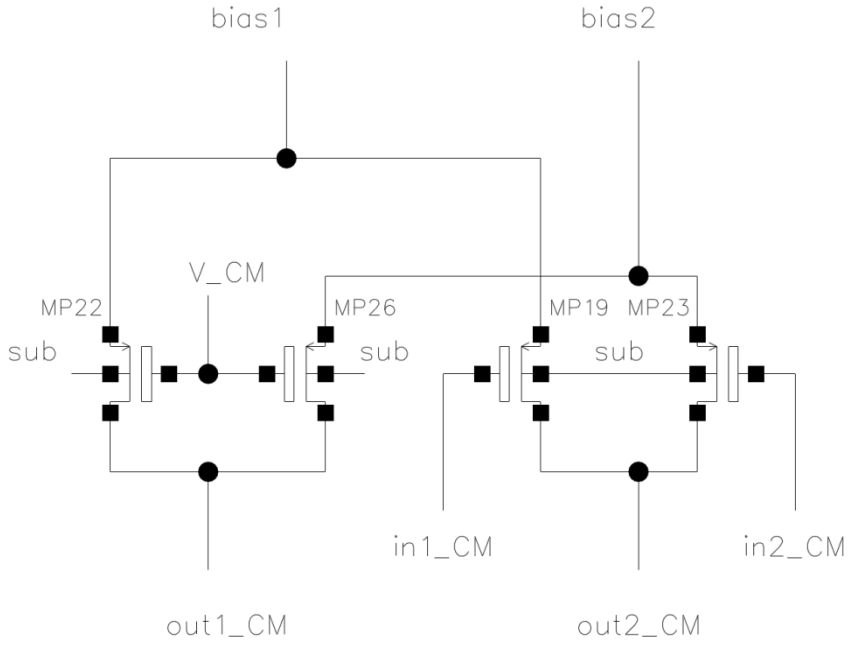

Figure 2.20 Schematic of the Common Mode Feedback block.

2.4.5. Current Source

The schematic of the current source is shown in Figure 2.21. Mp14, Mp15, Mp16 and Mp21 that connects to the gate of the transistor MP20 compose the differential amplifier. The resistors are connected along with the drains of the transistor MP18 and MP25 to measure the current flowing through this differential input pair. The transistor MP20 provides the required voltage to deliver the reference current because the differential input signals are at the same potential. So the current is set by the potential of the MP20, which is dependent on the input potential. A feedback structure is used to fix the current I_m. If the current I_m is equal to the reference value, this means the potentials of the input signals are the same. If the current is larger than the reference current, the value of the differential voltage of $(V_1 - V_2)$ appearing positive, this induces an increase of the gate potential of MP20 and thereby reduces the current I_m. Similarly the current is smaller than the reference current, the value of the differential voltage of $(V_1 - V_2)$ appearing negative, which induces an decrease of the gate potential of MP20 and increases the current I_m. The circuit is stable until I_m equals to current reference. In order to minimize the variation of current with interference and guarantee the stability of the feedback structure, capacitor is placed to the differential input pair [28].

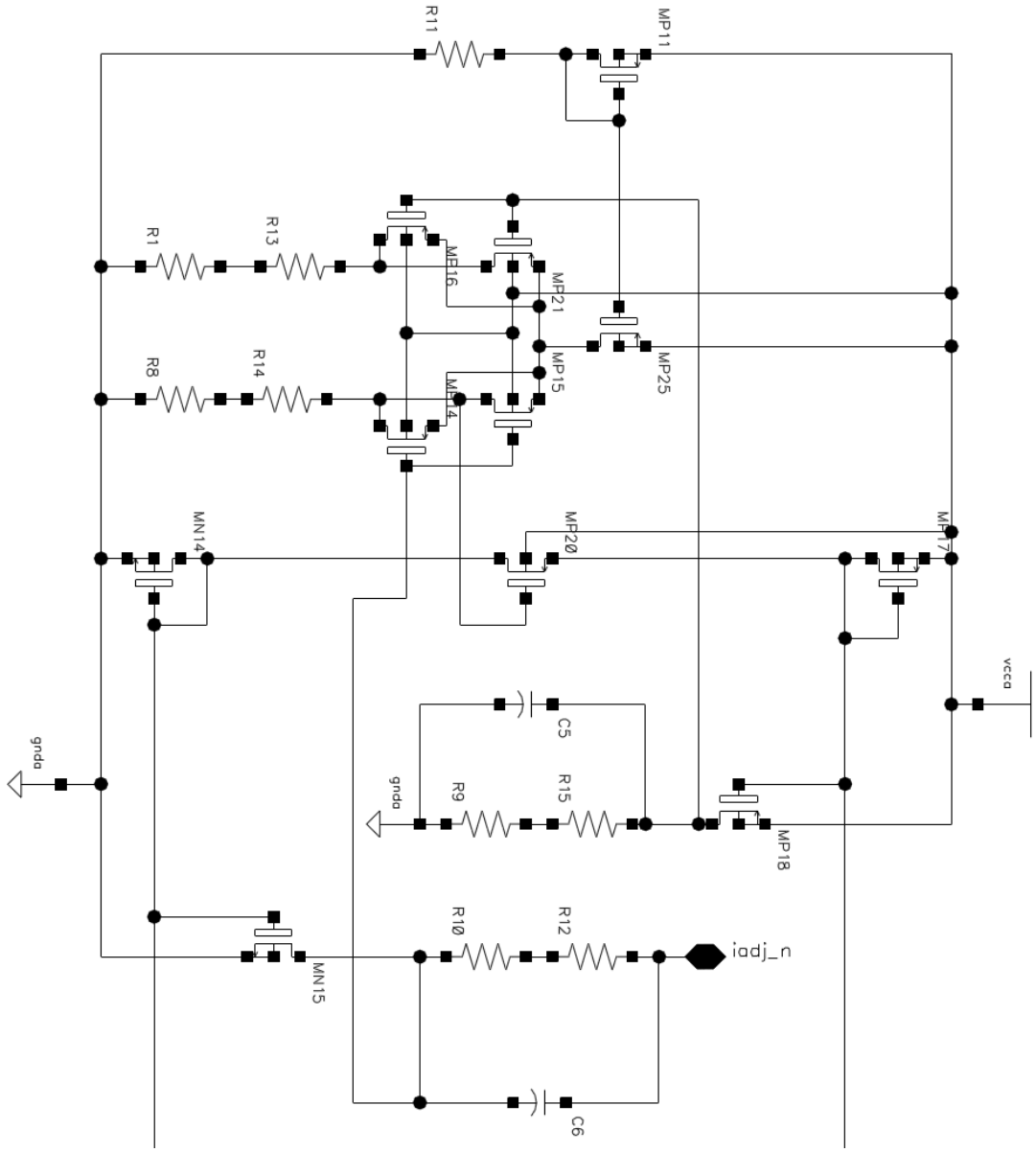

Figure 2.21 Schematic of the current source.

2.4.6. Active Filter Design

First-order filter structure using some of the basic OTA building blocks is introduced in this section. The structures of 1^{rst} low-pass filter and 1^{rst} high-pass filter are shown in the following figure.

The cut-off frequencies of the first-order filter of Figure 2.22 are given by the expression

$$f_{L,3dB} = \frac{G_m}{2C_L} = \frac{G_m}{2C_1} \tag{2-67}$$

$$f_{H,3dB} = \frac{G_m}{2C_H} = \frac{G_m}{2C_2} \tag{2-68}$$

where G_m is the transconductance of the two identical OTAs.

A functional block of the transconductance gains that may be separated into two parts: low-pass filter and high-pass filter are shown in Figure 2.22. If G_m of the two OTAs is fixed, the circuit has a fixed zero and adjustable pole. If the value of C decrease, the pole in this circuit move to the right which means the cut-off frequency increases but the zero is held constant.

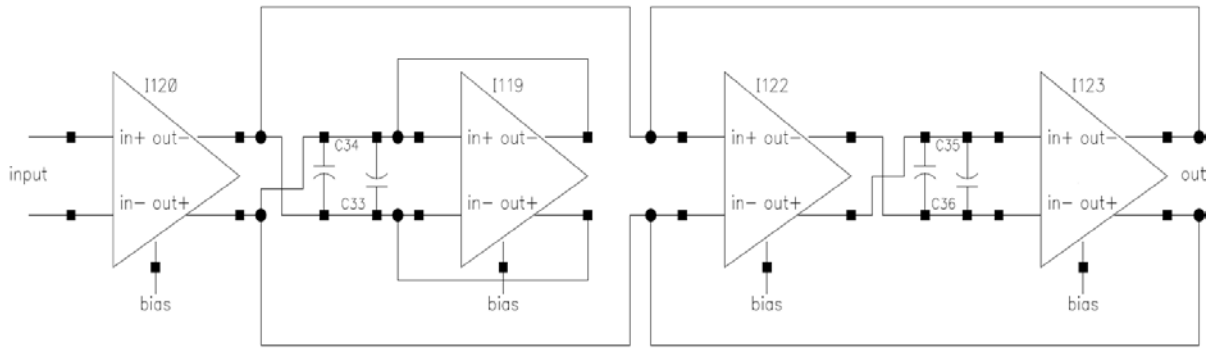

Figure 2.22 Architecture of the band-pass filter that is constructed with 1^{rst} order low-pass filter and 1^{rst} order high-pass filter.

Following Equation (2-67) and the above assumption that G_m is constant. Both the pole and zero from the transfer function of this circuit are adjustable by changing the ratio of G_m and C. The frequency response given by the low-pass filter's transfer function is shown in Figure 2.23, in which there is frequency shift in the shape of the transfer characteristics with the changes of capacitance value.

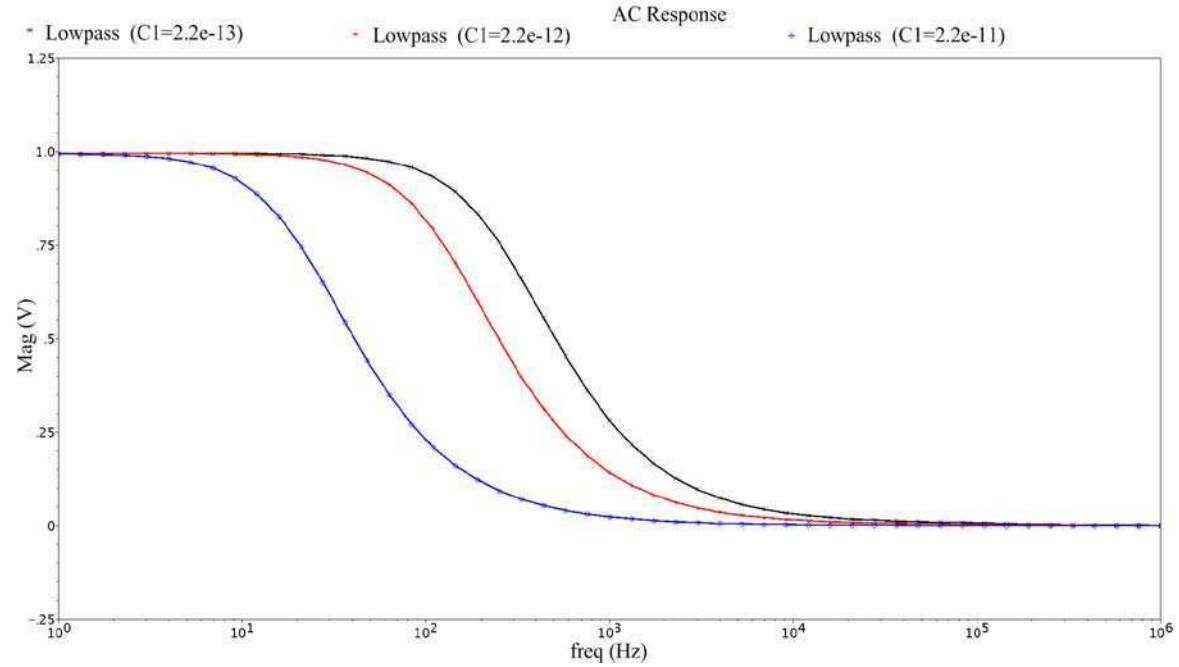

Figure 2.23 Simulation results of the 1^{rst} order low-pass filter.

Following Equation (2-67) and Equation (2-68) and the above assumption that G_m is constant. Both the pole and zero from the transfer function of this circuit are adjustable by

changing the ratio of G_m and C_L, C_H. The frequency response given by the band-pass filter's transfer function is shown in Figure 2.24, in which there is frequency shift in the shape of the transfer characteristics with the changes of capacitance value.

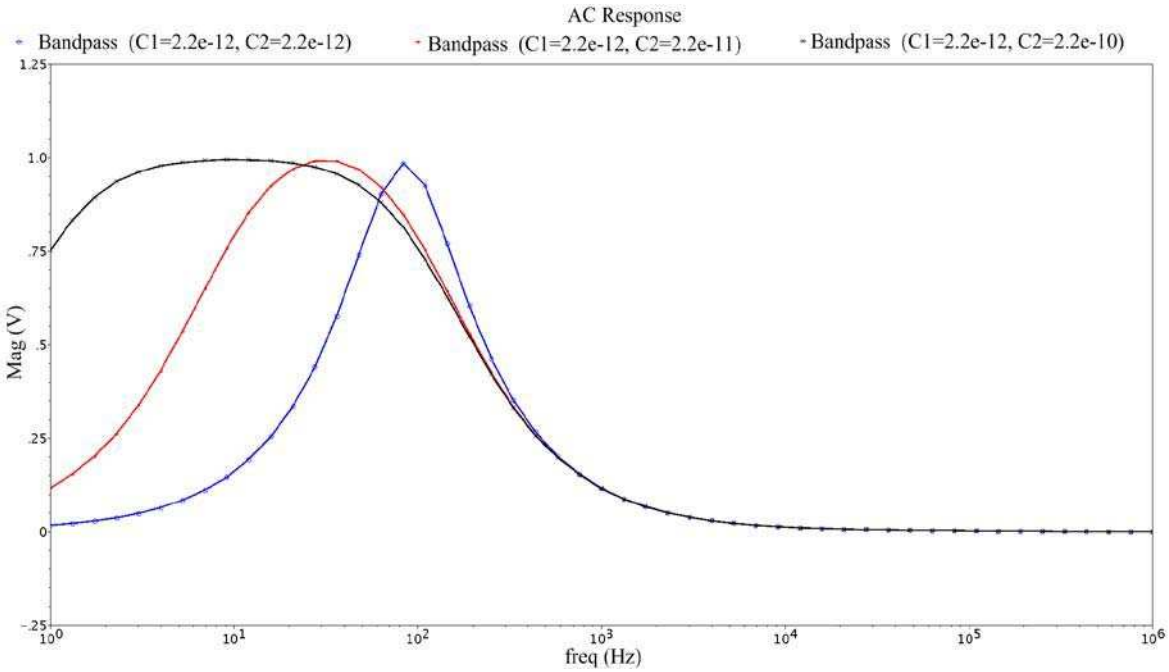

Figure 2.24 Simulation results of the 1^{rst} order band-pass filter.

Finally the characteristic of band-pass filter is shown in Figure 2.25 that consists of one low-pass and another high-pass filter to construct band-pass filter. If C_L and C_H are adjusted simultaneously and set to 3pf and 380pf respectively. 3dB bandwidth of the filter is in the range from 0.5Hz to 100Hz.

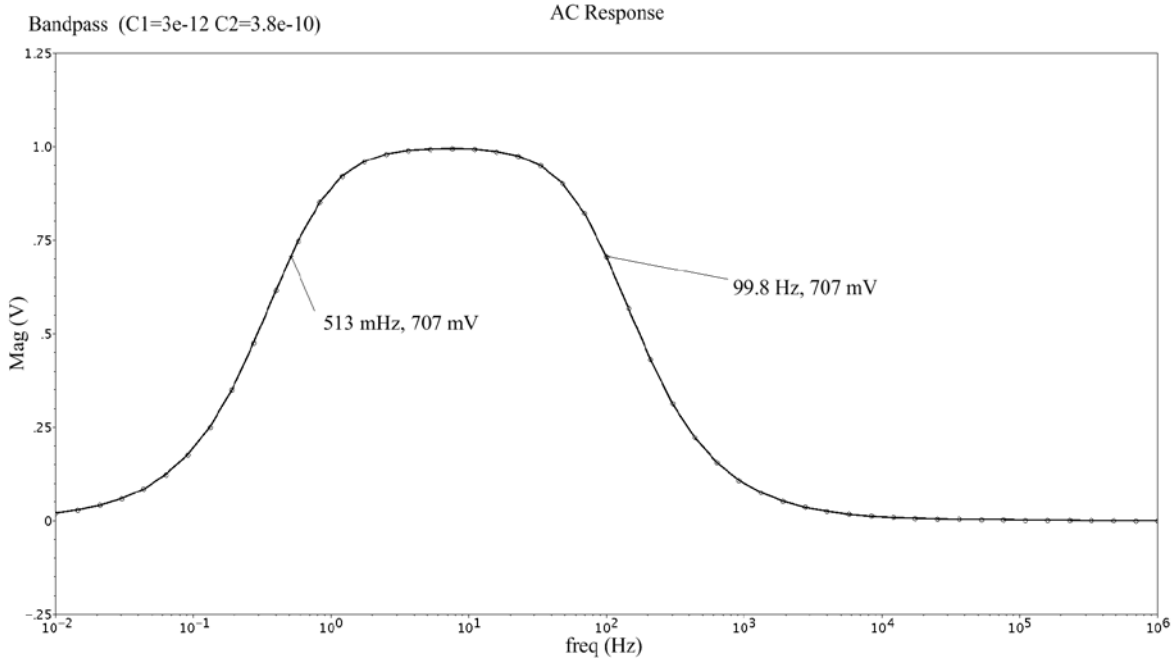

Figure 2.25 Bandwidth of the 1^{rst} order band-pass filter.

Transient responses of the filter are shown in Figure 2.26. The line with a constant value is the input signal and another line is the output signal. The gain is about 0.5 at 0.2Hz, thus the amplitude of the output waveform decreases to the half of the original value. The gain is about 1 at 20Hz, thus the output signal is as the same as the input signal. The gain is about 0.5 at 200Hz, thus the amplitude of the output waveform decreases to the half of the original value.

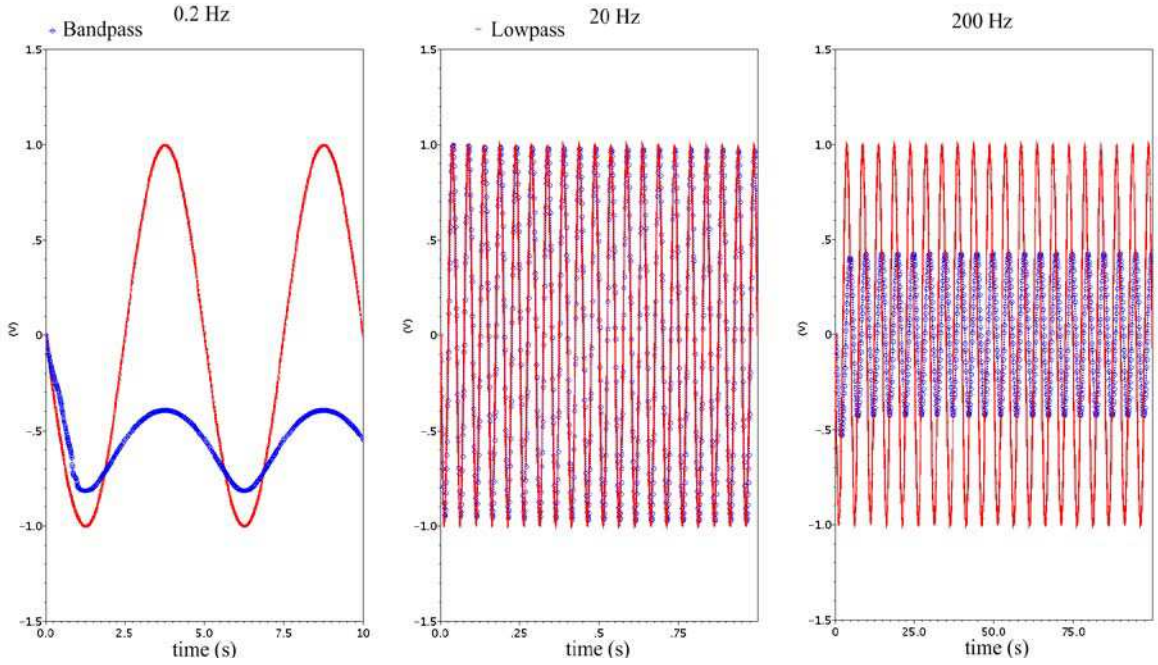

Figure 2.26 Simulation results of the 1^{rst} order band-pass filter.

2.5. 12-bit ADC

It is important to measure the qualities of analog voltage because the ADC returns a digital value that presents the analog data. The ECG frequency signal is low (<10Hz), and for a high resolution ECG signal the sampling frequency is 1KHz. Note that generally, the ECG signal is sampled at 250Hz. Thus, in our design we implement a single slope ADC, having the conversion time 40µs (sample frequency 125KHz max), which is largely enough to sample the ECG signal at 1 KHz as shown in Figure 2.27. The ADC is composed of 4 parts: T/H (track and hold), ramp generator, comparator and 12-bit serial register [29, 30].

2.5.1. Ramp

The input stage is still full differential input mode where the voltage of common mode is the half of the supply voltage. The ramp generator provides the linear voltage to the comparator, by means of two current generators made of two transistors (PMOS and NMOS). These transistors are charged by the two capacitors with a constant current. Subsequently, this slope is compared with the front-end input signal [31, 32].

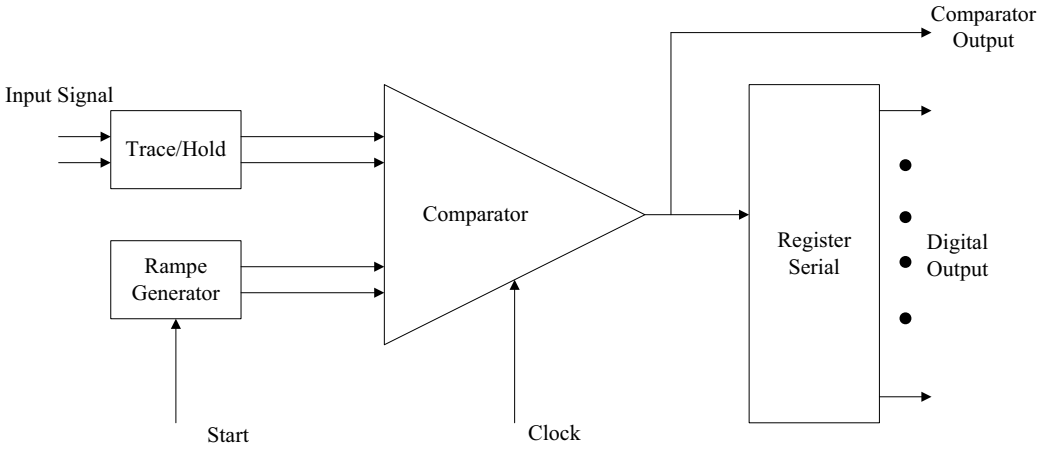

Figure 2.27 Bloc diagram of the A/D processing stage.

Then we can have a linear ramp voltage as follows

$$V_{ramp} = \frac{I}{C}t + V_{ramp}(0) \tag{2-69}$$

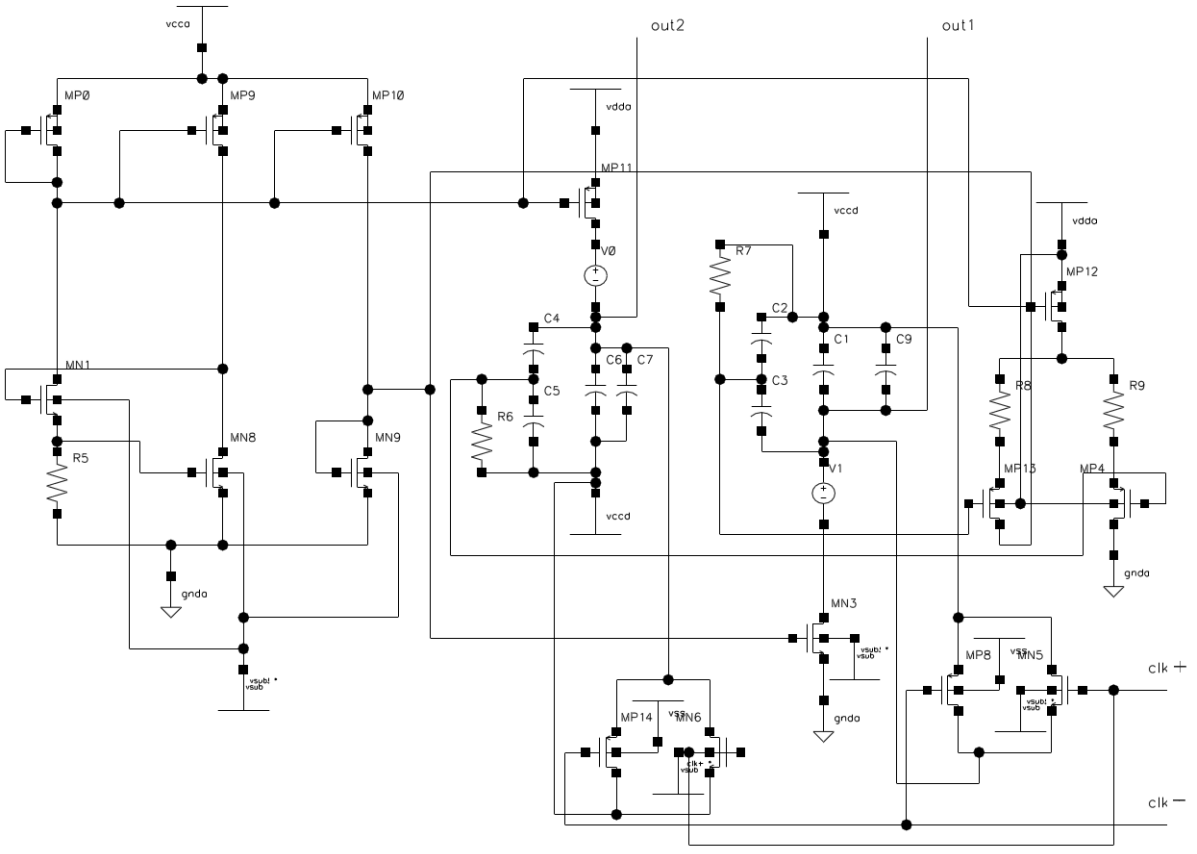

Figure 2.28 Schematic of the ramp.

It is necessary to make the current smaller to achieve the purpose that the output of the ramp generator slows enough to allow the static characteristic of the entire ADC dynamic range. Left part of the circuit including 6 transistors is used to provide a stable current supply that can reduce or eliminate the negative impact of temperature and voltage supply. The

current passes through the resistor placed in parallel with an NMOS transistor that is supplied by the voltage of this transistor. The generated current is 5μA measured from the PMOS transistor MP10 and an additional current for balance is $400n$A measured from the NMOS transistor MN9.

The total consumption is 56μW from the voltage supply 3.5V. The architecture of the switch consists of NMOS and PMOS pair with a resistance R_{on} of 200Ω and R_{off} of 83M Ω.

2.5.2. Input Front-end of Comparator

The goal of the input front-end of the comparator is to transform input signals to the same CM voltage with a CM sensing circuit, allowing the comparator to achieve better and the most delicate performance.

The output load is formed by resistors R11, R12 and capacitor C1. The sum of current inflows flows through the resistors. To reduce the noise generated by the current generator circuit, the current generator is formed by a differential architecture. As shown in Figure 2.29, input signals are a pair of positive input and negative input that have a substantially equal voltage.

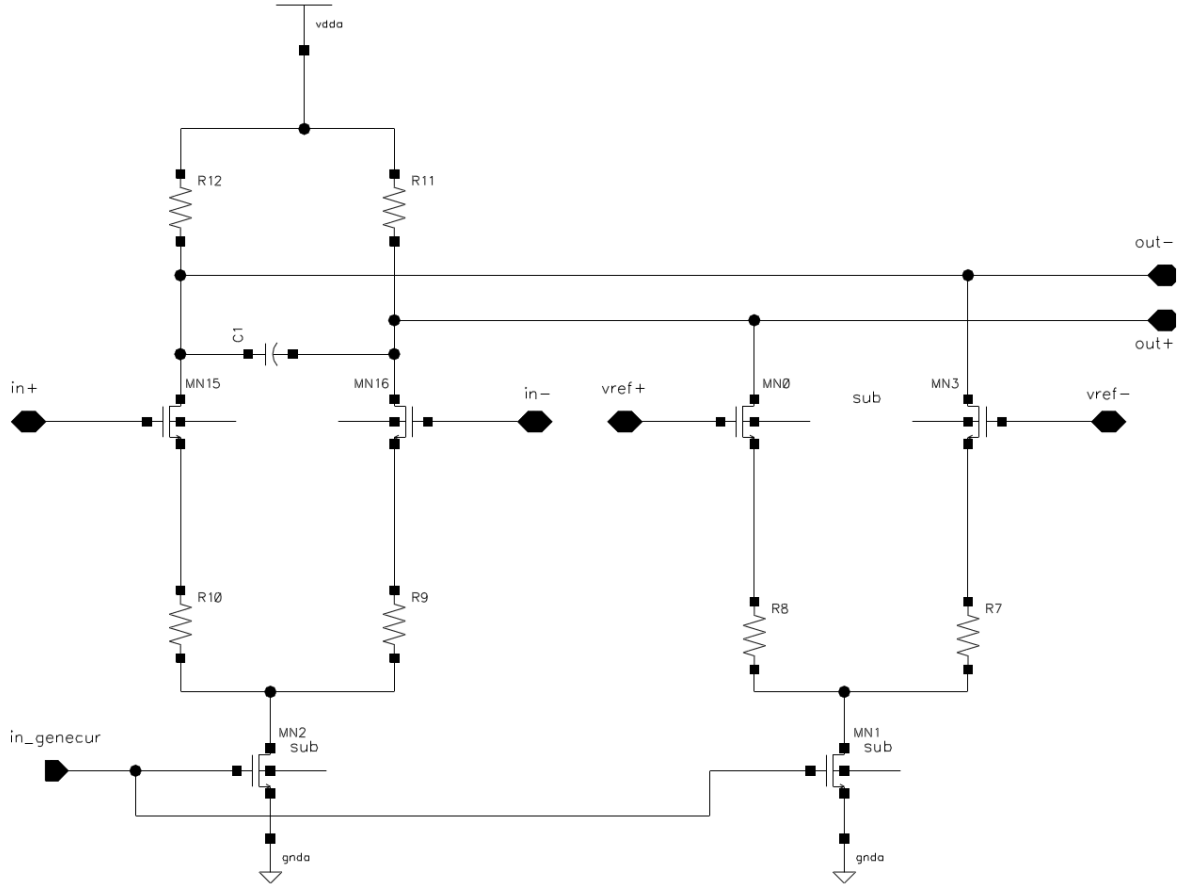

Figure 2.29 Schematic of the input stage.

2.5.3. Comparator

The comparator consists of three blocks: input, amplifier and latch. The input part is a differential amplifier. The second block is a positive feedback amplifier and the last stage is a latch which converts the output into a digital signal. The complete circuit of the comparator is shown in Figure 2.33.

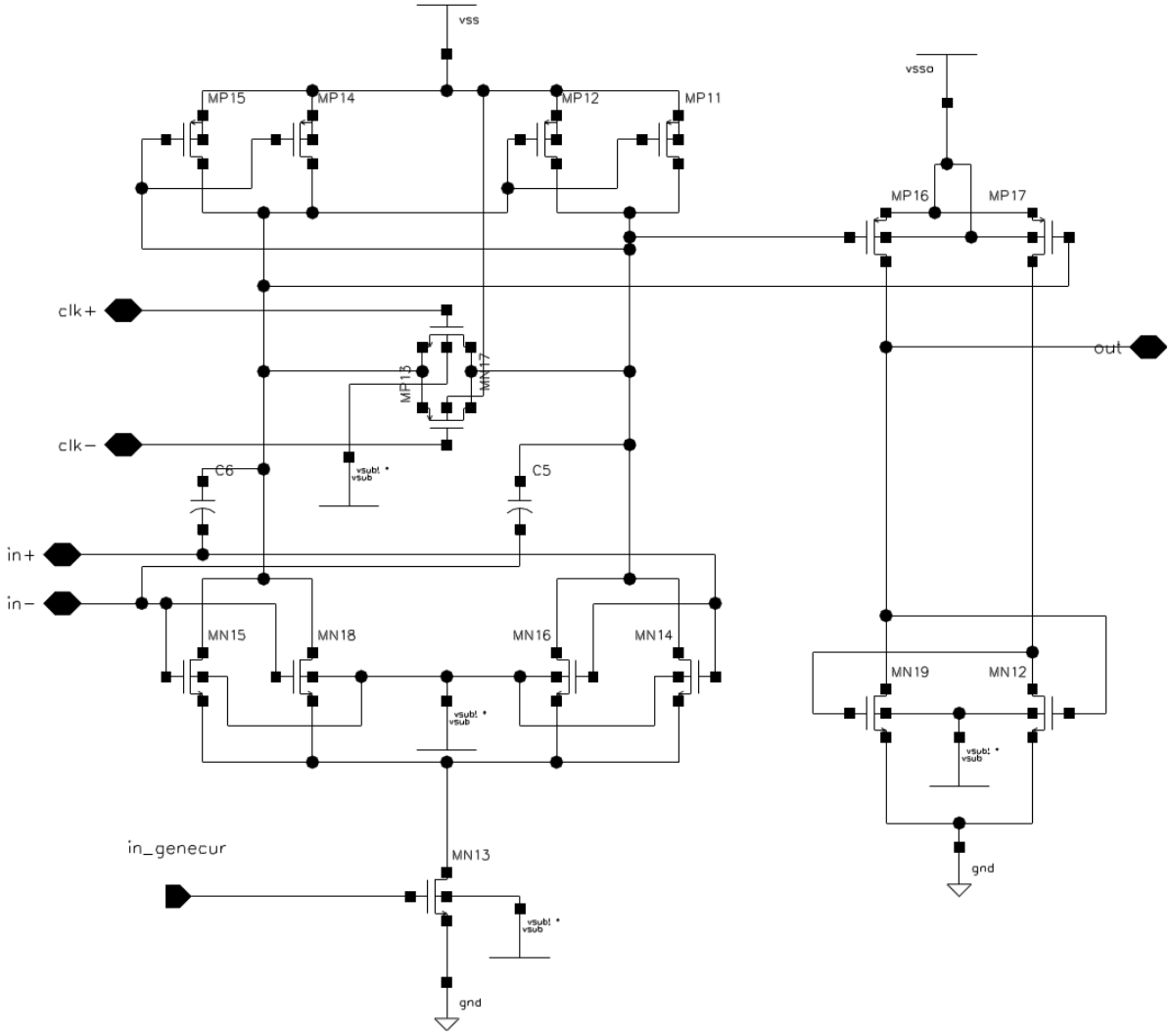

Figure 2.30 Schematic of the comparator.

The output of the comparator is operated by digital logics for bit-realignment in a pipeline architecture. The latching circuit of the comparator is timed with the clock signal to indicate the counter when to count or stop counting and reset. The rate of the counter is fixed by the precision clock frequency. As the counter counts up with a clock cycle, the input voltage is compared against the reference voltage by the ramp. The counter will start normal count when the comparator output goes high because the differential input voltage is greater than the reference voltage. The counter will stop until the comparator output is low. Then the shift register is to process the binary count is being output by the counter. Finally the counter will reset on the next clock cycle and repeat again. In general, 12 registers are necessary to decode

each comparator output that needs to be sampled with a register for 12 bit of resolution. In most applications, the cost of the logic in terms of power is rarely considered.

2.5.4. Simulation Results

A ramp is generated going from 1.75V to 1.875V and 1.625V to 1.75V which is the full scale range of the ADC. As discussed in the above section, a timer starts counting when the ramp starts. The process of the ramp is depicted in Figure 2.31.

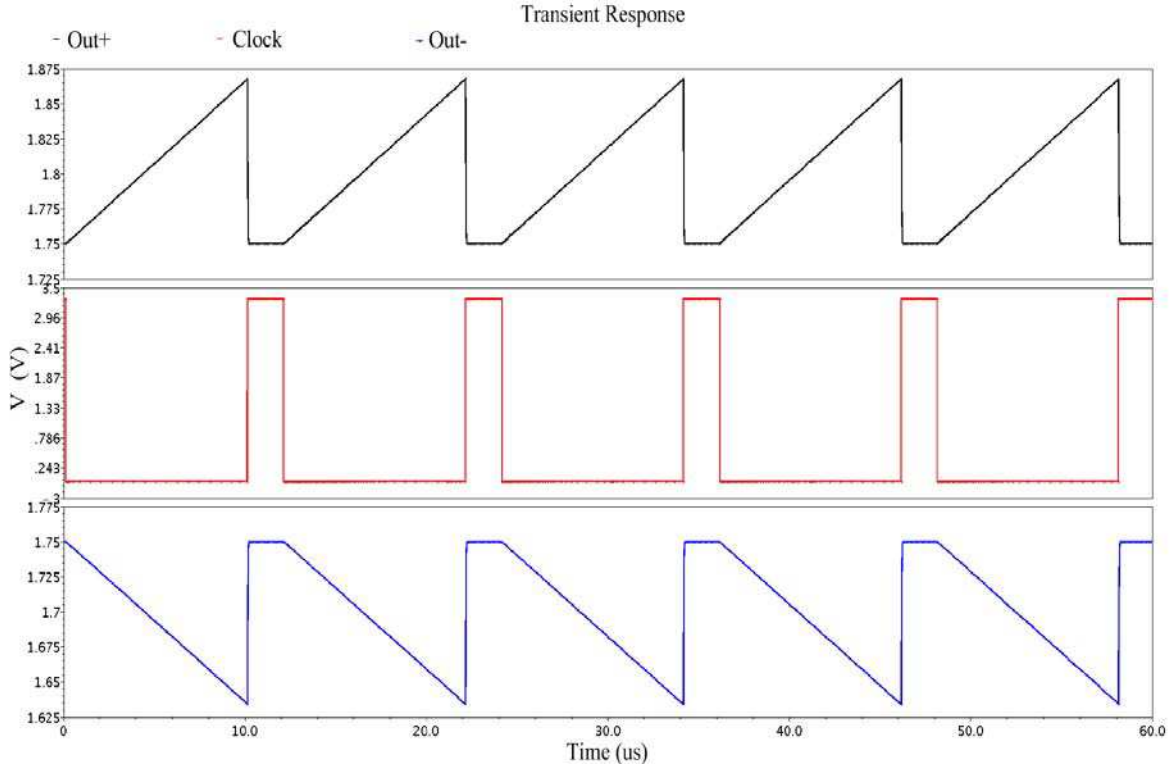

Figure 2.31 Simulation results of ramp.

Figure 2.32 illustrates the transient analysis of the ADC. The amplitude of the analog input signal of the ADC varies from 250μV to 1V. The digital codes are obtained correctly indicating that the ADC is functioning.

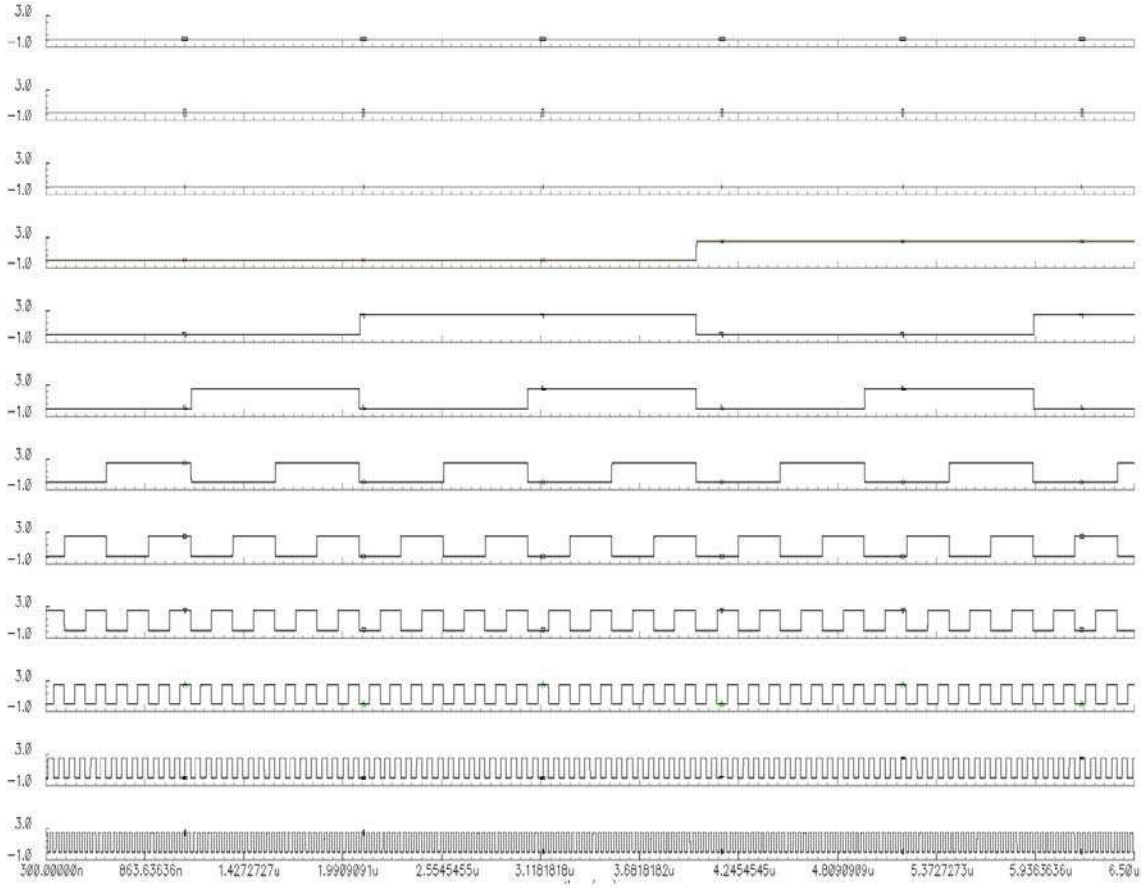

Figure 2.32 Transient response of ADC.

2.6. Oscillator

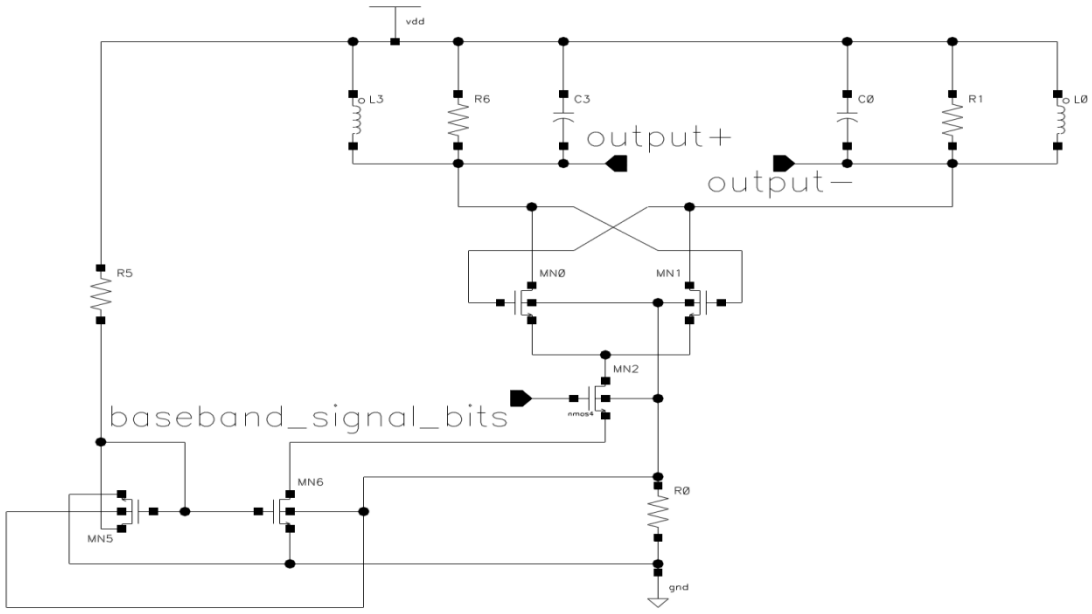

Figure 2.33 Schematic of the oscillator.

The schematic of the high frequency oscillator is shown in Figure 2.33. This oscillator uses a CMOS differential amplifier composing of transistors [33]. The current mirror circuit is used to provide the bias voltage of the transistor at VDD/2 to maximize the voltage swing and reduce the current needed for oscillation by half.

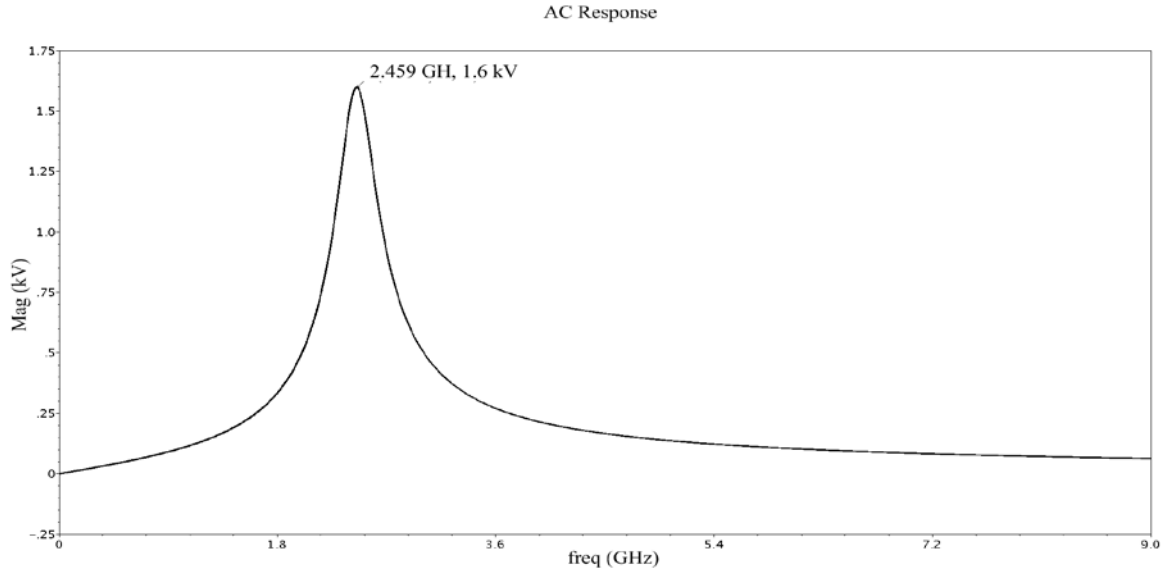

Figure 2.34 AC response of the oscillator.

Figure 2.34 shows a plot of AC response and output waveform of the oscillator. The measured zero to peak output voltage swing is 1.8V with a 3.5V power supply.

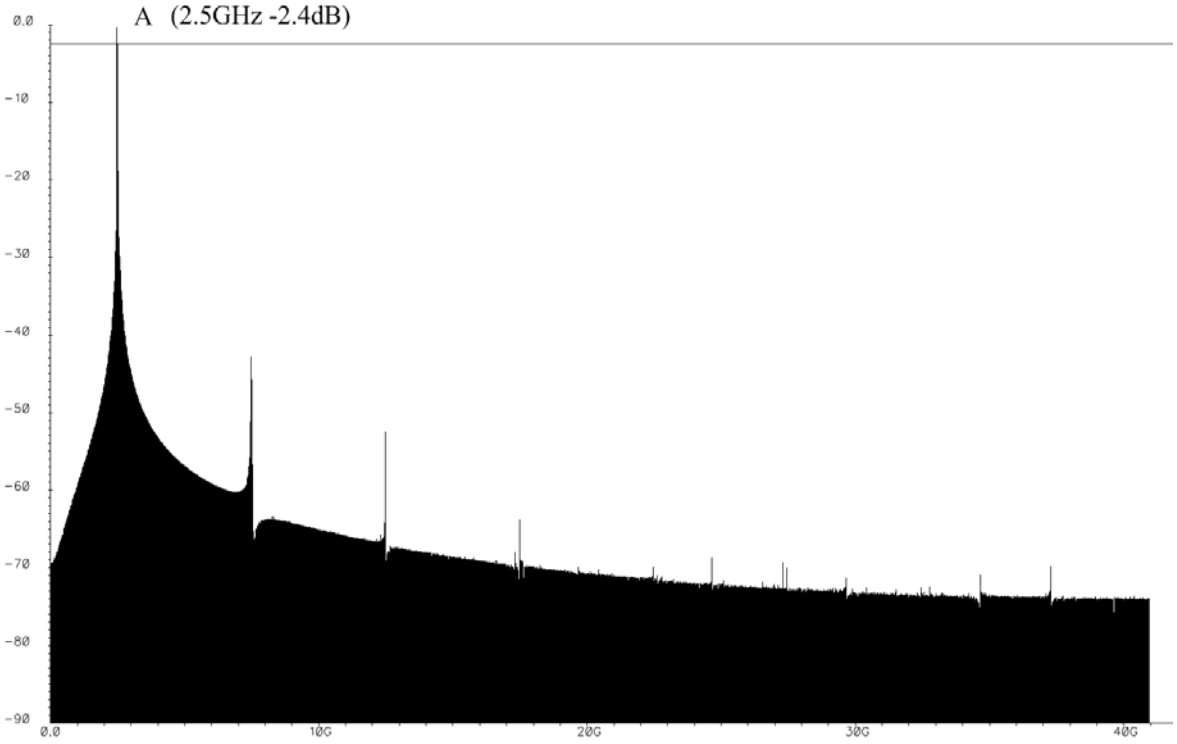

Figure 2.35 FFT of transient output waveform of the oscillator.

The oscillator is self biased for sustained oscillation at 2.46GHz. From the output waveform of the oscillator, the startup process is clearly shown. When the transistors charged

to the bias voltage, the oscillator begins to power up. A shorter time of this process increases loading and power consumption. Once the oscillation point is reached, the differential amplifier offers sufficient voltage gain and makes the oscillation amplitude stabilized. Faster amplitude growth time can be achieved at the expense of higher current consumption. Finally, the transistors turn into the triode region and the oscillator reaches steady state.

Figure 2.35 shows the FFT of transient output in the simulation, which has to obtain the greatest power gain at 2.5GHz. The nearest spurious tone measurement appears at 5 GHz away from the center frequency. Within the longer frequency range, the spurious tones are found at the points which are at integer multiples away from the center frequency. The nearest spurious tone is -40 dBc and the location being away from the center frequency makes the impression of the spurious tone on RF system minimal. In our design of system, the filter attenuates signals that are outside of the received bandwidth. Therefore, the spurious tones far beyond the bandwidth are substantially attenuated.

2.7. Mixer

The mixer is used to allow a frequency translation between a high RF frequency to 2.458GHz and a lower Intermediate Frequency (IF) to 88MHz. The topology of mixer has a differential interface as depicted in Figure 2.36. The transistors in the mixer behave as a switch and Local Oscillator (LO) signal drives the gate of the transistors to start work.

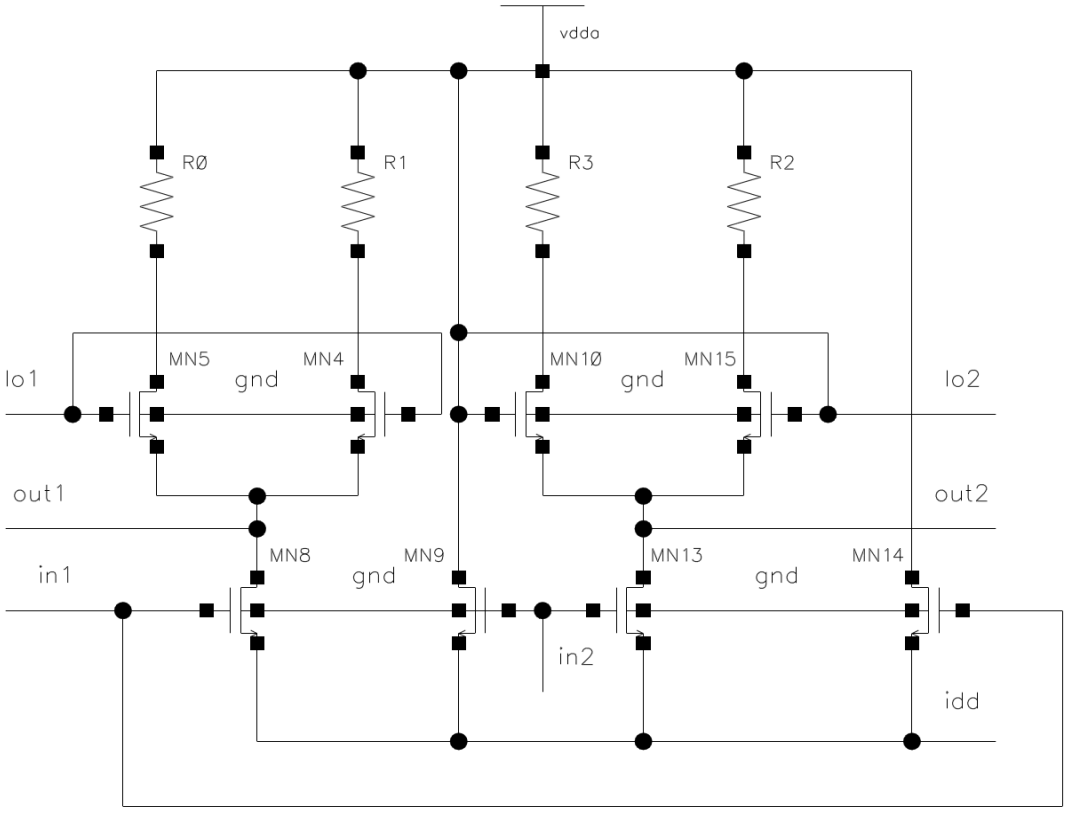

Figure 2.36 Schematic of the mixer.

Figure 2.37 shows the result of multiplying the RF signal by a LO signal. From the figure, Low frequency components in the waveform are clearly visible. It can be seen as a replica of the RF signal translated to the IF frequency. Through qualitative analysis of the method, how the mixer operates can be explained. However it is not sufficient to deduce the prediction. In addition, the mixer has additional losses due to square wave multiplication. It is necessary to make large signal simulation of the mixer for further accuracy prediction of its performance.

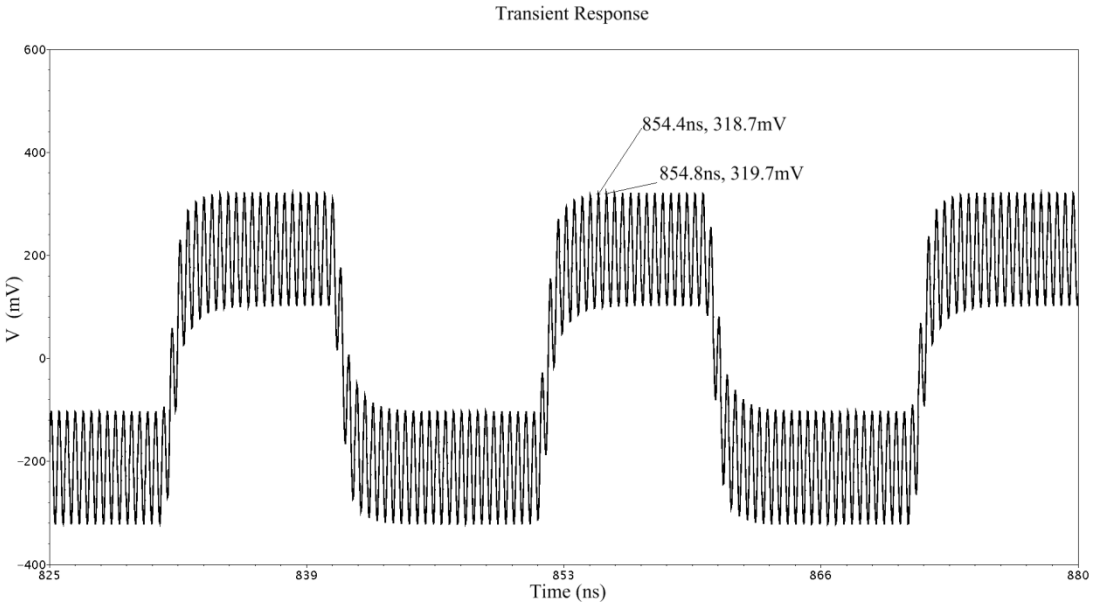

Figure 2.37 Transient response of the mixer versus time.

2.8. Layout and Experimental Measurements

There are some design considerations of the layout of the circuit. The geometry of a folded structure is to replace W/L transistor by two 0.5 W/L identical transistors that exhibit less substantially drain junction capacitance than the original transistor while proving the same aspect ratio. A lot of folded structure is used in our design. The next consideration is the mismatch that is developed from large transistors used in the input stage for the full differential input pair. The type of cross coupling is introduced to cancel the effect of the gradient generating from the mismatch.

Figure 2.38 Layout of final preamplifier.

The size of the layout is $230\mu m \times 330\mu m$ for the designed OTA in the Austriamicrosystems 0.35μm CMOS technology. The layout of the filter is shown in Figure 2.39. The typical transconductance value measured is around 6nA/V but it can be tuned through the voltage applied on terminal bias. Thus a low transconductance OTA designed in a 0.35μm CMOS technology where a differential input stage, a current divisor, a source degeneration and a CMFB are included. A band-pass filter that is constructed with a 1^{rst} order low-pass filter and a 1^{rst} order high-pass filter is designed based on OTA. The Gm-C topology filter has an adjustable cut-off 3dB power frequency 0.5Hz and 100Hz. The filter consumes 633.3μW while operating with $\pm 2.5V$ power supply.

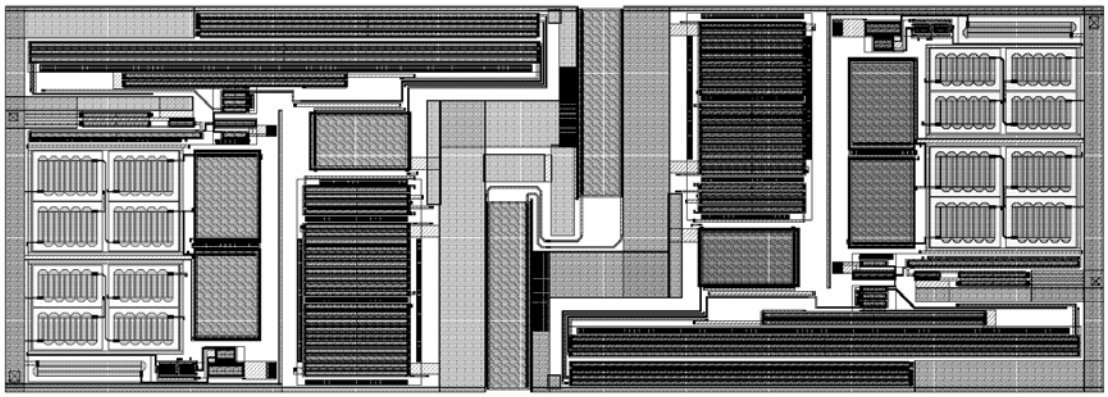

Figure 2.39 Layout of the 1^{rst} order band-pass filter.

The integrated circuit of SoC-Holter is shown in Figure 2.40. The preamplifier with large gain consumes 5.2mW which contributes a large portion of the energy consumption. The filter consumes 680μW. The proposed ADC permits fully integration, with a power consumption of 2.3mW including the power consumption of digital parts. And the total power consumption of the mixer with the oscillator is 1.66mW. The total power consumption of SoC-Holter is about 9.84mW while the device is in fully working condition.

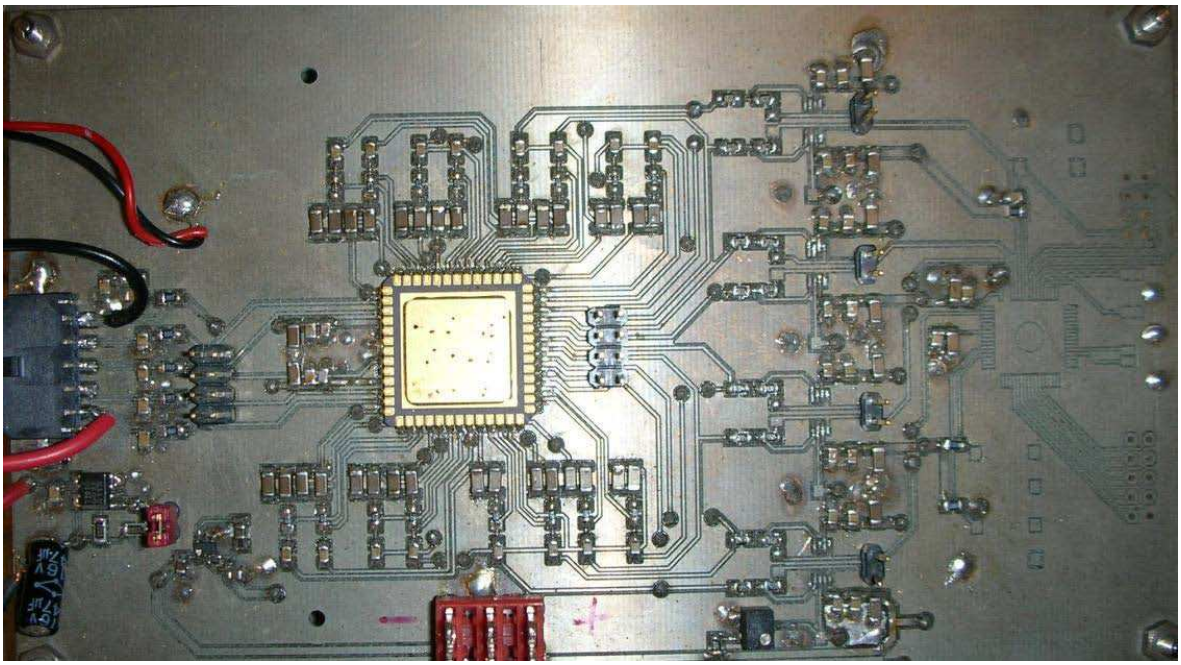

Figure 2.40 Circuit of the different analog blocks of SoC-Holter.

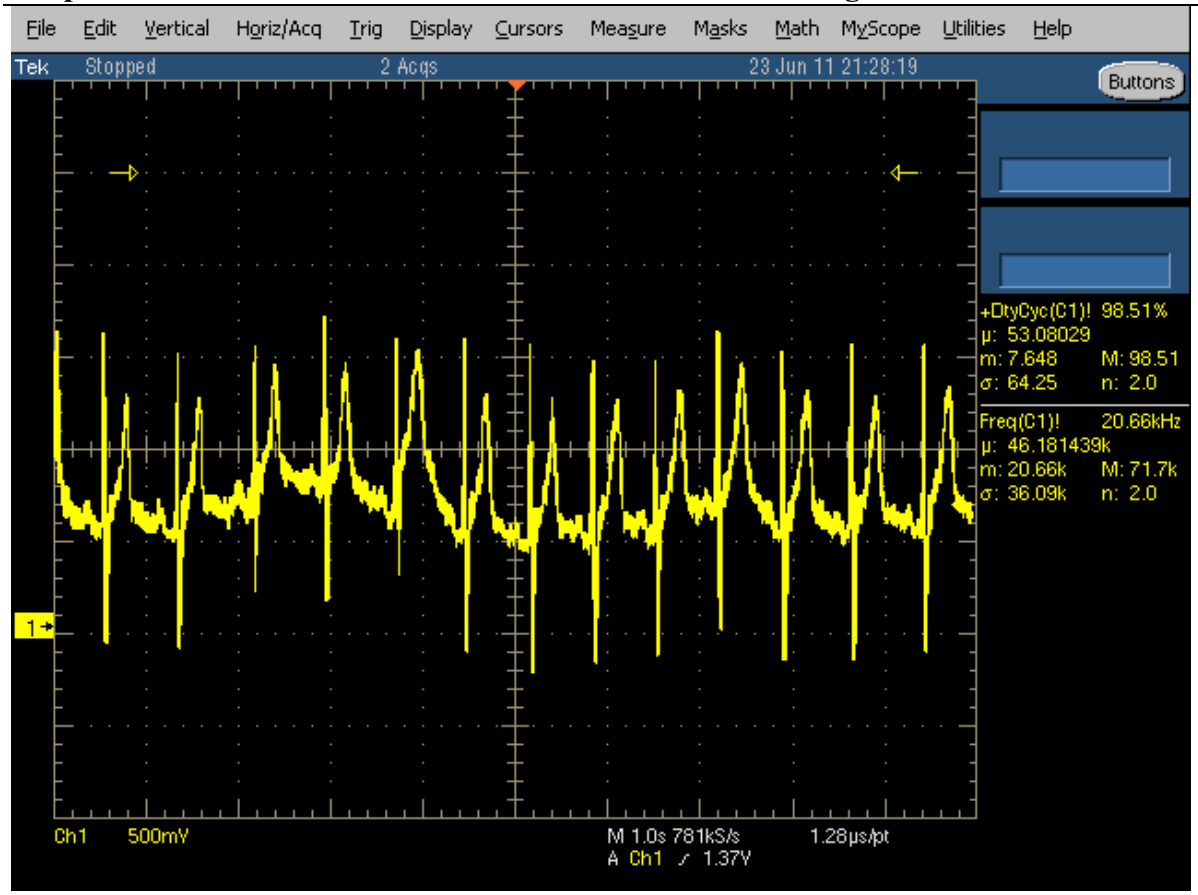

Figure 2.41 Actual oscilloscope traces of ECG signal near V_5 electrode.

Figure 2.41 gives a good indication of the signal from the differential amplifier and active one order filter applied to the ADC. The oscilloscope displays time on the horizontal (X) axis and voltage o its vertical (Y) axis. In Figure 2.41, the heart rate can be concluded approximate 84 bpm by counting 14 ECG circles in 10 seconds. The amplitude of the ECG signal is 1.5V. The experimental equipment is Tektronix TDS5104B oscilloscope.

2.9. Nano-controller

Note that the existing low power microcontrollers such as MSP430x (16-bit RISC core) [20] and ATMEGA128 (8-bit RISC) [34], on one hand, they do not have enough on chip resource (e.g. Flash memory to record 4 leads ECG signal continuously during 48h; and on the other hand they have more peripheral devices (UART, I²C, USB) than need. Thus, to minimize die size and energy consumption, we implemented a simple 8-bit RISC core dedicated to sample the ECG signal and save it directly into the flash memory or to process and send it through ZigBee wireless access medium which is connected to an UART or to record the sample data into a Flash memory through the SPI interface. Note that, the recorded ECG signal may be read by dedicated software (offline) through the SPI interface.

To minimize energy consumption a Nano-controller based on 8-bit RISC processor concept is implemented. The Nano-controller key features are (Figure 2.42):

- Firmware dedicated to RS232 connection with commercial wireless access medium such as Bluetooth or ZigBee (IEEE802.15.4),
- Firmware dedicated to SPI interface for flash memory.

Figure 2.43 presents the acquisition of data issues from the output of the ADC, and the digital data is sent to the RS232 interface in binary format (2 characters of 8-bit). Note that, with the dedicated Nano-controller only 6 Nano-instructions (8-bit) are necessary and the clock of the different blocks is activated only when need. Thus, the Nano-controller minimizes significantly the energy consumption of the SoC-Holter.

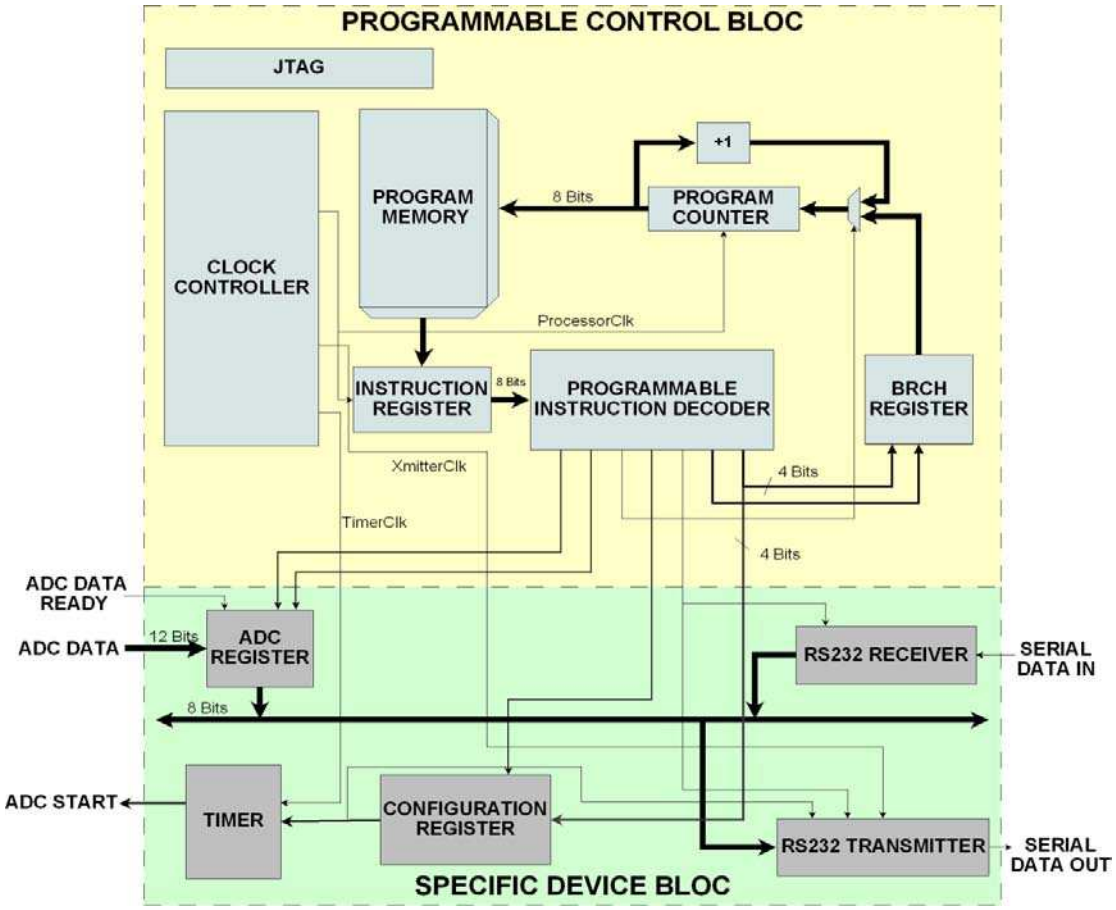

Figure 2.42 Bloc diagram of the nano-controller.

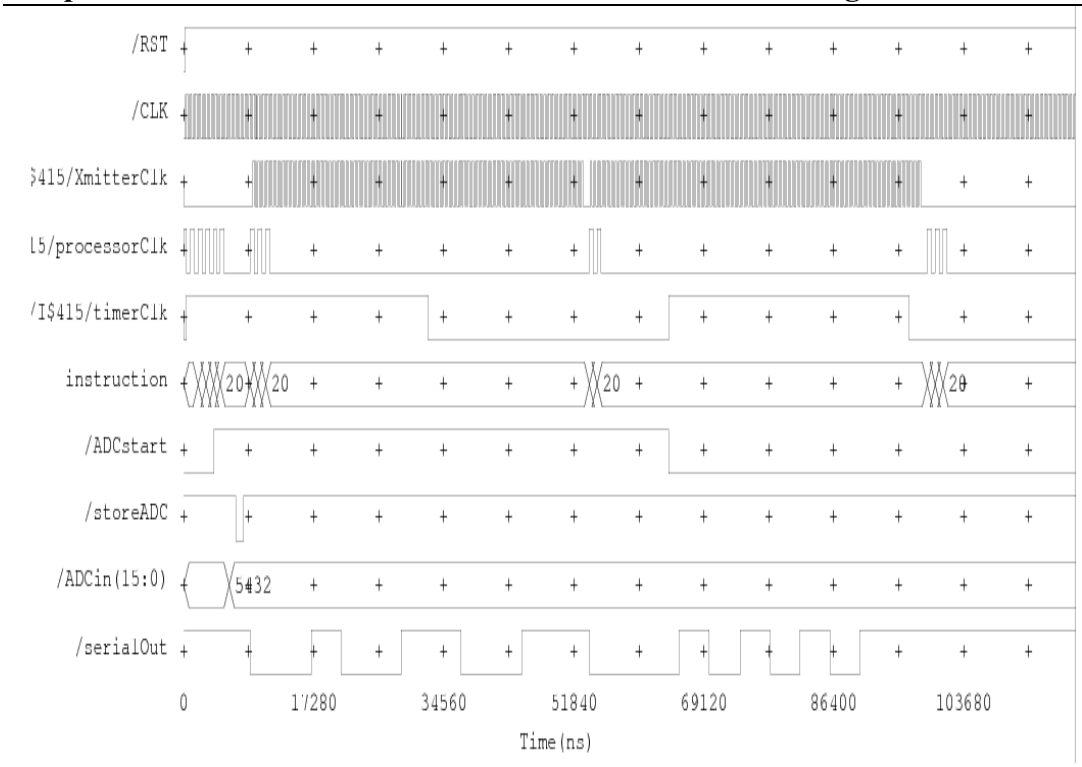

Figure 2.43 Transient response of the mixer versus time.

2.10. Conclusion

A SoC-Holter dedicated to monitoring cardiac arrhythmia is presented, and particularly the wearable single chip ECG sensor is investigated. A prototype based on commercial of-the-shelf components are implemented and tested but its form factor and energy consumption is still important for long time wearable ECG monitoring. Thus in this work, we show that it is possible to implement a single chip wearable Holter: SoC-Holter. By taking into account the specification for ECG signal, the objectives required were largely achieved. It is feasible to achieve the desired voltage gain and frequency range of the system by selecting appropriate circuit topologies. By using small transconductance OTA, the band-pass filter that passes frequencies within a range from 0.5 to 100Hz and attenuates frequencies outside that range has been presented. The Cadence software facilitated the analysis of the design and allowed for comparisons between theoretical expectations and actual simulations. The obtained results corresponded to expect performance. The Nano-controller is simulated and validated and we are starting to implement a single chip SoC-Holter which enables to record 1~4 leads ECG. Note that the current SoC-Holter may be used also to implement a wireless ECG node by connecting a ZigBee module through RS232 interface. Moreover to increase the lifetime of SoC-Holter, we will develop an embedded firmware within the Nano-controller that enables to classify normal and abnormal ECG signal. Consequently only the abnormal ECG signal will be recorded to be analyzed (offline). Finally we believe that with SoC-Holter a large number of high risk population may be user-friendly monitored to prevent efficiently sudden death.

Chapter 3
Implementation of Compressed Sensing for Telecardiology Sensor Network

3.1. Introduction of Electrocardiogram (ECG)

Cardiologists can listen to the heart of patient with a stethoscope by the method of auscultation, or feel for peripheral pulses. These methods are simple and nonspecific, but they cannot be used to identify a cardiac arrhythmia. The heart's activity could be recorded on an electrocardiogram (ECG or EKG), which measures the potential difference between two electrodes attached on the skin. The ECG works mostly by detecting and amplifying the cardiac electrical potentials on the skin during each heartbeat. The ECG provides intuitionistic impression of the activity of the heart. The monitoring and analysis of the ECG can provide a useful technique to diagnose cardiac arrhythmias from the disturbance in the rate and site of origin or conduction of the cardiac electric impulse on ECG signals. The morphology of the ECG and the period of the ECG give a general indication of the heart state to cardiologists in clinical diagnoses.

Arrhythmias are abnormal heartbeats usually caused in the heart. Cardiologists are able to diagnose cardiac arrhythmias by using the ECG. Since cardiac output is equal to the recorded ECG measurements that indirectly reflects the electrical activity in the heart. For example, Cardiologists need to monitor the effects of drugs in surgical procedures. So the effects on heart rhythm can be evaluated and determined from the recording of ECG. During each regular heartbeat, the movement of heart muscle is indirectly recorded on a screen or on paper by the rises and falls in the voltage amplitude of detected ECG signals. The display shows the variation in rhythm because the electrical impulse spreads across the heart and minor or major abnormalities on the recorded ECG measurements. Thus the ECG is an effective tool in detecting the symptom of coronary artery disease. However it is necessary to be noted that not all heart beats have audible or palpable evidence. But in the case of irregular heartbeat, non-effective pumping action of the heart produces premature or abnormal beats which indicates the occurrence of cardiac arrhythmias with the symptom of fast heart rate, slow heart rate or some skipped beats in the ECG signals.

3.1.1. Action Potentials in the Heart

The cells with a low concentration gradient of sodium ions and high levels of potassium ions will produce a cell membrane potential. Ion channels allow certain ions to pass through the cell membrane to make it more positive or less negative. The direction of inward and

outward depends on whether the membrane potential is at more positive or more negative than the reversal potential.

The action potential is produced by active channels which change the conductance as a function of voltage, as shown in Figure 3.1. The action has 5 phases during 0 to 4. In the beginning, the membrane potential is resting when the cell is not being stimulated. Once the membrane is stimulated, the transmembrane potential rises till reaching the threshold. Phase 0 is the rapid depolarization phase in which a rapid flow of sodium ion increases across the membrane of the cell, allowing positively charged sodium ions to move into the cell and increase the inside positive potential. Afterwards, these sodium channels inactivate at high voltage while potassium channels activate, allowing potassium ions to move out of the cell and decrease the membrane potential, till making a balance between inward movement and outward movement playing a key role during phase 2. During phase 3, the above channel closes, it results in the return of the transmembrane potential to its resting value because a flow of potassium ions crosses from inside to outside. The Na-K pump restores a low concentration of sodium ions and high level of potassium ions to maintain the cell membrane potential to their original values [35].

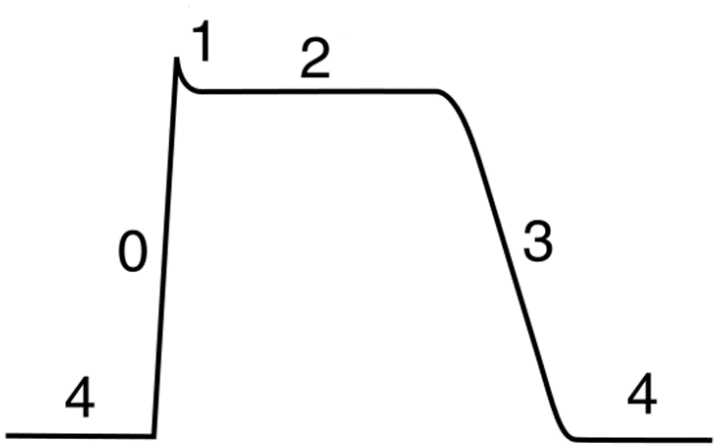

Figure 3.1 Action potential graph. The model is known as the Hodgkin-Huxley model.

- **The Fitzhugh-Nagumo model**

The Hodgkin–Huxley model is a mathematical model that describes the voltage dynamics of excitable cells. The standard Hodgkin-Huxley model is described by the following equations

$$I_M = C_M \frac{dV}{dt} + I_K + I_{Na} + I_L \tag{3-1}$$

where I_M is the total membrane current obtained from Ohm's law, C_M is the membrane capacitance, V denotes the membrane voltage, I_K is the potassium current, I_{Na} is the sodium current and I_L is leakage current which amounts physically to charged ions being passed through the membrane like a capacitor with channels for ion currents.

The Fitzhugh-Nagumo system can simplify the Hodgkin-Huxley model and accelerate to produce a spike by assuming the activation of sodium channels with two variables [35].

$$\frac{dV}{dt} = V - \frac{V^3}{3} - W + I \tag{3-2}$$

$$\frac{dW}{dt} = 0.08(V + 0.7 - 0.8W) \tag{3-3}$$

where V is the membrane difference across the cell membrane, W is a recovery variable which rises to bring the potential back to its resting value after the firing of an excitation pulse. I is the magnitude of stimulus current.

The Fitzhugh-Nagumo model is useful, because the activity now only depends on two variables V and W and thus its behavior can be more easily visualized and analyzed.

- **The conduction system of the heart**

The sinoatrial node, abbreviated SA node is the impulse generating tissue which consists of specialized muscle cells. The SA node is like an auto-excitation pacemaker which generates an action potential with a normal sinus rhythm at the rate about 70 per minute. This tissue is located on the right atrium of the heart. Action potentials from the SA node can propagate across the atria and terminate at the AV. But there is the only conduction pathway between atria and ventricles that means action potentials cannot pass directly across the boundary.

The atrioventricular node is abbreviated AV node that is located on the border between the right atria and the right ventricles at the rate about 50 pulses per minute in a normal heart. But in the abnormal situation, heart beats with higher frequency occur which arise in the AV node. The AV node is a specialized tissue providing the only conducting pathway between the atria to the ventricles in a normal heart. It implies that the AV node of normal condition is excited only by the arrival of such an impulse that propagates through it.

The bundle of His (known as the AV bundle) is composed of a common bundle connecting the atria with the ventricles of the heart which is provided by a specialized conduction system.

The bundle of His divides into a right branch and left bundle branch. An electrical impulse travels down the bundle of His from the AV node. Ultimately, the bundles ramify into many cardiac fibers which are distributed along the inner sides of the ventricular walls, allowing for rapid, coordinated and synchronous physiologic depolarization of the ventricles.

The waveforms of action potential in different specialized cardiac tissue constitute the common physical ECG signal. A normal ECG is produced as the projection of each wave with their combination result in the amplitude according to a variable angle.

- **Electrophysiology of the Heart**

The impulse which crosses the heart can be measured by the electrical current with electrodes placed on the patient's skin or chest. A cycle of normal sinus rhythm for the human heart is shown in Figure 3.2. It consists of different elements as shown in Table 3.1.

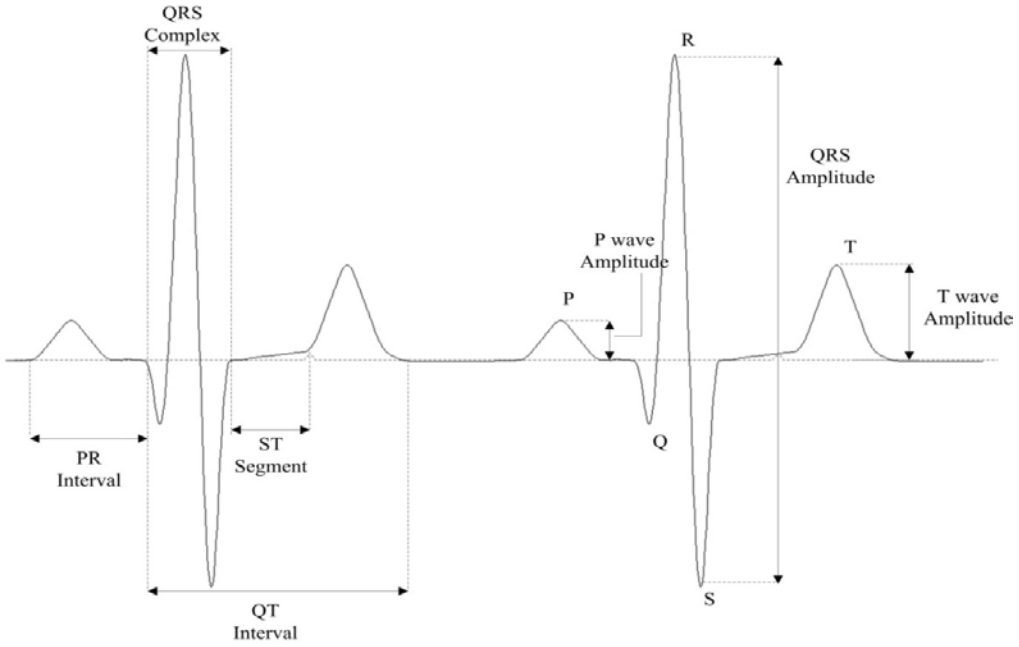

Figure 3.2 Schematic diagram of a typical ECG tracing in normal sinus rhythm.

A typical ECG tracing of a normal heart beat or cardiac cycle consists of the various deflections including some tall peaked P wave and T wave, a wide QRS complex and some small waves that are not always present. For example a small U wave is not easy to be observed, but it is visible in 50 to 75% of ECGs. Some important information of the current state of the heart can be provided by the characteristic of all particle and waves while we are comparing it with established normal ECG waveforms.

The ECG tracing is a series of waves that represent a lot of information of the heart. It can be tracked the response of abnormal rhythms of the heart. The abnormal rhythms are caused by conduction disorders which are abnormalities in the generation of electrical impulse. Electrolyte imbalances also provide the abnormal rhythms. Cardiac arrhythmias may be diagnosed by cardiologists in detecting the sequence of events on the ECG.

3.1.2. Interferences and Noise

Modern ECG monitor offers multiple filters for signal processing because there are several main types of interference and noise: baseline drift interference, power line network frequency and electrode contact noise. The power line network frequency operates on a different frequency in different countries, including its harmonics. 50Hz and 60Hz are two main power frequencies widely used in the world. It is necessary to reduce the power line noise and remove the baseline wander, because the amplitude of power line interference may be very high as 50% of peak-to-peak value of the ECG signal. Respiration and body movement can cause low frequency baseline wander. The drift of the baseline with respiration can be represented as a sinusoidal component at the frequency of the respiration combined with the ECG signal [37]. Poor electrode contact and body movements can cause random

shifts of the ECG signal amplitude, which can be regarded as the electrode contact noise abruptly changing the baseline of the ECG signal.

Table 3.1 A cycle of normal beat consists of waves, segments and intervals [36]

P wave	The firing spreads out from the sinoatrial (SA) node and activates the depolarization of the atrial in both the right and the left atriums. The duration of P wave is about 80 ms and the amplitude is 0.25 mV.
PR segment	PR segment is the delay of the electrical impulse at the atrioventricular (AV) node to allow for atrial contraction. It is the distance to measure the P wave and the QRS complex.
PR interval	The PR interval represents the time necessary for the electrical impulse to travel through the walls of the AV node. The PR interval which is more clinically relevant represents the atrial depolarization and AV delay. Normal measurements for the PR interval are usually 120 to 200 ms and the PR segment is the half of the former.
QRS complex	QRS complex reflects the ventricular depolarization, which has so large a muscle mass compared to the atria that the QRS complex usually has much larger amplitude than other elements. The duration is about 80 to 120ms. The amplitude of R is 0.16 mV, Q and S is 25% of R wave.
ST segment	ST segment is the period following the QRS complex at which ventricular depolarization is close to the end. ST segment merges into the start of ventricular repolarization and corresponds to the T wave. In general it lasts the same duration as QRS complex and isoelectric.
QT interval	The amount of time taken for ventricular depolarization and repolarization to occur. A prolonged QT interval on ECG reflects a propensity to entricular tachyarrhythmias, even to sudden death. It usually lasts 300 to 430 ms.
T wave	T wave represents the repolarization period of the ventricles. The amplitude is about 0.1 to 0.5 mV and the duration is 160ms.

Sources of artifacts from touching the electrode and motion of the patient can be eliminated, but the interference from the power line noise and the muscle tremors of patients is hard to control. The most common setting includes high-pass filter to remove baseline drift and low-pass filter to remove 50 or 60 Hz power line interference and remove other noise fetched by muscular contraction. Baseline drift/wander originates from variable contact between the electrode and the skin. A maximum skin contact and ability to reduce skin impedance help avoid baseline drift. Another solution is to employ digital filtration for

removal of baseline drift in [38]. Muscle tremor is an artifact signal which is usually generated by the arm and leg muscles. Some technicians use a filter to minimize artifact from muscle tremor, for example, they use Myogram filter with 25 Hz or 35 Hz. Moreover, the motion artifacts caused by fluctuations in skin potential due to skin stretch that has commonly irregular rhythm and irregular morphology can be eliminated using the filter [39].

3.1.3. Cardiac Arrhythmias

Cardiac arrhythmia is a term for abnormal electrical activity of the heart, which may be too fast or too slow and with an amplitude of regular or irregular [40]. Some life threatening emergencies like cardiac arrest, even sudden death are caused by cardiac arrhythmias. This medical emergency is different from a heart attack, where blood flow to the heart is impaired due to failure of the heart to contract effectively. Some arrhythmias which are very minor and may be merely annoying can be regarded as a normal sinus.

A common symptom of most cardiac arrhythmias is an awareness of abnormal heartbeat with irregular rhythm. The abnormal rhythm is usually too fast or too slow. If the heart has the problem to supply an adequate blood pressure for the heart's need, the rhythm may be too weak. These cardiac arrhythmias may be harmless but predispose to adverse outcomes. Some cardiac arrhythmias do not cause obvious symptoms in the heart rate because weak heartbeat cannot transport sufficient blood to the heart. Medical assessment of the abnormity uses cardiovascular variables such as heart rate, arterial blood pressure, stroke volume and the shape of electrocardiographic (ECG or EKG) which are the good response of fluctuations in heart beats. In general these variables in cardiovascular signals are treated as noise to be ignored. But These Cardiovascular variables reflect the relation between perturbations to cardiovascular function and the dynamic response of the cardiovascular regulatory systems. The method of analyzing these fluctuations in cardiovascular signals can provide a quantitative, noninvasive or minimally invasive method of assessing in cardiovascular regulation and stability by modern signal processing techniques.

The characteristics of the ECGs on shape, consistency and distance between the next two waveforms can provide more information about the conduction system, damaged areas and areas that are not receiving enough oxygen from the heart to meet needs. Especially the distance of various intervals in the complex of waveforms gives the learning about the conduction system. The diagnosis for the normal ECGs is made by following some of their own characteristics, where any difference may be regarded as a recognizable abnormality. A list for generating a characterization of a patient's supraventricular involves performing such characterization while the heart is being paced. Descriptions of cardiac arrhythmias are presented as follows.

- **Normal Sinus Rhythm**

Normal sinus rhythm represents the rhythm of a healthy human heart, where the sinus node generates an electrical impulse. The sinus rhythm of the normal heart ranges from 60 to 100 per minute. But the child's heart rate is usually much faster than the adult's one. Normal sinus rhythm is illustrated in Figure 3.3. All complexes are normal, the sinus rhythm and intervals are regular and all contents of waves and segments are standard. Heart rate is 78 bpm

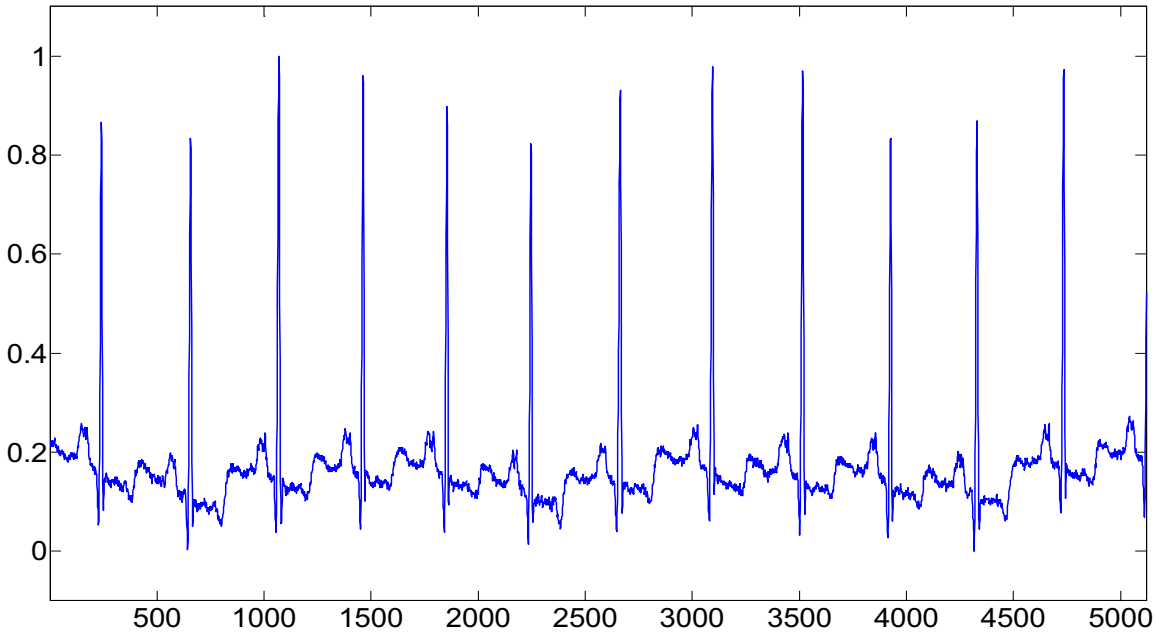

Figure 3.3 Normal Sinus Rhythm.

- **Sinus Bradycardia**

Sinus bradycardia represents the sinus rhythm of less than 60 bpm. This arrhythmia occurs because a slowed signal is generated from the sinus node. The ECG signal has a normal sinus rhythm but its rate is less than 60 per minute. Sinus bradycardia is illustrated in Figure 3.4. All complexes are normal, the sinus rhythm and intervals are regular and all contents of waves and segments are standard. However heart rate is 40 bpm.

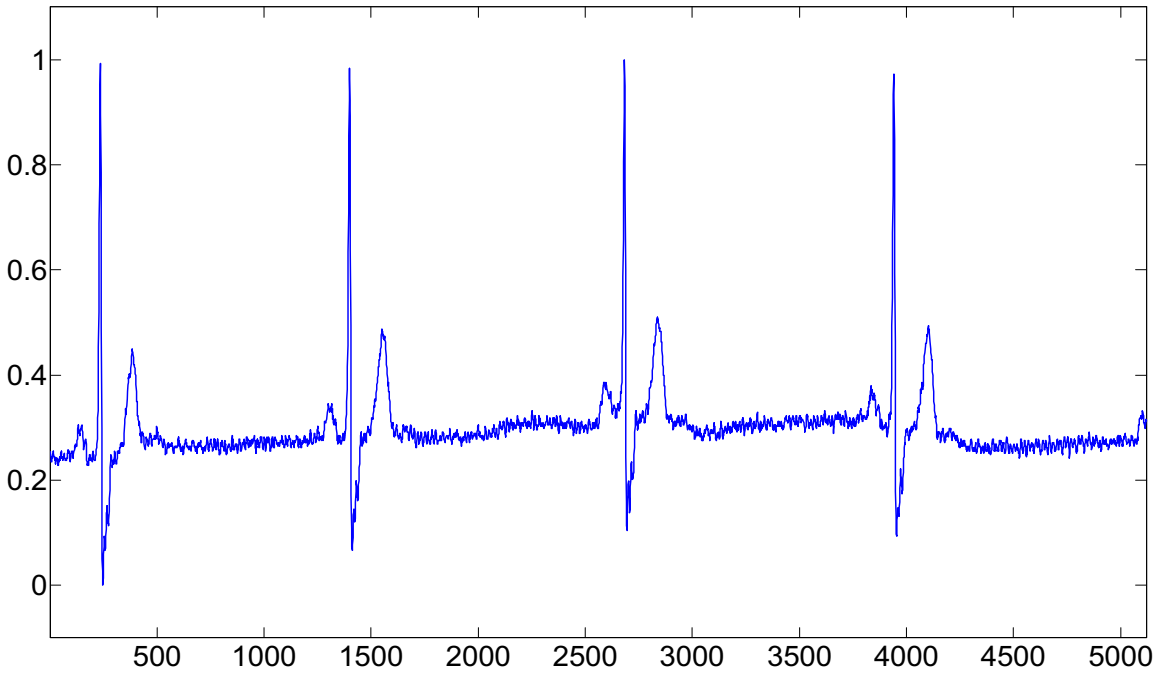

Figure 3.4 Sinus Bradycardia.

- **Ventricular Bradycardia**

This arrhythmia occurs because blocking of the electrical impulse produces a slow rhythm on its way of AV (Atrioventricular) node as shown in Figure 3.5. Heart rate is below 60 bpm and the signals come in varying degrees and severity.

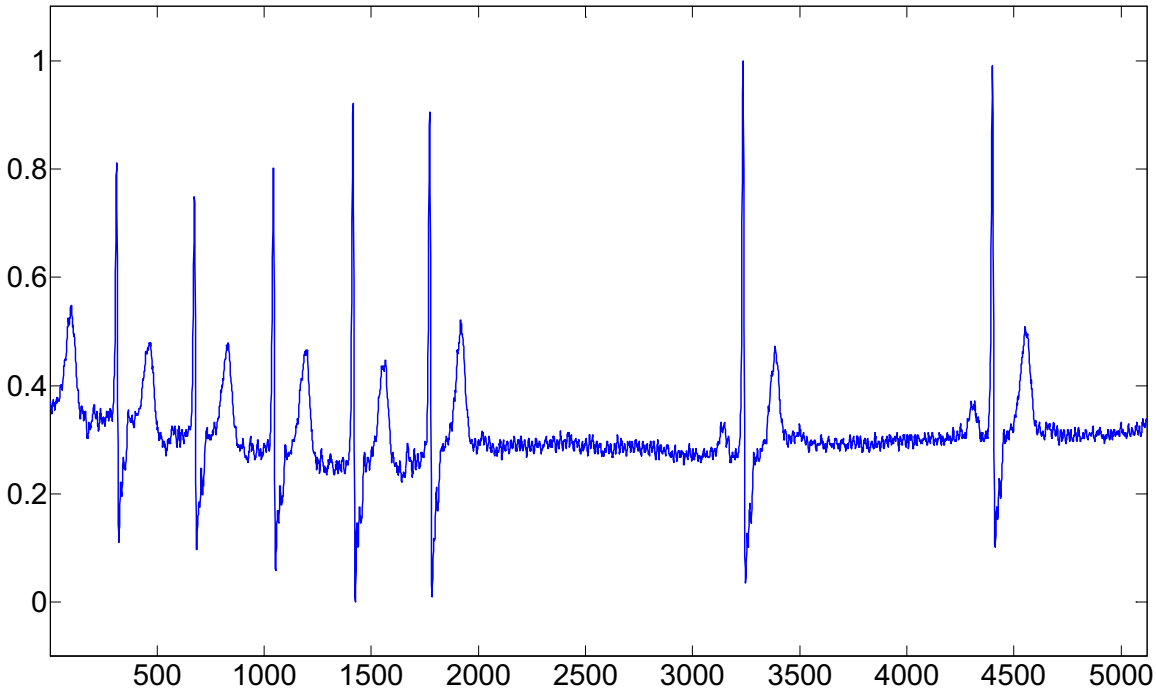

Figure 3.5 Ventricular Bradycardia.

- **Sinus Tachycardia**

Sinus tachycardia usually occurs in adults and children over 15 who have heart rate faster than 100 bpm caused by the sympathetic nervous system on the sinus node. The ECG signal has a normal sinus rhythm similar to sinus bradycardia but has a faster heart rate.

- **Ventricular Tachycardia**

In addition to sinus tachycardia, other tachycardias usually result from the addition of abnormal impulses, usually rapid, bizarre and wide QRS-complexes comparing to the normal cardiac cycle ones. The arrhythmia is called ventricular tachycardia because of the ventricular muscle which is at a high rate over 120 per minute. Ventricular tachycardia is shown in Figure 3.6. Heart rate is faster than normal rhythm due to premature ventricular contraction. There are three main causes to generate abnormal impulses on ventricular tachycardia: automaticity, reentry or triggered activity.

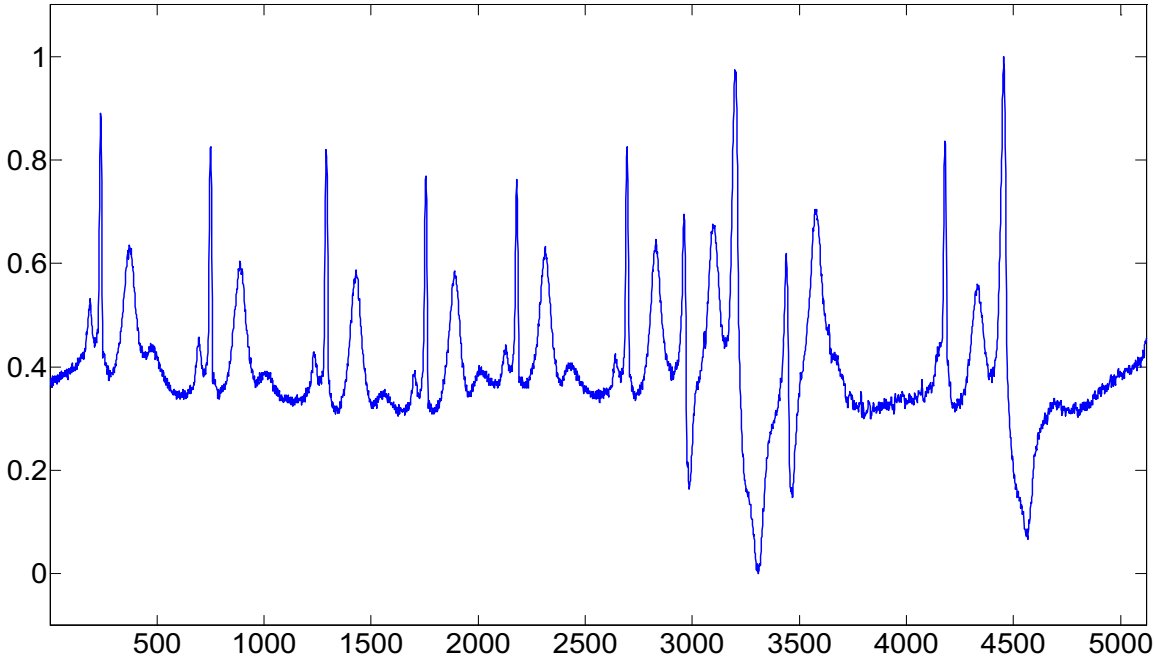

Figure 3.6 Ventricular Tachycardia.

- **Atrial Bigeminy**

Atrial bigeminy is actually a descriptor for a heart arrhythmia in which heartbeats occur in couplets. A regular (or sinus) beat is followed by an abnormal atrial beat. Atrial bigeminy is illustrated in Figure 3.7. Abnormal heartbeats follow every other concurrent normal beat.

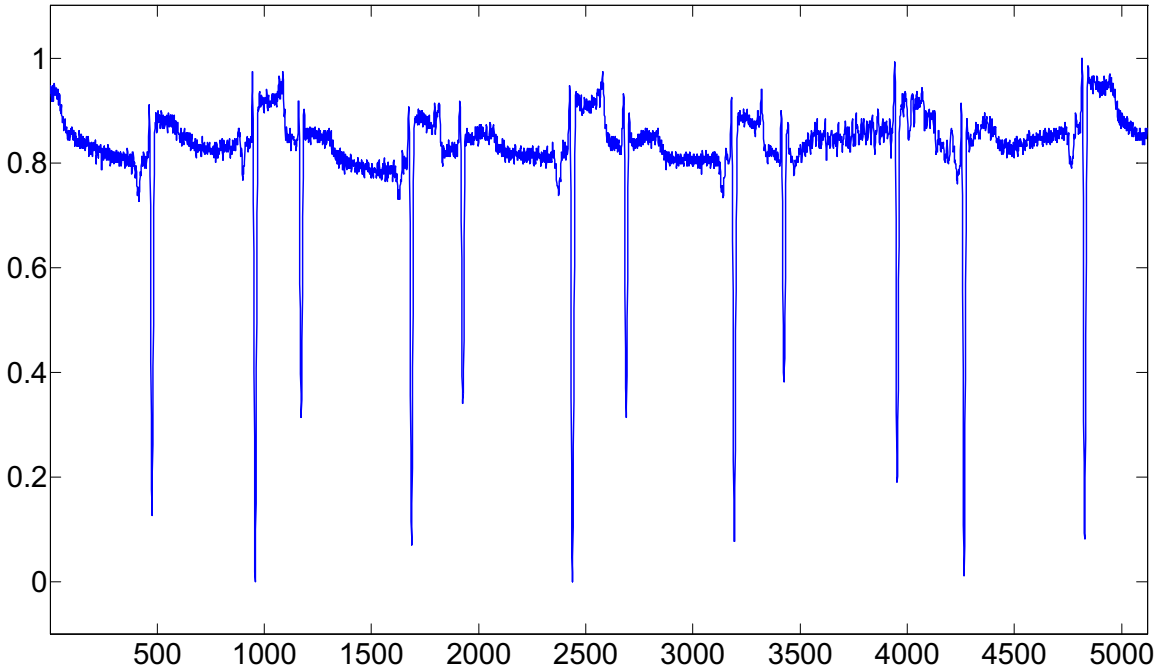

Figure 3.7 Atrial Bigeminy.

- **Ventricular Bigeminy**

An arrhythmia consisting of the premature ventricular beats (PVC) which follows a normal beat is termed ventricular bigeminy as shown in Figure 3.8. There are 11 normal heartbeats and 6 PVCs. It is obvious that every PVC is followed by one normal beat.

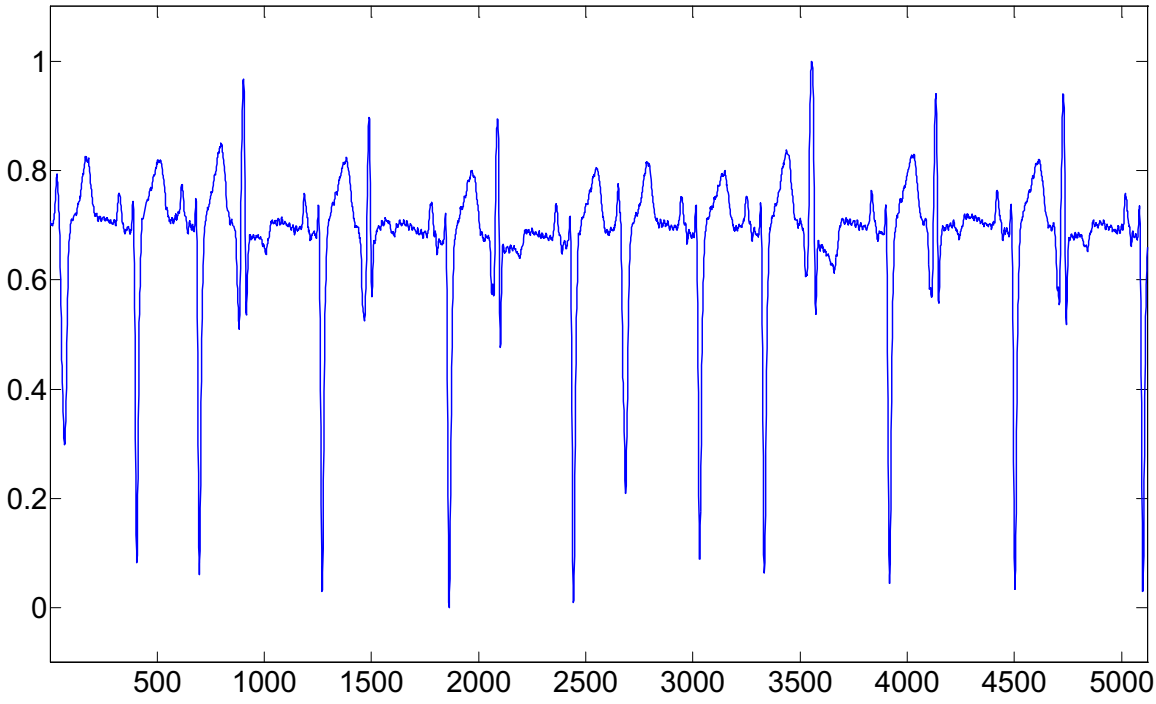

Figure 3.8 Ventricular Bigeminy.

- **Atrial Flutter**

An arrhythmia is also called as re-entry arrhythmia which occurs when an electrical impulse travels the abnormal circle within the heart as shown in Figure 3.9. A characteristic 'sawtooth' or 'picket-fence' in the ECG waveform is that the rhythm is usually very fast at about 300 bpm. Atrial flutter is associated with a fast heart rate of 150 bpm with the regular of 2:1 block. Therefore the waveform of atrial flutter depicts as a sawtooth. Comparison of atrial flutter and normal sinus in Figure 3.9 (a) the waveform of normal ECG signals in Figure 3.9(b) the waveform of atrial flutter, in which the rhythm is very high [41].

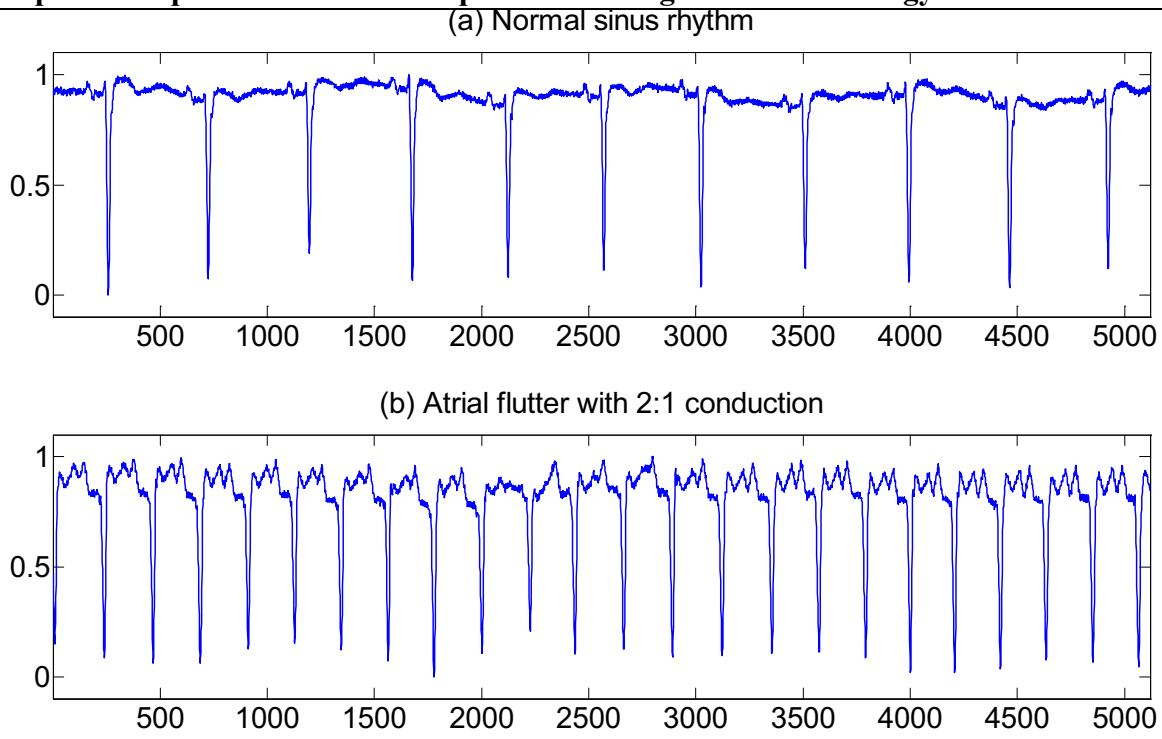

Figure 3.9 Atrial Flutter.

- **Atrial Fibrillation**

Got irregularly irregular ventricular rhythm and sometimes the heart rhythm may appear regular at first glance but it shows irregular in closer inspection as shown in Figure 3.10. Comparison of atrial flutter and normal sinus in Figure 3.10(a) the waveform of normal ECG signals in Figure 3.10(b) heart rate is a rapid and irregular accompanied with atrial fibrillation.

- **Supraventricular Tachyarrhythmia**

An arrhythmia occurs as the same pathology of atrial flutter as shown in Figure 3.11. It is a rapid rhythm of the heart and in contrast to the potentially deadlier. ECG signal has rapid rhythm that originates within AV node.

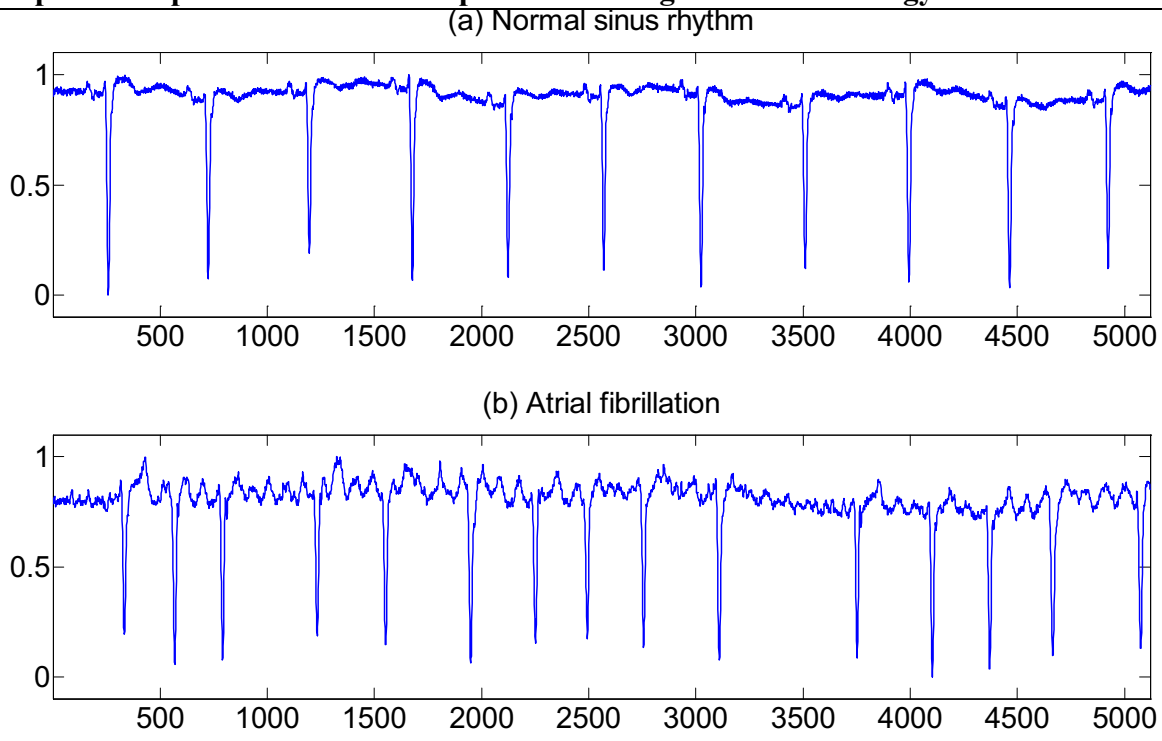

Figure 3.10 Atrial Fibrillation

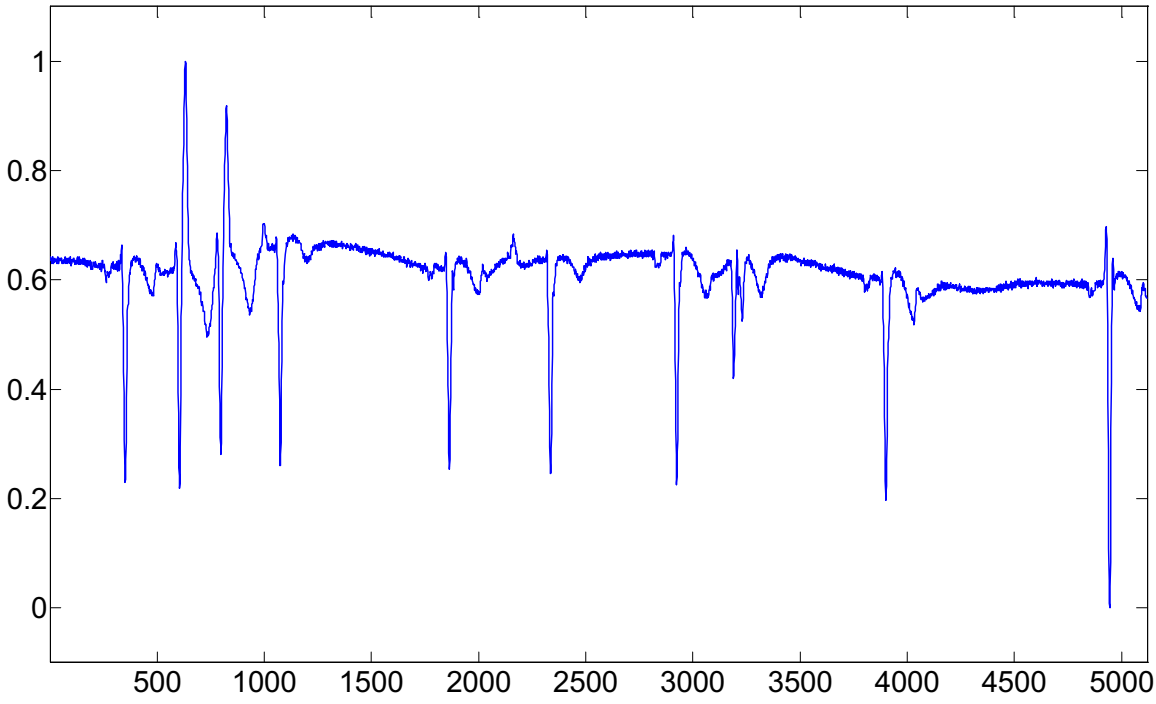

Figure 3.11 Supraventricular Tachyarrhythmia.

It is very easily confused with ventricular tachycardia but it has some differences including irregularly irregular rhythm and wider length of QRS complex of 120 ms, no secondary R wave or no lateral Q wave in leads

Cardiac arrhythmias can be classified into two groups according to the heart rate. One group includes VF (ventricular fibrillation) and VT (ventricular tachycardia) which mean a serious threat to the patient and require rapid clinical diagnosis. Detection of these arrhythmias is successfully investigated with high sensitivity and specificity [42-45]. Another group includes cardiac arrhythmias which do not require immediate diagnose but longtime monitoring and therapy to the patients who have a potential danger. Supraventricular tachyarrhythmia can be more dangerous compared with ventricular tachyarrhythmias as shown in [46].

The most important part of the ECG signal is the QRS complex, which is the beginning of the left ventricular contraction. Detection of QRS complex can provide the information on clinical applications. It is a fundament for post signal processing for ECGs, such as baseline wandering, the classification of the beats, etc. it is important to measure the duration and morphology of the QRS complex. Performance of measuring can be the percentage of successful and false detection, because the QRS complex has greater amplitude and better frequency resolution compared with the detection of other features (e.g. P wave). The time interval between the onset of Q wave and the end of S wave, which represents the duration of ventricular depolarization, is usually used to measure the changes occurred in ventricular depolarization and repolarization period [44]. Therefore, the classification of heartbeats is an important method to identify a cardiac arrhythmia.

3.1.4. Computational-based Algorithm for ECG Signals

Development in digital signal processing is the foundation of computational-based techniques which play an important role in ECG signal processing and analysis. A large number of researches are focused on the algorithm of detection of ECG waveform in view of the signal features and theoretical foundations [47]. In view of the signal features and theoretical foundations, the diagnostic techniques can be classified into several categories: amplitude only, amplitude and first derivative, first derivative only, spatial velocity of ECGs, digital filter, matching templates, neural network, wavelet and mathematical morphology. Two primary applications of ECG signal processing, QRS detection and anomaly element extraction, are examined, an overview of techniques and algorithms for the QRS detection and anomaly element extraction are discussed.

3.1.4.1. Algorithm based on Amplitude

The ECG signal has a noticeable spike-like shape and the most conspicuous component, the QRS complex. This clue inspires a simple detecting technology to detect the position and presence of ECG signals by setting an amplitude threshold for deciding QRS complex candidates. For example, the ECG samples fall beyond the amplitude threshold are regarded as potential QRS complex. The author Friesen introduced a method based on the algorithm Moiret-Mahoudex to obtain the QRS candidates [37].

The calculation of this amplitude threshold value is to acquire the average amplitude of the largest positive valued element in a fraction of the signal. The selection of the fraction

depends on the characteristic of ECG signal. R peak in the QRS complex could be ascertained to the highest amplitude of the detected QRS complex. All candidates are judged with a threshold, the maximum of the values enclosed by the parenthesis is treated as R peak.

3.1.4.2. Algorithm based on Derivative

RR interval can be measured by several first derivatives based QRS detection techniques described in the literature, and further the first and second derivatives are calculated from the ECG signals, which are presented in [48, 49]. The signal derivatives is to extract the components of the QRS complex while attenuate other components such as P and T waves. A scheme of simple derivative design is to mean three consecutive points on the first derivative array exceed a positive slope threshold and the next two consecutive points with a small duration of time which exceed the negative threshold, if the RR interval is derived based on amplitude of these candidates after the detection of the QRS complex. If we choose more ECG data compared to the threshold, more information about derivative, such as both of the first and second derivative, the basic algorithm will not change.

3.1.4.3. Algorithm based on Digital Filter

Useful information about frequency components of the QRS complex is typically ranged to 10Hz and 25Hz. A band-pass filter attenuates low and high frequencies but attains a middle range band of frequencies. The transfer function of the band-pass filter is obtained by multiplying the transfer functions of a low-pass filter and of a high-pass filter, where the cut-off frequency of the low-pass filter is higher than that of the high-pass filter. Other designs which are intended for the accurate measurements of heart rate variability and reliable QRS detection in ambulatory ECG signals application are presented in [50, 51]. These QRS detection algorithms can be used in analog domains. In amplified stage the ECG signals are attenuated the components outside the 0.5-35Hz frequency band. This enhances the performance of detection by attenuating various noise components and improve the SNR greatly so that the ECG signals can be amplified following the dynamic range of Analog to Digital Convertor, and symmetries the QRS complex for the threshold detection, which is essential to improve the performance of detection. The initial ECG signals pass through a 50-Hz notch filter which removes any residual power-line interference from the sampled signal. And then the filtered signals pass through a band-pass filter which attenuates the low frequency noise. Engelese and Zeekenberg [52] introduce the ECG signals passing through a differentiator with a 62.5Hz notch filter. Positive and negative thresholds are used with equal magnitude. The number of alternate thresholds crossing classifies the beginning of baseline shift. At first, the input signal passes through low-pass filter until a point with amplitude greater than the positive threshold is detected. This point is regarded as the onset of search region. Then if no other threshold crossing occurs within the next search region, the occurrence is classified as a baseline shift. Otherwise the filtered data is crossing the negative threshold and the positive threshold again in some cases, the occurrence is classified as a QRS candidate. The digital signal as noise occurs more threshold crossing.

The final filtering stage is a matched filter providing an optimal SNR and important symmetrical output pulse waveform. The waveforms of the matched output are calculated as

$$Y(t) = \sum_{i}^{N} k_i X(t-i) \tag{3-4}$$

where N is the length of the filter impulse response. The filter coefficients k_i are selected by presenting the interactive display of the band-pass filtered QRS complex. The matched filter impulse response is optimized by choosing the appropriate filter coefficients for each patient in the beginning of measurement.

3.1.4.4. Algorithm based on Artificial Neural Network

Artificial neural network (ANN) has been trained to perform in a field of ECG QRS detection. ECG signal classification is the most important application of ANN, which has been proposed in the literature.

The authors in [53] describe an adaptive and self-organizing pattern classification to dynamically respond to the characteristics of multi-channel ECG signals. This method carries out a non-supervised learning process to the morphologies that are presented as QRS, updating its weight and storing a representation of each QRS. Another important characteristic of the method is to modify SNR towards the final classification by the selective evaluation of the beat class differences in each channel as a function of the signal quality.

The authors use artificial Neural Networks for arrhythmia detection because of its capacity to reject unknown or ambiguous ECG signal [54, 55]. Silipo and Marchesi introduced an ANN structure combined with both pre-processing and post-processing techniques and evaluated the performance of arrhythmia classification, ischemia detection and recognition of chronic myocardial diseases [56]. In order to detect and classify the heartbeats, the authors used a simple neural architecture called as adaptive multilayer perceptron for the ECG QRS detection. This method improves the performance for noise reduction in the QRS complex that is degraded by nonlinear background noise. The design of neural network classifier is able to reliable identify detection of QRS complexes and has better noise immunity in a noisy environment. Some researchers use neuronal network algorithms namely the adaptive multilayer perceptron to classify QRS complex in ECG signal. In general, the implementation of QRS complex pattern classification is the use of the distinguished information between normal and abnormal beat morphologies. In the work of [56], the authors could achieve more successful in the classification of 12 different abnormal beat morphologies. The method computes a weighted sum of all ECG signals, and subtracts the sum from a predefined bias and passes the result through a threshold function whose output ranges from 0 and 1. The output activation is defined as

$$a_i = f(u_i) = \frac{1}{1 + exp\,(-u_i)} \tag{3-5}$$

and u_i is a weighted sum of all the ECG signals and a bias

$$u_i = \sum_{j=1}^{N} w_{ij} x_j + \theta_i \tag{3-6}$$

3.1.4.5. Algorithm based on Other Analysis Techniques

QRS detection algorithms based on time-frequency analysis described in [57] the smoother pseudo Wigner-Ville distribution is used to analyze the spectral components of heart rate variability (HRV). With auto discrete Wigner distribution and cross discrete Wigner distribution, the algorithm is used to estimate spectral changes in non-stationary RR intervals.

Algorithms based on mathematical morphology are developed in [58]. Erosion and dilation are the basic mathematical morphology operators originated from the field of imagine processing. The actual useful operators are opening and closing which are the combinations of erosion and dilation. The operation of erosion followed by dilation could be defined as opening operator and the operation of dilation followed by erosion could be defined as closing operator. The morphological operation of opening can remove signal peaks and closing can remove all valleys in the signal depending on the chosen structuring element.

Some researchers use a method of a nonlinear dynamics for the analysis of the ECG, which is a chaotic modeling for non-stationary time series. Calculation of the correlation dimension to discriminate a chaotic system is also a problem. In [59] the method is not well-suitable for real-time applications because a large amount of data is needed.

3.2. Direct Cardiac Arrhythmias via Compressed Measurements

3.2.1. Introduction

Power consumption and storage capacity of a Wearable Wireless ECG Sensor (WES) are challenging problems. To get a solution, we introduce a novel method based on Compressed Sensing (CS) technique to the WES. The main principle underlying this framework is to sample analog signals at sub-Nyquist rate at the ADCs and to classify directly compressed measurement into normal and abnormal state. Those compressed measurements which imply a risk of cardiac anomaly will be stored in a multimedia flash memory card or be transferred to the terminal of the network for cardiologists to make an offline diagnosis of cardiac arrhythmias by using the reconstructed signals from the compressed measurements. In this work, we demonstrate our proposed scheme to directly classify compressed ECG samples into normal and abnormal states, instead of having to reconstruct the entire signal to distinguish between normal and abnormal states. Our algorithm takes advantage of estimating parameters directly from the compressed measurements. Thereby it eliminates the reconstruct stage and reduces the computational complexity in WES. In addition, our framework provides

compressed ECG signals without loss of information, reducing significantly the power consumption for message sending and memory storage space in WES.

Cardiac arrhythmias present abnormal electrical activities due to cardiovascular diseases. In France, it has been estimated that more than 60,000 annual sudden deaths are due to cardiac arrhythmias [60]. In fact the traditional techniques such as Holter and R.test are not totally efficient in preventing sudden death caused by cardiac arrhythmias. Thus it is necessary to seek a new user-friendly technique to detect cardiac arrhythmias. Wireless Body Sensor Network (WBSN) enables wireless communication between the miniaturized body sensor unit and personal portable equipment worn on the body for the next generation of ambulatory personal telecardiology. Wearable wireless ECG Sensor (WES) seems to be a good tool to help prevent sudden death due to cardiac arrhythmia. This wearable, miniaturized and wireless sensor is able to monitor ECG signals and wireless report cardiac signals to a coordinator, which is responsible to transmit them to a local and remote surveillance server for telehealth [16, 60]. The LIMOS platform dedicated to real-time cardiac arrhythmia tele-assistance and monitoring is implemented responding to the recommendations provided by AHA. The recorded ECG signals from 4 lead electrodes are sampled at 500Hz by the WES. The WES is a real-time wireless portable product based on ultra low power microcontroller MSP430 from Texas Instruments. There are two main operating modes of the system: online and offline. In online mode, the sensors are placed on the user's bodies to gather ECG signals which are then transmitted to a local server at home or in the hospital, depending on a wireless medium such as WiFi, Bluetooth and ZigBee. In offline mode, ECG signals are converted to digital data and stored into a Multimedia flash Memory Card (MMC) without any analysis and diagnosis. Obviously the lifetime of the system in this mode is relative to the specifics of the device: the storage capacity of the MMC, the sampling rate of the device and the number of ECG leads.

Figure 3.12(a) presents a running mode in which the WES can be configured to send ECG signals or an anomaly message to the remote server for diagnosis by cardiologists. In Figure 3.12(b) presents a running mode in which ECG signals can be stored in the WES flash memory card. Figure 3.12(c) depicts a scene using the Holter system to monitor ECG at the hospital. Fig.1d shows our wearable wireless ECG sensor (WES).

The main constraints of the wearable wireless ECG sensor (WES) are energy consumption and form factor limited by rigorous restricted battery power. The primary energy consumption in our system is the Radio Frequency (RF) communication powered by battery which is not convenient to be changed or recharged. Many state-of-the-art ECG monitors fall short because they transmit uncompressed ECG signals over power hungry wireless networking. One method is to minimize the memory footprint of WES by minimizing the amount of the stored data and synchronously reduce the power consumption by decreasing the sending data. ECG signals are compressible and thus largely sparse in some transformed domains. Therefore compression algorithms which eliminate unwanted redundancy of the ECG signals are exploited. Traditional embedded ECG compression leads to complex signal processing over low-power microcontroller.

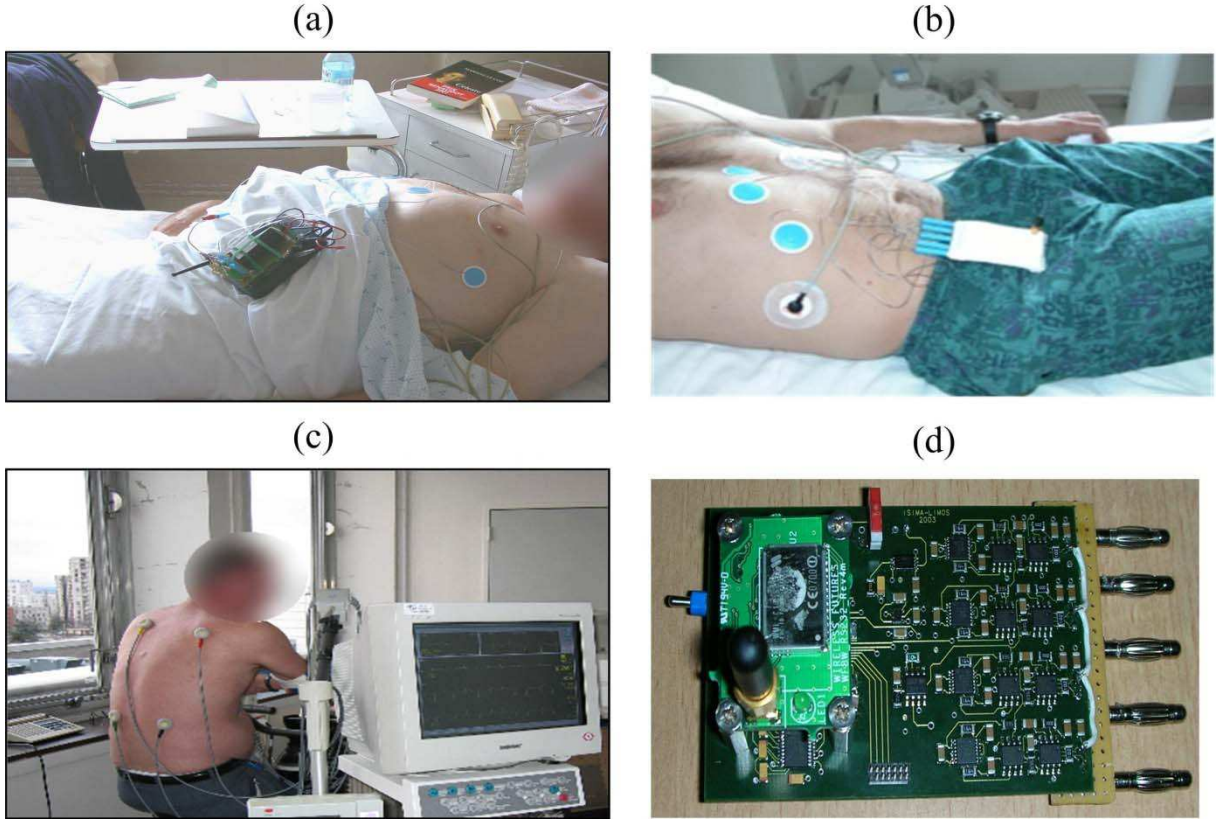

Figure 3.12 Wireless ECG Sensor continuously monitoring the patients suffering from cardiac arrhythmia.

The Compressed Sensing (CS) framework [61, 62] asserts that the underlying signal can be recovered precisely from fewer samples than that of traditionally used methods, so as the signal is sparse in a particular domain. As long as the ECG signals are sparse in transformation space, they can be represented by using only a few transform coefficients. In [63, 64], the authors introduce some practical application of CS on remote sensing approach. For example, the method of sampling Photoplethysmogram (PPG) signals with fewer samples than with uniform sampling and without losing the accuracy of heart rate and blood pressure estimated values are presented in [63]. A configuration of compressed sampling is shown in Figure 3.13(b), compared to the block diagram of traditional ADC in Figure 3.13(a). In Figure 3.13(a) traditional ADC converts a continuous quantity $x(t)$ or x_t to a discrete time digital representation $x(n)$ or x_n. In Figure 3.13(b) the CS-ADC samples time domain signal $x(t)$ and generates the lower measurement $y(m)$, M is smaller than N. The implementation of compressed sensing ADC results in sampling the input signal at a compressed rate. Consequently, it allows to lower the sample rate and to implement the compression algorithm in the sampling stage. The important advantages of the compressed sensing ADC are: 1) the ADC samples are at the lower clock rate compared to the previous counterpart, which results in a reduced power consumption of ADC; 2) stored data is already compressed without using the embedded microcontroller to compress data.

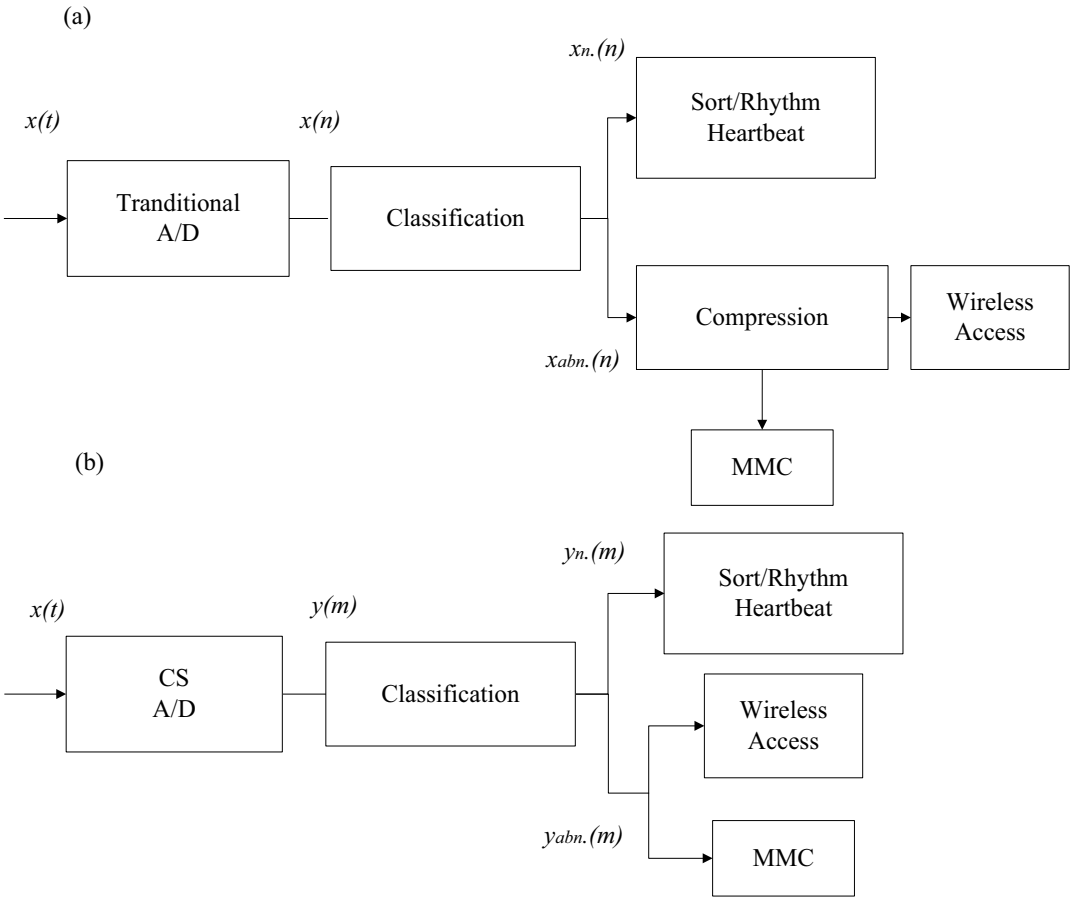

Figure 3.13 Comparison of traditional and CS ADC. (a) Traditional ADC converts a continuous quantity *x(t)* or x_t to a discrete time digital representation *x(n)* or x_n,(b) The CS-ADC samples time domain signal *x(t)* and generates the lower measurement *y(m)*, *M* is smaller than *N*. The subscript "n" refers to normal and "abn" indices abnormal.

Cardiac arrhythmia detection allows the classification of compressed samples but at the cost of increasing computational complexity over embedded microprocessor. Because the conventional classification algorithms need to reconstruct the original ECG signals from compressed samples, it is non-trivial especially in a power-constrained WES. This motivates us to develop a scheme for direct classification of the compressed samples of ECG signals into normal and abnormal ones while incurring minimum computational complexity. The compressed samples including abnormal ECG signals are transmitted to the local or remote surveillance, where the original ECG signals are reconstructed for providing more accurate and detailed information for cardiologists. The remaining samples holding irrelevant information of cardiac arrhythmias are all discarded except the information of heartbeat extracted from them. Direct cardiac arrhythmia detection avoids reconstructing the original ECG signals from the compressed samples to the Nyquist rate of samples on WES, and transfers computational complexity of reconstruction to the local or remote surveillance which has more powerful computation resource.

In the next section of this chapter, we present a viable way to reduce energy consumption and data storage of the WES by adopting the CS technique. Direct classification of compressed measurements leads us to directly detect cardiac anomaly by estimating the

presence of anomalous elements without reconstructing the entire signals. The reconstruction stage is completely eliminated on WES. Compressed measurements representing cardiac anomaly will be stored on WES and be constructed on other devices with more resource, such as a computer, to provide information to help make certain the type of cardiac arrhythmias for cardiologists. The above mentioned procedures are shown in Figure 3.14.

In order to achieve this object, the Bayesian Compressive Sensing (BCS) is adopted to estimate the parameters of the underlying signal from the compressed samples. A BCS framework is introduced by the author in [65] to estimate signal parameters directly from the compressed measurements. The author demonstrates a method to direct spectrum sensing from the compressed measurements and achieve the sampling reduction by using Compressed Sensing with much less computational complexity. The key algorithm contrived by the author is to directly estimate signal parameter from the compressed signal, thereby eliminating the reconstructed stage and reducing the computational complexity.

3.2.2. Cardiac signal model

The cardiac signal model is formally defined using the compressed sensing technology where the characteristics of ECG signal are considered.

3.2.2.1. Wavelet Transform for Cardiac Signal

The ECG signal study is a qualitative analysis of electrical impulses generated from the sinoatrial node spread the heart during the cardiac cycle. The QRS complex is the foremost ECG wave that is originated from ventricular depolarization. The symptoms of cardiac arrhythmia include fast, slow or irregular heartbeats associated with adverse events that the heart can’t pump blood effectively to meet the body's needs. Lack of blood supply for the heart causes the patient that can feel lightheaded, dizzy, or faint. The presence of the QRS complex is an important component to identify cardiac arrhythmias. Heart rate can be expressed as beats per minute (bpm) by counting the number of QRS complex per minute. In the contest of adult medicine, bradycardia is the resting heart rate of less than 60 bpm. Tachycardia refers to a heart rate that is greater than 100 bpm. The rhythm of regular or irregular is determined by calculating the RR intervals that is the duration between two consecutive R waves of the ECG. The irregular rhythm is usually associated with atrial flutter, atrial fibrillation of sinus arrest.

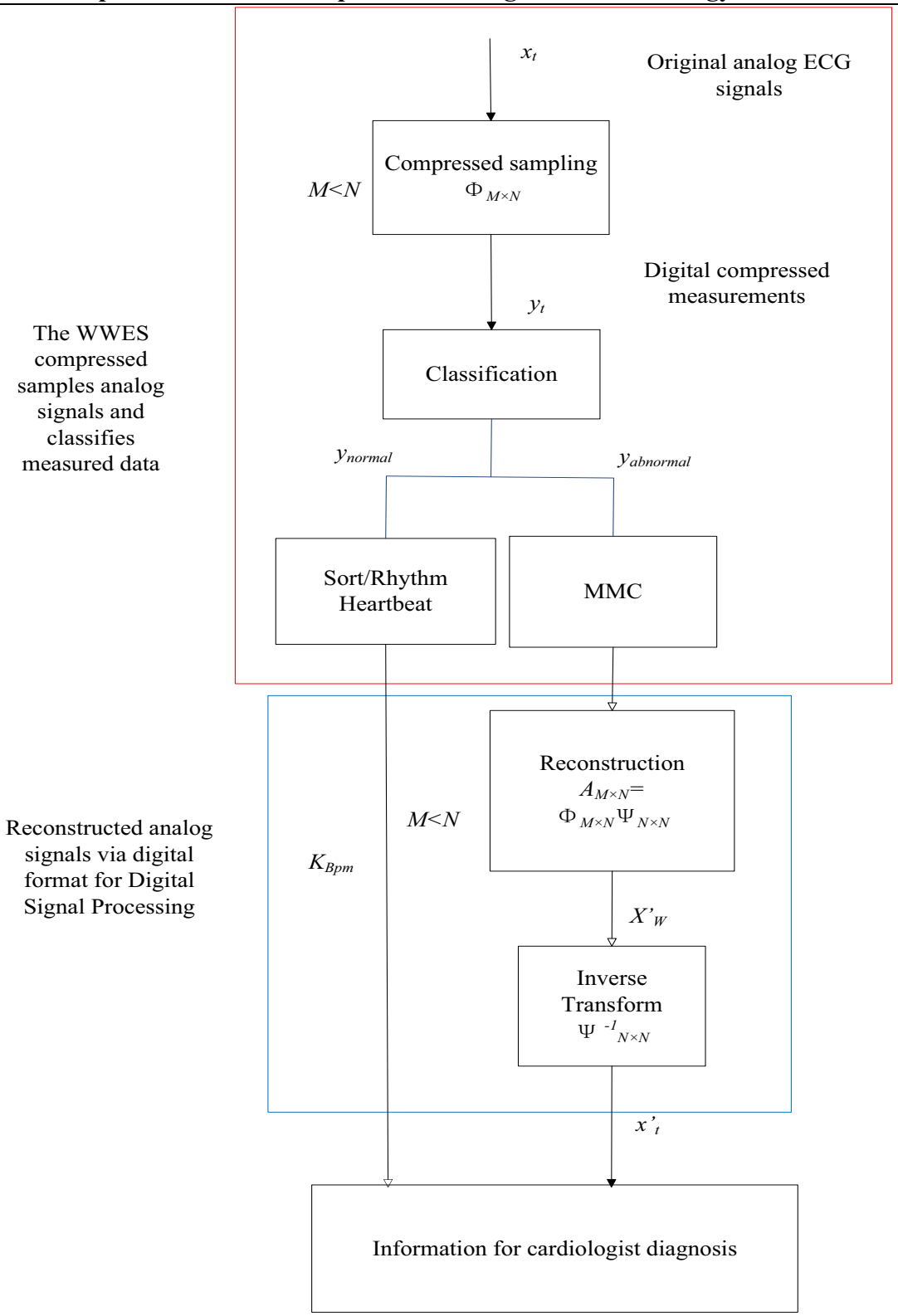

Figure 3.14 WES compressed samples of analog ECG signals according to CS theory, the classification algorithm obtains heart rate from measurements of normal ECG signals which are discarded later, and stores measurements of abnormal ECG signals into MMC. Reconstructed digital ECG signals and normal heart rate are provided to cardiologist to diagnose.

Wavelet transform is being adopted in the field of analyzing medical signal [66]. From the discussion of these articles, we can confirm that ECG signals can be sparsely represented in Wavelet-transform space, by choosing significant wavelet coefficients and abandoning all the other smaller coefficients [67, 68]. The Wavelet-transform space consists of various wavelet bases at different scales. The sparse wavelet transform can be represented by $N \times N$ matrix W. Where W is given by

$$W_{i,j}(t) = 2^{-\frac{j}{2}} w\left(2^{-j}t - k\right) \tag{3-7}$$

The components of transform matrix W are constructed by the translation and dilation of a mother wavelet $w(t)$, provided by Haar wavelet or other wavelets [69]. So it is possible to represent the transient elements in original signal by relatively small number of wavelet coefficients.

The following paragraphs will describe the basic concepts of Continuous Wavelet Transform (CWT). A coefficient $C(a, b)$ is calculated by a chosen wavelet and a section of the original signal that presents the correlation between the wavelet and this fragment of the signal. The higher $C(a, b)$ implies that the chosen wavelet and the signal have high similarity. CWT is very efficient in determining the damping ratio of oscillating signals and very resistant to the noise in the signal.

In practice, a discrete Wavelet Transform (DWT) is more convenient in numerical analysis and functional analysis. In other words, DWT is actually wavelet transform in which the wavelets are discretized.

Let the original ECG signals are denoted by a data vector, $x = (x_1, \cdots, x_N)$, where N is the length of the data vector. So we can define the discrete wavelet transform with respect to $w(t)$, as

$$d_{i,j} = \sum_{i=1}^{N} x_t(i) w_{i,j}(t) \tag{3-8}$$

Discrete analysis of ECG signals is more appropriate than continuous analysis. The basic shape of a healthy ECG heartbeat is well known by cardiologists. The reconstruction of the original signal does not need all wavelet values of decomposition because the energy of ECG signal is finite. Thus continuous transform for ECG signal is redundant and unnecessary. Discrete transform is sufficient for the analysis of the continuous-time ECG signal. The original ECG signal is characterized by discrete transform. The information associated with the symptom of a pathological condition is not lost in this case.

3.2.2.2. Multiresolution Analysis

DWT acts on the signal as a filter bank whose frequency characteristics are linked to the chosen wavelet basis. It is necessary to find the fast wavelet transform for machine computation. Multiresolution analysis is the designed method that the decomposition, with respect to an orthonormal base of $L^2(R)$, is replaced by an iteration where high-pass and low-pass filtering followed by downsampling.

At first, $f(t)$ is in $L^2(R)$ space, which is of space L^2 including all square integrable functions which consist of a sequence of nested subspaces.

In practical, this solution satisfies the relations regularity and self-similarity in time (space) and scale (frequency). The scaling function is chosen to satisfy the continuity, smoothness and tail requirements. The subspace V_j is generated by a suitable wavelet function with the integer shifts and scales. It is important to form the family of wavelet by orthonormal basis for the reference space V_0.

$$\{V_j\} \subset L^2(R) \tag{3-9}$$

The spaces V_j are nested. In mathematics, the closure of $L^2(R)$ space consists of the union of all V_j. Thus V_j is dense in $L^2(R)$. But the intersection of all V_j is empty.

$$f(x) \in V_j \Leftrightarrow f(2x) \in V_{j+1} \tag{3-10}$$

For the sake of self-similarity; all subspace V_j are invariant with the shift controlled by integer multiples of 2^{-j}. $f \in V_j$ and $g \in V_j$ can deduce

$$f(x) = g\left(x + m2^{-j}\right) \tag{3-11}$$

where m is a constant.

Because $V_0 \in V_1$, every function in V_0 can be presented as a linear combination of the functions in V_1. Coefficients are defined as $h_k = \langle \beta(x), \sqrt{2}\beta(2x-k) \rangle$, for $|k| \leq N$ and $h_k = 0$ for $|k| > N$.

$$\beta(x) = \sum_{k=-N}^{N} h_k \sqrt{2}\beta(2x-k) \tag{3-12}$$

The mother wavelet is provided as

$$\alpha(x) = \sqrt{2} \sum_{k=-N}^{N} (-1)^k h_{1-k} \beta(2x-k) \tag{3-13}$$

The space V_j is spanned by $\beta_{j,k}(x)$. Consider the orthonormal complement W_j of V_j to V_{j+1},

$$V_{j+1} = V_j \oplus W_j \tag{3-14}$$

This means all bases of V_j are orthonormal to all members of W_j. It shows that $\sqrt{2}\alpha(x-k)$ is an orthonormal basis of W_1. The similarity property of multiresolution analysis gives that $2^{j/2}\alpha\left(2^{j/2}x-k\right)$ is a basis of W_j. Also the family of $2^{j/2}\alpha\left(2^{j/2}x-k\right)$ is a basis of $L^2(R)$.

For a given function $f \in L^2(R)$, one can find $f_N \in V_N$, approximate f up to preassigned precision. If $f_i \in V_i$ and $g_i \in W_i$, the wavelet decomposition of f is given as

$$f_N = f_{N-1} + g_{N-1} = \sum_{i=1}^{M} g_{N-i} + f_{N-M} \tag{3-15}$$

Sub-band coding scheme is known as multiresolution analysis by using Mallat's pyramidal algorithm in signal processing. The L^2 sequence h_k and g_k are quadrature mirror filters. Therefore with digital filtering techniques, it is possible to obtain an effective time-scale representation of a digital signal.

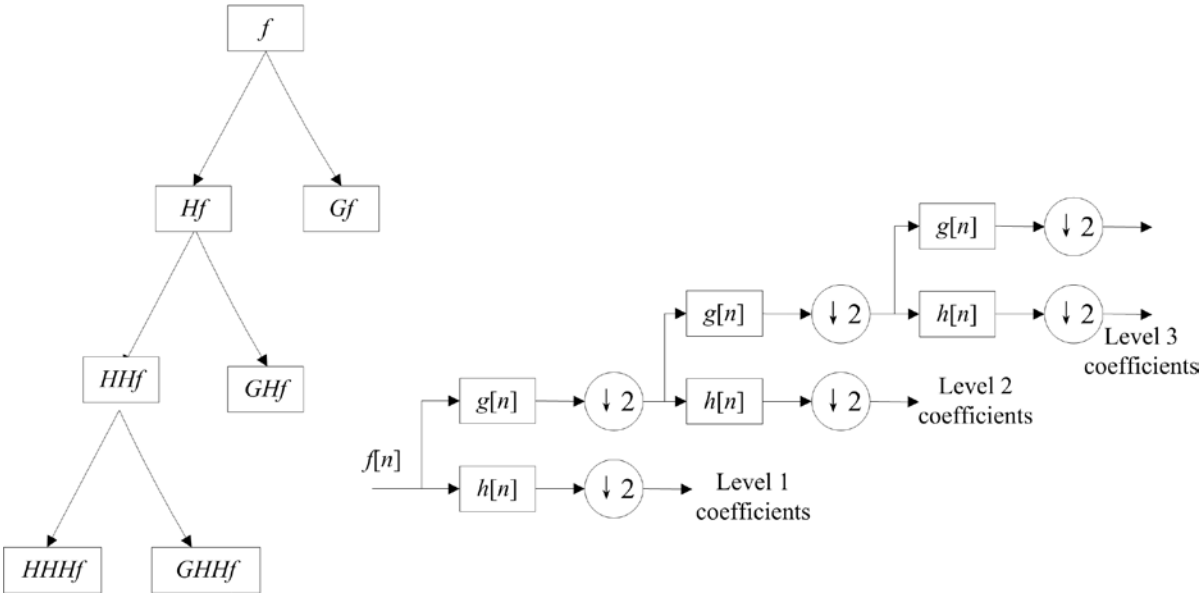

Figure 3.15 Pyramid algorithm or sub-band coding and a 3 level filter bank.

The sequence h_k is a low-pass filter while g_k is high-pass filter, and satisfying

$$g_k = (-1)^n h_{1-n} \tag{3-16}$$

The increase in frequency resolution is achieved while repeating the process of decomposition. The structure of two channels is called a filter bank. Detail coefficients are the outputs of the high-pass filter and approximation coefficients are the outputs of the low-pass filter. The outputs size is halved by down-sampled. It can be represented by a binary tree, in which every node represents an appropriate sub-space of the original signal localized in the different time-frequency plane. So the operator representation of filters is the most compact way to use wavelet transformation to describe the decomposition procedure from a signal.

The discrete signal is presented by a sequence $f = \{f_n\}$ that can be decomposed. The operators H and G are defined by the coordinatewise relations as

$$(Hf)_k = \sum_k h(n-2k)f(n) \tag{3-17}$$

$$(Gf)_k = \sum_k g(n-2k)f(n) \tag{3-18}$$

The operator H and G correspond to digital filters $h(k)$ and $g(k)$ in the wavelet decomposition. Thus the discrete signal can be presented by wavelet transform as

$$f \to \left(Gf, GHf, GH^2f, \dots, GH^{k-1}f, H^k f\right) = (D_k, D_{k-1}, \dots, D_1, A) \tag{3-19}$$

where $D_k, D_{k-1}, \dots, D_1$ are coefficient details and A is coefficient approximation.

The ECG decomposition depicts different energy partitions for resolution levels of the beats of normal and abnormal cases. Abnormal waveforms are located on the coarser levels when normal patterns appear on the finest scales. Figure 3.16 shows a detailed view of the decomposition for an isolated beat. Orthonormal decomposition of ECG signal is depicted according the order from the top (the original signal) to bottom (the details of D1 to D9). The two first levels contain the high frequency information. The levels 3-5 hold the information related to the P wave and QRS complex. It can be seen that T wave appears only on the lowest levels.

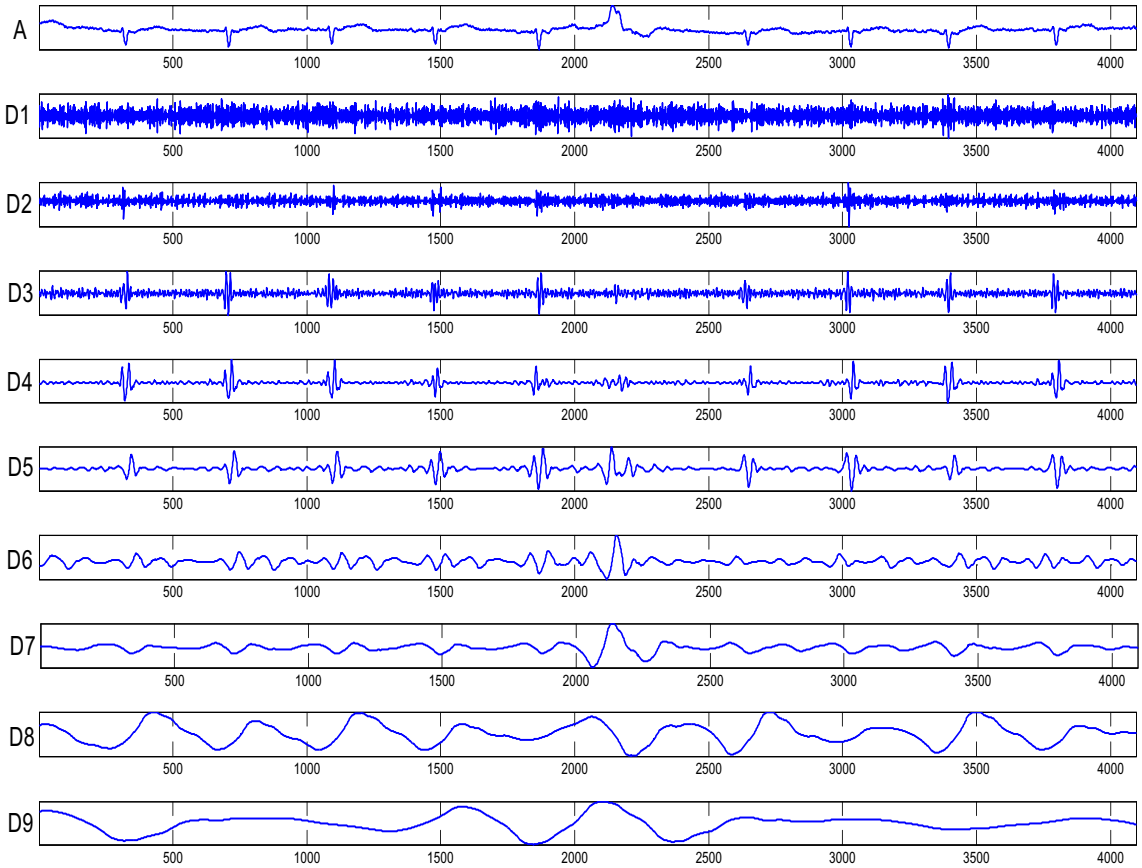

Figure 3.16 Orthonormal decomposition of ECG signal.

QRS complex which is the major component of ECG signals is enhanced due to obvious resolution when the other components are less visible. The result also points out that no additional information is obtained when the decomposition is treated as more and more levels of detail. Thus, the choice of the number of decomposition levels is the same significant as the selection of wavelet base.

Comparing parameters are derived from orthogonal wavelets. The energies are estimated at each resolution level. The local extrema of the decomposition mean the value and location of the QRS complex. The significant extrema or a set of extrema are observed at levels 3 to 5. It displays the value and position of normal beats. And the energies related to levels 6 and 7 represent the value and position of an abnormal beat. The analysis confirms the visual

inspection of the decomposition that abnormal patterns have the main energy on levels 6 and 7 and the most important contribution appears on level 3 to 5 for normal beats.

The author Senhadji introduces a wavelet-based approach that provides excellent performance of 99.8% detection for the MIT/BIH arrhythmia database [41]. They have demonstrated a feature extraction method based on wavelet transformation for discriminating between normal and abnormal cardiac patterns. The WT has also been applied to the detection of ventricular late potentials (VLP), which are small signals with the frequency content above 40Hz leading to coronary heart disease, myocardial infarctions and ventricular arrhythmia. VLP can be typically found in the QRS complex. WT is also applied to characterize beat-to-beat fluctuation of the heart rate under varying physiological conditions. The detection accuracy of the WT is superior to other time-frequency methods by Khadra and Dickaus [67].

3.2.2.3. The DWT Matrix Representation

DWT can be presented the linear operations. Therefore, it is possible to define DWT by matrix notation. The length of the input signal is set to 2^J. A matrix G_k is created by using the filter g. H_k can be obtained by changing h_i by $(-1)^i h_{N+1-i}$. The constant N is a parameter corresponding to time shift and the position of the analyzing wavelet on the time scale. So the Daubechies wavelets are a family of filters with vanishing moments. The number of vanishing moments is determined by a standard choice for N. The matrix $\left[\frac{H_k}{G_k}\right]$ is a basis-changing matrix that is used to change different objects in 2^{J-k+1} dimensional space.

We can use a filter bank to expanse discrete-time signals. It has been mentioned in the filter bank literature that these filters are involved in such system. The structure of system is shown as

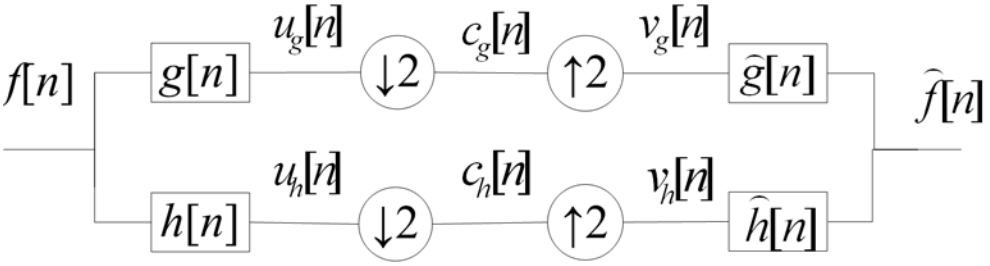

Figure 3.17 Two channel filter bank.

The signals pass through a low-pass filter H and are down-sampled by keeping only even-numbered components. Similarly, the signals passing through a high-pass filter G are processed with the same procedure. In the mathematical discipline of linear algebra, linear transformation can be represented by Toeplitz matrix that is constant along all diagonals.

$$Hf = \begin{bmatrix} \vdots & \vdots & \vdots & \vdots & \vdots & \vdots & \vdots & \vdots & \vdots \\ \vdots & h(3) & h(2) & h(1) & h(0) & 0 & 0 & 0 & \vdots \\ \vdots & 0 & h(3) & h(2) & h(1) & h(0) & 0 & 0 & \vdots \\ \vdots & 0 & 0 & h(3) & h(2) & h(1) & h(0) & 0 & \vdots \\ \vdots & 0 & 0 & 0 & h(3) & h(2) & h(1) & h(0) & \vdots \\ \vdots & \vdots & \vdots & \vdots & \vdots & \vdots & \vdots & \vdots & \vdots \end{bmatrix} \begin{bmatrix} \vdots \\ f(-1) \\ f(0) \\ f(1) \\ f(2) \\ \vdots \end{bmatrix} = \begin{bmatrix} \vdots \\ u_h(-1) \\ u_h(0) \\ u_h(1) \\ u_h(2) \\ \vdots \end{bmatrix} \tag{3-20}$$

then down-sampling by keeping only even-numbered components:

$$H_{\downarrow 2} f = \begin{bmatrix} \vdots & \vdots & \vdots & \vdots & \vdots & \vdots & \vdots & \vdots \\ \vdots & h(3) & h(2) & h(1) & h(0) & 0 & 0 & \vdots \\ \vdots & 0 & 0 & h(3) & h(2) & h(1) & h(0) & \vdots \\ \vdots & \vdots & \vdots & \vdots & \vdots & \vdots & \vdots & \vdots \end{bmatrix} \begin{bmatrix} \vdots \\ f(0) \\ f(2) \\ \vdots \end{bmatrix} = \begin{bmatrix} \vdots \\ u_h(0) \\ u_h(2) \\ \vdots \end{bmatrix} = \begin{bmatrix} \vdots \\ c_h(0) \\ c_h(2) \\ \vdots \end{bmatrix} \tag{3-21}$$

when the two filters H and G are combined, we get the Toeplitz matrix that is presented as

$$Tf = \begin{bmatrix} \vdots & \vdots & \vdots & \vdots & \vdots & \vdots & \vdots & \vdots & \vdots \\ \vdots & h(3) & h(2) & h(1) & h(0) & 0 & 0 & 0 & \vdots \\ \vdots & g(3) & g(2) & g(1) & g(0) & 0 & 0 & 0 & \vdots \\ \vdots & 0 & 0 & h(3) & h(2) & h(1) & h(0) & 0 & \vdots \\ \vdots & 0 & 0 & g(3) & g(2) & g(1) & g(0) & 0 & \vdots \\ \vdots & \vdots & \vdots & \vdots & \vdots & \vdots & \vdots & \vdots & \vdots \end{bmatrix} \begin{bmatrix} \vdots \\ f(0) \\ f(1) \\ f(2) \\ f(3) \\ \vdots \end{bmatrix} = \begin{bmatrix} \vdots \\ c_h(0) \\ c_g(0) \\ c_h(1) \\ c_g(1) \\ \vdots \end{bmatrix} \tag{3-22}$$

reconstruction of the signal can be achieved using the synthesis $\hat{T}$

$$\hat{T}c = \begin{bmatrix} \vdots & \vdots & \vdots & \vdots & \vdots & \vdots & \vdots & \vdots & \vdots \\ \vdots & \hat{h}(3) & \hat{h}(2) & \hat{h}(1) & \hat{h}(0) & 0 & 0 & 0 & \vdots \\ \vdots & \hat{g}(3) & \hat{g}(2) & \hat{g}(1) & \hat{g}(0) & 0 & 0 & 0 & \vdots \\ \vdots & 0 & 0 & \hat{h}(3) & \hat{h}(2) & \hat{h}(1) & \hat{h}(0) & 0 & \vdots \\ \vdots & 0 & 0 & \hat{g}(3) & \hat{g}(2) & \hat{g}(1) & \hat{g}(0) & 0 & \vdots \\ \vdots & \vdots & \vdots & \vdots & \vdots & \vdots & \vdots & \vdots & \vdots \end{bmatrix} \begin{bmatrix} \vdots \\ c_h(0) \\ c_g(0) \\ c_h(1) \\ c_g(1) \\ \vdots \end{bmatrix} = \begin{bmatrix} \vdots \\ \hat{f}(0) \\ \hat{f}(1) \\ \hat{f}(2) \\ \hat{f}(3) \\ \vdots \end{bmatrix} \tag{3-23}$$

finally

$$\hat{f} = \hat{T}c = \hat{T}Tf \tag{3-24}$$

to satisfy the requirement of reconstruction,

$$I_{2^{J-k}} = [\hat{H}_k \quad \hat{G}_k] \left[\frac{H_k}{G_k}\right] = \hat{H}_k H_k + \hat{G}_k G_k \tag{3-25}$$

and

$$I = \begin{bmatrix} H_k \\ \overline{G_k} \end{bmatrix} [\hat{H}_k \quad \hat{G}_k] = \begin{bmatrix} H_k\hat{H}_k & H_k\hat{G}_k \\ G_k\hat{H}_k & G_k\hat{G}_k \end{bmatrix} \tag{3-26}$$

where $H_k\hat{H}_k = I$, $G_k\hat{G}_k = I$, $H_k\hat{G}_k = G_k\hat{H}_k = 0$,

Now in an orthonormal case with J-step wavelet transformation, equivalent filters are given by

$$H^J(z) = H^{J-1}H\left(z^{2^{J-1}}\right) = \prod_{k=0}^{J-1} H(z^{2^k}) \tag{3-27}$$

$$G^J(z) = H^{J-1}G\left(z^{2^{J-1}}\right) = G\left(z^{2^{J-1}}\right)\prod_{k=0}^{J-2} H(z^{2^k}) \tag{3-28}$$

in time domain, all outputs can be described as

$$GH^{J-1}f(n) \tag{3-29}$$

$$C = W_J f(n) \tag{3-30}$$

where

$$W_1 = \begin{bmatrix} H_1 \\ \overline{G_1} \end{bmatrix} \tag{3-31}$$

$$W_2 = \begin{bmatrix} \begin{bmatrix} H_2 \\ \overline{G_2} \end{bmatrix} H_1 \\ \overline{G_1} \end{bmatrix} \tag{3-32}$$

$$W_3 = \begin{bmatrix} \begin{bmatrix} \begin{bmatrix} H_3 \\ \overline{G_3} \end{bmatrix} H_2 \\ \overline{G_2} \end{bmatrix} H_1 \\ \overline{G_1} \\ \\ \end{bmatrix} \tag{3-33}$$

...

Next, we represent a viable way to reduce the energy consumption and data storage of the WES by adopting the CS technique. Direct classification of compressed measurements leads us to directly detect cardiac anomaly by estimating the presence of anomalous elements without reconstructing the entire signal. The reconstruction stage is completely eliminated on WES. Compressed measurements representing cardiac anomaly will be stored on WES and be constructed on other devices with more resource, such as computer, to provide the information to make certain the type of cardiac arrhythmias for cardiologist. A flow chart of the abovementioned procedures is shown in Figure 3.14.

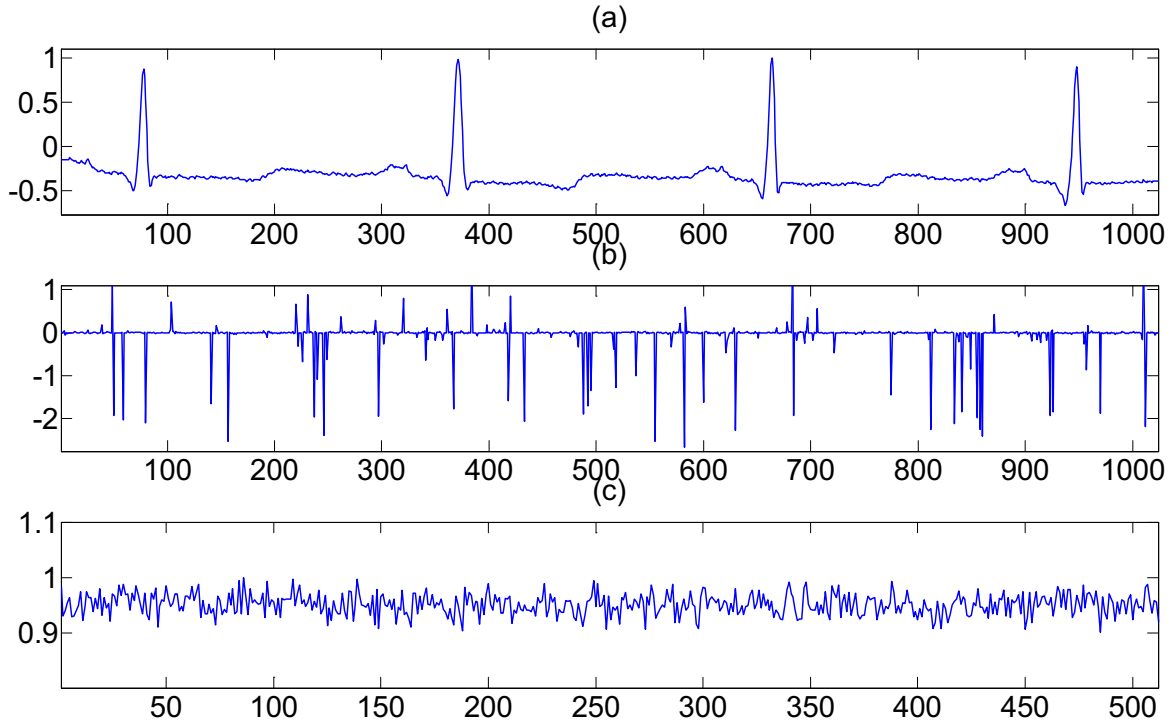

Figure 3.18 Compressed sensing of ECG. (a) Original ECG signals of 1024 points with normalized values in the range, (b) Its wavelet transform coefficients arranged in random sequence for enhanced visibility, most wavelet coefficients are close to zero, only a few of them are conduce to information of ECG signals. (c) From measurements by sampling 512 points from ECG signals in (a).

ECG signals are projected on sparse presentation. The original signal is illustrated in Figure 3.18(a) and its wavelet transform is depicted in Figure 3.18(b). To enhance visibility these wavelet coefficients have been arranged in random order. From the figures, we can get a verdict: most wavelet coefficients are small, and few coefficients are large. If we set an appropriate threshold, all wavelet coefficients under the threshold is set to zero and only wavelet coefficients which are greater than the threshold are kept. Thus, we maintain only less than 100 wavelet coefficients of high amplitude and set the rest wavelet coefficients to zero. The outcome of measurements in Figure 3.18(c) can be seen as the randomization of the sequence of ECG signals, which are affected by the role of sensing matrix.

ECG signals are sparse in the wavelet transform domain, which reminds us to express them by using fewer measurements than original sample [62, 70]. For example, with Bayesian model, all of the unknowns are treated as stochastic quantities with a probability distribution function [71].

3.2.3. Compressed Sensing

Sparsity identifies the signal of interest. A continuous time signal may be sampled at least two times faster than the signal bandwidth without losing information following the Shannon/Nyquist sampling theorem. Sparsity implies one idea that this signal can be represented by smaller length compared with suggested by its bandwidth. The discrete signal

as $f \in R^N$ is more likely to express original signals with much smaller than its finite length. Many natural and manmade signals and images have several concise representations to eliminate the redundancy. In other words, these original signals and images could be expressed sparse or compressible in the proper basis Ψ.

Wavelet expansions often provide concise representations of natural signals. Thus most natural signals are compressible when expressed in a convenient basis. Most of wavelet coefficients are close to zero and only relatively few coefficients contain most of the information. The number of these wavelet coefficients is very fewer than the pixels of image. So the image can be expressed by wavelet coefficients, it is a form of data compression suited for image called Wavelet Transform.

The sensing process of the ideal sampling may be expressed as

$$y_t = \Phi x_t = \Phi\psi X_w = AX_w \tag{3-34}$$

where the measurement matrix Φ is a $M \times N$ projection matrix and x_t represents the Nyquist rate $N \times 1$ vector with $x_t[n] = x(t)|_{t=nT_0}$. The compressed measurement $y_t[m]$ is essentially the projection of x_t onto the basis. ψ is an N-points wavelet transform matrix mapping the time domain signal to the wavelet domain where X_w is sparse. X_w may have all but K elements set to zero. $K < M < N$, this denotes that the number of M measurements is fewer than K degrees of freedom for N length signal sampled at the Nyquist rate in time domain. $A = \Phi\psi$ expresses the relation between compressed samples y_t to the transformed domain signal X_w.

Compressed sensing has proven that a N samples time signal x_t could be represented by a vector X_w that is K-sparse in other transform domain based on the basis ψ. Original time domain signal x_t may be reorganized from compressed measurement y_t, a vector composed of M linear projections of x_t by the measurement matrix Φ. Hence the measurement matrix Φ could be built to the dimension of $M \times N$.

The measurement matrix Φ can be defined as Gram–Schmidt process by selecting a finite, linearly independent set and generating an orthogonal transposed set [72]. The incoherent results by acquiring correlations with random distributed signal as a white noise is good and it implies that Φ can be generated with Gaussian distribution, which exhibits very low coherence characteristics with any fixed representation. Then using the projection operator by

$$proj_{\phi_{k-1}} = \frac{\langle \phi_{k-1}, \phi_k \rangle}{\langle \phi_{k-1}, \phi_{k-1} \rangle} \phi_{k-1} \tag{3-35}$$

where $\langle \cdot \rangle$ denotes the inner product of the components of measurement matrix Φ. We can project one vector orthogonally onto another one.

The procedure of Gram–Schmidt is shown as follows:

$$\phi_k = \phi_k - \sum_{j=1}^{k-1} proj_{\phi_j}(\phi_k) \tag{3-36}$$

$\phi_{M \times N}$ is generated in advance following the pseudo-random matrix generator. Measurements are calculated in an iterative manner.

We can get the M-dimensional measurement vector Y which is obtained from the original ECG signals X and it is defined as

$$Y_{M\times 1} = \Phi_{M\times N} X_{N\times 1} \tag{3-37}$$

Therefore the recovery of X_w is an ill-posed problem which could be estimated accurately if X_w is sparse over a known orthonormal basis. The coefficients of X_w may be approximated using an optimization algorithm under an appropriate norm. Solving sparse solutions of underdetermined systems of linear equations by ℓ_0 norm is an NP-complete optimization problem and requires exhaustive computation [71]. In [73-75] authors directly minimize the ℓ_0 norm to obtain faster linear programming solvers. ℓ_2 norm will almost never converge to the K-sparse solution in [76], so the ℓ_1-regularized formulation is defined as

$$\hat{X}_w = arg\min_{X_w} \|y_t - \Phi\psi X_w\|_{\ell_2}^2 + \tau\|X_w\|_{\ell_1} \tag{3-38}$$

where τ is a regulation parameter controlling the relative importance of the Euclidian error and the sparseness, converting the problem of the optimum X_w to the basis pursuit by iterative threshold.

- **Incoherence**

Incoherence identifies the sensing modality, which is a statistic to express the relation between the sensing matrix Φ and the representation matrix ψ. The incoherence of the measurement/sparsity pair Φ and ψ is opposite to the number of required measurements. The greater is the former, the smaller will be the latter. Measurements are acquired from the objects with a sparse representation in ψ which is spread out in the transform domain. The signals f can be represented with smaller number of fixed waveforms in time domain that are incoherent with the sparsifying basis ψ.

Compressed sensing or sampling provides a way to economically translate analog data into already compressed signals, without losing the useful information content embedded in the signal, which can be a sparse representation in the special basis. So the long length original signal is condensed into a small amount of data or measurements. Using CS theory, measurement infrastructures such as ECG sensor are able to very efficiently capture the information of ECG signal that is sparse in some transform domains without trying to comprehend that signal. Further, an optimization method is used to reconstruct the original signal with more samples from the small amount of recorded data as well as to accelerate the digital solutions. As the result, CS could provide efficient solution for signal acquisition and be widely used in a variety of applications. CS samples the original signal at a low rate and processes later an incomplete set of measurements to reconstruct the signal but increasing computational complexity.

- **Incoherent Sampling**

The choice of sensing basis Φ and its appropriated representation basis Ψ which is orthogonal basis of Φ allows us to define the domain in which measurements are sparse. The incoherence between the sensing matrix Φ and the representation matrix Ψ is not essential but could simplify the treatment process.

The relation between the sensing matrix Φ and the representation matrix Ψ could be represented by the coherence that means the largest correlation between any two elements of Φ and Ψ. It is obvious that the coherence is larger if elements of Φ and Ψ are more correlated. Otherwise, if elements of Φ and Ψ are less correlated, the coherence is smaller. In other words, the mutual coherence between sensing matrix and representation matrix which influences the number of samples needed to recover the original signal. Low coherence pairs of Φ and Ψ are very important to Compressive Sampling.

The canonical basis is chosen as the sensing basis to further explain

$$\varphi_k(t) = \delta(t-k) \tag{3-39}$$

and the representation basis is the Fourier basis

$$\psi_j(t) = n^{-1/2} e^{i\,2\pi\,jt/n} \tag{3-40}$$

The sensing matrix corresponds to the sampling plan in time or space domain. Maximal incoherence is obtained by the time-frequency pair obeying mutual conjugate of any elements in Φ and Ψ. It means that the basis of canonical scheme should incoherent with the Fourier basis. The bases of spikes and sinusoids have been proved to meet the condition in one dimension and further maximally incoherent in any dimension.

- **Noiselet Measurements and Wavelet Presentations**

If a signal has a compact representation when expressed in the wavelet domain, then it can be spread out in the noiselet domain. Thus it could choose wavelets bases for the representation basis ψ and noiselet for the sensing basis. The wavelet system ψ consits of the orthonormal Haar wavelet basis and Φ is an orthonormal system of the noiselets, then the product of Φ and ψ has entries of constant magnitude. Thus a signal with N-length that has S-sparse representation in the Haar wavelet domain can be reconstructed from the $SlogN$ of its randomly selected noiselet coefficients. Whereas the traditional acquisition method is to measure N-length samples, which are transformed into wavelet coefficients and store the S of them with larger amplitude. It is very consumptive to only record very few data compared with sensed measurements. Using CS theory, it is possible to extract the S important wavelets coefficients from a fraction of the number of measurements without any prior knowledge of location information. The noiselet system is maximally incoherent with the Fourier basis, so as the canonical or spike basis. In order to create efficient noiselets sensing matrices incoherent with signal which is sparse in the Haar/Daubechies wavelet basis, some items should be noticed, 1) the noiselet sensing matrix with the real and imaginary parts are binary valued, measurements are inner product with a sign pattern, it makes easily implement numerically efficient CS in an actual acquisition system. 2) a real valued signal in the noiselet basis has a property that its noiselet spectrum is always flat. Only one half of the noiselet spectrum is required to perform useful CS measurements. Therefore it processes faster than the algorithm looks.

- **Random Matrices as Sensing Basis**

Random and Gaussians matrices have been shown to largely incoherent with any fixed basis ψ. The rows of Φ are selected uniformly at random, which contains data frame with independent sampled $N \times N$. We can say the sensing matrix Φ is standard orthogonal. Each

data frame defines an orthonormal basis for uniform weights. The sensing basis consists of random variable with independent identically distributed entries, which will also exhibit maximally incoherence with any fixed representation basis Ψ. It is high probability that Gaussian white noise basis is incoherent with any fixed orthonormal basis. Efficient incoherent systems ought to acquire correlations with random waveforms as white noise.

The information of $f(t)$ is obtained by linear function recording the values $y_k = \langle x, \varphi_k \rangle$ $k = 1, \dots, M$. We need reconstruct a vector $X \in R^N$ from linear measurements Y, it is noticeable that $M \ll N$, where it means fewer measurements than unknown signal values. If measurements display sinusoidal waveform, then Y is a vector of coefficients which are projected on some special basis. Then we can use the number of available measurements, M, to present the dimension of the signal $f(t)$, N. In the application of WSN, it implies fewer sensors to sense, or the sensing process may be fast because the object can be only measured a few times than original situation.

The accurate reconstruction is to approximate $f(t)$ from $M \ll N$ measurements without losing the information about the original signal. In general, realistic signal $f(t)$ may not have a sparse representation in spatial domain, in other words, the size of $f(t)$ may not be relatively small in a transform domain. Instead, they may only be compressible in some domain with a nearly sparse set. However the signal can be transformed into the coefficients of elements by signal processing, which are sparse in the transform domain. For the vector $X \in R^N$, with S-sparse approximation, which means X_S is the approximation of X by setting the others excluding the S largest entries to zero. It turns out that one can actually recover X_S exactly by obtaining the minimal recovery error of $\|X - X_S\|$ with the sensing matrix obeys what is known as the uniform uncertainty principle.

It is feasible to recover the *S*-largest entries of an *N*-dimensional unknown vector X from *M* measurements by minimizing ℓ_2 as follows

$$\|X^* - X\|_{\ell_1} \leq C\|X - X_S\|_{\ell_1} \tag{3-41}$$

where it is well behaved with some positive constants *C*.

If measurements function is rewriting as

$$Y = AX + z \tag{3-42}$$

where A is the new sensing matrix with $M \times N$ dimensions about X, and z expresses an unknown error term and a stochastic trend. For each integer $S = 1, 2, \dots, K$. The matrix A is satisfied the *S*-restricted isometry property with restricted isometry constant δ_S as the smallest number such that

$$(1 - \delta_S)\|X\|_{\ell_2}^2 \leq \|AX\|_{\ell_2}^2 \leq (1 + \delta_S)\|X\|_{\ell_2}^2 \tag{3-43}$$

which holds for almost all *S*-sparse vectors X.

The sensing matrix A is needed to be determined over the design requirement which allows us to recover as many entries of X from few compressive measurements as possible.

It has been noted by Donoho in his researches that some sort of "blessing of high-dimensionality" could help the solution of reconstruction. Because the high-dimensional

sphere has a statistical property that contains many vectors while maintaining approximate orthogonality.

3.2.4. Bayesian Compressed Sensing

From a Bayesian perspective [77], all of the unknowns are treated as stochastic quantities and characterized by a prior probability distribution function. A prior distribution $p(X_w|\gamma)$ of an unknown parameter is the probability distribution that presents uncertainties about the parameter. In reality, the time domain signal is

$$x_t = \psi(X_w + X_S) = \psi X_W + x_s \tag{3-44}$$

A vector X_S is the projection of the original signal x_t onto wavelet bases. x_t is N samples in time domain, and X_S is identical to the smallest M elements in transform domain.

In reality, measurements may be noisy, the sensing process can be expressed as:

$$y_t = \Phi x_t + n_m = AX_w + n_s + n_m = AX_w + n \tag{3-45}$$

where sensing matrix Φ is constituted through random principle, n_m is the measurement noise, and the components of n_s is a zero-mean Gaussian noise as a consequence of Central Limit Theorem [78] for large $N - M$. Where n is zero-mean uncorrelated Gaussian noise with unknown variance β_0. Therefore, the measurement of the compressed samples is written like a Gaussian likelihood model with a conditional distribution $p(y_t|X_w\ , \beta_0)$.

$$p(y_t|X_w, \beta_0) = (2\pi)^{-\frac{M}{2}} \beta_0^{\frac{M}{2}} exp\left(-\frac{\beta_0}{2}\|y_t - AX_w\|^2\right) \tag{3-46}$$

Equation (3-45) provides a mathematical solution by reconstructing the sparse frequency domain samples X_w which tries to solve a linear regression problem due to the constraint or premise that the signal X_w is sparse in this domain. One element of X_w could be presented using the Laplace density function [79].

$$p(X_i|\lambda) = \left(\frac{\lambda}{2}\right) exp\left(-\frac{\lambda}{2}\|X_i\|_1\right) \tag{3-47}$$

A zero-mean Gaussian prior on each element of X_w is defined as the similar properties of the Laplace prior analysis.

$$p(X_w|\gamma) = \prod_{i=1}^{N} N(X_i|0, \gamma_i) = (2\pi)^{-\frac{N}{2}} \prod_{i=1}^{N} \gamma_i \, exp\left(-\frac{{X_w}_i^2}{2\gamma_i^2}\right) \tag{3-48}$$

where $\gamma = [\gamma_1, \gamma_2, \cdots \gamma_N\ ]$. In the second stage of the hierarchy, each γ_i can be independently modeled as

$$p(\gamma_i|\lambda) = \left(\frac{\lambda}{2}\right) exp\left(-\frac{\lambda\gamma_i}{2}\right) \tag{3-49}$$

With these posterior distributions, we can use Bayes' rule to calculate the posterior probability of each unknown parameter under the condition of complete joint probability distribution over all the variables.

$$p(X_w|y_t,\gamma,\beta_0) = \frac{p(y_t|X_w,\beta_0)p(X_w|\gamma)}{p(y_t|\gamma,\beta_0)} = (2\pi)^{-\frac{N}{2}}|\Sigma|^{-\frac{1}{2}}exp\ (-\frac{1}{2}(X_w-\mu)^T\Sigma^{-1}(X_w-\mu) \quad (3\text{-}50)$$

with a multivariate Gaussian distribution $N(\mu,\Sigma)$ with mean and covariance

$$\mu = \beta_0\Sigma A^T y_t \quad (3\text{-}51)$$

$$\Sigma = (\Lambda + \beta_0 A^T A)^{-1} \quad (3\text{-}52)$$

where $\Lambda = diag\{1/\gamma_i\}$. The covariance Σ is negated and inverted for a Gaussian approximation

This is then negated and inverted to give the covariance for a Gaussian approximation to the posterior distribution of the weights center at μ. The problem of the hyperparameter posterior is replaced by the search of its most-probable value γ_{MP}, σ^2_{Mp}. Relevance vector machine (RVM) solves this problem by analyzing the property of the marginal likelihood function in [80]. The advantage of RVM is to reduce the predicted time of the proposed framework, enabling the reconstruction to always operate with the minimum number of samples.

A searching for parameters γ and β_0 is the most computational complex component and not necessary since we do not need the entire signal. The principle is to estimate the parameters of QRS complex instead of the signal in its entirety.

$$p(X_w|y_t,\gamma,\beta_0)p(y_t|\gamma,\beta_0) = p(y_t|X_w,\beta_0)p(X_w|\gamma) \quad (3\text{-}53)$$

It is impossible to directly compute the posterior of the right-hand side since the normalizing integral could not be performed. By decomposing the right-hand side in Equation (3-53), and gathering together all terms in X_w appeared within the exponential, and computing the following equation which is now completely in terms of the parameters γ and β_0.

$$p(y_t|\gamma,\beta_0) = \int_{-\infty}^{\infty} p(y_t|X_w,\beta_0)p(X_w|\gamma)d\,X_w = (2\pi)^{-\frac{M}{2}}|Z|^{-\frac{1}{2}}ex\,p\left(-\frac{1}{2}y_t^T Z^{-1}y_t\right) \quad (3\text{-}54)$$

where

$$Z = A\Lambda^{-1}A^T + \beta_0 I \quad (3\text{-}55)$$

and I is the $M \times M$ identity matrix.

The algorithm seeks to find the marginal likelihood by maximizing its parameters of γ and β_0 as the type-II maximum likelihood method. In particular, we use the marginal likelihood to refer to the evidence for the hyperparameters in which the evidence procedures are maximized.

It is convenient to denote an expectation by maximizing the logarithm of the Equation (3-54). It is convenient to denote an exception by the expectation maximization formulation in [76]

$$\mathcal{L} = -\frac{1}{2}log|Z| - \frac{1}{2}y_t^T Z^{-1}y_t \quad (3\text{-}56)$$

Some equivalence for solving the maximization problem is shown below

$$log|Z| = log\left(|\Lambda|^{-1}\left|\beta_0^{-1}I\right||\Lambda + \beta_0 A^T A|\right) = -log|\Lambda| - Nlog\beta_0 - log|\Sigma| \tag{3-57}$$

$$y_t^T Z^{-1} y_t = y_t^T(\beta_0 I - \beta_0 A\Sigma A^T \beta_0)y_t \tag{3-58}$$

The derivative of the Equation (3-56) is given as

$$\frac{d\mathcal{L}}{d\gamma_i} = \frac{1}{2}\left[-\frac{1}{\gamma_i} + \frac{\mu_i^2 + \Sigma_{ii}}{\gamma_i^2}\right] \tag{3-59}$$

where Σ_{ii} is the i^{th} diagonal element of Σ. Setting this equals to zero results in

$$\gamma_i = \mu_i^2 + \Sigma_{ii} \tag{3-60}$$

And estimate the other hyperparameter of the noise precision β_0 by the same procedure to take the derivative of Equation (3-56) respect to each hyperparameter and set it to zero.

$$\beta_0 = \frac{M - \sum_i(1 - 1/\gamma_i\Sigma_{ii})}{\|y_t - A\mu\|^2} \tag{3-61}$$

$\Sigma_{ii} \in [0,1]$ measures the accuracy of the point estimate μ by the data. For γ_i is small, where X_w is highly constrained. Conversely, when γ_i is large, that means the points fit the data.

3.2.5. Anomaly Detection using BCS

In essence, BCS is a useful theorem to map the compressed time domain measurements y_t to the Nyquist rate transformed domain sampled signal X_w. It may be a desired model to reconstruct entirely the signal X_w, however a good overall signal of X_w is not our primary concern. Our goal is to detect abnormal ECG signal but not to diagnose cardiac arrhythmias in real-time. Based on the above analysis, measurements of patients' heart status are classified as normal and abnormal [81, 82]. There are mainly two abnormal situations: 1) irregular peak value, as depicted in Figure 3.19; 2) irregular distance between peaks of ECG signals, as depicted in Figure 3.20. On next step we try to estimate the parameters of QRS complex, including location, magnitude and signal parameter estimation.

The statistical signal analysis of ECG signals has special characteristics and can well be applied to show the difference between normal and abnormal status. We can obtain the energy function of signal if we apply Equation (3-44) shown below:

$$\begin{aligned} E_y &= \sum_{i=1}^{N}\left|\phi_k(i)\left(x(i) + n(i)\right)\right|^2 \\ &= \sum_{i=1}^{N}\left(x^2(i){\phi_k}^2(i) + 2x(i)n(i){\phi_k}^2(i) + n^2(i){\phi_k}^2(i)\right) \\ &= C_{\phi,2}E_x + 2C_{n,1}C_{\phi,2}\sum_{i=1}^{N}x(i) + C_{n,2}C_{\phi,2} \end{aligned} \tag{3-62}$$

where $C_{\phi,2}$ is the statistical estimation of the root mean square of sensing matrix Φ, $C_{n,1}$ is the statistical estimation of the expectation of the noise and $C_{n,2}$ is the statistical estimation of the root mean square of the noise. Following the energy function, we have the same form of the signal

$$E_x = \sum_{i=1}^{N} x^2(i) \tag{3-63}$$

And $C_{\phi,1}$ is introduced that is the statistical estimation of the expectation of the sensing matrix Φ.

$$y_t = \sum_{i=1}^{N} \left(\phi_k(i)\left(x(i) + n(i)\right)\right) = C_{\phi,1} \sum_{i=1}^{N} x(i) + C_{n,1} C_{\phi,1} \tag{3-64}$$

The characteristic of the signal is deduced by both the measurement matrix Φ and the value of measurement vector Y. Derived from the above equation, the estimation of ECG signal using the compressed samples can be stated as

$$E_x = \frac{(E_y - C_{n,2} C_{\phi,2} - 2C_{n,1} C_{\phi,2} \frac{y_t - C_{n,1} C_{\phi,1}}{C_{\phi,1}})}{C_{\phi,2}} \tag{3-65}$$

A composite feature pointing to describe the QRS complex is made by 4 parameters

$$\{p_{i,}\, m_i, \Sigma_{ii}, E_x\} \tag{3-66}$$

where p_i represents the location of QRS complex, m_i represents the magnitude of QRS complex, Σ_{ii} represents the estimation error and E_x represents estimated energy of entire ECG signals.

The algorithm calculating β_0 is repeated while iteratively updating the posterior statistics Σ and μ of the QRS complex, until a suitable convergence criterion has been satisfied. In practice, many of γ_i tend to infinity that implies a posteriori certain of those X_w are zero. Estimating γ_{MP} for one element of X_w is not necessary and a waste of time, since the detection of anomaly does not lie in reconstructing the entire signal. By the composite feature of fusing parameter describing the QRS complex and the energy function, the algorithm is utilized to estimate the compressed measurements describing QRS complex with fewest number of samples.

3.3. Simulation

In previous work shown in [16], heart rate (HR) is estimated by defining the number of QRS peaks in the ECG signal. According to this idea, the first step of our experiment is to divide the compressed measurements into two categories: normal and abnormal. The second step is to estimate HR from measurements on behalf of the normal signal. The last step is to save measurements which represent abnormal ECG signals sequence into the Flash memory. To diagnose the cardiac arrhythmias (by cardiologists), the stored compressed measurements

should be entirely reconstructed to original ECG signals through the algorithm mentioned earlier. The last procedure is to operate in remote surveillance terminal, transferring the power consumption and computational complexity on WES to the local or remote server.

We use CS technique to acquire the measurements. Then we obtain indirectly the estimated energy of the ECG signal from measurements. In order to distinguish the measurements, we analyze the distance between adjacent peaks and value of the peaks. All the peaks of greater magnitude than a threshold are regarded as abnormal situation, likewise, all peaks that have a short distance apart from each other, or as multiple peaks in one portion, are considered as marker area, representing abnormal situation. In order to guarantee that all abnormal portions are detected, at the same time peaks in the vicinity are useful for cardiologists to diagnose cardiac arrhythmia. To increase the efficiency of the classification, it is necessary to consider a patient ECG normal state. The patient's clinical status is provided by cardiologists or physicians.

To experiment with the compressed sensing assessment, two different signals of the identical type representing the most significant symptom of cardiac arrhythmia are chosen from the database CSD, which includes the clinic ECG records acquired at the cardiology department of the Gabriel Montpied hospital of Clermont-Ferrand (CHRU de Clermont-Ferrand). The data recorded at 500Hz was amplified with 1000 gain and then processed by a band-pass filter between 8 and 125Hz.

3.3.1. Energy Estimation of QRS Complex

The tested data of ECG signals containing two significant symptoms of cardiac arrhythmia have the duration of 30 minutes. In the experiments, the measurement matrix ϕ is constructed to a $M \times N$ matrix with i.i.d draws of a Gaussian distribution $\mathcal{N}(0,1)$ with the normalized magnitude of each element. Then the data are divided in segment of $N = 1024$ samples. Compression ratio is fixed at 0.5, resulting in $M = 512$ projections.

The energy estimation of signal holds the information about the location and amplitude of peaks as shown in Figure 3.19 and Figure 3.20. Figure 3.19 and Figure 3.20 provide a more detailed view of the relation of signal in abnormal situations and its measurements. These figures show that the actual signal estimated energy and the estimation of its measurements hold most information of normal and abnormal heartbeats. In Figure 3.19, there are 12 normal peaks between 2 abnormal peaks as QRS complex is in the opposite direction. And Figure 3.20 shows a premature ventricular complex (abnormal peak) in the middle part.

From the above figures, it is easy to see that the peaks of variance are correspondent to each QRS complex in the area where normal heartbeat occurred. The (a) and (b) subplots of the figures identify two points which have basically the same amplitude and the same distance for all peaks encircling the area of normal ECG signals. In the area of abnormal ECG signals in Figure 3.19, the amplitude of the abnormal QRS complex is far greater than the normal one, without the loss of location information. Another abnormal situation is an abrupt change of heartbeat which induces irregular interval between QRS complex peaks of ECG signals. This case is depicted in the last plot of Figure 3.20. These signals have normal amplitude but abnormal cardiac rhythm. Since the distribution variance of measurements of ECG signals, it

is clear that the QRS peaks of abnormal signals are not as steep as normal signals. Thus we calculate the distribution energy divided into segments. In this abnormal situation there is more than one heartbeat in one segment which shows multiple QRS peaks. The length of the segment tracks heart rate of normal signal.

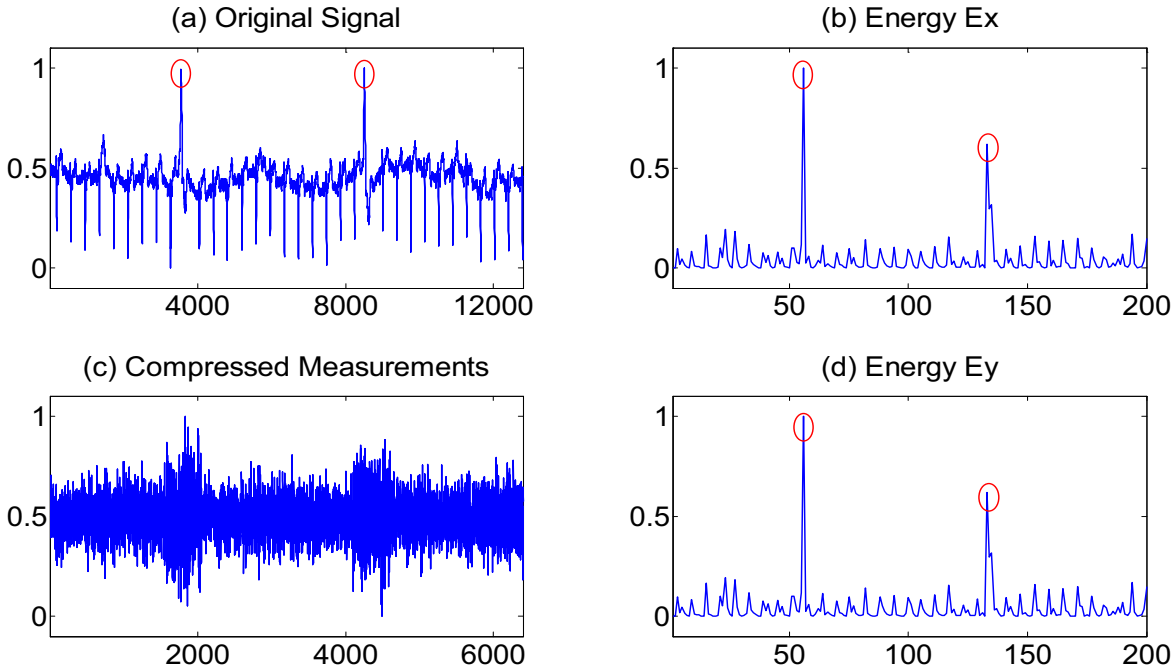

Figure 3.19 Statistical characteristic of irregular peak values of ECG signals. (a) Original ECG signals are expressed with 12800 points data. Irregular ECG signals are marked by red circle. (b) Estimated energy of signals in (a), red line is threshold of estimated energy of the normal ECG signals. (c) Compressed measurements of signals in (a), the length is 6400 owing to the compression ratio 50%. (d) Estimated energy of measurements in (c).

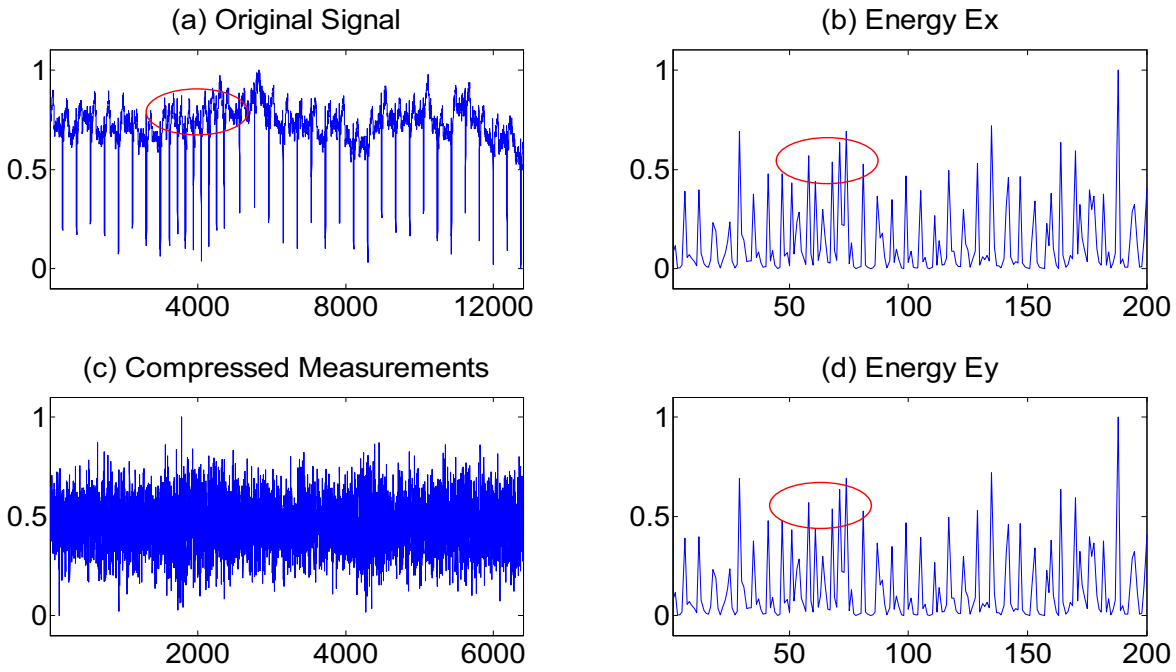

Figure 3.20 Statistical characteristic of irregular distance between the peaks of ECG Signals. (a) Original ECG signals are expressed with 12800 points data. Irregular ECG signals are marked by red circle. (b) Estimated energy of signals in (a), a red circle marks irregular distance of the abnormal ECG signals. (c) Compressed measurements of signals in (a), the length is 6400 owing to the compression ratio 50%. (d) Estimated energy of measurements in (c), a red circle marks measurements presenting abnormal ECG signal.

3.3.2. Detection of QRS Complex with BCS

In this simulation, we present some simulation results to demonstrate the advantage of directly estimating QRS complex with compressed measurements of the entire signals. There are two primary performance indicators of the BCS signal detection of QRS complex against the reconstruction of the entire ECG signals, with which computation time is to measure the computational complexity, and reconstruction error is to measure the accuracy of the inversion.

The simulations in Figure 3.21 and Figure 3.22 illustrate ECG signals with anomalies of irregular value. In Figure 3.21(a) there are two irregular values which do not match the normal value of the QRS complex. In Figure 3.21(b) compressed measurements show the characteristics similar to Gaussian white noise, while showing significant differences in the location of abnormal ECG signals. In Figure 3.21(c) and Figure 3.21(d) we compare reconstructed ECG signal for overall signal and primary component, QRS complex. Figure 3.22 illustrates wavelet coefficients of ECG signals, reconstructed ECG signal and reconstructed QRS complex. All wavelet coefficients are arranged in random sequence for enhanced visibility.

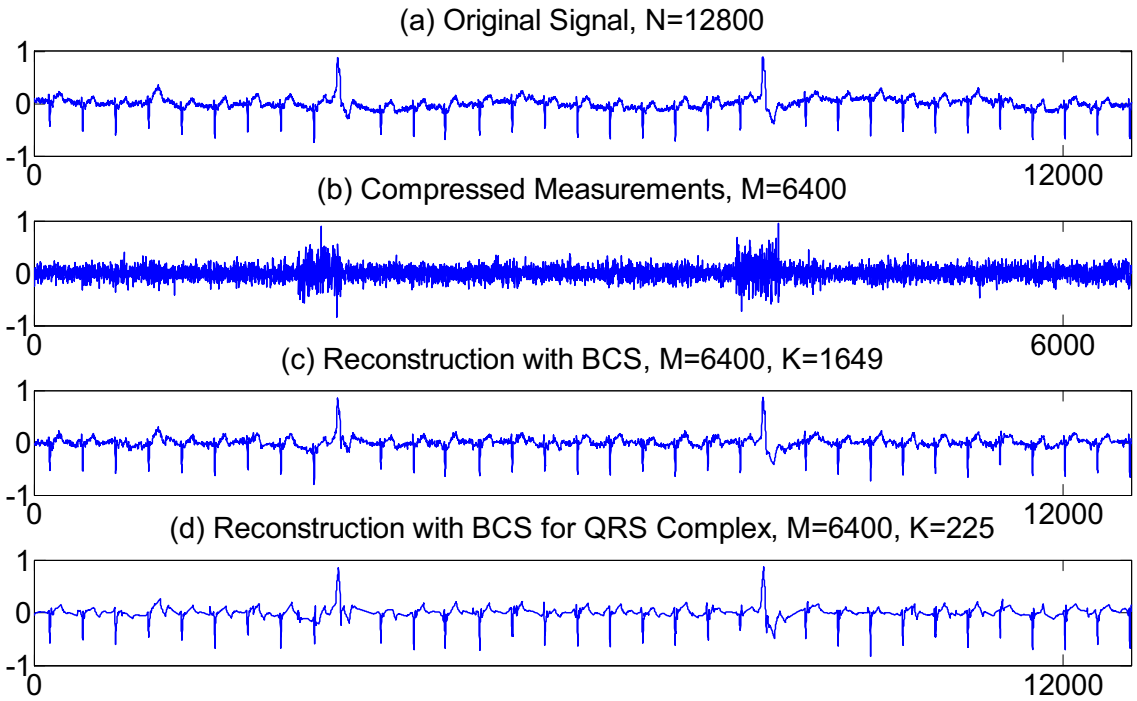

Figure 3.21 Comparison of signal reconstruction on irregular value case. (a) Original signal, (b) compressed measurements, (c) Reconstruction with 1649 non-zero wavelet coefficients, (d) Reconstruction with 225 non-zero wavelet coefficients.

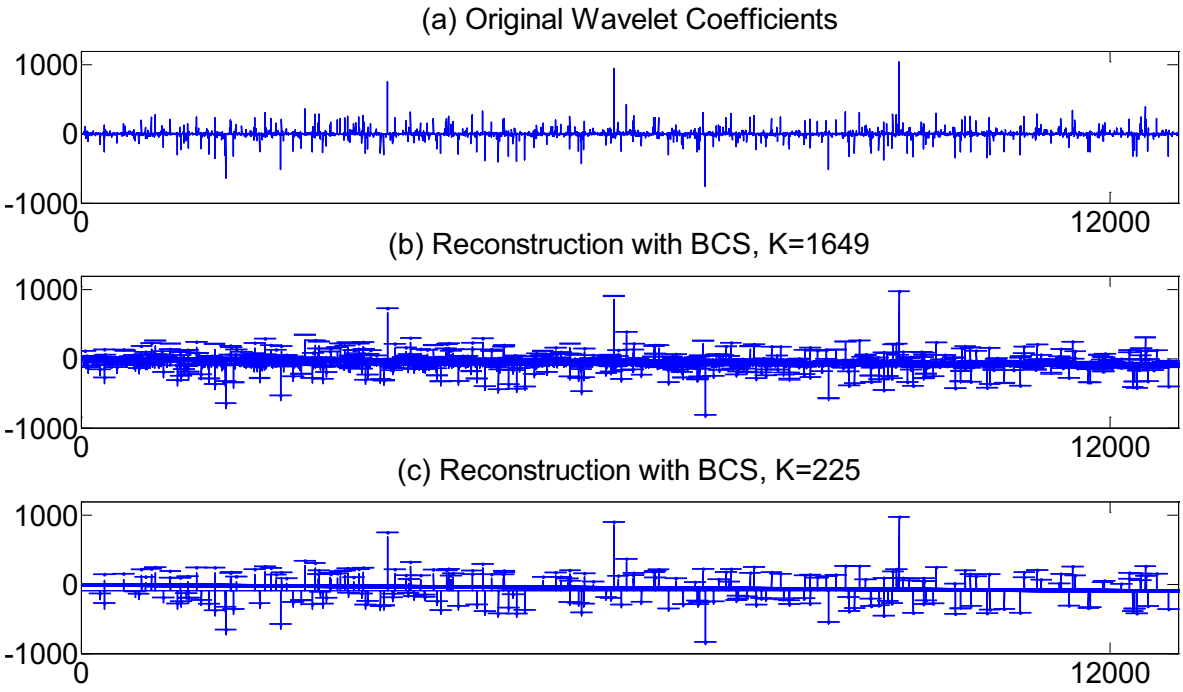

Figure 3.22 Comparison of sparse expansion. (a) Wavelet coefficients of original signal. (b) Reconstruction with BCS and non-zero estimates are 1649, (c) Reconstruction of primary QRS complex with BCS and non-zero estimates are 225.

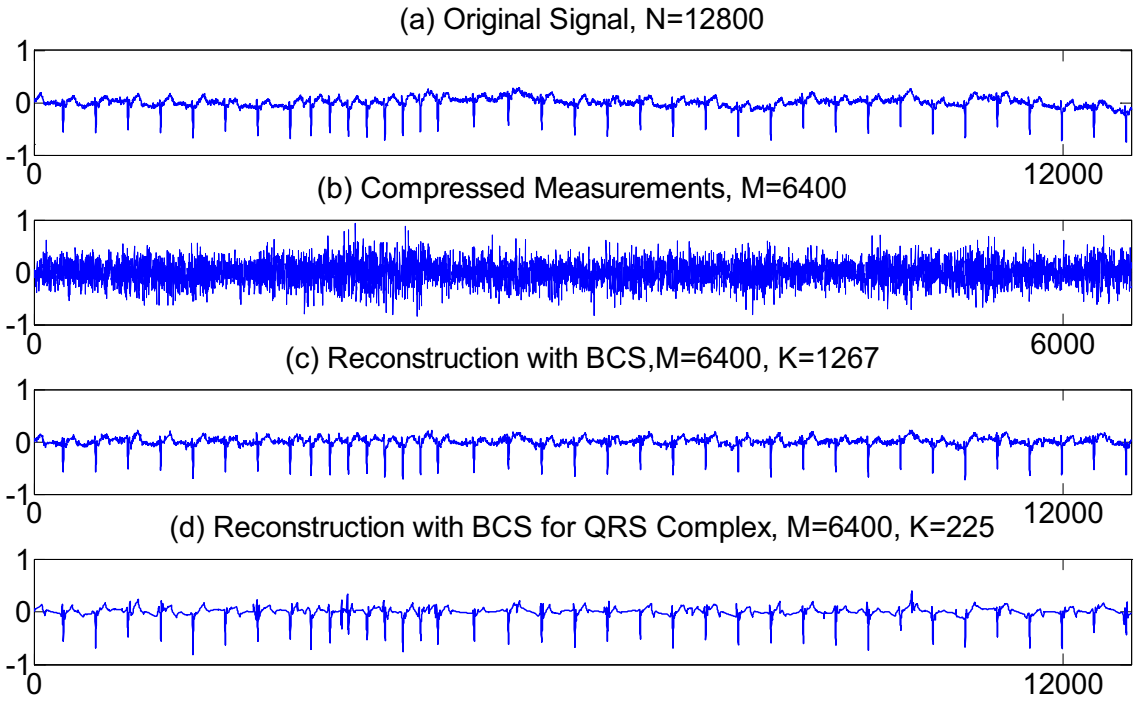

Figure 3.23 Comparison of signal reconstruction on irregular distance case. (a) Original signal, (b) Compressed measurements, (c) Reconstruction with 1649 non-zero wavelet coefficients, (d) Reconstruction with 225 non-zero wavelet coefficients.

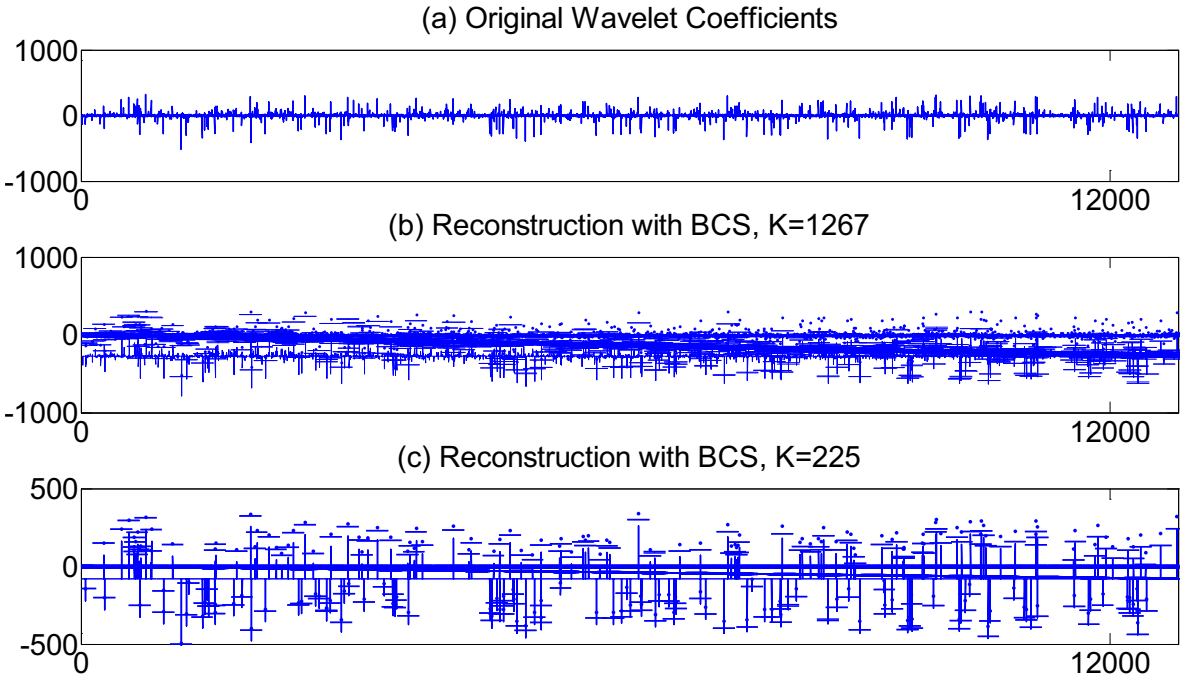

Figure 3.24 Comparison of sparse expansion. (a) Wavelet coefficients of original signal. (b) Reconstruction with BCS and non-zero estimates are 1267, (c) Reconstruction of primary QRS complex with BCS and non-zero estimates are 225.

The simulations in Figure 3.23 and Figure 3.24 illustrate ECG signals with anomalies of irregular interval. In Figure 3.23(a), there are several irregular distances which do not match the normal distance of the QRS complex. In Figure 3.23(b) compressed measurements show the characteristics similar to Gaussian white noise, while showing significant differences in the location of abnormal ECG signals. In Figure 3.23(c) and Figure 3.23(d) we compare reconstructed ECG signal for overall signal and primary component, QRS complex. Figure 3.24 illustrates wavelet coefficients of ECG signals, reconstructed ECG signals and reconstructed QRS complex. All wavelet coefficients are arranged in random sequence for enhanced visibility.

3.3.3. Analysis of Reconstruction (1)

ECG signals have a sparse presentation on wavelet basis, where Daubechies 4 as well as Symlets 4 has proven a successful method in expressing ECG signals with sparse representation onto the appropriate wavelet base for the implementation of compressed sensing. Coiflet transforms provide sparser representation for ECG signals. Three indices including computation time, reconstruction error and the number of sparsity are used to evaluate compressed sensing based on different wavelet bases.

To evaluate quantitatively the performance of the recovery, a variety of experiments demonstrate that the impression of choice of wavelet basis according to normal and pathological ECG signals obtained from the MIT-ECG and COG database. The pseudo-SNR is defined as a quantitative standard

$$SNR_{pseudo} = 20\ log \frac{\|f\|_2}{\|f - f_{re}\|_2} \tag{3-67}$$

And f are the original ECG signals and f_{re} is the corresponding recovery counterpart.

Table 3.2 Type comparison inverse transform

Wavelet	Computing Time (s) Entirety/QRS	Sparsity Entirety/QRS	$\text{SNR}_{\text{pseudo}}$ (dB) Entirety/QRS
Haar	0.5917/0.0335	194/9	24.67/9.55
Db4	0.1688/0.0117	124/9	37.52/12.39
Db8	0.2050/0.0114	124/9	40.92/12.39
Sym4	0.2758/0.0122	132/9	41.01/12.39
Sym8	0.1737/0.0105	122/9	41.21/12.39
Coif2	0.1518/0.0099	117/9	39.41/14.34
Coif4	0.2654/0.0121	124/9	41.62/13.76
Vaid	0.2846/0.0097	150/9	38.71/11.57
Bat1	0.2694/0.0100	143/9	36.83/14.30
Bat3	0.2556/0.0125	168/9	23.74/12.37

The different results of pseudo-SNR of ECG signal change with various wavelet bases which include Haar, Daubechies 4, Daubechies 8, Symlet 4, Symlet 8, Coiflet 2, Coiflet 4, Vaidyanathan, Battle 1 and Battle 3. The results show ECG signals have sparser representation on Daubechies, Symlet and Coiflet transform. As beforehand stated, the primary elements of ECG signals are QRS complex. For Compressibility assessment, the number of signals is fixed at 1024 and the sparsity is fixed at 9. The performance of the wavelet-based reconstruction is evaluated. The results show the better recovery performance in appropriate transform basis.

The content of Table 3.2 shows a much sparser representation of the original signal is generated on Coiflet 2, but the reconstructed performance is worse than the other wavelet transformations. The computational time is only relative to the number of measurements and the sparsity. The computational time is less as the signal has sparser exponent on the wavelet transform with the same length of compressed measurements.

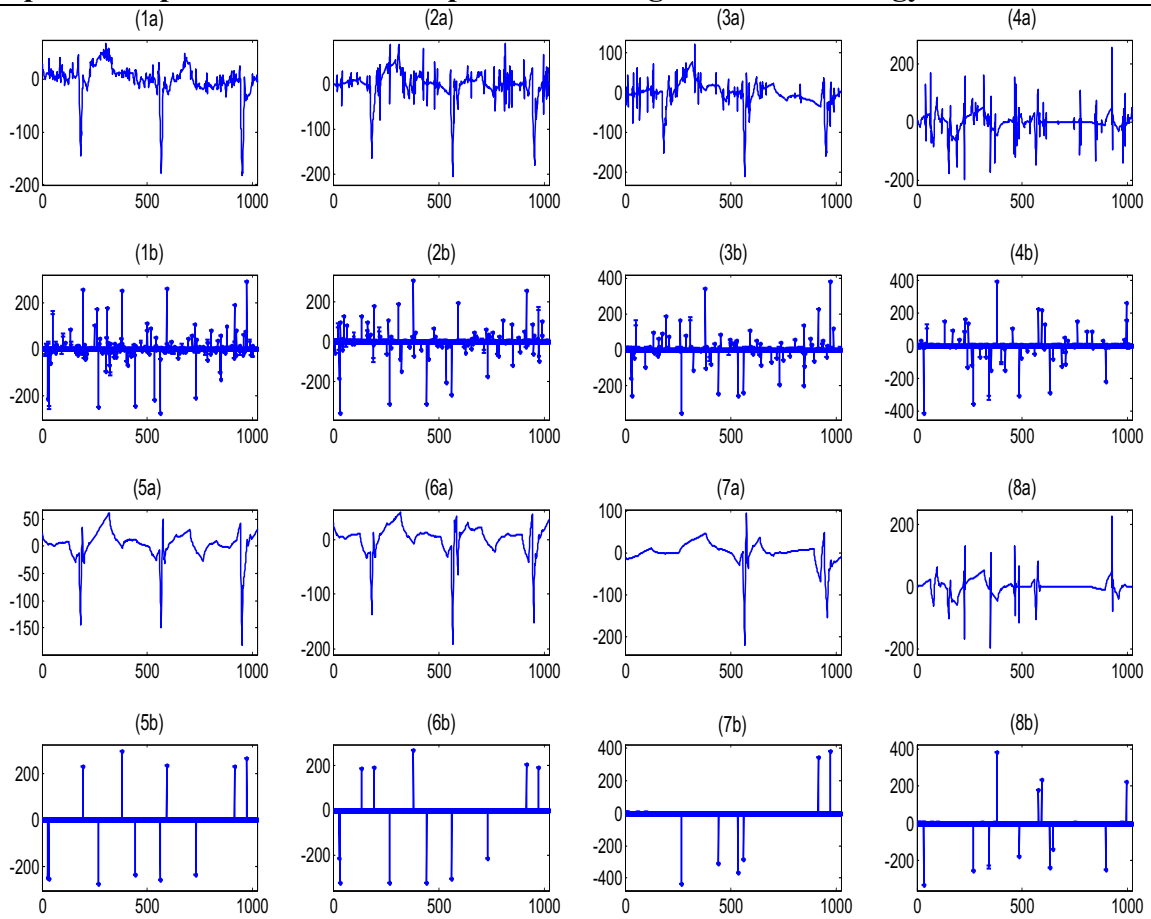

Figure 3.25 Number of measurements versus construction performance, Comparison directly detection of QRS complex and entire signal. (1) Reconstructed signal and wavelet coefficients with BCS, M=400, K=187, SNR_{pseudo}=26.19dB, (5) Reconstructed signal and wavelet coefficients with BCS, M=400, K=11, SNR_{pseudo}=8.90dB, (2) Reconstructed signal and wavelet coefficients with BCS, M=200, K=106, SNR_{pseudo}=8.76dB, (6) Reconstructed signal and wavelet coefficients with BCS, M=200, K=11, SNR_{pseudo}=7.23dB, (3) Reconstructed signal and wavelet coefficients with BCS, M=150, K=83, SNR_{pseudo}=10.07dB, (7) Reconstructed signal and wavelet coefficients with BCS, M=150, K=6, SNR_{pseudo}=2.78dB, (4) Reconstructed signal and wavelet coefficients with BCS, M=100, K=59, SNR_{pseudo}=−3.81dB, (8) Reconstructed signal and wavelet coefficients with BCS, M=100, K=11, SNR_{pseudo}=−0.55dB.

Example in Figure 3.25 demonstrates the relation between construction performance and the length of measurements. When the compression ratio is around 0.5 or even higher, the reconstructed entire signal is of very good quality. We only reconstruct 11 wavelet coefficients, less than 10% versus the number of needed reconstructed wavelet coefficients for entire signal. To estimate the location and magnitude of QRS complex, we do not need to precisely reconstruct wavelet coefficients for missing those details does not affect the classification of normal signal and anomaly and provide an approximation of the recorded heart rate. When the compression ratio is less than 0.1, as shown in the subplot 4 of the Figure 3.25, the reconstructed entire signals does not have any sense and the cardiologists cannot diagnose cardiac arrhythmias because the constructed signal has lost almost all of its useful information. Also the number of reconstructed wavelet coefficients of the QRS complex is important at the classification stage. As shown in the subplot 7 of the Figure 3.25, if the

number of reconstructed wavelet coefficients of QRS complex is less than 10, say 6, the first QRS complex is lost.

Non-zero contents of the sparse exponent of signal are less following the greater compression ratios, as shown in Figure 3.26. However more non-zero contents mean more information for original signal and can achieve higher resolution of the minor waves including T, U and P waves. Figure 3.27 demonstrates the fact that it should be avoided using greater compression ratios considering the reconstructed performance

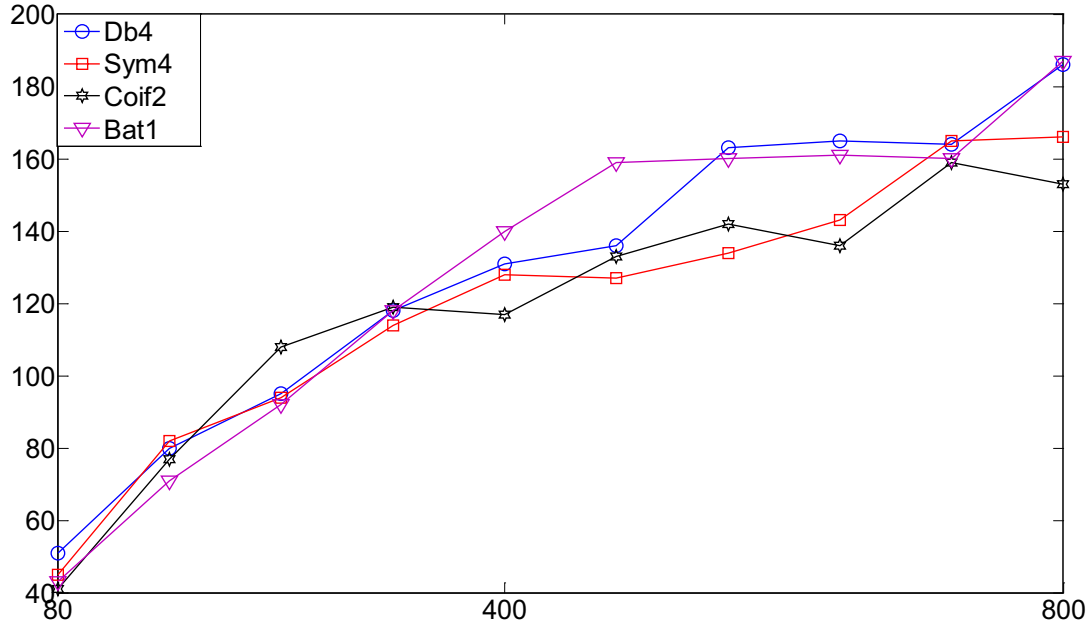

Figure 3.26 The sparse exponents of signal on different wavelet transform. The exponent is sparer as more measurements implying lower compression ratio.

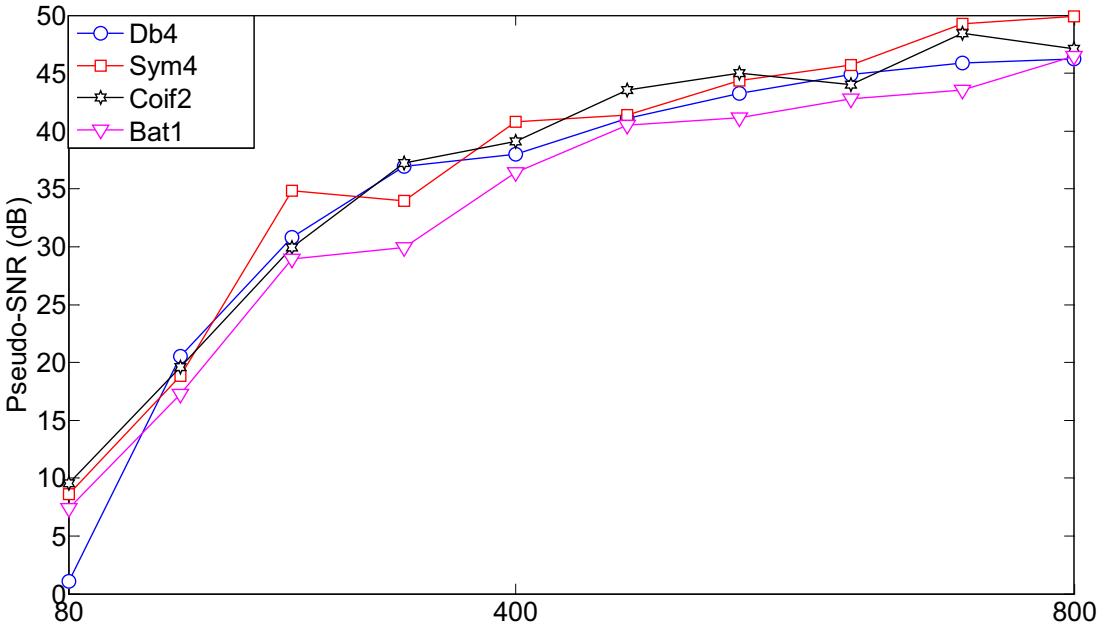

Figure 3.27 Comparison of reconstruction performance on different wavelet transform and compression ratio. More measurements mean more accuracy of the reconstructed signal.

3.3.4. Analysis of Reconstruction (2)

Our equipment enables to monitor 4 leads ECG signals. Depending on the results of these four leads, heart rate is assured to be 80 BPM (beats per minutes). Stored information is divided into two types. On one hand in case that the normal ECG signal is detected, only the time reference heart rate will be saved. On the other hand, when an abnormal ECG signal is detected, a sequence of ECG signal will be saved including time reference. The abnormal ECG sequence includes pre and post anomaly events (3 ECG signal frames are saved: one frame before, one frame after the frame having abnormal event). The purpose of saving pre and post anomaly frames is to satisfy the need of cardiologists to diagnose efficiently cardiac arrhythmias. Original ECG data are stored at a rate of 24Kbit per second in the previous WES system. As in sampling with CS mechanism, the analog signal is converted into a sequence of digital samples which represent the measurement instead of ECG signals. The data of measurement are stored at a rate of 11.25Kbit per second without classification. At last we describe the storage of system using the classification of measurements to remove the measurement data representing normal ECG signal and only keep the measurement data with possible pathological information. For the length of 384 seconds of patient's signal, the last storage consumption is 312.23Kbit with discarding the data segments with normal ECG signals, compared with 9216Kbit of the previous system and 4320Kbit of the WES with CS mechanism on 0.5 compression ratio. Energy savings are measured on the same compression ratio of 0.5, which are primarily taken on the device of ADC and RS232-Bluetooth. The voltage supply on ADC stage is 2.5V. Power consumption of ADC on WES during the cycle time is 777μW, as compared to 453.5μW on CS mechanism where it offers a lower sampling frequency. For compression ratio of 0.5, the power saved would be of 323.5μW, as a ratio of 0.44. Reducing data transmission to a half allows saving half of the original power expenditure in the ideal situation, however actually the savings of 1/3 is achieved.

The final experiment is to illustrate the performance of power consumption, storage and reconstruction. Experiment data from four patients is recorded during 80 minutes. Figure 3.28 shows system performance at different sampling rates. The classification algorithm successfully divided the ECG measurements into normal and abnormal instance, so the heart rate and the decrease of storage are constant. The reduction of power in ADC is clearly visible with the rising of compression ratio. The performance of reconstruction is greatly dependent on the choice of measurement matrix Φ.

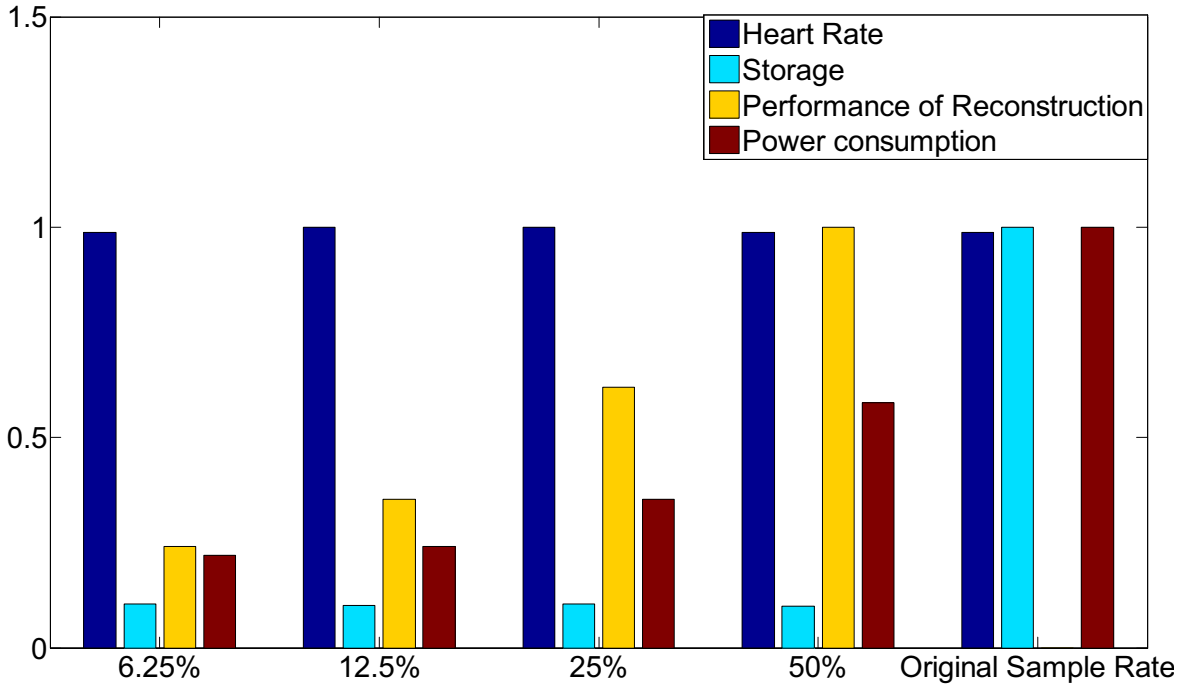

Figure 3.28 Heart Rate, storage, performance and power consumption for Compressive Sensing versus original sampling.

3.3.5. Experiments in Cardiac Arrhythmias

In this section, experimental results of different cardiac arrhythmias are presented. The ECG data tested in this experiment is acquired from the MIT-BIH arrhythmia database [41]. The performance of direct cardiac arrhythmia detection via compressed measurements is demonstrating and verifying the flexibility of the algorithm. The performance of the algorithm is also shown to be excellent with a high sensitivity to various cardiac arrhythmias.

The MIT-BIH arrhythmia database contains 48 half-hour excerpts of two-channel ambulatory ECG recordings. In most records, one of the signals is a modified limb lead II, obtained from the electrode located on the chest. Another is usually a modified lead V_1 (occasionally V_2 or V_5, and in one instance V_4 which is also placed on the chest. Analog outputs were filtered using a pass-band from 0.1 to 100 Hz relative to real time, well beyond the lowest and highest frequencies recoverable from the recording. The recordings were digitized at 360Hz with 11-bit resolution over a 10 mV range [41]. Cardiologists who worked independently added annotation for all beats. Because the sampling rate of our wearable sensor is 500Hz, the recordings of the MIT-BIH arrhythmia database are transformed before processing.

- **Normal Sinus Rhythm**

The ECG signal denoted by record 100 is shown in Figure 3.29, which begins at 0 second and continue 10 seconds from the first channel. There are 12 normal sinus rhythms characterized by a regular cardiac rate in which the duration of the normal QRS complex is less than 100ms. Heart rate calculated on this sector is 72 within 60-100bpm.

E_X of the original ECG signal and E_Y of measurements are shown in Figure 3.30 using the algorithm introduced in section 3.2.5. The figure shows that the actual signal estimated energy and the estimation of its measurements hold most information of heartbeats.

Figure 3.31 illustrates wavelet coefficients of ECG signal, reconstructed ECG signal and reconstructed QRS complex. All wavelet coefficients are arranged in random sequence for enhanced visibility.

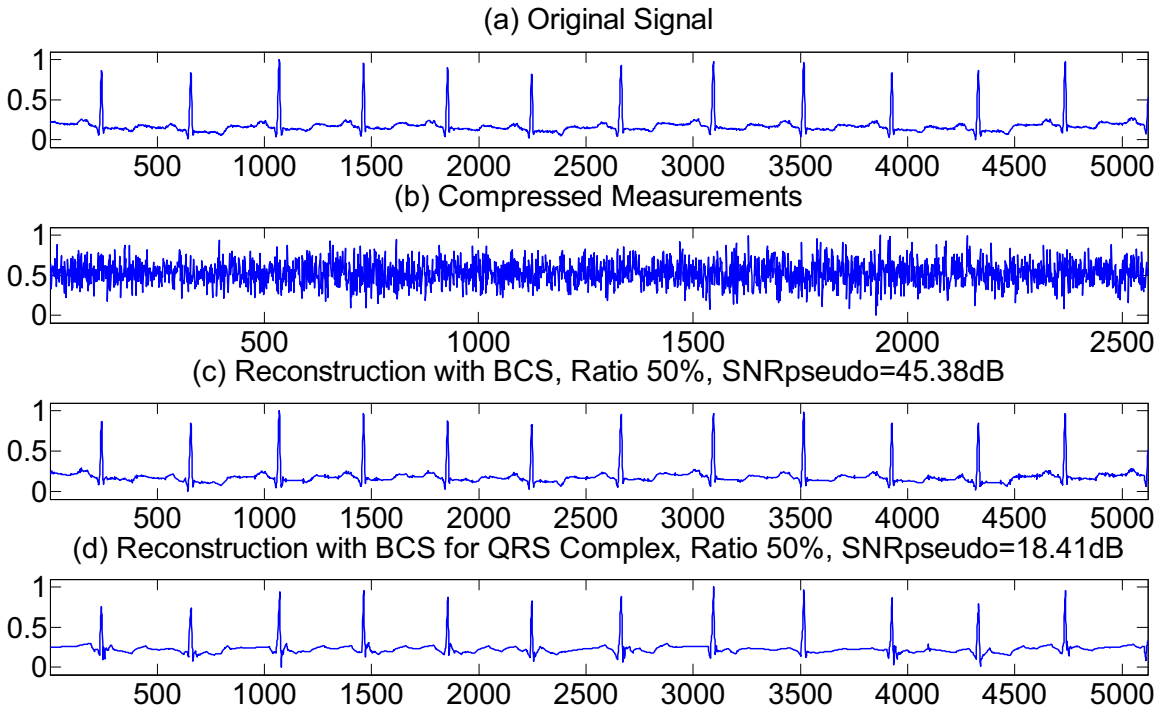

Figure 3.29 Comparison of signal reconstruction in normal sinus rhythm. (a) Original signal, (b) Compressed measurements, (c) Reconstruction with 702 non-zero wavelet coefficients, (d) Reconstruction with 105 non-zero wavelet coefficients.

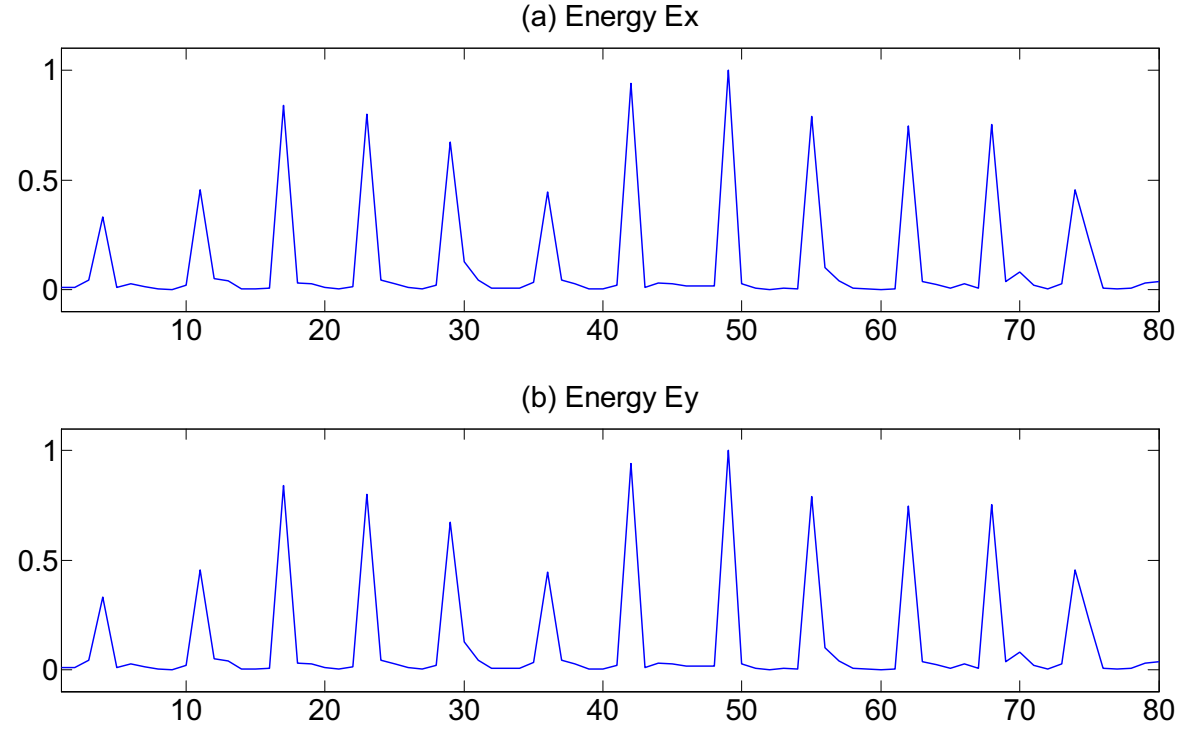

Figure 3.30 Statistical characteristic of ECG Signals in normal sinus rhythm. (a) Estimated energy of original ECG signals. (b) Estimated energy of compressed measurements.

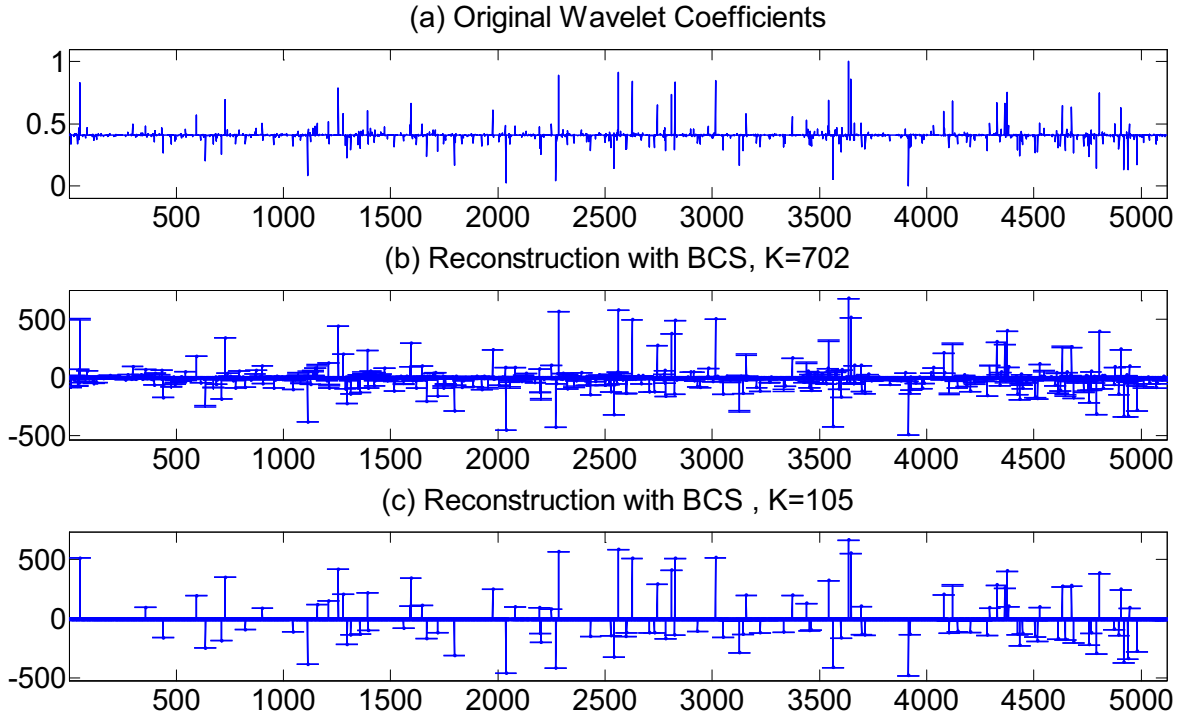

Figure 3.31 Comparison of sparse expansion. (a) Wavelet coefficients of original signal. (b) Reconstruction with BCS and non-zero estimates are 702, (c) Reconstruction of primary QRS complex with BCS and non-zero estimates are 105.

- **Sinus Bradycardia**

The ECG signal denoted by record 232 is shown in Figure 3.32, which begins at 23 minutes 53 second and continue 10 seconds from the first channel. There are only 4 normal sinus rhythms characterized by a regular cardiac rate. Heart rate calculated on this sector is 24 below 60bpm.

E_X of the original ECG signal and E_Y of measurements are shown in Figure 3.33 using the algorithm introduced in section 3.2.5. The figure shows that the actual signal estimated energy and the estimation of its measurements hold most information of heartbeats. There are obviously 4 periods including a large and a small peak. The large peak represents QRS complex and the small peak represents T wave.

Figure 3.34 illustrates wavelet coefficients of ECG signal, reconstructed ECG signal and reconstructed QRS complex. All wavelet coefficients are arranged in random sequence for enhanced visibility.

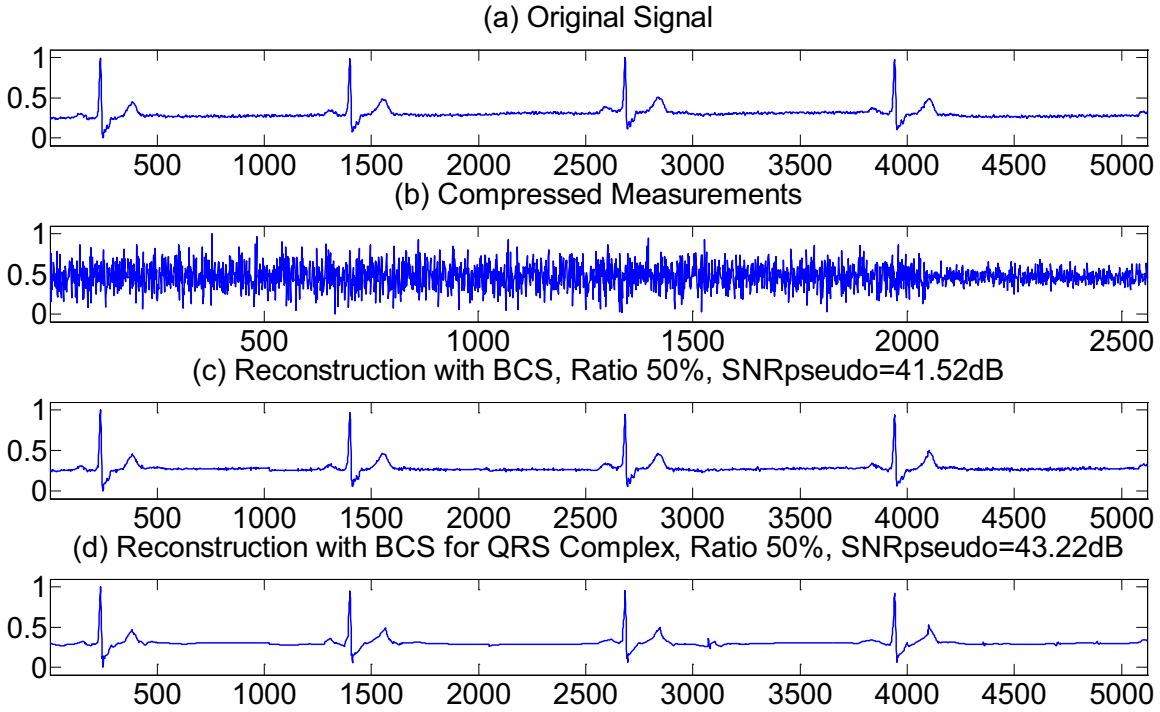

Figure 3.32 Comparison of signal reconstruction in sinus bradycardia. (a) Original signal, (b) Compressed measurements, (c) Reconstruction with 762 non-zero wavelet coefficients, (d) Reconstruction with 105 non-zero wavelet coefficients.

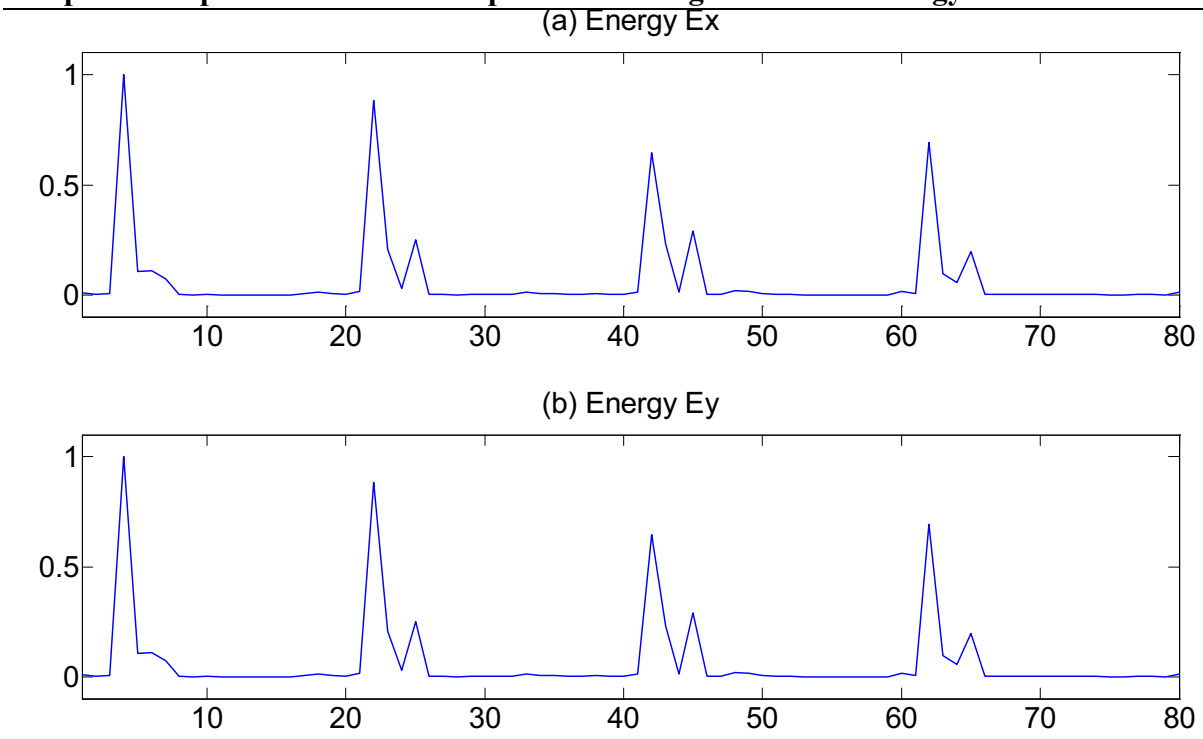

Figure 3.33 Statistical characteristic of ECG Signals in sinus bradycardia. (a) Estimated energy of original ECG signals. (b) Estimated energy of compressed measurements.

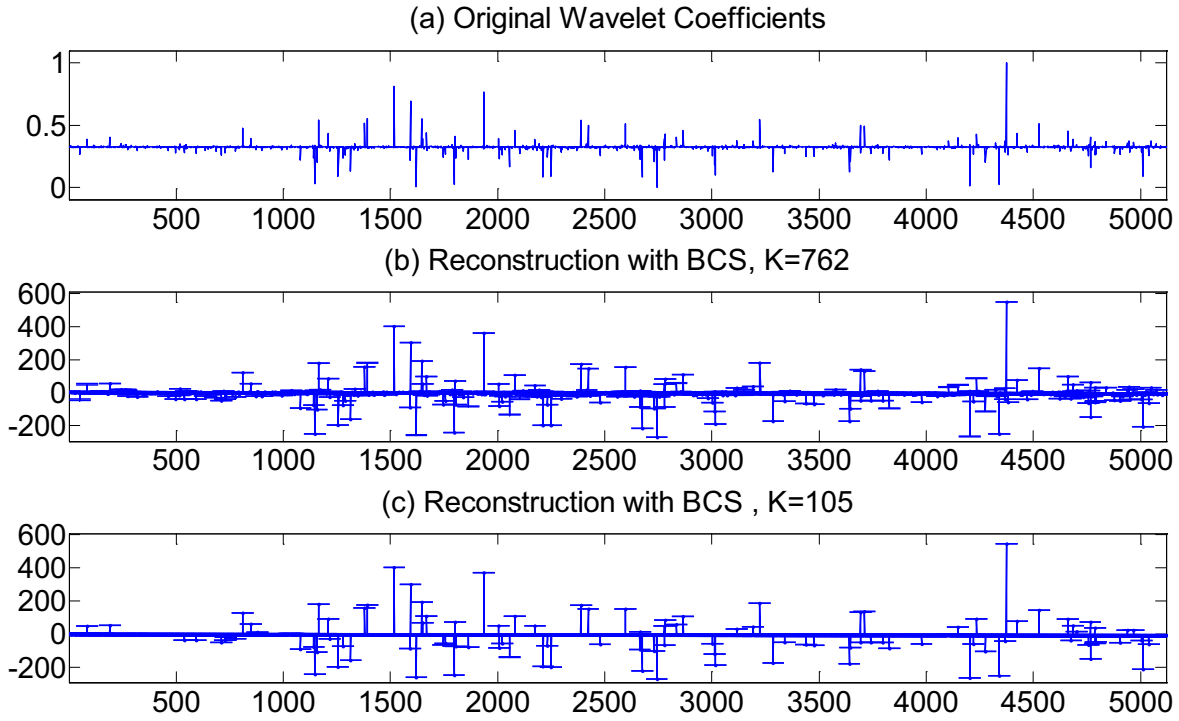

Figure 3.34 Comparison of sparse expansion. (a) Wavelet coefficients of original signal. (b) Reconstruction with BCS and non-zero estimates are 762, (c) Reconstruction of primary QRS complex with BCS and non-zero estimates are 105.

- **Ventricular Bradycardia**

The ECG signal denoted also by record 232 is shown in Figure 3.35, which begins at 23 minutes 47 second and continue 10 seconds from the first channel. Figure 3.35 depicts original ECG signal with a normal rhythm in which periodic changes in heart rate could be observed. The regular rhythm of normal heart beats is at the rate of 75 followed by a pause in sinus node resulting in a slowing of rate at 20. A P-P interval in recorded ECG signal of sinus pause is relatively longer than the usual, but less than 3 seconds. And the P-P interval of sinus arrest is usually longer than sinus pause.

E_X of the original ECG signal and E_Y of measurements are shown in Figure 3.36 using the same algorithm. The figure shows that the actual signal estimated energy and the estimation of its measurements hold most information of heartbeats. There are obviously 7 periods including a large and a small peak, where the fourth is smaller. The large peak represents QRS complex and the small peak represents T wave.

Figure 3.37 illustrates wavelet coefficients of ECG signal, reconstructed ECG signal and reconstructed QRS complex. All wavelet coefficients are arranged in random sequence for enhanced visibility.

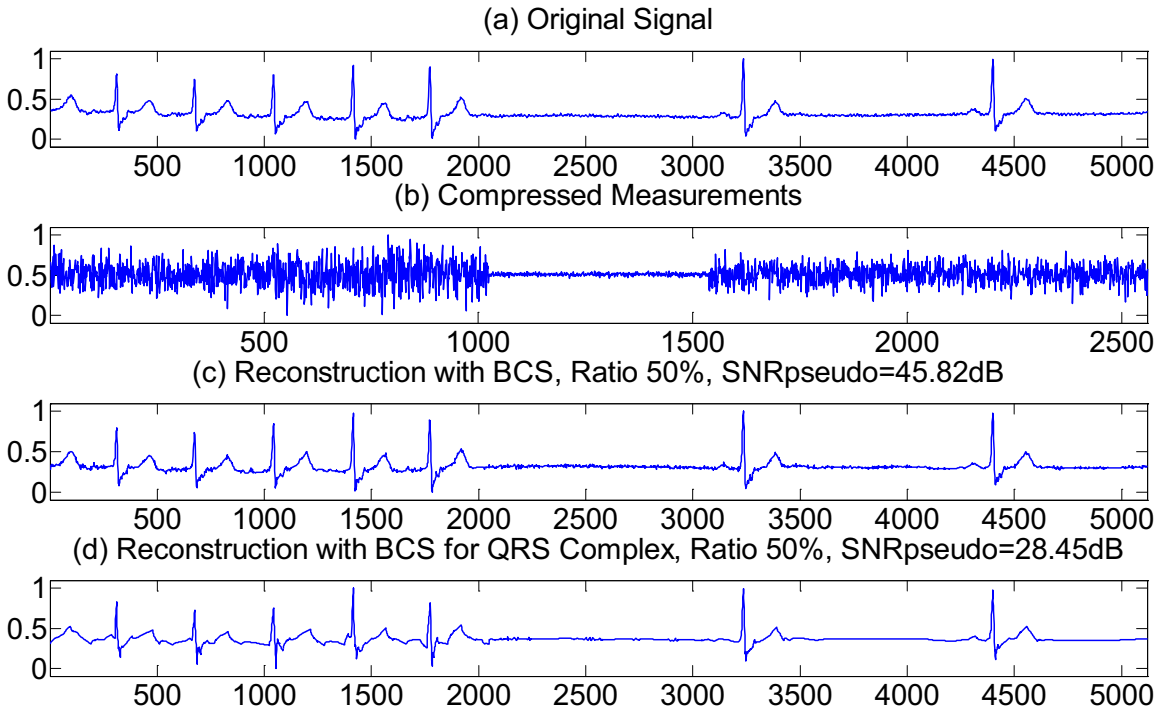

Figure 3.35 Comparison of signal reconstruction in ventricular bradycardia. (a) Original signal, (b) Compressed measurements, (c) Reconstruction with 974 non-zero wavelet coefficients, (d) Reconstruction with 105 non-zero wavelet coefficients.

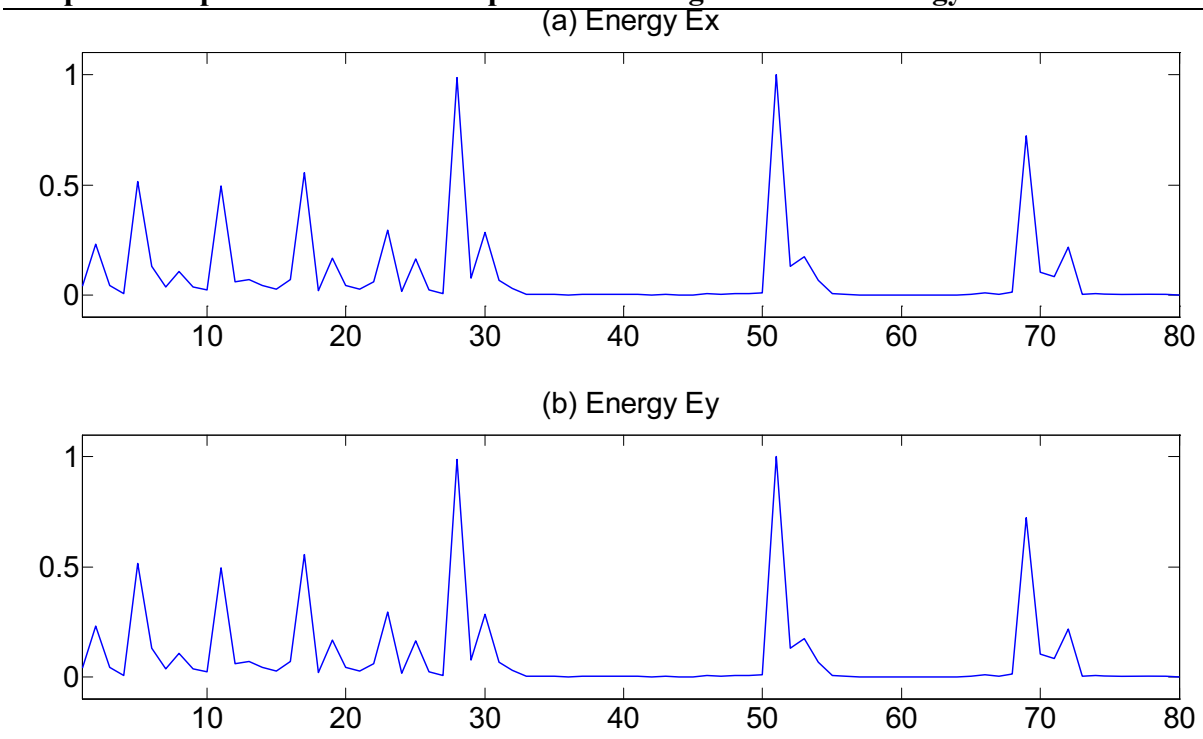

Figure 3.36 Statistical characteristic of ECG Signals in ventricular bradycardia. (a) Estimated energy of original ECG signals. (b) Estimated energy of compressed measurements.

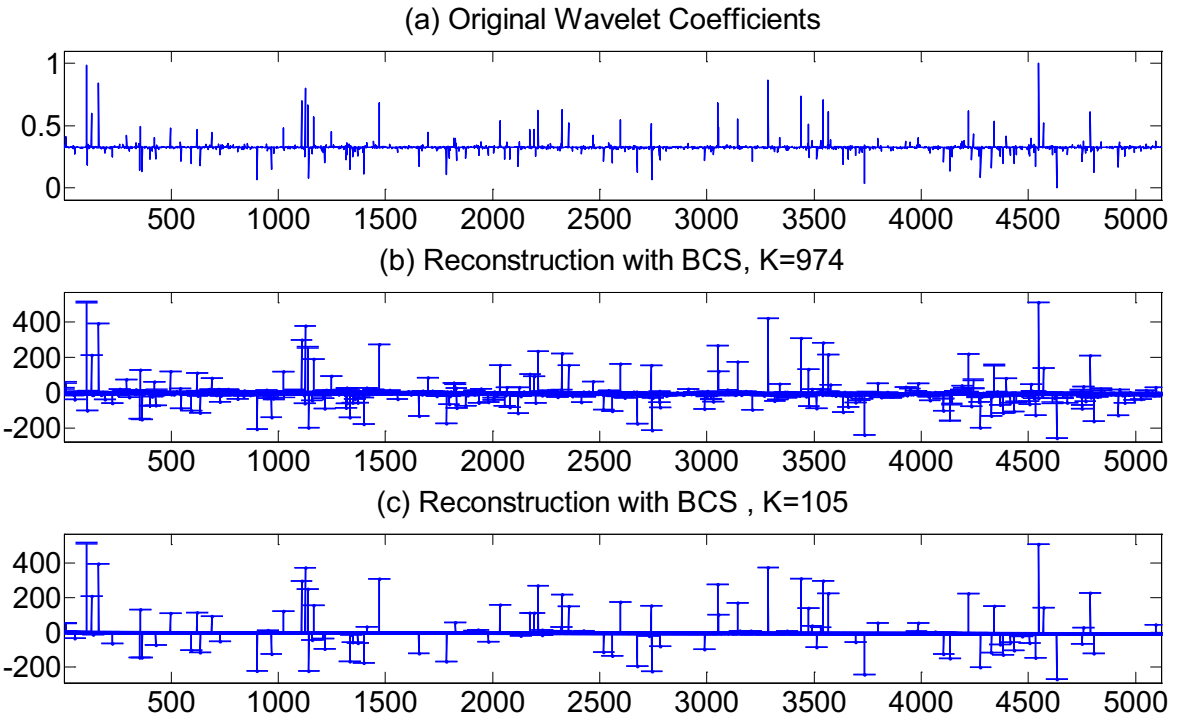

Figure 3.37 Comparison of sparse expansion. (a) Wavelet coefficients of original signal. (b) Reconstruction with BCS and non-zero estimates are 974, (c) Reconstruction of primary QRS complex with BCS and non-zero estimates are 105.

- **Ventricular Tachycardia**

The ECG signal denoted also by record 106 is shown in Figure 3.38, which begins at 2 minutes 51 second and continue 10 seconds from the first channel. Figure 3.38 depicts 6 ECG signal with a normal rhythm in which periodic changes are observed in heart rate followed by the initiation of polymorphic ventricular tachycardia, which has beat-to-beat variations in morphology. There are 3 premature ventricular contractions (PVC) following the 6 normal beats, then next a normal beat and a PVC.

E_X of the original ECG signal and E_Y of measurements are shown in Figure 3.39 using the same algorithm. The figure shows that the estimated energy of PVC is greater than normal beats. QRS complex and T wave are clearly displayed in Figure 3.39.

Figure 3.40 illustrates wavelet coefficients of ECG signal, reconstructed ECG signal and reconstructed QRS complex. The number of non-zero wavelet coefficients in Figure 3.40 (C) is 618 presenting 11 normal and abnormal beats, comparing the counterpart in Figure 3.37 (c) that is 974 for 7 normal beats. This observation manifests that the sparsity of signal onto the transform domain is not necessarily related to the number of heartbeats.

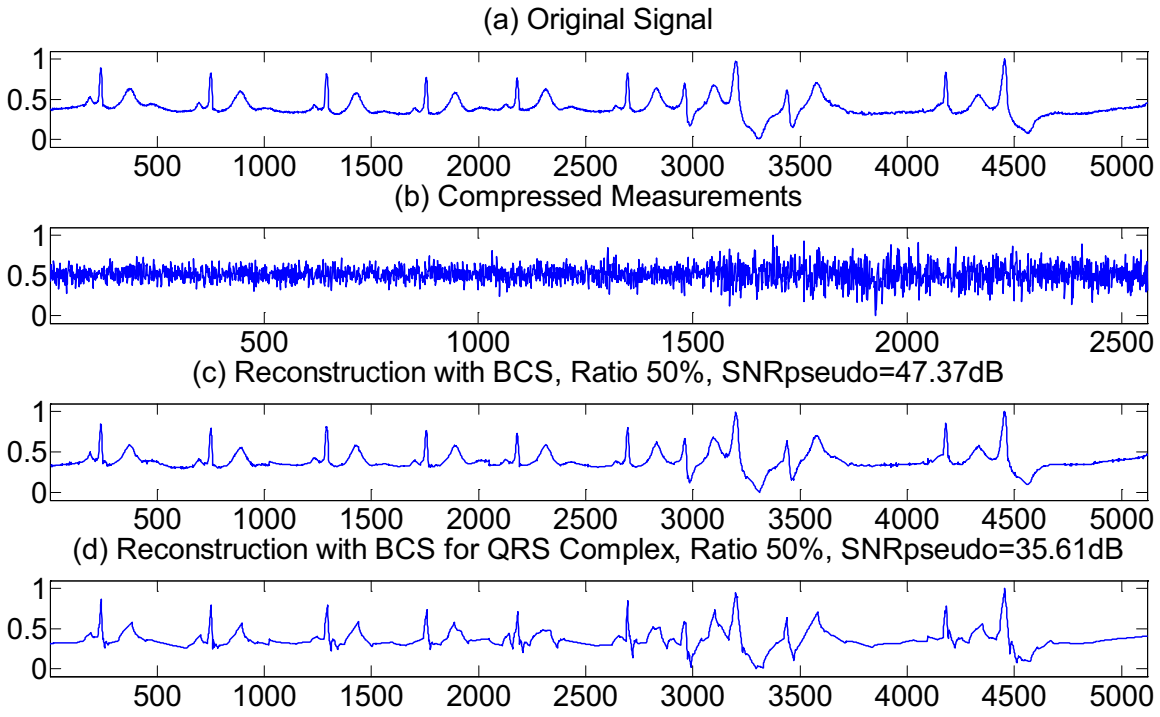

Figure 3.38 Comparison of signal reconstruction in ventricular tachycardia. (a) Original signal, (b) Compressed measurements, (c) Reconstruction with 618 non-zero wavelet coefficients, (d) Reconstruction with 105 non-zero wavelet coefficients.

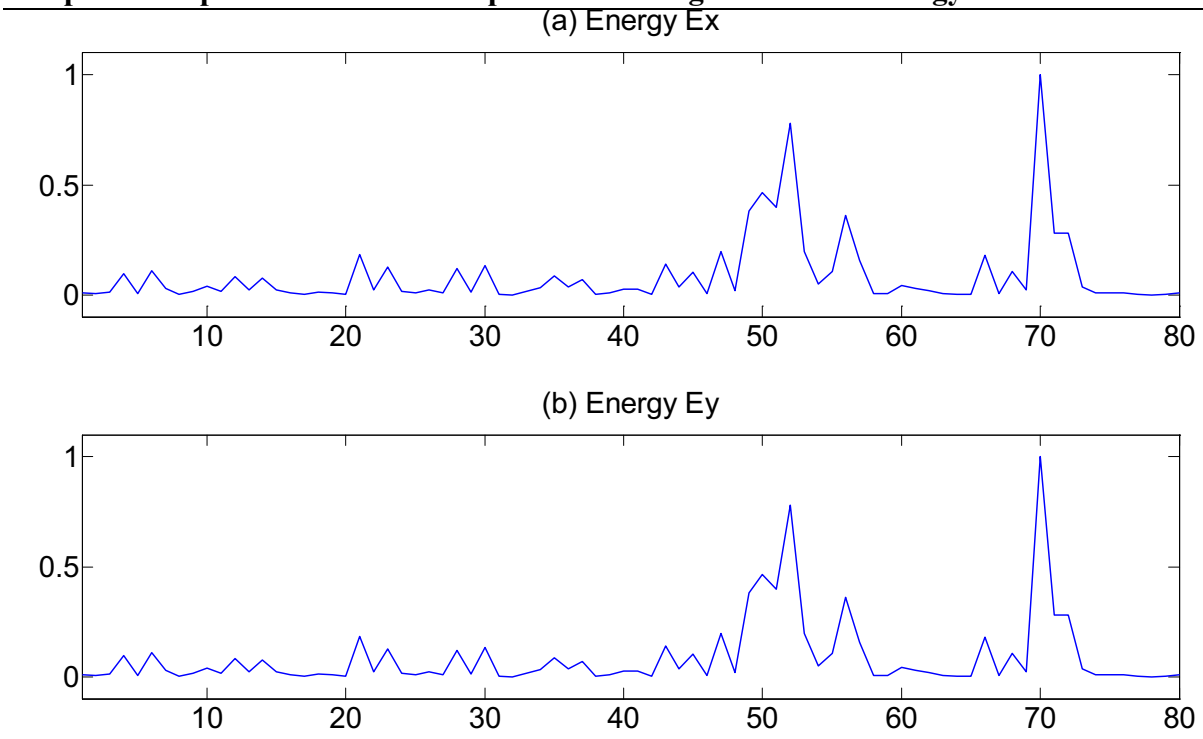

Figure 3.39 Statistical characteristic of ECG Signals in ventricular tachycardia. (a) Estimated energy of original ECG signals. (b) Estimated energy of compressed measurements.

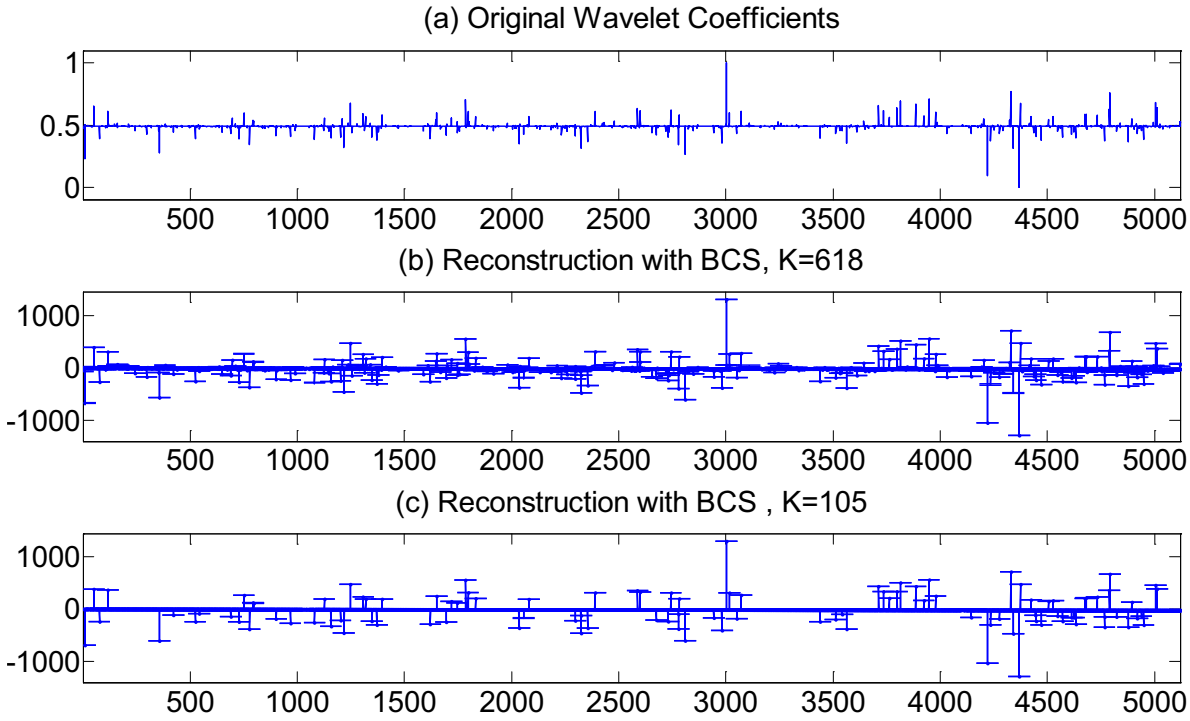

Figure 3.40 Comparison of sparse expansion. (a) Wavelet coefficients of original signal. (b) Reconstruction with BCS and non-zero estimates are 618, (c) Reconstruction of primary QRS complex with BCS and non-zero estimates are 105.

- **Atrial Bigeminy**

The ECG signal denoted also by record 222 is shown in Figure 3.41 which begins at 20 minutes 7 second and continue 10 seconds from the second channel. Figure 3.41 depicts 14 beats with periodicity in pairs in which a normal beat is closely followed an atrial premature beat (APB).

E_X of the original ECG signal and E_Y of measurements are shown in Figure 3.42 using the same algorithm. The amplitude of normal beat and APB is very close and difficult to be distinguished. But the rhythm confirms the occurrence of atrial bigeminy and the position in the time domain.

Figure 3.43 illustrates wavelet coefficients of ECG signal, reconstructed ECG signal and reconstructed QRS complex.

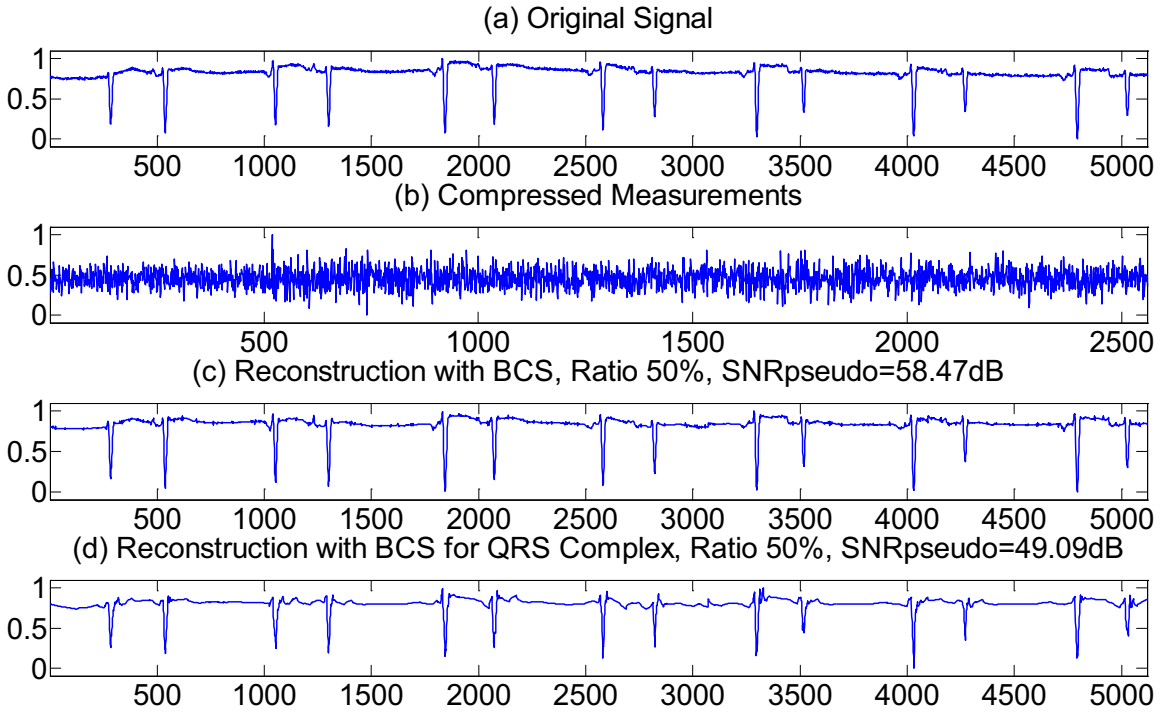

Figure 3.41 Comparison of signal reconstruction in atrial bigeminy. (a) Original signal, (b) Compressed measurements, (c) Reconstruction with 650 non-zero wavelet coefficients, (d) Reconstruction with 105 non-zero wavelet coefficients.

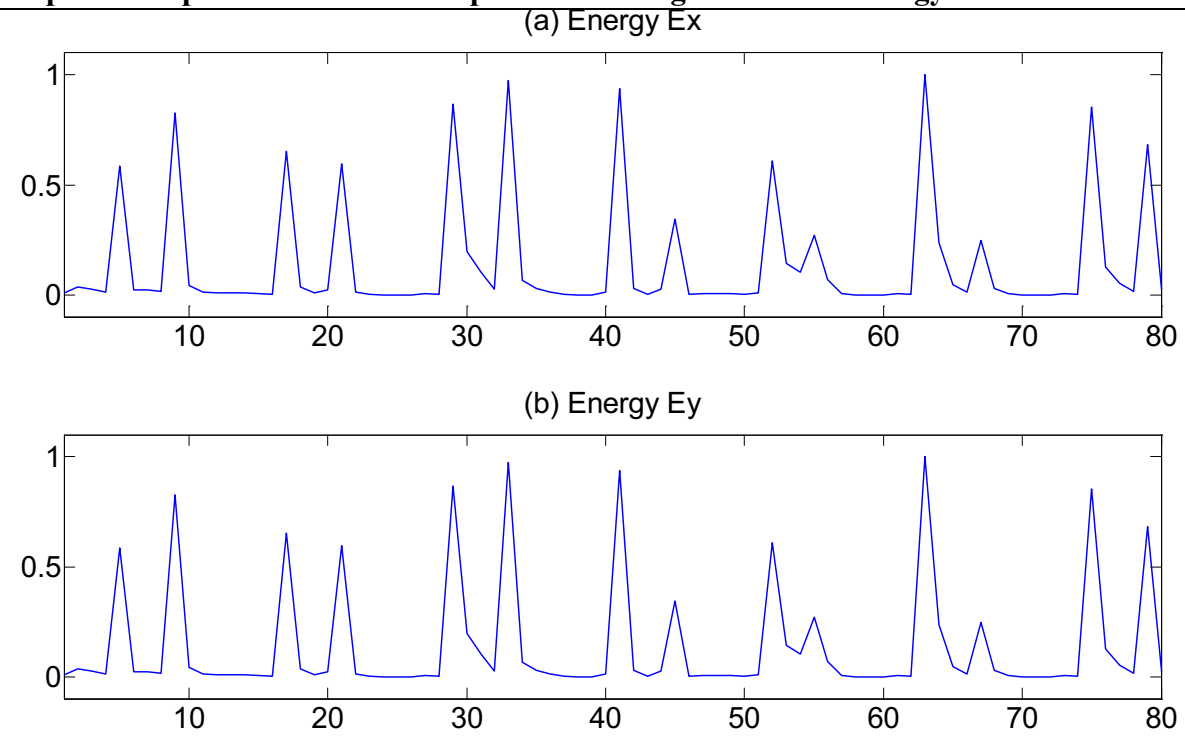

Figure 3.42 Statistical characteristic of ECG Signals in atrial bigeminy. (a) Estimated energy of original ECG signals. (b) Estimated energy of compressed measurements.

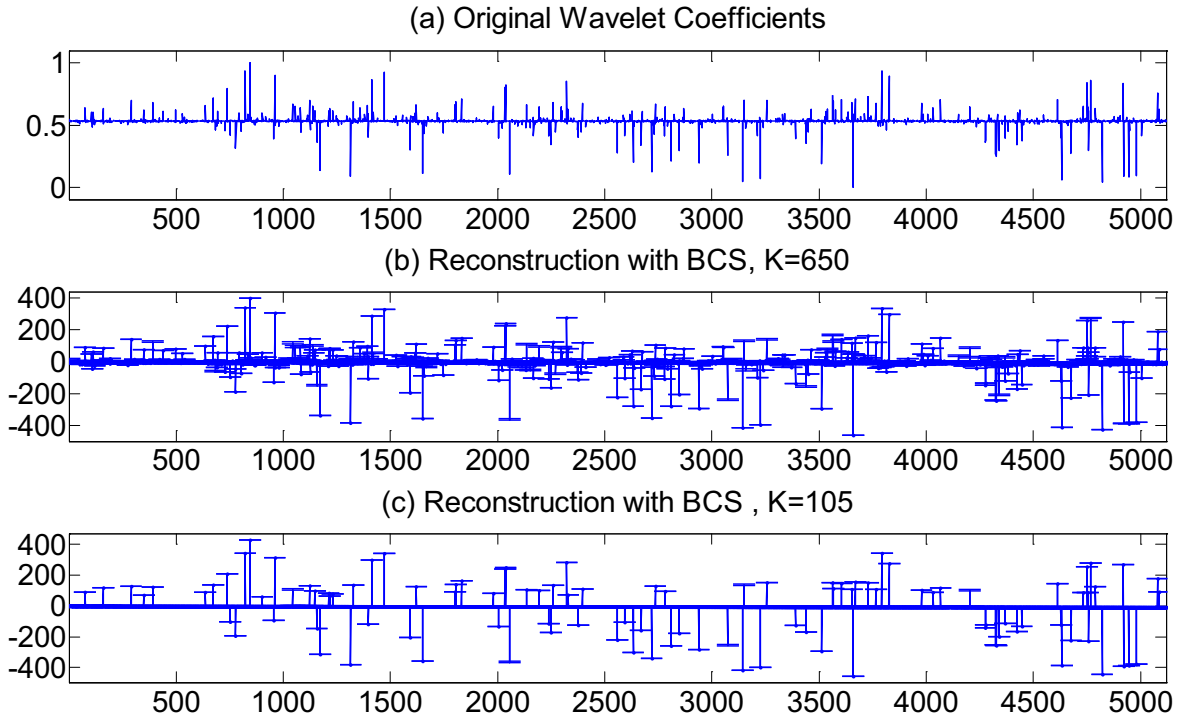

Figure 3.43 Comparison of sparse expansion. (a) Wavelet coefficients of original signal. (b) Reconstruction with BCS and non-zero estimates are 650, (c) Reconstruction of primary QRS complex with BCS and non-zero estimates are 105.

- **Atrial Flutter**

The ECG signal denoted also by record 202 is shown in Figure 3.44 which begins at 25 minutes 58 second and continue 10 seconds from the second channel. Figure 3.41 depicts 24 normal heart beats at the regular cardiac rate. Heart rate calculated on this sector is 432bpm with a $2:1$ heart block, in which only one third of these impulses will be conducted and a ventricular rate is of 144 bpm.

E_X of the original ECG signal and E_Y of measurements are shown in Figure 3.45 using the same algorithm. The number of peaks in Figure 3.45 is 24, which is used to calculate heart rate and get the results of 144 bpm.

Figure 3.46 illustrates wavelet coefficients of ECG signal, reconstructed ECG signal and reconstructed QRS complex. There are 832 non-zero wavelet coefficients of the original signal. But in fact the performance of reconstruction onto only about one hundred coefficients is also very well.

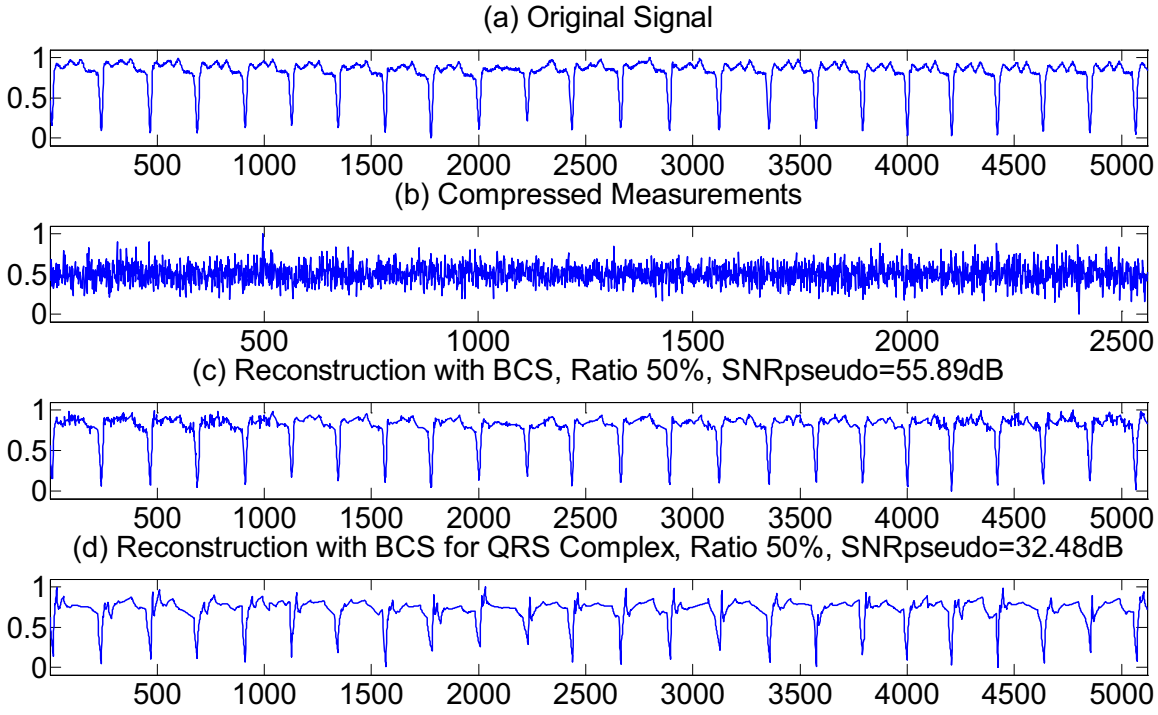

Figure 3.44 Comparison of signal reconstruction in atrial flutter. (a) Original signal, (b) Compressed measurements, (c) Reconstruction with 832 non-zero wavelet coefficients, (d) Reconstruction with 105 non-zero wavelet coefficients.

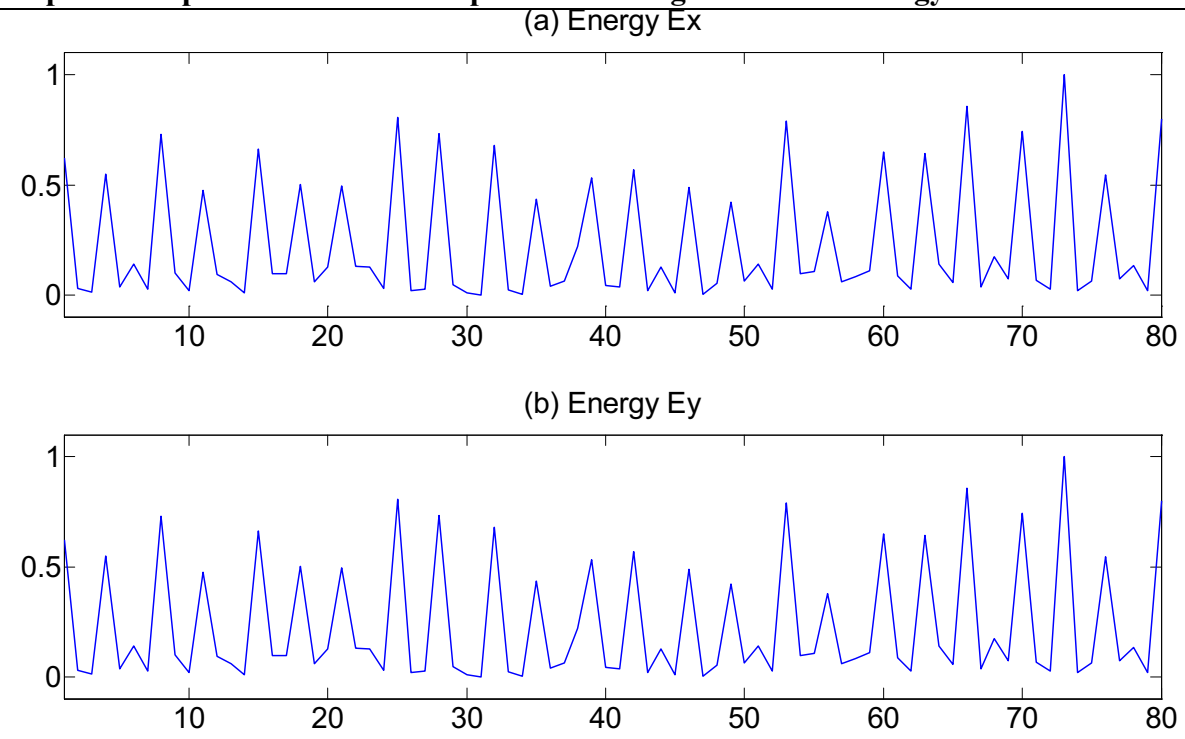

Figure 3.45 Statistical characteristic of ECG Signals in atrial flutter. (a) Estimated energy of original ECG signals. (b) Estimated energy of compressed measurements.

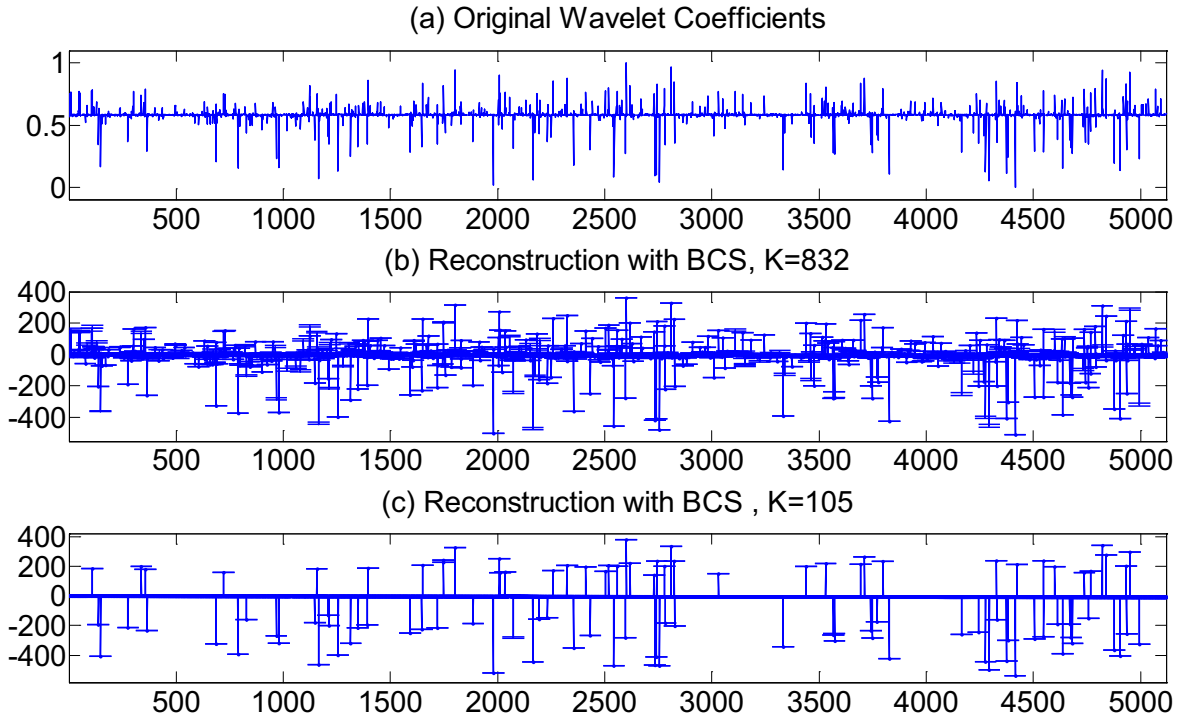

Figure 3.46 Comparison of sparse expansion. (a) Wavelet coefficients of original signal. (b) Reconstruction with BCS and non-zero estimates are 832, (c) Reconstruction of primary QRS complex with BCS and non-zero estimates are 105.

- **Atrial Fibrillation**

The ECG signal denoted also by record 202 is shown in Figure 3.47 which begins at 21 minutes 41 second and continue 10 seconds from the second channel. Figure 3.47 depicts 15 normal heart beats characterized by an irregular cardiac rate in which QRS complexes are normal with the duration less than 100ms. Heart rate calculated on this sector varies 46-127 bpm.

E_X of the original ECG signal and E_Y of measurements are shown in Figure 3.48 using the same algorithm. We can judge the occurrence of arrhythmia from the dramatic changes on the heart rate.

Figure 3.49 illustrates wavelet coefficients of ECG signal, reconstructed ECG signal and reconstructed QRS complex. There are 759 non-zero wavelet coefficients of original signal. But in fact the performance of reconstruction onto only about one hundred coefficients is also very well.

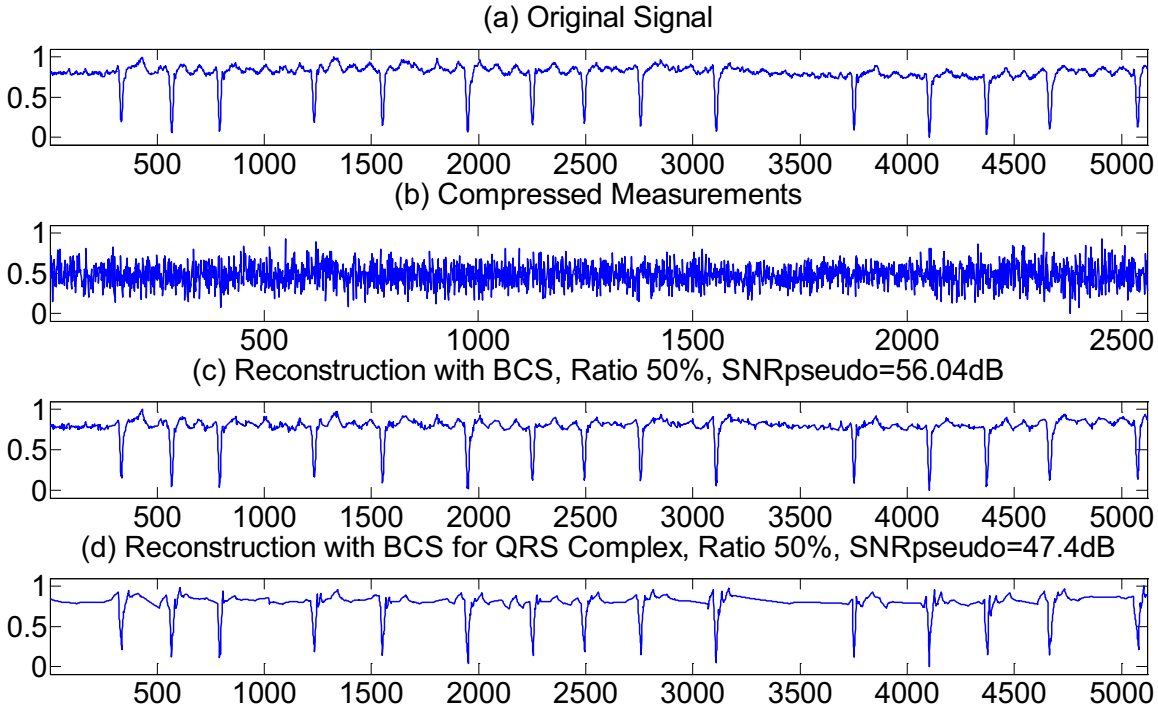

Figure 3.47 Comparison of signal reconstruction in atrial fibrillation. (a) Original signal, (b) Compressed measurements, (c) Reconstruction with 759 non-zero wavelet coefficients, (d) Reconstruction with 105 non-zero wavelet coefficients.

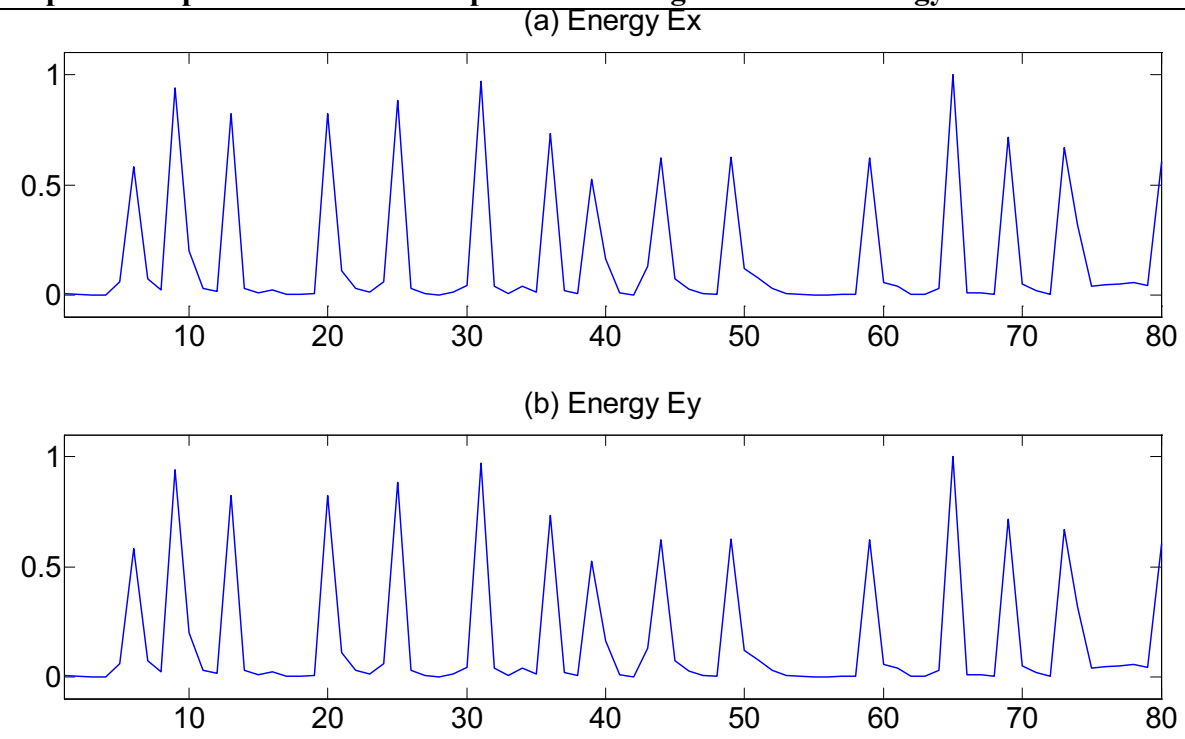

Figure 3.48 Statistical characteristic of ECG Signals in atrial fibrillation. (a) Estimated energy of original ECG signals. (b) Estimated energy of compressed measurements.

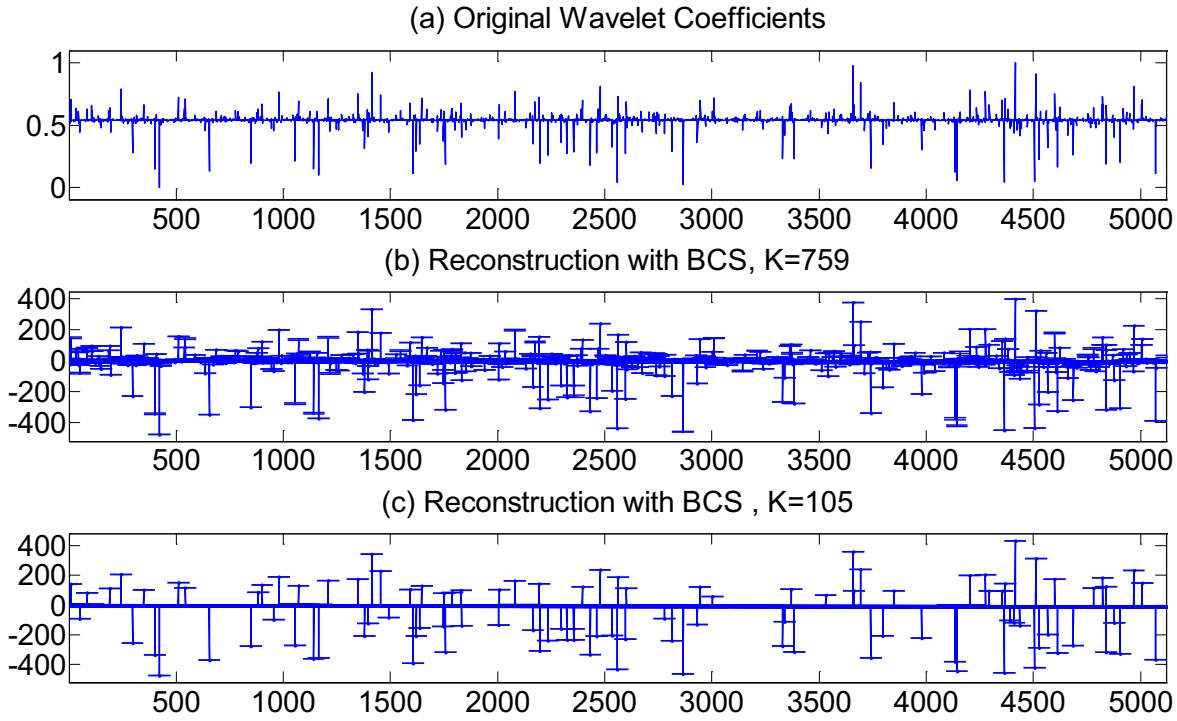

Figure 3.49 Comparison of sparse expansion. (a) Wavelet coefficients of original signal. (b) Reconstruction with BCS and non-zero estimates are 759, (c) Reconstruction of primary QRS complex with BCS and non-zero estimates are 105.

- **Ventricular Bigeminy**

The ECG signal denoted also by record 233 is shown in Figure 3.50 which begins at 2 minutes 18 second and continue 10 seconds from the second channel. The waveform is very close to the counterpart of atrial bigeminy with the difference that a normal beat is followed by a PVC. Figure 3.50 depicts 10 normal beats and 7 PVC in the waveform.

E_X of the original ECG signal and E_Y of measurements are shown in Figure 3.51 using the same algorithm. There are 9 normal beats with significant amplitude different to PVC with false detection of one.

Figure 3.52 illustrates wavelet coefficients of ECG signal, reconstructed ECG signal and reconstructed QRS complex.

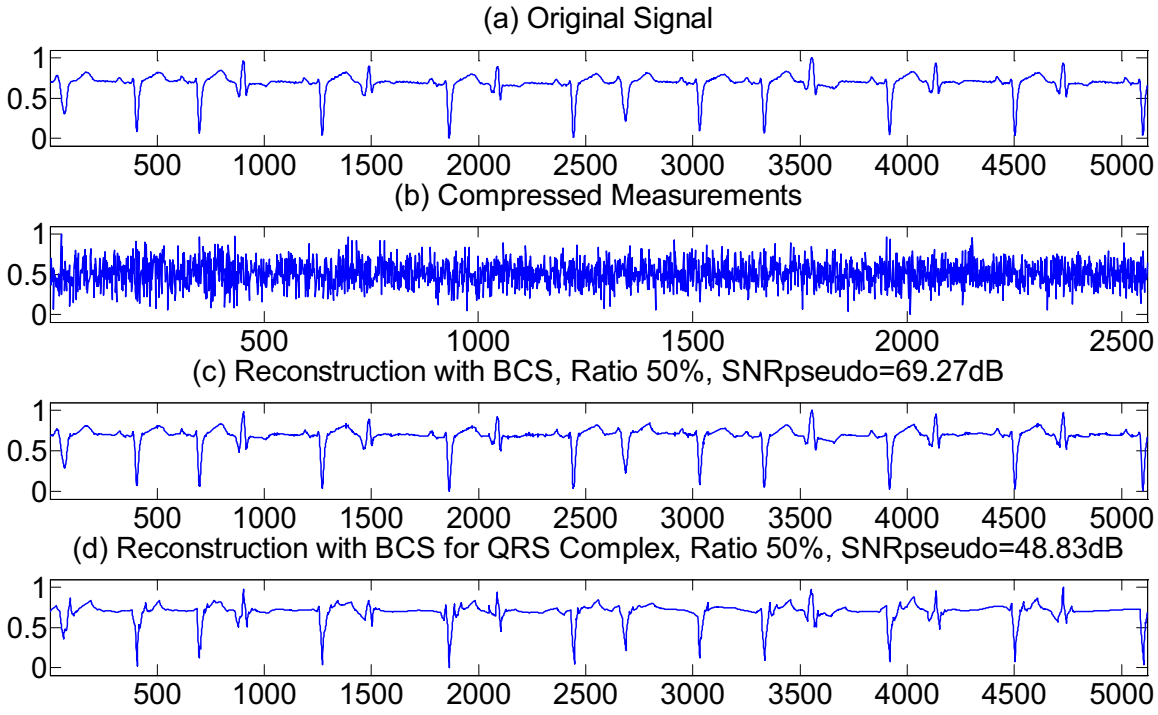

Figure 3.50 Comparison of signal reconstruction in ventricular bigeminy. (a) Original signal, (b) Compressed measurements, (c) Reconstruction with 627 non-zero wavelet coefficients, (d) Reconstruction with 105 non-zero wavelet coefficients.

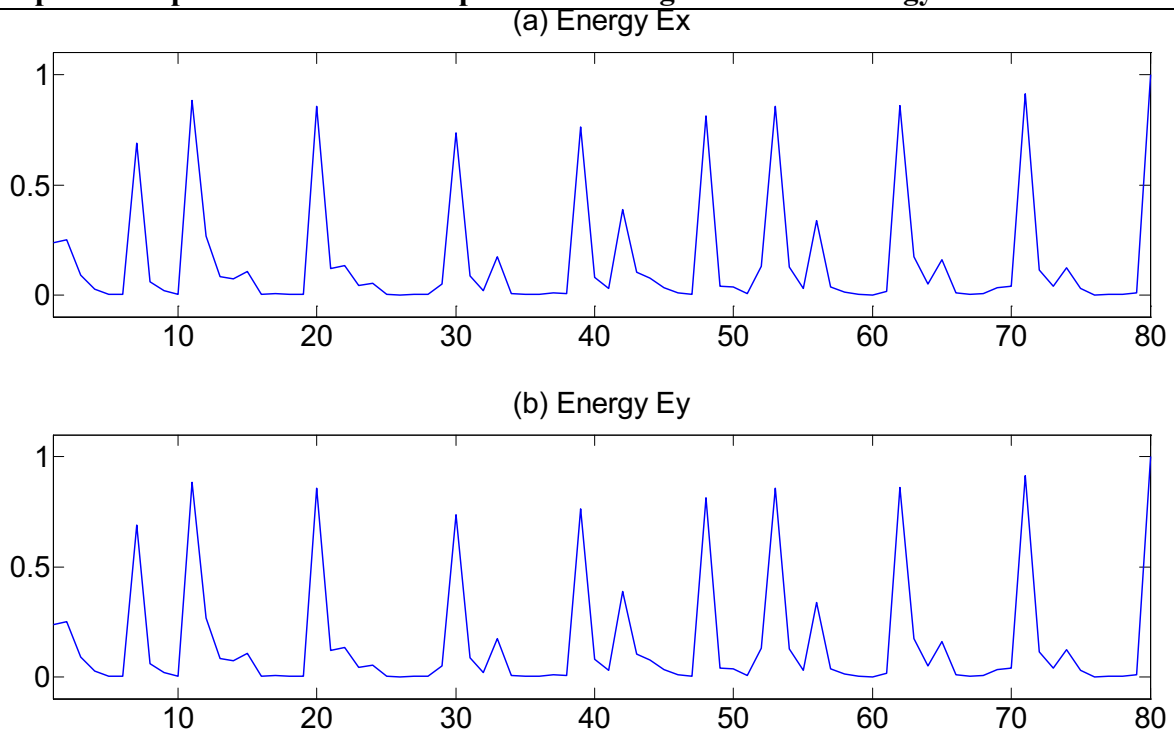

Figure 3.51 Statistical characteristic of ECG Signals in ventricular bigeminy. (a) Estimated energy of original ECG signals. (b) Estimated energy of compressed measurements.

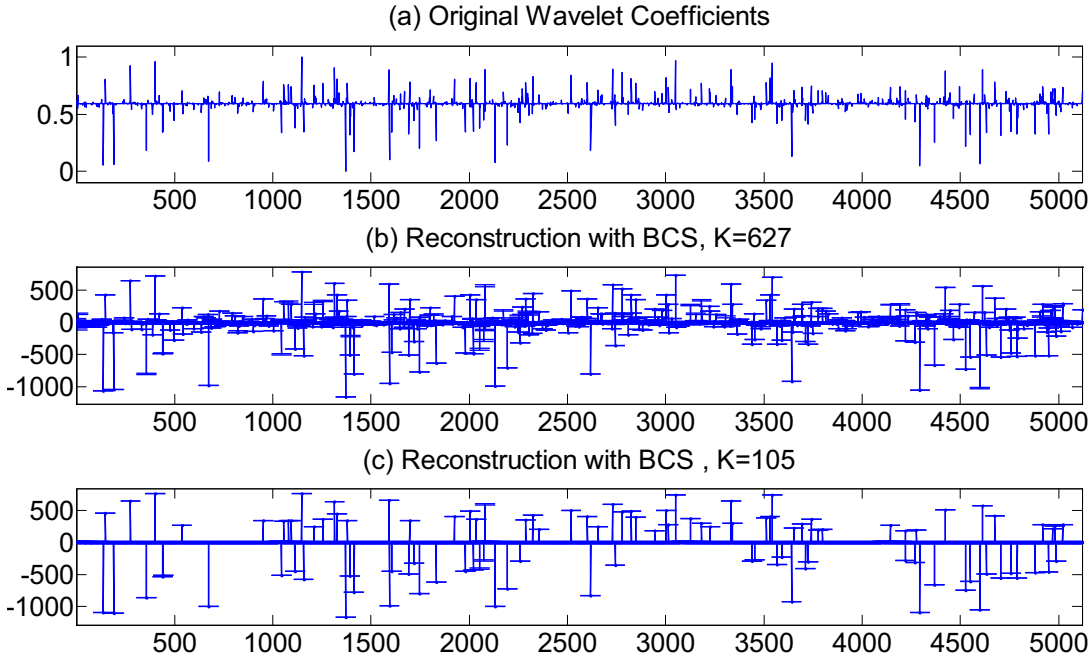

Figure 3.52 Comparison of sparse expansion. (a) Wavelet coefficients of original signal. (b) Reconstruction with BCS and non-zero estimates are 627, (c) Reconstruction of primary QRS complex with BCS and non-zero estimates are 105.

- **Supraventricular Tachyarrhythmia**

The ECG signal denoted also by record 201 is shown in Figure 3.53 which begins at 26 minutes 24 second and continue 10 seconds from the second channel. There are 2 aberrated atrial premature beats following the first beat that is a normal beat, and followed by an atrial premature beat.

E_X of the original ECG signal and E_Y of measurements are shown in Figure 3.54 using the same algorithm. There are 9 peaks with irregular heart rhythm.

Figure 3.55 illustrates wavelet coefficients of ECG signal, reconstructed ECG signal and reconstructed QRS complex.

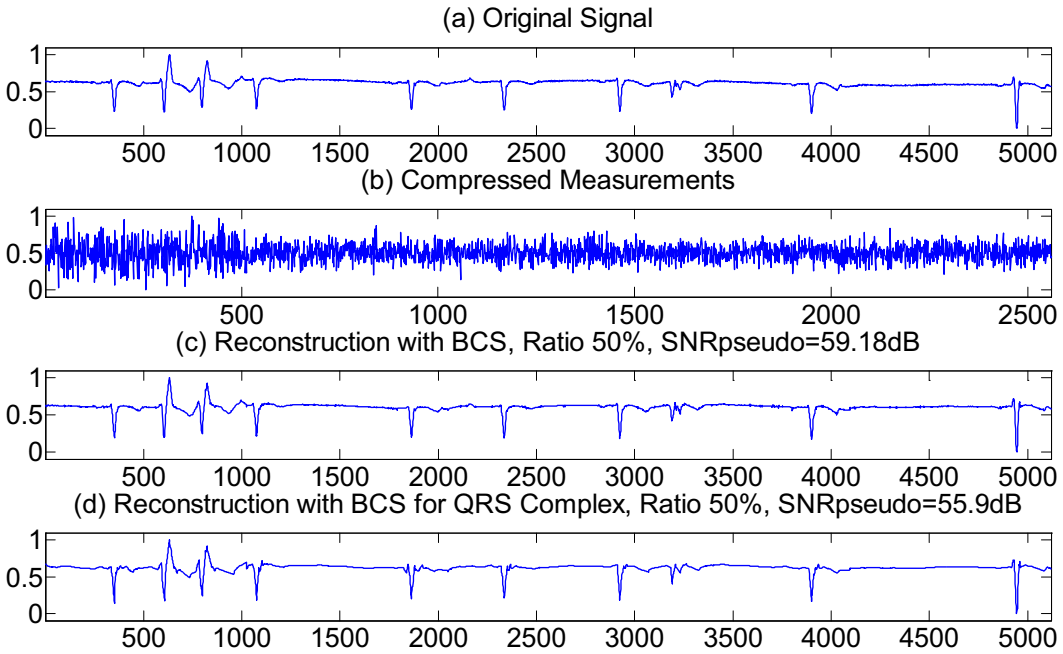

Figure 3.53 Comparison of signal reconstruction in supraventricular tachyarrhythmia. (a) Original signal, (b) Compressed measurements, (c) Reconstruction with 576 non-zero wavelet coefficients, (d) Reconstruction with 105 non-zero wavelet coefficients.

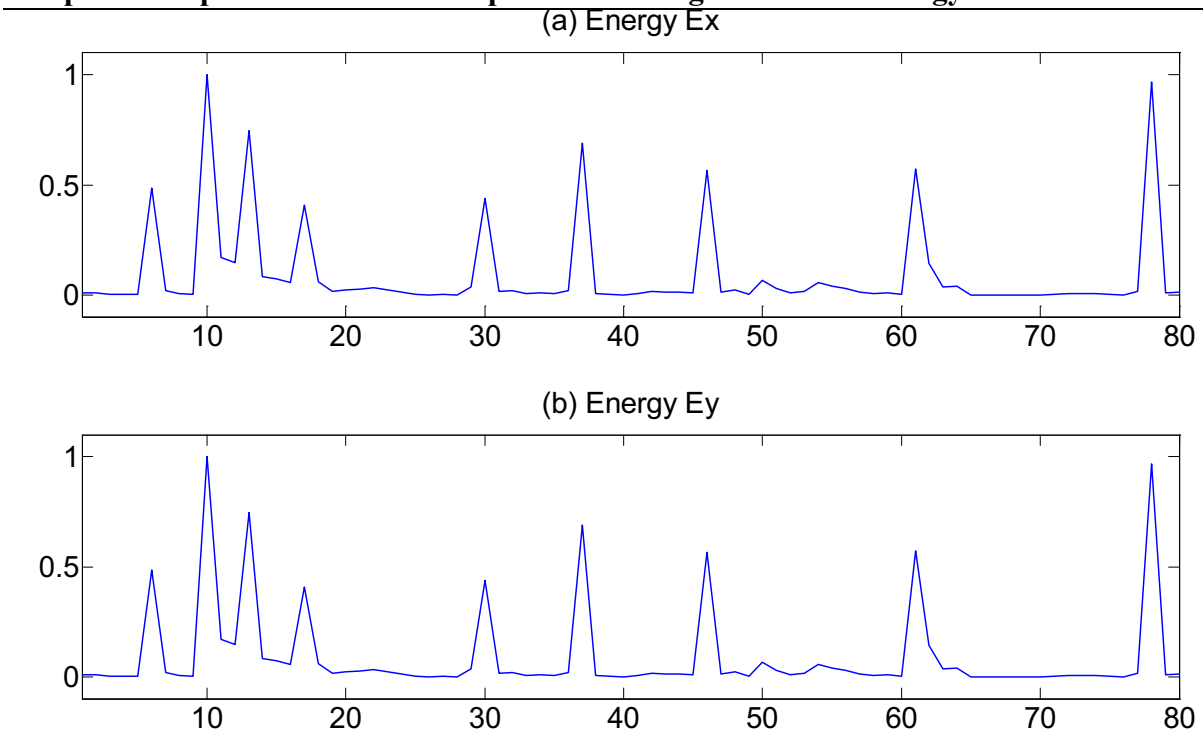

Figure 3.54 Statistical characteristic of ECG Signals in supraventricular tachyarrhythmia. (a) Estimated energy of original ECG signals. (b) Estimated energy of compressed measurements.

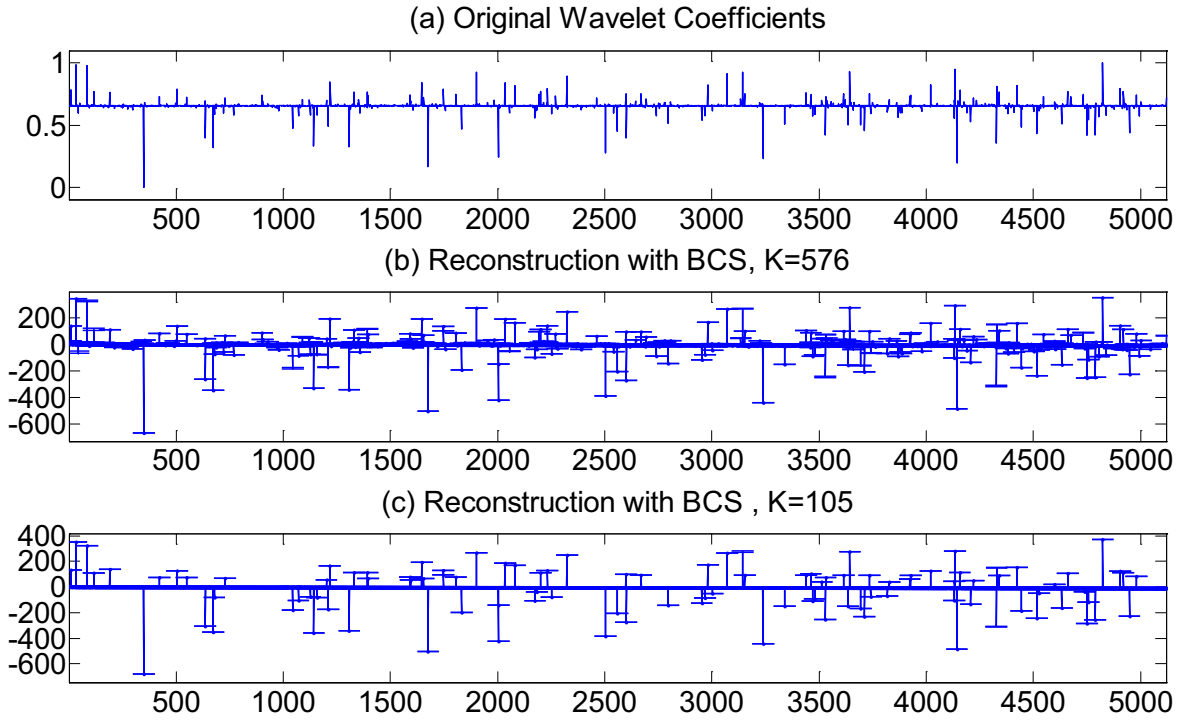

Figure 3.55 Comparison of sparse expansion. (a) Wavelet coefficients of original signal. (b) Reconstruction with BCS and non-zero estimates are 576, (c) Reconstruction of primary QRS complex with BCS and non-zero estimates are 105.

3.4. Conclusion

After introducing the architecture of SoC-Holter, we have shown that the implementation of the compressed sensing (CS) in cardiac arrhythmia monitoring is very profitable. CS is a powerful technique but its reconstruct algorithm increases the cost of computational complexity which is nontrivial especially in the power and storage constrained WES (wearable wireless ECG sensor). This motivates our development of BCS cardiac arrhythmia detection method which directly classify ECG signal with compressed measurements. The cardiac signal of ECG presents a sparse exponent in the wavelet transformed domain. This observation instructs us to combine CS and ADC part to decrease storage consumption. In this CS-based framework, we reconstruct the ECG signal based on BCS at the terminal of the network for cardiologists to offline diagnose cardiac arrhythmias. To decrease signal processing complexity and power consumption, we developed this technique to detect the presence of QRS complex without reconstruction of ECG signals in WES. Based on this technique, we can classify the recorded data into the normal and anomaly categories directly from the compressed measurements. Multiple simulations demonstrate the relationship between the minimum number of measurements and the performance of direct cardiac arrhythmia detection and the reconstructed entire ECG signals. We may conclude that, an appropriate choice of the length of compressed measurements and wavelet transform allow us to achieve our primary goal of significantly reducing the storage and power consumption on WES, and providing more accuracy reconstructed ECG signal for cardiologists in diagnosing this specific heart disease.

Chapter 4
Distortion Effect of Electrode Location

4.1. Introduction

Ambulatory ECG system as Holter can extend the usefulness of the ECG for continuously recording a patient's ECG data over a long period such as 24 hours in his daily activities without interference. Technologists in practice tend to design a monitoring system with a limited number of leads. At first a theoretical method is used to operate the recorded ECG measurements on the surface of the thorax, indirectly evaluating the electrical impulse in the heart. The human body can be considered as a volume conductor.

Cardiologists use the ECG as a diagnostic tool to determine cardiac abnormalities from the potentials measured from the surface of the human body. Apparently the physical characteristics of the heart cannot directly be derived from external potentials. However if the knowledge of the potential generator is given, the body surface potential can be specified.

Cardiac activation can be described by the sequence of instantaneous locus recording. Electrocardiography (ECG) represents the time course of electrical record in the one dimensional, and Vectorcardiogram (VCG) is achieved by several leads corresponding to orthogonal leads. A number of physical and mathematical models are introduced to analyze the spatial representation of electrical pulse generated by the heart in three spatial planes (horizontal, frontal and sagittal). Each moment of depolarization can be represented by an instantaneous electric dipole. All individual dipoles form together to generate the hypostatic dipole of the cardiac activity by a vector. If describing the electrical activity in the heart each instant as a single vector, a spatial VCG is established. Models are typically based on one basic in which the human torso has imbedded electrical sources. By placing artificial bipolar sources in the torso, the relation between the cardiac activity and body surface potentials may be announced.

In contrast to conventional recoding ECG signal where scalar traces allow for assessment of wave morphology, difference ECG signal is assessed based on WES. Difference ECG signal is measured by two electrodes placed closely together. Therefore the reduction of the long wires connected between the electrodes and WES is of great benefit to minimize the motion artifact and make the carrier more comfortable.

The effect of electrode location on the QRS-complex recorded is firstly investigated by Simonson [83]. Analysis of the influence can inform the placement of ECG leads by gathering the same information that is projected onto the body's surface as standard ECG signal.

4.1.1. Theoretical Analysis of Volume Source

An ECG is a recording that measures the electrical activity of the heart by the potentials produced on the surface of the skin. The graphic recording of these potentials as a function of time can reveal the relation between the heart and surface potentials. Einthoven is the first man to suggest that the cardiac electromotive force in the heart could be summed and represented by a vector [35]. The heart can be represented by a number of dipolar sources imbedded in a volume conductor. The dipole can be considered as a simple model to describe the relation of the cardiac activity and body surface potentials.

4.1.2. Lead Vector

The dipole can be presented as a vector from the source to the sink. The model represents geometry properties and electrical activity of the heart. An electric dipole can be simply explained to a pair of electrical charges that are separated by a very small distance and have equal magnitude but opposite sign. So a cardiac dipole can be depicted as a vector with magnitude and direction by displacing from negative to positive source.

Lead vector can represent the dipole of depolarization and repolarization including the value of direction and magnitude. We can suppose that there has an arbitrary surface lying within a volume conductor and the potential ϕ lies on this surface. The potential field at a point P is the function to measure the difference in electric potential caused by a unit dipole $\overline{i}$ in the X direction in a fixed location. The potential ϕ has the similar expression in the Y and Z directions. The potential at a point P can be calculated in terms of dipoles in each coordinate direction. The scale value of this potential can be expressed by mathematical expression to the linear combination of all dipoles in each coordinate direction. Lead vector $\overline{c}$ is an approxiamate discription of the projected proportionality in three-dimensional space.

The scale potential at the point P is obtained by the source dipole $\overline{p}$ and the lead vector $\overline{c}$.

$$\overline{p} = p_x\overline{i} + p_y\overline{j} + p_z\overline{k} \tag{4-1}$$

$$\overline{c} = c_x\overline{i} + c_y\overline{j} + c_z\overline{k} \tag{4-2}$$

Mathematically, the potential ϕ_p can be obtained from the scalar product of dipole $\overline{p}$ and the lead vector $\overline{c}$ by using Equation (4-3)

$$\phi_p = \overline{c} \cdot \overline{p} = |\overline{c}||\overline{p}|\cos(\alpha) \tag{4-3}$$

Generally speaking, it is not necessary to consider the influences of volume conductor when the potential of the point is calculated. However, the location of the point on the surface of the volume conductor will change and affect the result of the potential. The reason is that the arbitrary source of the dipolar at a fixed point Q is inside the volume conductor. The interpretation of the potential should take into account relevant location of the potential of the reference. The value of the lead vector is determined by several factors: 1) the location Q of the dipole $\overline{p}$, 2) the location of the field point P, 3) the shape of the volume conductor, 4) the volume resistivity of conductor.

The potential of the reference can be assumed to zero because it is arbitrary. The magnitude or direction of the dipole $\overline{p}$ is not taken into account either for determining the value of the lead vector, because this value is relevant only to the property of the lead and volume conductor.

Through the above discussion, the detected ECG signal can be characterized the produce by the activation front in the heart, there both the depolarization and repolarization fronts propagate towards both positive and negative electrodes. Because the dipoles are always directed toward the positive electrode, the depolarization front toward the positive electrode and produces a positive signal, the angle between $\overline{p}$ and $\overline{c}$ is positive. Corresponding to the contrary, a signal is negative when the propagation of activation is far away from the positive electrode. The repolarization is following the same principle but on the exact contrary. When the repolarization front propagates toward the positive electrode, the signal is negative.

The lead vector $\overline{c}_0 \cdots \overline{c}_n$ for the dipole $\overline{p}$ at a fixed location can be expressed by each location $P_0 \cdots P_n$ of P that lies on the surface of the volume conductor. So we have

$$\phi_i = \overline{c}_i \cdot \overline{p} \tag{4-4}$$

then the potential difference between any points P_i and P_j

$$V_{ij} = \phi_i - \phi_j \tag{4-5}$$

so

$$V_{ij} = \phi_i - \phi_j = \overline{c}_i \cdot \overline{p} - \overline{c}_j \cdot \overline{p} = \overline{c}_{ij} \cdot \overline{p} \tag{4-6}$$

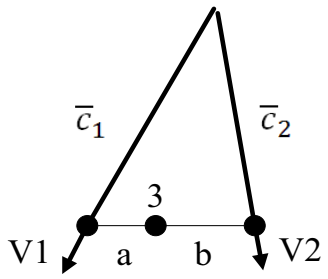

Figure 4.1 Determination of the point 3 on the surface of body corresponding to an image space point located between V_1 and V_2.

The potential difference V_{ij} can be simply depicted as the scalar product of the heart vector with the lead vector. If we imagine the thorax as the sphere, the potential of the point at the surface of the sphere can be obtained using the upper equation which is determined by the electrical potential difference between two points both located on the surface of a volume conductor. The potentials ϕ_1 and ϕ_2 at V_1 and V_2 due to the dipole may be established with scalar products with lead vectors V_1 and V_2, respectively. Rewrite ϕ_i and ϕ_j as ϕ_1 and ϕ_2. For determining the voltage V_{ij} between V_i and V_j, the lead vector $\overline{c}_{ij} = \overline{c}_i - \overline{c}_j$ is first determined. The voltage V_{12} is relevant to the lead vector $\overline{c}_{12}$ and the dipole $\overline{p}$, and the value can be mathematically obtained by the scalar product of them. We can imagine that there is an arbitrary line that has been drawn to connect the two points V_1 and point V_2 on one image surface. So the lead vector can be assumed as the relationship between a point on the surface of a volume conductor and a point O, somewhere in the heart region. So potentials are

available to measure on the potential fields of volume conductor that any arbitrary potential inside volume conductor is considered to zero and the potentials have the same property.

The basic of Vectorcardiography is to illustrate the human body by three orthogonal leads containing all the information of the heart.

Suppose point 3 that lies in the surface constructed by the lead vectors V_1 and V_2 as shown in Figure 4.1. From the figure, the relationship between lead vectors $\overline{c}_1$, $\overline{c}_2$, and $\overline{c}_{p3}$ can be discribed as

$$\overline{c}_{p3} = \overline{c}_1 + \frac{a}{a+b}(\overline{c}_2 - \overline{c}_1) = \overline{c}_2 - \frac{b}{a+b}(\overline{c}_2 - \overline{c}_1) \tag{4-7}$$

therefore, the voltage measurement of the point P must fulfill the requirement

$$\overline{c}_{p3} \cdot \overline{p} = \overline{c}_1 \cdot \overline{p} + \frac{a}{a+b}(\overline{c}_2 - \overline{c}_1) \cdot \overline{p} = \overline{c}_2 \cdot \overline{p} - \frac{b}{a+b}(\overline{c}_2 - \overline{c}_1) \cdot \overline{p} \tag{4-8}$$

$$\phi_{p3} = \phi_1 + \frac{a}{a+b}(\phi_2 - \phi_1) = \phi_2 - \frac{b}{a+b}(\phi_2 - \phi_1) \tag{4-9}$$

ideally, the voltages of these electrodes re-measured with respect to a remote reference ϕ_{ref}, infinity.

$$\phi_{p3} - \phi_{ref} = \frac{b}{a+b}\phi_1 - \phi_{ref} + \frac{a}{a+b}\phi_2 - \phi_{ref} \tag{4-10}$$

because the characteristic of ϕ_{ref}, $\phi_{ref} = \phi_{ref} + \phi_{ref}$

$$V_{p3} = \frac{b}{a+b}V_1 + \frac{a}{a+b}V_2 \tag{4-11}$$

4.2. Vectorcardiographic lead system

The concept of lead vector introduced in the above section can induct a method named Vectorcardiography (VCG) to record the magnitude and direction of electrical pulses that are generated by the volume source. The VCG to solve the inverse problem of a parametric model assumes that the heart source may be approximated as a finite homogeneous torso with a fixed-location, variable-amplitude and orientation current dipole. The basic principle of Vectorcardiography is to describe the cardiac electric generator accurately with an equivalent dipole displaying in vector form. Theoretically it is obvious to display the behavior of the dipole based on a continuous series of vectors around the center of the thorax in orthogonal coordinate system.

Williams introduced a method to constitute an orthogonal coordinate system of vectorcardiogram from standard limb leads in 1914 [84]. Later the monocardiogram was firstly deduced by Hubert Mann in 1920 [35]. Mann obtained successive projection of the vector loop on the frontal plane based on the principle that the Einthoven triangle can descript the limb lead voltage. The same work was done by Burch, who displayed the vector loop on the oscilloscope [35]. Burch made use of vector theory to produce an independent vector loop with any two different ECG leads applied. Frank Norman Wilson with his team developed a

lead system based on rectangular body axes that added to the Einthovon limb leads an electrode located on the back. Schellong in Germany independently developed systems for displaying loops the concept of a frontal plane loop [35].

VCG lead systems described above are actually uncorrected VCG lead systems, which do not consider distortions caused by the volume conductor formed by the thorax. The assumption that the direction of vector connected an electrode runs in parallel with the orientation of the corresponding lead vector is not accurate. So E. Frank developed Vectorcardiography in the early 30's. The basic idea of his theory is to view the human body as a three dimensional structure. This VCG lead system is corrected VCG lead system, which is to perform the electric heart vector in orthogonal measurements fulfilled two requirements: orthogonalization and normalization. Orthogonalization is to measure the electric heart vector on orthogonal coordinate axes. Normalization is to detect components of the electric heart vector with the same sensitivity.

Ernest Frank designed corrected VCG lead system based on a finite and homogeneous thorax model using his previous work of image surface [85]. The electrode location is chosen to 4 directions around the thorax, in addition including one electrode on the neck and another on the left foot. Finally the establishment of normalized coordinated axes is based on these electrodes. McFee and Parungao (1961) developed a VCG lead system, which based on a lead field theory and placed more electrodes close to the heart to achieve an appropriate lead field within the heart. VCG lead system applies linear analysis by taking two of the three axial leads at one time. Another method of VCG called as stereovectorelectrocardiography (SVEC) was introduced by Otto H. Schmitt and Ernst Simonson developed in 1955. SVEC interprets a lead field of the thorax by the relationship of 14 electrodes. The specialty of SVEC is to orient more symmetrically in relation to the sagittal plane. Another mathematical method of the Gabor-Nelson theorem that can be used to estimate one equivalent dipole of a volume source from the observations is introduced by Dennis Gabor and Clifford V. Nelson. Using the knowledge of the volume conductor's geometry, Fischmann, Barber and Weiss constructed the orthogonal Lead system that ascertains the location of the equivalent dipole based on the observations within or at the surface of the volume conductor [35].

As Figure 4.2 shown, a standard coordinate system in space is constructed by three leads that are represented by right-left axis (X), head-to-feet axis (Y) and front-back (anteroposterior) axis (Z). We can imagine that the resultant cardiac vector (dipole) corresponding to the magnitude and direction of the electrical pulses of the heart. If the resultant vector varies the magnitude and alters from zero amplitude to the maximum, then decreases back to zero magnitude, the tips of the vector with variable magnitude onto three mutually perpendicular coordinates should trace out a loop in space, which is the continuous vector loop of one cardiac cycle in mutually perpendicular planes. The projections of the vector loop on the different plane are shown in Figure 4.2. The projection on the frontal plane represents the changes in the X and Y axes throughout the cardiac cycle. Similarly the projection on the sagittal plane represents the variations in the Z and Y axes throughout the cardiac cycle. And the projection on the transverse plane, also called the horizontal plane, represents the variations in the X and Z coordinates throughout the cardiac cycle. As we discussed earlier, the frontal plane loop can be obtained by displaying the X and Y coordinates during the cardiac cycle. The sagittal and transverse loops can be obtained by adopting a similar approach, and the final results are shown in Figure 4.2.

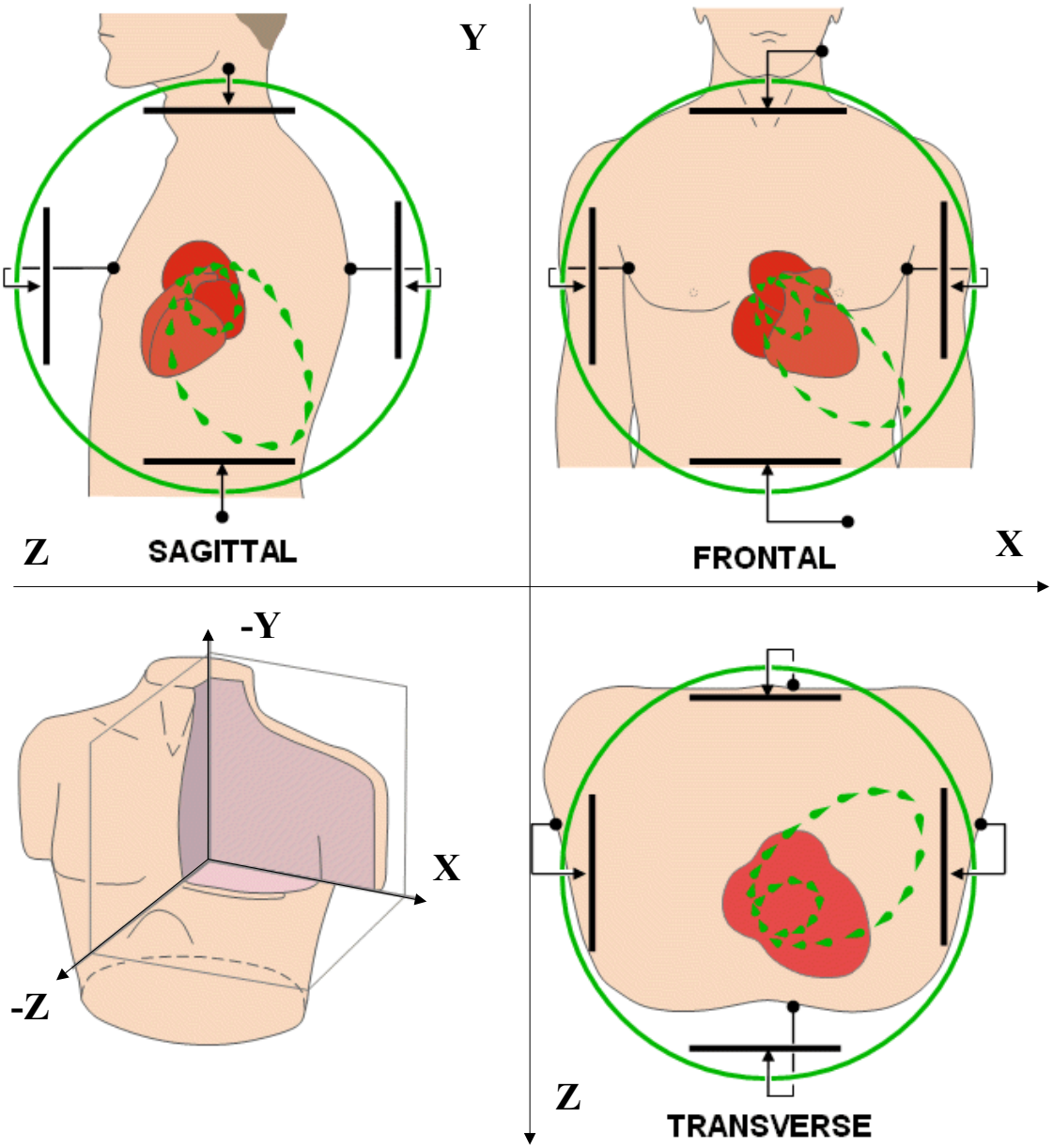

Figure 4.2 The basic of Vectorcardiography is illustrated the human body by three orthogonal leads and projected on the various planes from [86].

An inference that any pairs of leads can produce loops is acquired from or based on the above discussion of the theory of VCG. However, in reality the vector loop tends to another situation and is a straight line rather than a loop because such leads may have directions which are not well separate. It is undertaken to solve this problem in connection with the empirical study of the cardiac circle.

4.2.1. Bipolar Limb Leads

Einthoven introduced bipolar limb leads in [87] to measure the potential between two points on the human body. These three bipolar leads are illustrated as V_I, V_{II} and V_{III} presented mathematically as follows:

$$V_I = \phi_{LA} - \phi_{RA} \tag{4-12}$$

$$V_{II} = \phi_{LL} - \phi_{RA} \tag{4-13}$$

$$V_{III} = \phi_{LL} - \phi_{LA} \tag{4-14}$$

Where the notations ϕ_{LA}, ϕ_{RA} and ϕ_{LL} are the potential at the left arm, right arm and left leg respectively. Then expressed in terms of vector theory

$$\overline{c}_I \cdot \overline{p} = \overline{c}_{LA} \cdot \overline{p} - \overline{c}_{RA} \cdot \overline{p} \tag{4-15}$$

$$\overline{c}_{II} \cdot \overline{p} = \overline{c}_{LL} \cdot \overline{p} - \overline{c}_{RA} \cdot \overline{p} \tag{4-16}$$

$$\overline{c}_{III} \cdot \overline{p} = \overline{c}_{LL} \cdot \overline{p} - \overline{c}_{LA} \cdot \overline{p} \tag{4-17}$$

since dot product is distributive over scalar addition, the vector of lead I can be defined on account of unipolar limb leads of left arm (LA) and right arm (RA)

$$\overline{c}_I = \overline{c}_{LA} - \overline{c}_{RA} \tag{4-18}$$

The vector of lead II can be defined on account of lead vectors for unipolar limb leads of left leg (LL) and right arm (RA)

$$\overline{c}_{II} = \overline{c}_{LL} - \overline{c}_{RA} \tag{4-19}$$

The vector of lead III can be defined on account of lead vectors for unipolar limb leads of left leg (LL) and left arm (LA)

$$\overline{c}_{III} = \overline{c}_{LL} - \overline{c}_{LA} \tag{4-20}$$

From the above equations, it is easy to come to the conclusion that at any instant in the cardiac cycle, the following relationship between these three leads is as shown below

$$V_I + V_{III} = V_{II} \tag{4-21}$$

This is known as Einthoven's law, where the polarity of lead is reverse in Einthoven's triangle for uprighting QRS complexes.

4.2.2. Unipolar Limb Leads

Unipolar limb leads is to represent the potential variation in which the negative pole is a composite pole. The virtual 'Central Terminal' is introduced by Wilson et al [88]. The virtual lead is produced by connecting electrodes on each arms and the left leg. It seems as place an electrode in the center of the heart. It is assumed one artificial voltage representing average potential of the body. The value of the artificial voltage approximates the potential as zero but it should be noticed that this is incorrect.

$$\phi_W = \frac{1}{3}(\phi_{RA} + \phi_{LA} + \phi_{LL}) \tag{4-22}$$

then the potential V_P that means the potential of the arbitrary electrode P can be expressed as unipolar lead

$$V_P = \phi_P - \phi_W = \phi_P - \frac{1}{3}(\phi_{RA} + \phi_{LA} + \phi_{LL}) \tag{4-23}$$

Wilson's central terminal is the average of potentials and then it can be considered to what independent of other potentials in particular and therefore a satisfactory reference potential. The term of unipolar lead indicates that the potential of the central terminal is relatively constant and only the potential variations of the exploring electrode are recorded. The results of clinical applications demonstrate the central terminal potential keeps consistent in practice. In fact, it is unnecessary to consider the effect of the central terminal for actual calculation of potential since the influences in the unipolar lead cancel each other out. Only consequence may be the baseline turbulence by the central terminal. It can be reduced by the technique or algorithm developed for removing. Frank had investigated the variation of the central terminal potential in his writings [89]. From the conclusions, the average of maximal deviation of the Wilson terminal voltage would be 0.14mv under ideal conditions, which implies the electrical potential difference measured between the central terminal and the exploring electrode regardless of location.

It is easy to obtain the following equation that

$$V_{RA} + V_{LA} + V_{LL} = 0 \tag{4-24}$$

4.2.3. Augmented Unipolar Limb Leads

Unipolar limb leads are derived from the similar procedure as the above introduction. It also measures the potential difference between two electrodes, but the negative electrode is a modification of Wilson's central terminal. The new central terminal is calculated by the average of the potentials at the right arm and the left leg. Mathematically, the potential of modified V_{RA} is expressed as

$$\begin{aligned} aVR &= \phi_{RA} - \frac{1}{2}(\phi_{LA} + \phi_{LL}) \\ &= \frac{3}{2}\phi_{RA} - \frac{1}{2}(\phi_{RA} + \phi_{LA} + \phi_{LL}) \\ &= \frac{3}{2}(\phi_{RA} - \frac{1}{3}\phi_W) = \frac{3}{2}V_{RA} \end{aligned} \tag{4-25}$$

Similar considerations are applied to calculate the potentials of the other augmented limb leads as aVL and aVF.

$$aVL = \frac{3}{2}V_{LA} \tag{4-26}$$

$$aVF = \frac{3}{2}V_{LL} \tag{4-27}$$

It seems that every modified limb lead increases the potential by 50%.

$$aVR + aVL + aVF = 0 \tag{4-28}$$

4.2.4. Unipolar Chest Leads

For measuring the potentials close to the heart precordial leads (chest leads) are introduced by Wilson, which are labeled and placed on the patient's body as depict in Figure 4.3. The received signal of the electrode is a composite of electrical signal from the other electrodes. The transverse plane is also considered as horizontal plane (HP). The six unipolar precordial leads named V_1 to V_6 derived from an electrode measured with reference to the 'Wilson Central Terminal' (WCT).

V_1: located at the 4th intercostal space on the right, two spaces below the sternal angle.

V_2: located at the 4th intercostal space on the left, parallel on opposite side of the sternal angle.

V_3: found between V_2 and V_4.

V_4: left 5th intercostal space at the midclavicular line.

V_5: located between V_4 and V_6, and even horizontally with V_4.

V_6: located at the same horizontal level as V_4 and V_5, but at the left 5th intercostal space.

Because the leads V_2 and V_3 are close to the heart. They have the very high sensitivities of the electrical forces in the transverse plane. Compared with the other leads, they must enhance the form of vector lead. If we choose four points to locate the electrodes, as V_1, V_2, V_4 and V_5. As depicted as E. Frank, precordial leads are projected onto the transverse plane. The finite and homogeneous torso model is used in calculating the lead vectors [90].

4.2.5. 12-lead ECG relationship

12 lead system is a representation of the electrical activity in the heart recorded from leads including bipolar limb leads I, II and III, augmented unipolar limb leads aVR, aVL and aVF, and six unipolar precordial precordial leads $V_1 - V_6$. Limb leads are closely related as mentioned in the above contents of bipolar and unipolar. It is obvious in mathematically

$$aVR = -\frac{1}{2}(I + II) \tag{4-29}$$

$$aVL = I - \frac{1}{2}II \tag{4-30}$$

$$aVF = II - \frac{1}{2}I \tag{4-31}$$

Because bipolar limb leads I, II and III, augmented unipolar limb leads aVR, aVL and aVF are derived from the same measurement points. So these six leads are redundant and any two among them hold exactly the same information as the other four leads one. It suggests us to use an alternative strategy that adopts leads I and aVF to present the others. The following equations show the relationships between these leads

$$\mathrm{II} = \mathrm{aVF} + \frac{1}{2}\mathrm{I} \tag{4-32}$$

$$\mathrm{III} = \mathrm{aVF} - \frac{1}{2}\mathrm{I} \tag{4-33}$$

$$\mathrm{aVR} = -(\frac{3}{4}\mathrm{I} + \frac{1}{2}\mathrm{aVF}) \tag{4-34}$$

$$\mathrm{aVL} = \frac{3}{4}\mathrm{I} - \frac{1}{2}\mathrm{aVF} \tag{4-35}$$

These equations actually point out a method to only store two of limb leads to save space without loss of information. And the remaining four can be derived from the relationships between these leads. The benefit of this method is to save one third of the data necessary in terms of long-term application, where it is only necessary to measure the eight independent leads among 12 leads and the remaining four being calculated by them. However, in practice this method sometimes creates considerable misunderstanding. The reason for this paradox is because the equations described above do not take into account the difference in the size and body habitus. Whether in the idealized concept of Einthoven triangle and the Burger triangle, the electrical equivalent of human body is described with a dipole source model. The author in [91] indicated that a dipole source model is a feasible method to explain at least 90% of the heart's electric activity. Precordial leads are important to detect non-dipolar components, which are the evidence of clinical effects. The extra advantage of precordial leads is to provide diagnostic significance because they are located close to the heart. In these precordial leads, the lead V_2 is a good choice since it is located closer to the heart area than the others. So the 12-lead ECG system could be considered to consist of nine redundant leads and three independent leads, which include two independent leads of the limb leads and one independent lead of precordial leads.

In summary, the theoretical model needs to be experimentally tested and the description of the electrical equivalent of human body is more precise. In addition the equations described need to more match the empirical standpoint and are thus independent of body size and body habitus.

In mathematical terms, all observed leads can be constructed from a linear combination of the given XYZ basis of orthogonal space coordinates.

$$\phi_{lead} = aX + bY + cZ \tag{4-36}$$

where X, Y and Z express the value of each orthogonal leads respectively and a, b, c are fix coefficients that are inferred from the theory of image space introduced by Ernest Frank. In practice the number of electrodes for the monitoring situation may be reduced to the actual requirement. The information of the heart as the traditional system can be obtained with the remaining leads.

The principle of the method is to consider the human body as a three dimensional structure. The three orthogonal vector leads are constructed to present the electrical activity in the heart. Frank's method is to make a VCG directly projected onto three cardiac planes: frontal, horizontal and sagittal. The same electric episodes that are simultaneously recorded over two orthogonal axes constitute one projection. Because we use precordial leads to measure the potential of the surface close to the heart. It has to be developed to record simultaneous episodes on axes X and Y as they transverse the horizontal plane. There is a proposed method that attempts to synthesize the VCG from the 12 lead ECG. The authors introduce a feasible way to use inverse Dower transformation in [35]. As mentioned above, the method calculates the axes of various weighted features of the VCG leads using fix coefficients which are determined by the study of Frank's image space. The transformation matrix to derive the eight independent leads among the 12 lead ECG is given as

$$s(n) = Dv(n) \tag{4-37}$$

$$D = \begin{bmatrix} -0.515 & 0.157 & -0.917 \\ 0.044 & 0.164 & -1.387 \\ 0.882 & 0.098 & -1.277 \\ 1.213 & 0.127 & -0.601 \\ 1.125 & 0.127 & -0.086 \\ 0.831 & 0.076 & 0.230 \\ 0.632 & -0.235 & 0.059 \\ 0.235 & 1.066 & -0.132 \end{bmatrix} \tag{4-38}$$

where $s(n) = [V_1(n), V_2(n), V_3(n), V_4(n), V_5(n), V_6(n), (n), (n)]^T$ and $v(n) = [X(n), Y(n), Z(n)]^T$. D is called the Dower transformation matrix. So we can obtain the inverse Dower transformation matrix T to synthesize the VCG leads from the ECG data

$$T = (D^T D)^{-1} D^T \tag{4-39}$$

The author gives three expressions to calculate three orthogonal leads X, Y and Z of Frank's system using the standard leads system [92].

$$X = -(-0.172\,V_1 - 0.074\,V_2 + 0.122\,V_3 + 0.231\,V_4 + 0.239\,V_5 + 0.194\,V_6 + 0.156\,\mathrm{I} - 0.010\,\mathrm{II}) \tag{4-40}$$

$$Y = (0.057\,V_1 - 0.019\,V_2 - 0.106\,V_3 - 0.022\,V_4 + 0.041\,V_5 + 0.048\,V_6 - 0.227\,\mathrm{I} + 0.887\,\mathrm{II}) \tag{4-41}$$

$$\mathrm{Z} = -(-0.229\,V_1 - 0.310\,V_2 - 0.246\,V_3 - 0.063\,V_4 + 0.055\,V_5 + 0.108\,V_6 + 0.022\,\mathrm{I} + 0.102\,\mathrm{II}) \tag{4-42}$$

Thus it is possible to have the instantaneous cardiac vector from these above scalar coordinates.

The transformation matrix is not the only because some of the leads are redundant. Uijen et al [93], derived their own transfer matrix where the leads aVR and aVL are specified rather than I and II.

$$X = -(-0.01\,V_1 + 0.04\,V_2 + 0.04\,V_3 + 0.05\,V_4 + 0.07\,V_5 + 0.37\,V_6 - 0.52\mathrm{aVR} + 0.82\,\mathrm{aVL}) \tag{4-43}$$

$$Y = (0.03\,V_1 - 0.02\,V_2 - 0.02\,V_3 + 0.03\,V_4 - 0.07\,V_5 + 0.08\,V_6 - 1.53\text{aVR}1.09\text{ aVL}) \quad (4\text{-}44)$$

$$Z = -(-0.26\,V_1 - 0.28\,V_2 - 0.14\,V_3 + 0.04\,V_4 - 0.15\,V_5 + 0.34\,V_6 + 0.43\text{ aVR}0.01\text{ aVL}) \quad (4\text{-}45)$$

Willems also drew up similar results by adopting the same approach [94]. He used the leads II and instead of I and II. There is obvious difference between actual XYZ leads and derived XYZ leads which are available in the CSE study. Willems made a conclusion that the optimum comparison between different leads system is given by these scaling coefficients [95].

$$X = -(-1.27\,V_1 - 0.55\,V_2 + 0.72\,V_3 + 1.86\,V_4 + 1.92\,V_5 + 1.53\,V_6 + 0.58\text{ II} - 0.82\text{ III}) \quad (4\text{-}46)$$

$$Y = (-0.71\,V_1 - 0.71\,V_2 + 0.10\,V_3 + 0.35\,V_4 + 0.12\,V_5 - 0.15\,V_6 + 2.58\text{ II} + 3.04\text{ III}) \quad (4\text{-}47)$$

$$Z = -(-1.71\,V_1 - 2.26\,V_2 - 2.02\,V_3 - 0.80\,V_4 + 0.31\,V_5 + 0.97\,V_6 - 0.80\text{ II} - 1.62\text{ III}) \quad (4\text{-}48)$$

And similarly, the X, Y and Z leads in children were calculated by using a set of coefficients deduced from the publication of Edenbrandt and Macfarlane [96]. Not like those above formulas, there is not the coefficients for V_3 but be replaced by the coefficients for V_{4R} that are new concepts and obtained (-0.537, 0.096, -0.272) in the 12-lead ECG derivation of Dower.

Although the VCG axis is developed for the recordings of three orthogonal leads, it can still follow the same principle on the horizontal plane when only two orthogonal axes are available.

As discussed earlier, the model of Vectorcardiography (VCG) is based on the assumptions that the infinite homogeneous volume conductor is valid and a dipole has a variable magnitude but on a fixed location. In clinic, it is hard to achieve these assumptions and therefore the ECG signals from the ideal signal deduced from VCG.

The standard 12-lead ECG system is discussed here in detail. Figure 4.2 illustrates that the ECG could be considered as the locus of the tip of the vectors. Three loops represent the position of all the instantaneous vectors during cardiac depolarization for the P wave, QRS complex and T wave. Electrical activity in ventricles is represented by the morphology of QRS loop, which includes the important information to diagnose cardiac arrhythmias.

4.3. Signal model

It is possible to describe the activity inside the heart based on corrected orthogonal leads XYZ to a volume conductor for the simultaneously recorded measurements. The locations of the six precordial leads are shown in the left subplot of Figure 4.3, and an idealized

description of the directions associated four precordial leads is shown in the right subplot of Figure 4.3. The lead directions of V_1, V_2, V_4 and V_5 are derived from the model of Frank image surface, where the direction means that the component of the resultant cardiac electrical force is measured and the amplitude means that the leads have different sensitivity [97]. It is obvious that V_2 has a higher sensitivity because it is closer to the heart. All the modified leads originate from an imaginary center of the heart that is also known as the Wilson central terminal. The loops arranged in decreasing order of the size are QRS loop, T loop and P loop. It should be noted that the length of each lead vector indicates the sensitivity of leads $V_1 - V_6$ [98].

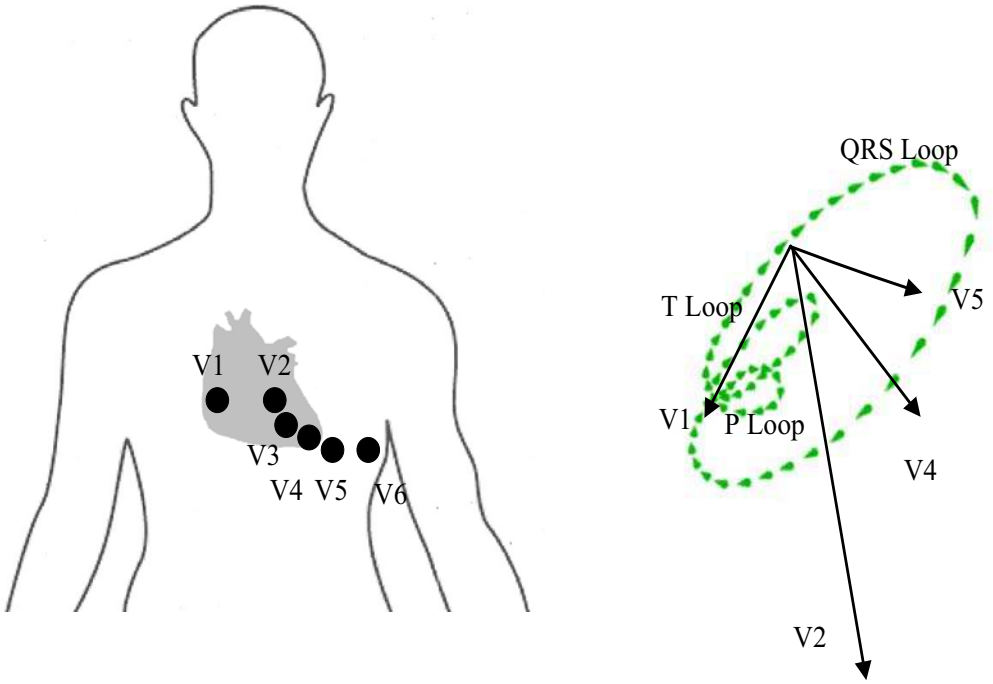

Figure 4.3 The lead vectors in a finite, homogeneous torso model calculated from the model of Hyttinen.

The procedures of the electrical currents generated in the heart reflect a P wave, a QRS complex and a T wave in ECG during one cardiac cycle. As we discussed in the previous chapters, the QRS complex is more important for diagnostic purposes for body surface ECG. The electrical activity associated with the QRS complex can be represented by a vector circumrotated surround a fixed position which is considered as the center of the heart. This vector is given as a function of time, so this way of presenting the vector is the parametric of the locus of QRS loop. On the HP, the vector draws a locus presenting QRS loop during each cardiac cycle.

There are 3 important points:

1 the tangent line to the locus of vector of QRS loop. In first half of the QRS loop, which gives a point presenting the R wave

2 the tangent line to the locus of vector of QRS loop. In last half of the QRS loop, which gives a point presenting the S wave

3 the vector of QRS loop is orthogonal to lead vector, which gives a point presenting the ECG signal crossing the baseline.

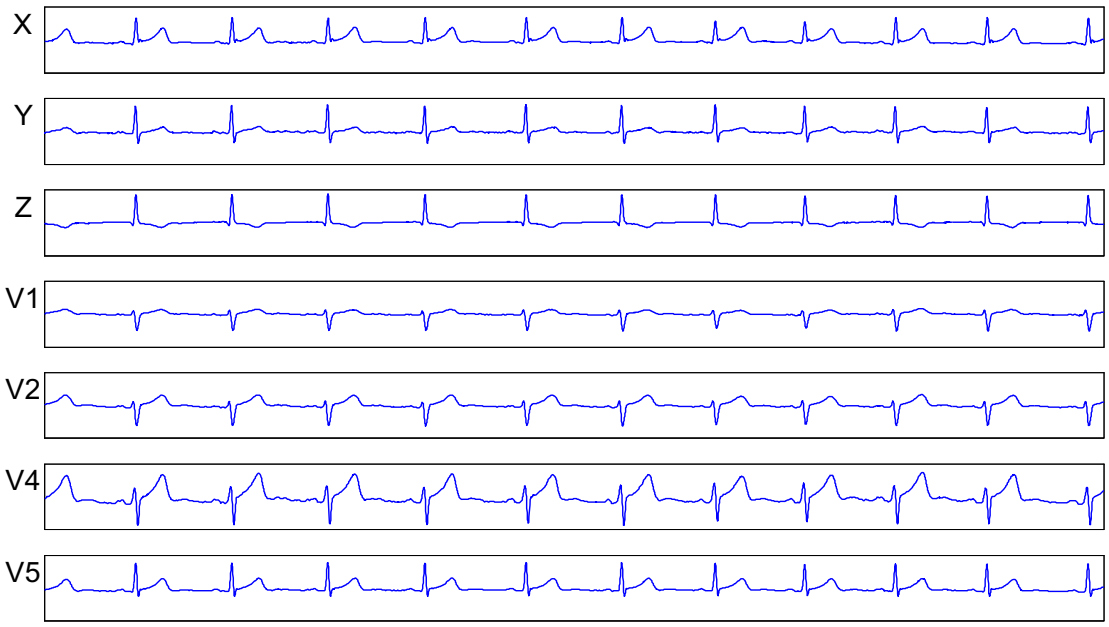

Figure 4.4 The three VCG leads X, Y and Z. These body surface potentials can be depicted by graphical recording as a function of time, V_1, V_2, V_4 and V_5, (a) The VCG lead X, (b) The VCG lead Y, (c) The VCG lead Z, (d) Recorded ECG signal of V_1, (e) Recorded ECG signal of V_2, (f) Recorded ECG signal of V_4, (g) Recorded ECG signal of V_5.

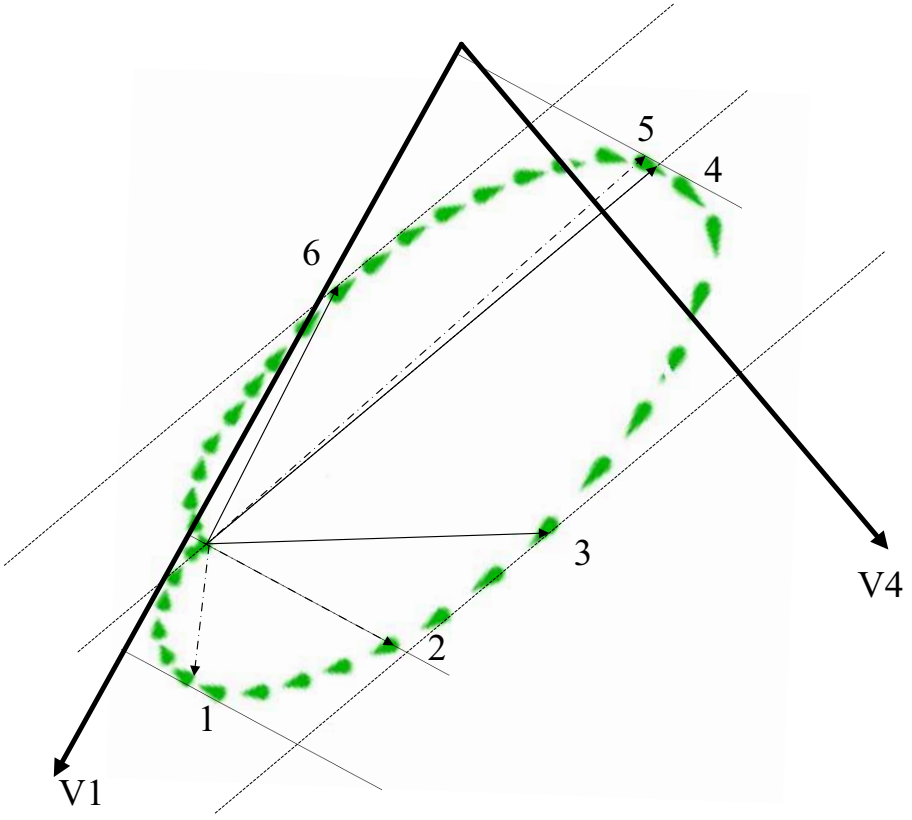

Figure 4.5 QRS loop based on the ECG signals of V_1, V_2, V_4 and V_5. There are 6 important points relative the lead vector V_1 and V_4.

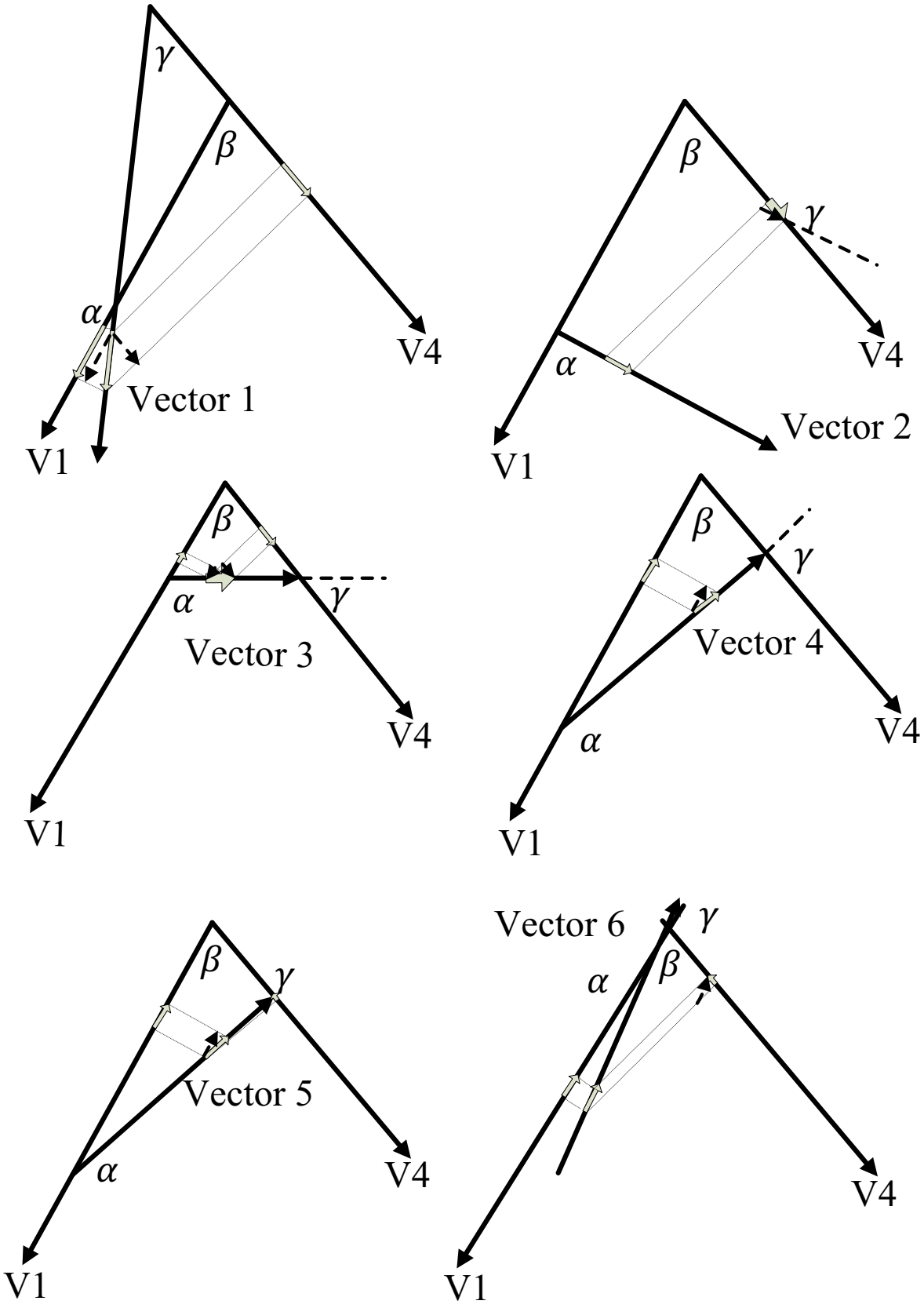

Figure 4.6 The normal sequence of ventricular depolarization.

The model is constructed based on the principle of Einthoven-Wilson model that equivalent, stationary dipole located in the center of the heart. But actually the heart is not in the center of this equilateral triangle, moreover, the body of human is not exactly in homogeneous electric fields. The electrical field of the heart changes its direction and intensity in time. The projection on the transverse (horizontal) plane represents the variation in the axis X and Z coordinates. It is simple to plot one cardiac circle along the X coordinate and Z coordinate to form the transverse plane loop as follows QRS loop based on the ECG signals of V_1, V_2, V_4 and V_5. There are 6 important points relative to the lead vector V_1 and V_4 [99].

α is an angle of vector and lead vector 1, β is an angle of lead vector 1 and lead vector 4, γ is an angle of vector and lead vector 4, the amplitude of the vector is ℓ_0, the amplitude of the lead vector V_1 is ℓ_1, the amplitude of the lead vector V_4 is ℓ_4. The scalar amplitudes of one pair of leads parallel to the X and Z axes provides the information in the small number of QRS complex. Figure 4.6 shows the relationship between the leads of ECG signal and VCG. It is possible to mathematically construct a vector loop from knowledge of the ECG signal.

Point 1 means the ECG waveform at V_1 reach R wave, the loop is inscribed counterclockwise

$$\ell_1 = cos(\alpha_{1,pre})\ell_0 \tag{4-49}$$

$$\ell_4 = cos(\gamma)\ell_0 = cos(\alpha_{1,pre} - \beta)\ell_0 \tag{4-50}$$

and $\gamma = \alpha - \beta$

so

$$\ell_1 = \frac{cos\ (\alpha)}{cos(\gamma)}\ell_4 = \frac{cos\ (\alpha_{1,pre})}{cos(\alpha_{1,pre} - \beta)}\ell_4 \tag{4-51}$$

Because cosine function is monotonic in the interval of $[0, \pi]$, $cos\ (\beta - \alpha)$ and cosα are positive. It means the amplitude of V_1 and V_4 direct positive.

Point 2 means the ECG waveform at V_1 reach back to baseline, $\alpha = \pi/2$, and $\gamma = \pi/2 - \beta$

$$\ell_1 = cos(\alpha)\ell_0 = 0 \tag{4-52}$$

$$\ell_4 = cos(\gamma)\ell_0 = cos(\pi/2 - \beta)\ell_0 = sin\ (\beta)\ell_0 \tag{4-53}$$

Point 3 means the ECG waveform at V_4 reach R wave, $\gamma = \pi - \alpha + \beta = \alpha_{2,pre}$ so $\alpha = \pi - \alpha_{2,pre} + \beta$.

$$\ell_1 = cos(\pi - \alpha)\ell_0 = cos(\alpha_{2,pre} - \beta)\ell_0 \tag{4-54}$$

$$\ell_4 = cos(\gamma)\ell_0 = cos(\pi - \alpha + \beta)\ell_0 = cos(\alpha_{2,pre})\ell_0 \tag{4-55}$$

$$\ell_1 = \frac{cos\ (\pi - \alpha)}{cos(\gamma)}\ell_4 = \frac{cos(\alpha_{2,pre} - \beta)}{cos(\alpha_{2,pre})}\ell_4 \tag{4-56}$$

Point 4 means the ECG waveform at V_1 reach back to baseline, $\gamma = \pi/2$

$$\ell_1 = cos(\pi - \alpha)\ell_0 = -cos(\alpha)\ell_0 \tag{4-57}$$

$$\ell_4 = cos(\gamma)\ell_0 = 0 \tag{4-58}$$

Point 5 means the ECG waveform at V_1 reach Q wave, $\alpha = \alpha_{1,post}$, $\gamma = \pi - \alpha + \beta$

$$\ell_1 = cos(\pi - \alpha)\ell_0 = cos(\pi - \alpha_{1,post})\ell_0 = -cos(\alpha_{1,post})\ell_0 \tag{4-59}$$

$$\ell_4 = cos(\gamma)\ell_0 = cos(\pi - \alpha_{1,post} + \beta)\ell_0 = -cos(\alpha_{1,post} - \beta)\ell_0 \tag{4-60}$$

$$\ell_1 = \frac{cos(\pi - \alpha)}{cos(\gamma)}\ell_4 = \frac{cos(\alpha_{1,post})}{cos(\alpha_{1,post} - \beta)}\ell_4 \tag{4-61}$$

Point 6 means the ECG waveform at V_4 reach Q wave, $\gamma = \beta - (\alpha - \pi) = \alpha_{2,post}$ so $\alpha = \pi + \beta - \alpha_{2,post}$

$$\ell_1 = cos(\alpha - \pi)\ell_0 = cos(\alpha_{2,post} - \beta)\ell_0 \tag{4-62}$$

$$\ell_4 = cos(\gamma)\ell_0 = cos(\alpha_{2,post})\ell_0 \tag{4-63}$$

$$\ell_1 = \frac{cos(\alpha - \pi)}{cos(\gamma)}\ell_4 = \frac{cos(\alpha_{2,post} - \beta)}{cos(\alpha_{2,post})}\ell_4 \tag{4-64}$$

Table 4.1 Deviation from transverse plane

	V_1	V_4
1	$\cos(\alpha_{1,\mathrm{pre}})$	$\cos(\alpha_{1,\mathrm{pre}} - \beta)$
2	0	$\sin(\beta)$
3	$\cos(\alpha_{2,\mathrm{pre}} - \beta)$	$\cos(\alpha_{2,\mathrm{pre}})$
4	$-\cos(\alpha)$	0
5	$\cos(\alpha_{1,\mathrm{post}})$	$\cos(\alpha_{1,\mathrm{post}} - \beta)$
6	$\cos(\alpha_{2,\mathrm{post}} - \beta)$	$\cos(\alpha_{2,\mathrm{post}})$

As shown in Table 4.1, we can construct a VCG in the horizontal plane. The locus of the vector loop is given by the measurements simultaneously recorded along X and Z leads. The vector 1 illustrates the electric activity of the ventricular depolarization. Because it starts from the left ventricular septum, therefore the resultant vector points to the right, the angle α is a sharp corner. The projection of the resultant vector 1 on the vector leads of V_1 and V_4 is positive so the detected ECG signals on position V_1 and V_4 are also positive as shown in Figure 4.8. The next phase is the occurrence of depolarization procedures generated on both sides of the heart, and the effects of their electric activities gradually fade until the locus of the QRS loop reaches the location of the vector 2. The amplitude of the QRS complex of ECG signal at location V_1 is close to zero, back to the baseline, suggesting that the wave of depolarization passes through the heart in one direction that has no component in the same direction on the vector lead V_1. The next course is to propagate the depolarization front from the right ventricle to the left ventricular wall. And after a while the resultant vector reaches

the maximum pointing to the left because there is no depolarization generated on the right side. The amplitude of the resultant vector decreases because the depolarization is back to both left and right ventricular region. When all propagating activation front is finished, there is no signal either. The QRS loop is almost always inscribed in a counterclockwise direction in this plane.

It is easy to obtain the same conclusion from the above figure, where at first the direction of the vector presents the direction of vectors within the heart is similar to the direction of lead vector. Then the magnitude of recorded measurements of that lead vector increase because a positive deflection. Since the leads V_1 and V_4 are facing forward, the waveform of recorded ECG signals are increased from the baseline and positive value. Then the resultant vector moves from the right towards the left, leads V_1 and V_4 would produce a negative deflection, the amplitude tends to decrease towards the baseline and to maximum negative value in the end. When the depolarization is back to basal regions of both left and right ventricles the amplitude of waveform tend back to the baseline.

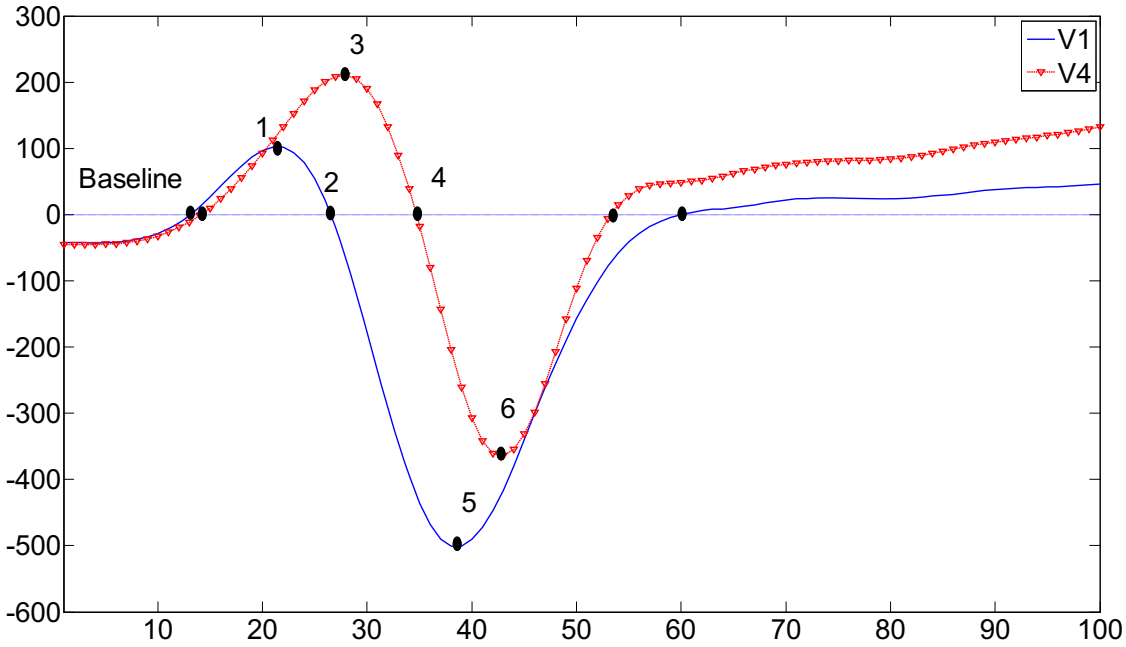

Figure 4.7 Derivation of the ECG signals of V_1 and V_4 from the transverse plane loop. Dots are several key points.

4.3.1. VCG Alignment Algorithm

While using ambulatory ECG system as Holter to monitor the patients' heart activity in hospital or clinic, it is desirable that this system record a long duration of 24 hours of ECG data without interfering their daily activities. Technologists in practice tend to design a monitoring system with a limited number of leads. At first a theoretical method is used to evaluate the source of the electrical pulse from measurements [100].

It can be assumed that there are the effects of the rotation between successive VCG loops and reference loop. The author introduced a method for deriving the rotation angles of the

vector axis around three-dimensional orthogonal axes based on the analysis of the LS estimation [101]. As the above mentioned contents, E. Frank has developed a VCG model in the early 30's.

E. Frank introduced QRS-VCG alignment EDR algorithm based on the observation that the QRS loop morphology remains the elementary element, whereas the actual recorded signals is the time variation of a periodic signal. The difference of successive VCG loops is resulting from the changes in space orientation depended in the phase that they occur in one heart circle. The VCG loop of the QRS complex of the observed signals are expressed as Z, as a $3 \times N$ matrix. The reference loop Z_r is $3 \times (N + 2\Delta)$ and has 2Δ additional samples in order to allow for Z_r with different time intervals can be aligned to the observed loop Z [102, 103]. A normalized distance ε is defined as

$$\varepsilon_{min} = \min_{\alpha,Q,\tau} \frac{\|Z - \alpha Q Z_r J_\tau\|_F^2}{\|\alpha Q Z_r J_\tau\|_F^2} \tag{4-65}$$

where α is the scalar amplitude factor, Q is the rotation matrix and J_τ is the time shift matrix. The final alignment is determined by these three transformations.

The Frobenius norm is defined by

$$\|X\|_F^2 = \sum_{i=1}^{M} \sum_{j=1}^{N} |x_{ij}|^2 \tag{4-66}$$

The integer N denotes the length of samples that contains one QRS complex, M is the number of dimensions of coordinate system in which the vector leads are projected. The rotation matrix Q is orthogonal, so $QQ^T = I$, where I is the unit matrix. The introduction of the time shift matrix J_τ may help ensure the two loops are temporally well-aligned by increasing redundancy 2Δ.

$$J_\tau = [0_{\Delta+\tau} \quad I \quad 0_{\Delta-\tau}] \tag{4-67}$$

The dimensions of the unit matrix I is $N \times N$, and shift matrixes $0_{\Delta+\tau}$, and $0_{\Delta-\tau}$ are $N \times (\Delta + \tau)$ and $N \times (\Delta - \tau)$ respectively.

The first step to solve the alignment is to estimate α and Q for every value of τ based on the criteria that the normalized distance ε is minimal. Then reselection of τ for which ε is minimum. So Q is fixed by the optimal estimator as follows

$$\hat{Q}_\tau = U_\tau V_\tau^T \tag{4-68}$$

where the matrixes U_τ and V_τ^T are the results of singular value decomposition of the matrix $D_\tau = Z J_\tau^T Z_r^T$. The matrixes are containing the left and right singular vectors respectively. When the estimator of Q is identified to $\hat{Q}_\tau$, the scalar α also has an estimator obtained by

$$\hat{\alpha}_\tau = \frac{tr(Z^T Z)}{tr(Z^T \hat{Q}_\tau Z_r J_\tau)} \tag{4-69}$$

finally, estimator of the minimum distance ε_{min} is obtained by repeating the procedure that τ is selected all values within the interval $-\Delta \leq \tau \leq \Delta$. It should be noted that the value of selected τ could subject to the following expression

$$\hat{\tau} = arg \min_{-\Delta \le \tau \le \Delta} \frac{\left\| Z - \hat{\alpha}_\tau \hat{Q}_\tau Z_r J_\tau \right\|_F^2}{\left\| \hat{\alpha}_\tau \hat{Q}_\tau Z_r J_\tau \right\|_F^2} \tag{4-70}$$

The rotation matrix Q in three dimensional system has the rotation angles $\emptyset_x$, $\emptyset_y$, and $\emptyset_z$, which could be considered as three successive rotations around each axis (lead).

$$\begin{aligned} Q &= \begin{bmatrix} 1 & 0 & 0 \\ 0 & cos\,\emptyset_x & sin\,\emptyset_x \\ 0 & -sin\,\emptyset_x & cos\,\emptyset_x \end{bmatrix} \begin{bmatrix} cos\,\emptyset_y & 0 & sin\,\emptyset_y \\ 0 & 1 & 0 \\ -sin\,\emptyset_y & 0 & cos\,\emptyset_y \end{bmatrix} \begin{bmatrix} cos\,\emptyset_z & sin\,\emptyset_z & 0 \\ -sin\,\emptyset_z & cos\,\emptyset_z & 0 \\ 0 & 0 & 1 \end{bmatrix} \\ &= \begin{bmatrix} * & sin\,\emptyset_z\,cos\,\emptyset_y & sin\,\emptyset_y \\ * & * & sin\,\emptyset_x\,cos\,\emptyset_y \\ * & * & * \end{bmatrix} \end{aligned} \tag{4-71}$$

where the asterisk $*$ denotes an omitted matrix entry. The estimates of rotation angles can be obtained by identifying all the different elements in the above equation to find the proper elements of Q. The identification yields the following estimates:

$$\hat{\emptyset}_y = arc\sin \hat{Q}_\tau(1,3) \tag{4-72}$$

$$\hat{\emptyset}_x = arc\sin \frac{\hat{Q}_\tau(2,3)}{\cos \hat{\emptyset}_y} \tag{4-73}$$

$$\hat{\emptyset}_z = arc\sin \frac{\hat{Q}_\tau(1,2)}{\cos \hat{\emptyset}_y} \tag{4-74}$$

The effect of rotation angles and time synchronization is studied by means of performance measure in relation to the reference loop. This measure procedure can be defined as

$$\varsigma_{\hat{z}}^2 = \left\| \hat{Z} - Z_r \right\|_F^2 \tag{4-75}$$

where it measures sample-to-sample morphologic variability after loop alignment. The below figure reflects morphologic variability before and after alignment. The same reference loops are plotted as a solid line. In the Figure 4.8(a), the morphologic variability is mainly due to time unsynchronization. The variabilities of rotation angles in the leads X and Y affect not only the morphology of the estimated QRS complex but also the degree of deviation. On the other hand the variability of rotation angle in the leads Z has more influence to the amplitude than the degree of deviation. This is because the model is constructed on the transverse plane mainly based on the precordial leads. It is obvious that the estimation of the model is lack of sufficient information of the leads Z of VCG.

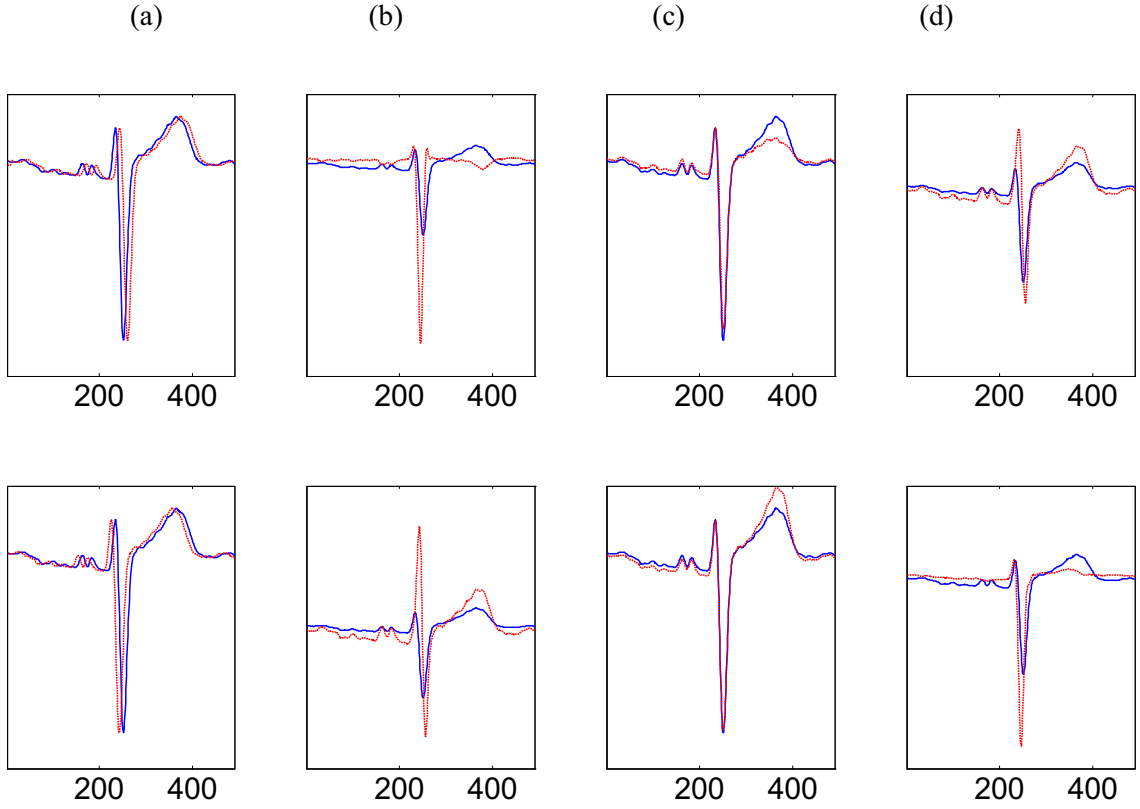

Figure 4.8 Morphologic variability. The reference loop is indicated with a solid line, the superimposed signal is indicated with a dotted line. (a) With the integer time shift ±*2 ms* that means the part of QRS of signal is not synchronized with the reference loop, the time shift is ±*4 ms*, (b) After rotation around the *X*-axis (Φ_x=±15^O), (c) After rotation around the *Y*-axis (Φ_y=±15^O), (d) After rotation around the *Z*-axis (Φ_z=±15^O).

The reference loop is derived from the first 5 successive QRS loops. Then the loop alignment technique is used to process the ECG signal based on the reference QRS loop. Figure 4.9 displays the estimated rotation angles and variable magnitude of the VCG leads as well as the standard V_1 signal. It is easy to conclude that changes are relatively small in the direction of the electrical axis for successive beats with similar morphologies. Authors in [104] cited the conclusion that angle fluctuations is in the range of $\pm 15^{o}$. Author indicates that the rotation matrix is diagonally dominant in this range of angles but higher ECG noise levels will destruct the diagonal structure of the rotation matrix Q. If Q maintains the symmetrical structure with the small noise, the values of three identical rotation angles do not exceed 26.7^{o}. However the actual ECG signals are affected by a series of impacts as short term oscillation due to respiratory activity and muscular noise, and other factors to make the ECG signals dramatically change. The rotation angles of $\widehat{\emptyset}_x$ and $\widehat{\emptyset}_z$ do not change very dramatic, only in the scope of $\pm 5^{o}$, but $\widehat{\emptyset}_y$ changes in the larger range, around $\pm 50^{o}$. In most of the duration, $\widehat{\emptyset}_y$ changes also in the range of $\pm 5^{o}$, but in some QRS loops, it jumps to $\pm 50^{o}$.

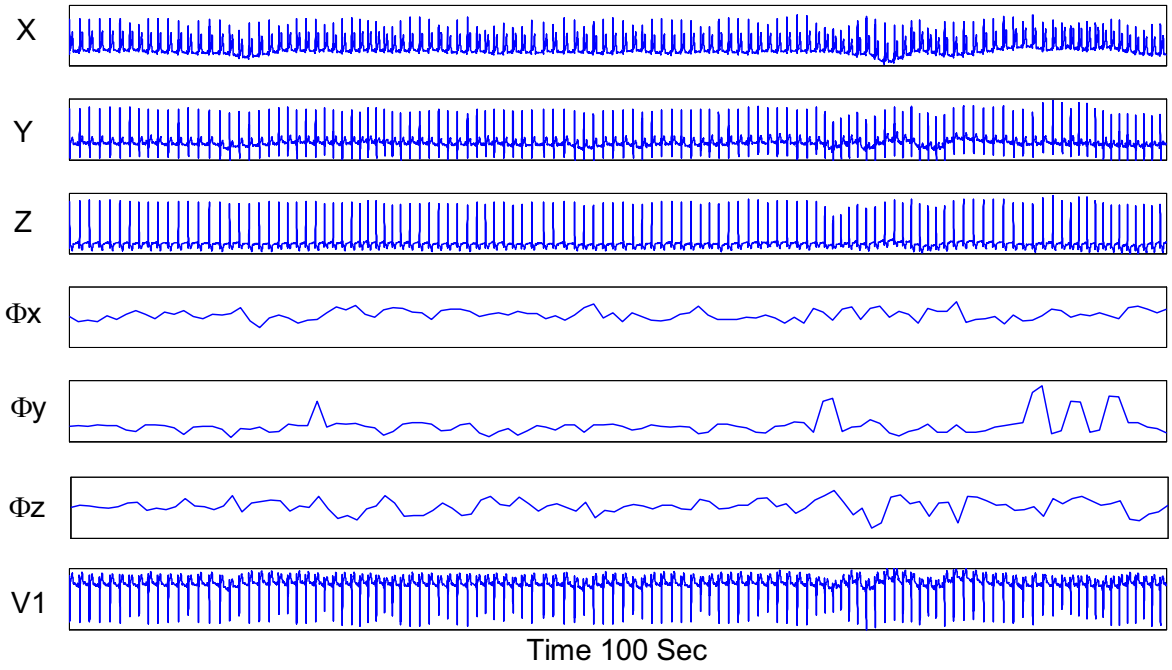

Figure 4.9 Example of estimated rotation angles $\widehat{\emptyset}_x$, $\widehat{\emptyset}_y$ and $\widehat{\emptyset}_z$ using QRS-VCG loop alignment algorithm. The VCG signals and the estimated rotation angles are shown following the order from top to bottom. The bottom graph is the actual recorded signal on the position of V_1.

4.4. Simulation

All ECG data are gathered using two wearable ECG sensors each with the same factor. One sensor 'A' acquires four leads simultaneously, converts analog signal into digital data at a rate of 500 samples per second for the purpose of further analysis, where the voltage or voltage difference between actual body surface and a special reference electrode fixed on the neck. The wearable sensor 'A' contains three channels ambulatory ECG recordings with the standard form. The wearable sensor 'B' acquires three leads simultaneously as the same process, but the reference electrode fixed on the position of the precordial leads. So we determine the terminology required to a clear understanding of the signal. The voltage between actual body surface and the special reference electrode fixed on the neck is called standard voltage of actual body surface, or simply as the voltage. The voltage between actual body surface and the reference electrode fixed on the position of the precordial leads is called the voltage difference. Note that the voltage difference measured between two electrodes in close proximity, determining the voltage difference has some special characteristics.

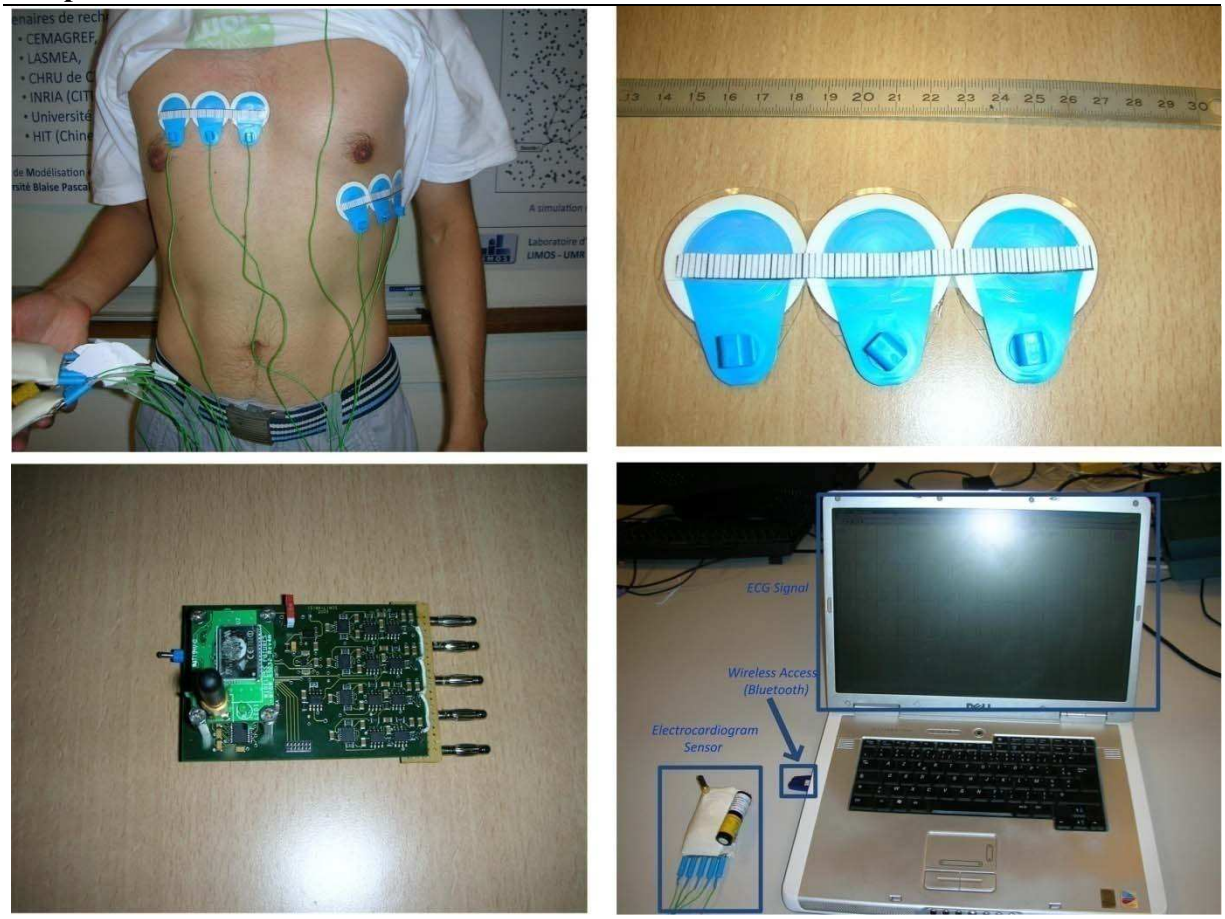

Figure 4.10 (top-left) The volunteer with ECG recording and WES, (top right) ECG electrode, (bottom-left) A wearable ECG sensor with real time measurement and wireless medium (Bluetooth), (bottom-right) Real time display of measurements of the electrocardiogram.

A standard voltage of V_1 is depicted in the subplot on the top of the figure. The adjacent electrodes are placed on its left V_1' and right V_1'' , parallel with V_2. Then there are 6 subplots below, which are the voltage of two locations adjacent to V_1 and the voltage difference between V_1 and its neighbors, further more detailed description of QRS complex. It is obvious that the ECG signals of next locations of V_1 have the approximate morphology as V_1, in addition to different amplitude range. The voltage differences shown on the right subplots display the similar property. The number of the subplots on the Figure 4.11 follows the order from top to bottom and from left to right.

The recorded ECG signals from the electrode located close to V_1 have similar morphology but different amplitude. The recorded ECG signal of right located electrode has higher amplitude because the position is closer to the heart than V_1. For the same principle, The recorded ECG signal of left located electrode has lower amplitude because the position is farther to the heart than V_1. It is easy to conclude that these leads are located in the same plane. In fact even if a resultant vector formed by two electrodes placed on the body is parallel to lead vector V_1, it is almost impossible to accurately measure the projection onto this vector replaced by projecting onto the spread of excitation in that direction. The cause of this anomaly is because of the effect of the inhomogeneities within the thorax. Burger and van Milaan tried to modified the shape of the Einthoven triangle to solve this problem [105].

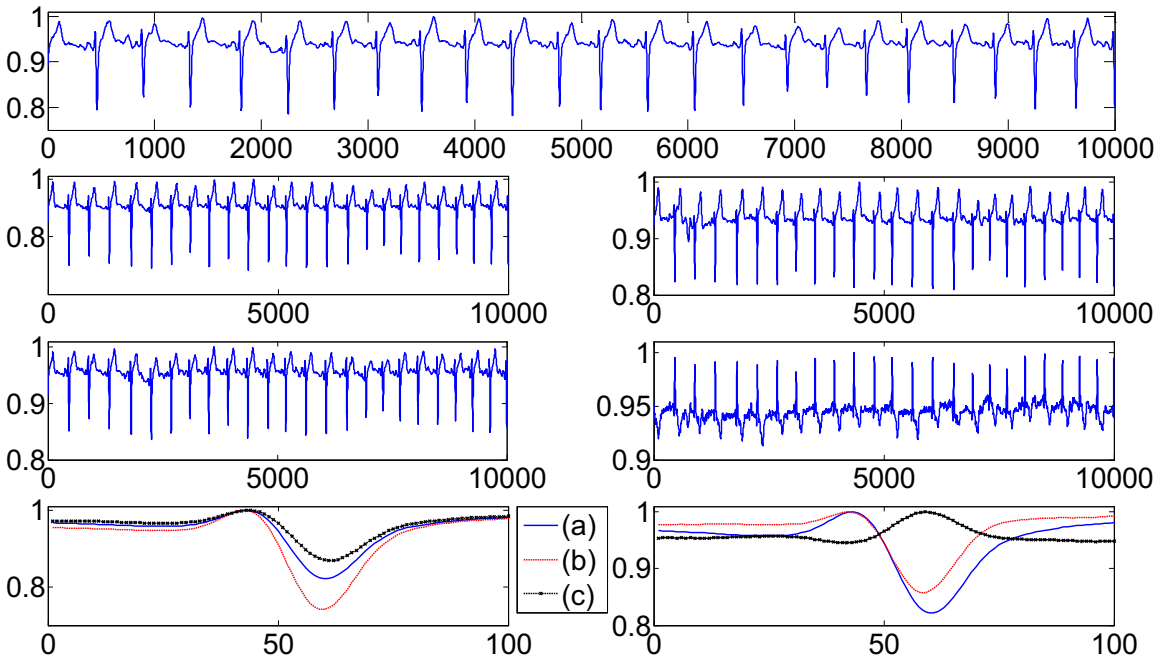

Figure 4.11 (1) Standard ECG signals of V_1, (2) Standard ECG signals of V_1', (3) Standard ECG signals of V_1'', (4) Detailed description of QRS complex of standard ECG signals, (5) Difference ECG signals between V_1' and V_1, (6) Difference ECG signals between V_1'' and V_1, (7) Detailed description of the part of difference ECG signals in the same interval of QRS complex of standard ECG signals.

4.4.1. Experimental Model

We can extend the concept of lead vector to measure the voltage of unipolar lead relative to a remote reference or the voltage of a bipolar lead formed by a lead pair. In this experiment, we consider the relation of unipolar lead and bipolar lead, and examine the corresponding voltage of the leads, and compare the voltage difference between any two points.

The voltage of bipolar lead of P_i and P_j is

$$V_{ij} = \phi_i - \phi_j \tag{4-76}$$

where the voltage is measured by the leads are located at P_i and P_j. So it can be called the voltage difference of P_i and P_j.

The voltage of unipolar leads of P_i and P_j are expressed as

$$V_i = \phi_i - \phi_{ref} \tag{4-77}$$

$$V_j = \phi_j - \phi_{ref} \tag{4-78}$$

Ideally, the voltages of these electrodes are measured between them and a remote reference electrode. The value of the remote reference electrode is generally regarded as infinity.

$$V_{ij} = \phi_i - \phi_j = \phi_i - \phi_{ref} - (\phi_j - \phi_{ref}) = V_i - V_j \quad (4\text{-}79)$$

In our lead system, the reference potential or the 'zero' potential of the body is chosen the point of attachment for electrode on the neck. Using the electrode attached on the right leg as a reference potential for the voltage of the neck and the V1, since it is the farthest position form the heart of most human.

$$V_{neck} = \phi_{neck} - \phi_{RL} \quad (4\text{-}80)$$

$$V_{V_1} = \phi_{V_1} - \phi_{RL} \quad (4\text{-}81)$$

so the potential differences between the V_1 lead may be determined. The standard voltage of V_1 is defined as

$$V_{V_1} = \phi_{V_1} - \phi_{neck} = V_{V_1} - V_{neck} \quad (4\text{-}82)$$

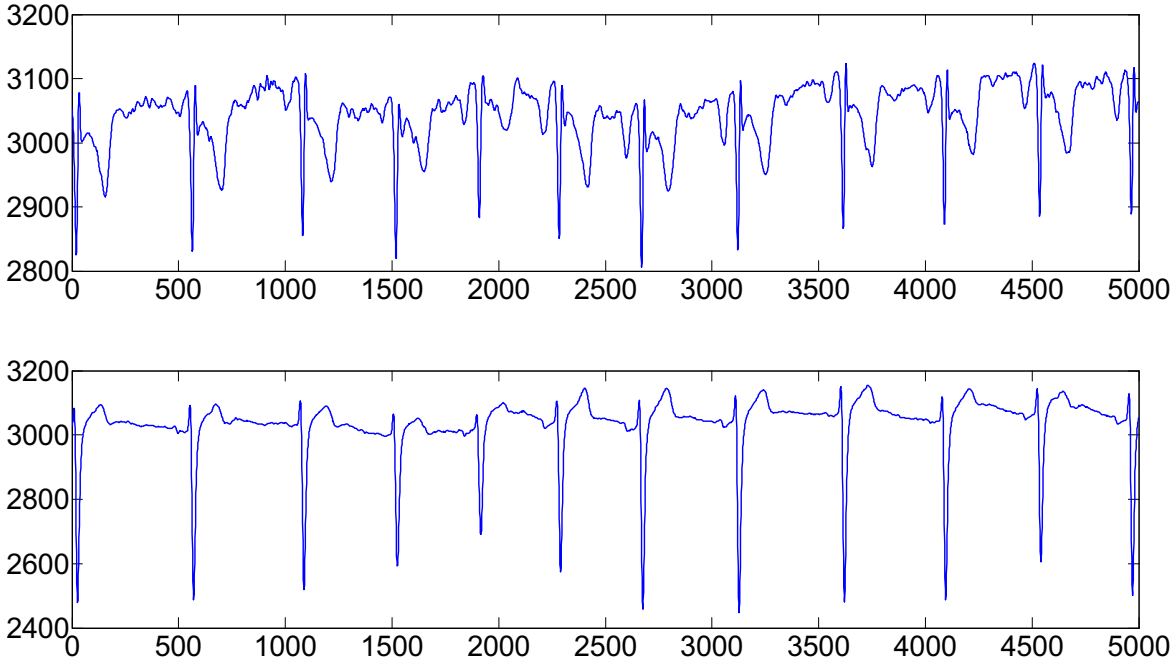

Figure 4.12 (top) The voltage between the neck and right leg, (bottom) The voltage between the standard position V_1 and right leg.

So the voltage between the points of P_i and P_j is evaluated by a bipolar lead, which is the scalar product of the arbitrary vector $\overline{c}_{ij}$ and the dipole expressing electrical activity inside the heart. The positive and negative of difference signal V_{ij} is in terms of the direction of the arbitrary vector $\overline{c}_{ij}$, as the opposite of V_{ji}.

$$V_{ij} = \phi_i - \phi_j = -(\phi_j - \phi_i) = -V_{ji} \quad (4\text{-}83)$$

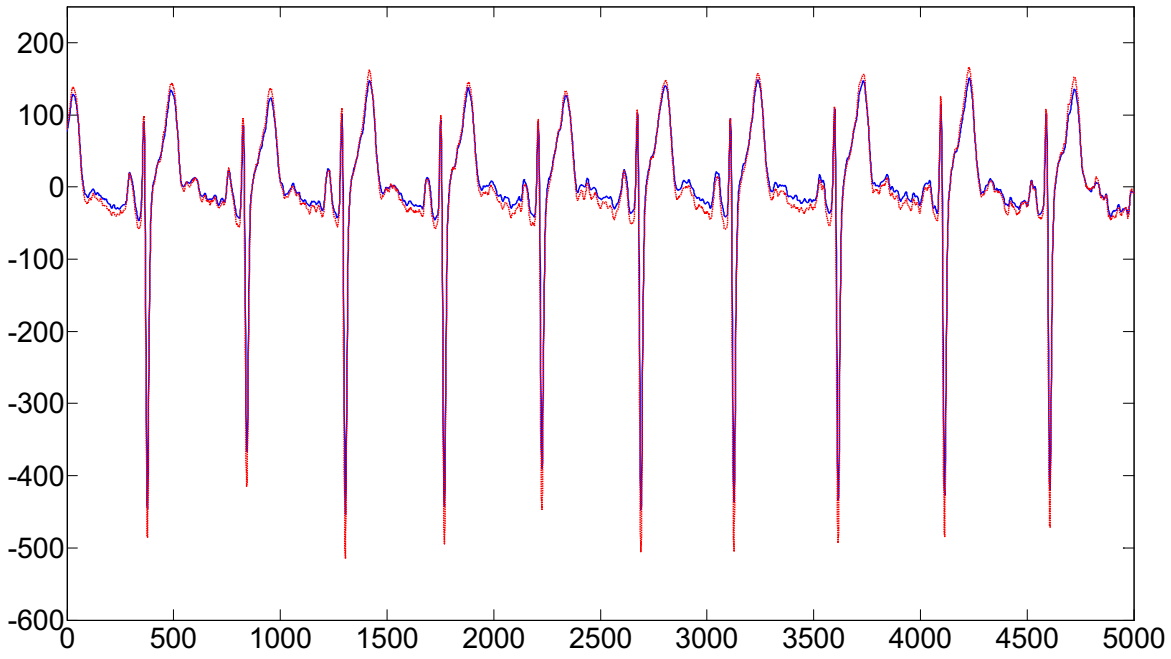

Figure 4.13 The difference of V_1 and V_{neck}, the voltage is recorded between the standard position V_1 and the neck.

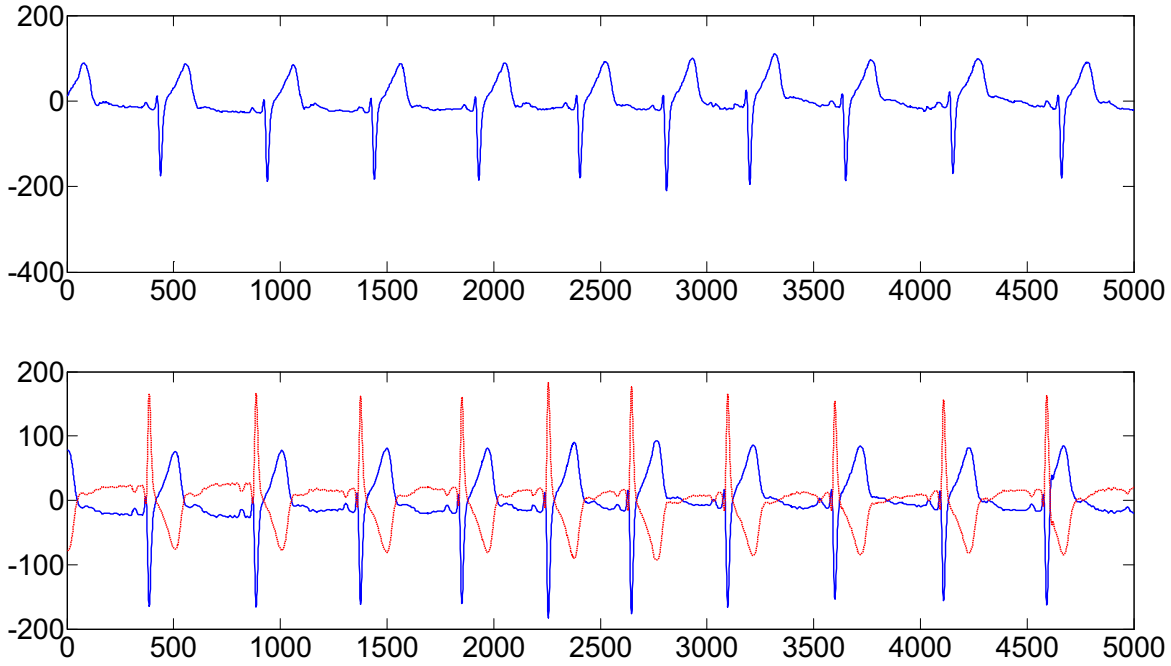

Figure 4.14 (top) The voltage is recorded between the standard position V_1 and the closed electrode, (bottom) The blue line is the difference between the voltage of V_1 and the voltage of its neighbor, and the red line is the reverse difference.

4.4.2. Vector Lead Model

The electrode $V_1^{'}$ close to the right of V_1 is placed 2 cm away electrode V_1 and the other electrode $V_1^{''}$ close to the left of V_1 is placed 2 cm away electrode V_1. So the distance between electrodes $V_1^{'}$ and point $V_1^{''}$ is about 4 cm. we can suppose that these three lead vectors are originated the same point form the heart region, and the tips of them sweep out an image surface. So an arbitrary line L_{ab} intersects the image surface in points $V_1^{'}$ and $V_1^{''}$. The point V_1 divides the line inside the image surface following the equation mentioned above.

$$\phi_{V_1} = \phi_{V_1} + \frac{1}{2}(\phi_{V_1} - \phi_{V_1}) = \frac{1}{2}\phi_{V_1} + \frac{1}{2}\phi_{V_1} \tag{4-84}$$

where $a = 2\text{cm}$, $b = 2\text{cm}$, so the ratio is $1/2$. Ideally, the voltage of these electrodes is measured with respect to a remote reference ϕ_{ref}, infinity.

$$\phi_{V_1} - \phi_{ref} = \frac{1}{2}\phi_{V_1} + \frac{1}{2}\phi_{V_1} - \phi_{ref} \tag{4-85}$$

Because the characteristic of ϕ_{ref}, $\phi_{ref} = \phi_{ref} + \phi_{ref}$

$$\phi_{V_1} - \phi_{ref} = \left(\frac{1}{2}\phi_{V_1} - \phi_{ref}\right) + (\frac{1}{2}\phi_{V_1} - \phi_{ref}) \tag{4-86}$$

$$V_{V_1} = \frac{1}{2}V_{V_1} + \frac{1}{2}V_{V_1} \tag{4-87}$$

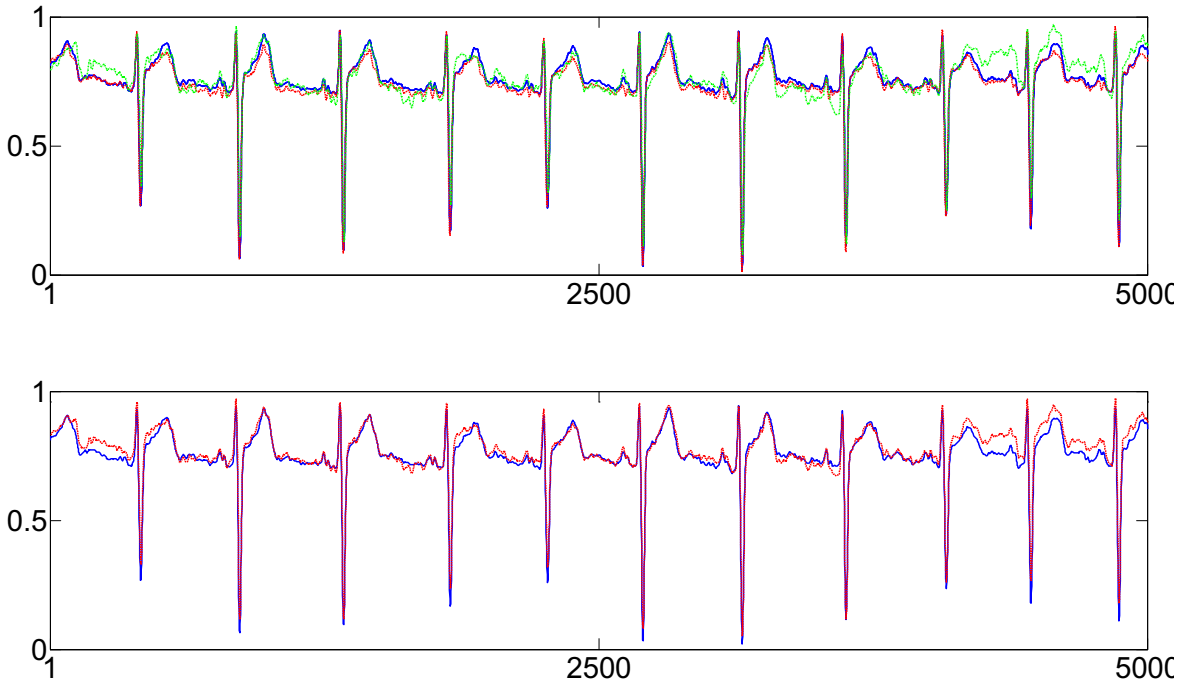

Figure 4.15 (top) The voltage is recorded of the standard position V_1 and its closed electrodes V_1' and V_1'', (bottom) The voltage of V_1 and the result of the disposal.

4.4.3. QRS Detection

In this section, experimental results for QRS detection are presented. A desired pass-band frequency is approximately 5 to 15Hz to maximize the energy of the QRS complex, and minimize the influence of baseline wander, muscle artifact and other interference. The author in [106] introduces a filter that is fast, real-time recursive. The band-pass filter is desired to a cascaded structure of a low-pass and high-pass filter to achieve a 3 dB gain in the pass-band of 5-15Hz.

The transfer function for a second-order low-pass filter is as shown below

$$H(Z) = \frac{(1 - z^{-6})^2}{(1 - z^{-1})^2} \tag{4-88}$$

the mathematical description of its difference equation is as shown below

$$y(nT) = 2y(nT - T) - y(nT - 2T) + x(nT) - 2x(nT - 6T) + x(nT - 12T) \tag{4-89}$$

where T is the sampling period and the gain is 36 with the 11Hz cut-off frequency. There are obviously 6 sample delays to the filter processing.

The transfer function of the high-pass filter is as shown below

$$H(Z) = \frac{(-1 + 32z^{-16} + z^{-32})}{(1 + z^{-1})} \tag{4-90}$$

its difference equation is mathematically described as

$$y(nT) = 32x(nT - 16T) - [y(nT - T) + x(nT) - x(nT - 32T)] \tag{4-91}$$

where T is the sampling period and the gain is 32 with the 5Hz cut-off frequency. There are obviously 16 sample delays to the filter processing.

The filtered signal is differentiated to provide the QRS-complex slope information. The transfer function of the five point derivative filter is as shown below

$$H(Z) = \frac{1}{8}T(-z^{-2} - 2z^{-1} + 2z + z^2) \tag{4-92}$$

its difference equation is mathematically described as

$$y(nT) = \frac{1}{8}T[-x(nT - 2T) - 2x(nT - T) + 2x(nT + T) + x(nT + 2T)] \tag{4-93}$$

then the differentiated signal is squared and averaged as

$$y(nT) = [x(nT)]^2 \tag{4-94}$$

The author introduces a method to obtain waveform feature information by passing through moving-window integration, also detecting the slope of the R wave. The width of QRS complex is indicating the width of the moving window and the offset indicator. The integration window will merge the QRS complex and T wave with wide window, or cause several peaks with narrow window. The width of the moving window is determined empirically and be recommend to overlay 150ms by the author.

It is easy to ascertain a peak as a local maximum determined by observing when the ECG signals after averaging. The QRS complexes may be missed from the detection because the threshold is too high. Otherwise the false QRS complexes may occur from the detection because the threshold is too low. Thus, if the threshold is too high, the number of false negative errors may increase while the number of false positive QRS detections may increase if the threshold is too low.

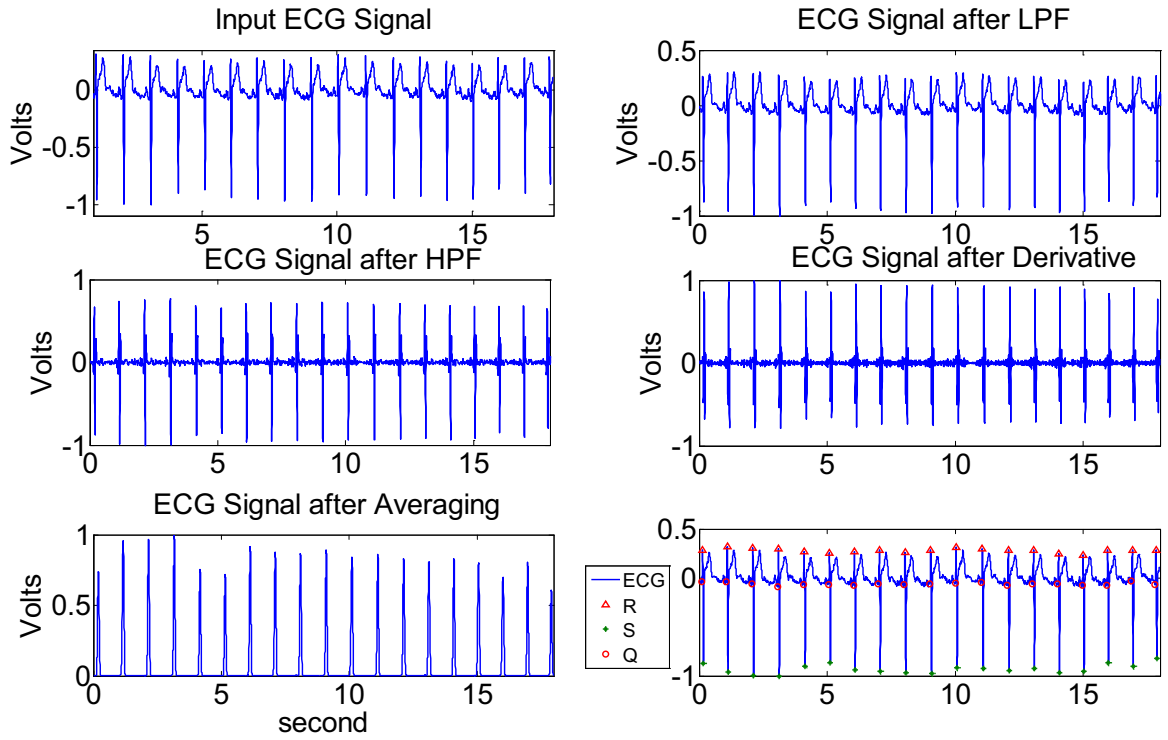

Figure 4.16 *QRS* complex detection algorithm processing steps for the actual recorded ECG signals of volunteer (25 years old, male). (top-left) Actual recorded signal, (top-right) Output of low-pass filter, (center-left) Output of high-pass filter, (center-right) Output of differentiator, (bottom-left) Output of squaring and averaging process, (bottom -right) ECG signals with *QRS* complex.

4.4.4. Vector Lead Model of V_1

Ideally, the voltages of these electrodes are measured with a remote reference where the value is generally regarded as infinity. So the voltage difference between V_1 and $V_1^{'}$ can be presented as

$$V_{de} = V_{V_1} - V_{V1} \tag{4-95}$$

Similarly the voltage difference between V_1 and $V_1^{''}$ can be presented as

$$V_{de} = V_{V_1} - V_{V1} \tag{4-96}$$

The voltage difference $V_{de}^{'}$ is linear combination of ECG signals at V_1 and ECG signals at $V_1^{'}$. Its characteristic should have the same property as the characteristics of the other two components. Difference signal and standard ECG signal are shown in Figure 4.18, furthermore modeled as be compared to the same reference model which is derived from the

reference model of V_1. The basis of this assumption is based on the reason that their location is close to each other. In general, the ECG signals exhibit quasi-periodic and nearly quasi-periodic property. As discussed in Section 4.3.1, we regard the reference loop as the template that motivate us to continuous update the reference loop in order to get the estimated loop fitting to the actual recorded ECG signals.

The parameters of the estimated loop are obtained by minimizing the normalized Euclidean distance between the two loops where another is reference loop.

$$\hat{Z}_{V_1} = \begin{bmatrix} \hat{X} \\ \hat{Y} \\ \hat{Z} \end{bmatrix} = \hat{\alpha}_{V_1} \hat{Q}_{V_1} Z_r J_\tau \tag{4-97}$$

and

$$V_{V_1} = -0.515\hat{X} + 0.157\hat{Y} - 0.917\hat{Z} \tag{4-98}$$

The observation of recorded ECG signals indicates that the morphology of these signals at three points located together are similar only difference on the amplitude. So

$$\hat{Z}_{V_1} = \hat{\alpha}_{V_1} \hat{Q}_{V_1} Z_r J_\tau \tag{4-99}$$

Given our previous discussion, we can take the impact that the variance of rotation angles is to the magnitude of the signal attributed to scaling factor α. The scaling factor α could be modified by making loop expansion or contraction. So the above equation is rewritten as

$$\hat{Z}_{V_1} = \hat{\alpha}_{V_1} Z_r J_\tau \tag{4-100}$$

and

$$\hat{Z}_{V_1} = \hat{\alpha}_{V_1} Z_r J_\tau \tag{4-101}$$

Figure 4.17 shows the results of estimation from the reference loop. On the top three subplots, estimated ECG signals are indicated by dashed line and actual recorded ECG signals are indicated by solid line.

The characteristics of standard ECG signals recorded by the sensor ‘A’ are given in the above content. Now we discuss the information directly obtained from the signal difference of the sensor ‘B’ comparing with the standard signal V_1. It is cautioned that we do not detect exactly QRS complex in this procedure because the recorded signal is not standard ECG signal but signal difference. Figure 4.18 displays the result of the proposed method that detects the peak of QRS complex to clearly demonstrate how the algorithm works and its effectiveness to identify the position of QRS complexes. In the experiment, the sampling frequency of raw digital ECG signals is 500 Hz. Using wavelet transform used in the previous chapter for compressed sensing/sampling, components in the range 0-0.5 Hz are removed to reduce of baseline wander. After calculating mean and standard deviation for each class and probability of QRS and non-QRS, the entropy is a suitable criterion in the design of optimum feature selection. Then calculating the values of entropy in two clusters, the centers of clusters C_1 and $C_2$are obtained. The threshold is set to C_{th}. Cluster center whose value is greater than C_{th}, is designed as C_1 and another is considered to be C_2. The elements in C_1 are assigned value 1 to indicate the existence of QRS complex and otherwise the elements in C_2 are assigned value 0 to indicate the non-existence of QRS complex. It is important to choose an

appropriate threshold to classify QRS complex. As the QRS complex detection, only detection of the position of QRS complexes may be missed because the threshold is too high. Otherwise the false results may occur from the detection because the threshold is too low. More detailed descriptions are shown in Figure 4.19.

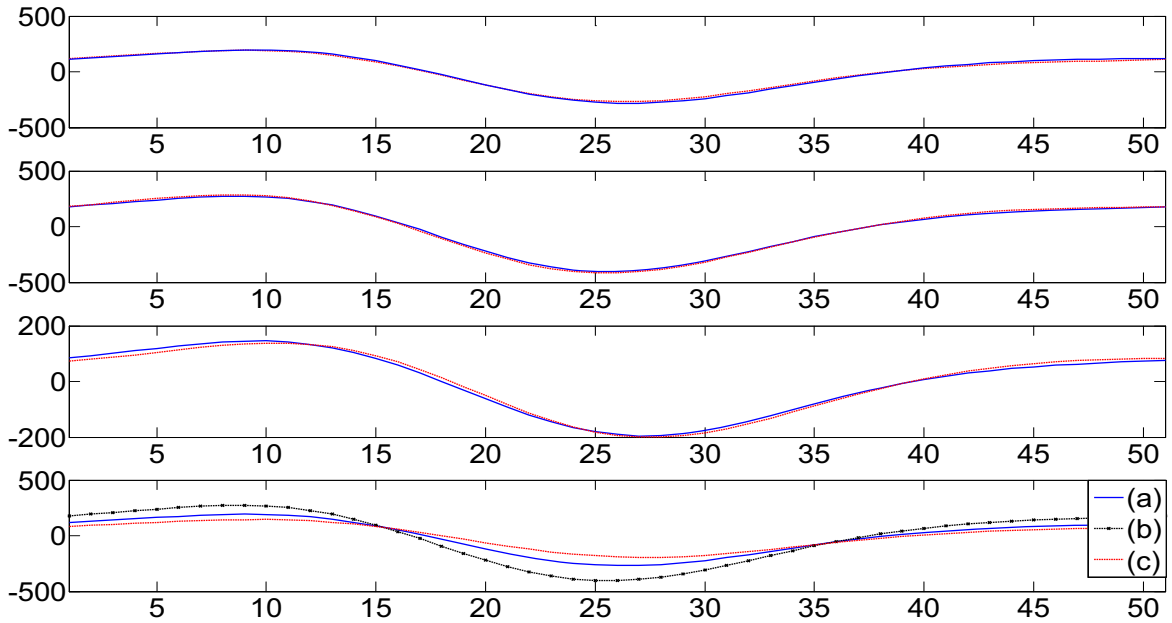

Figure 4.17 Morphologic variability shown of these three ECG signals. Estimated ECG signals are shown by dashed line and the actual recorded ECG signals are shown by solid line. On the bottom subplot, the estimated ECG signals on different locations by the same reference loop.

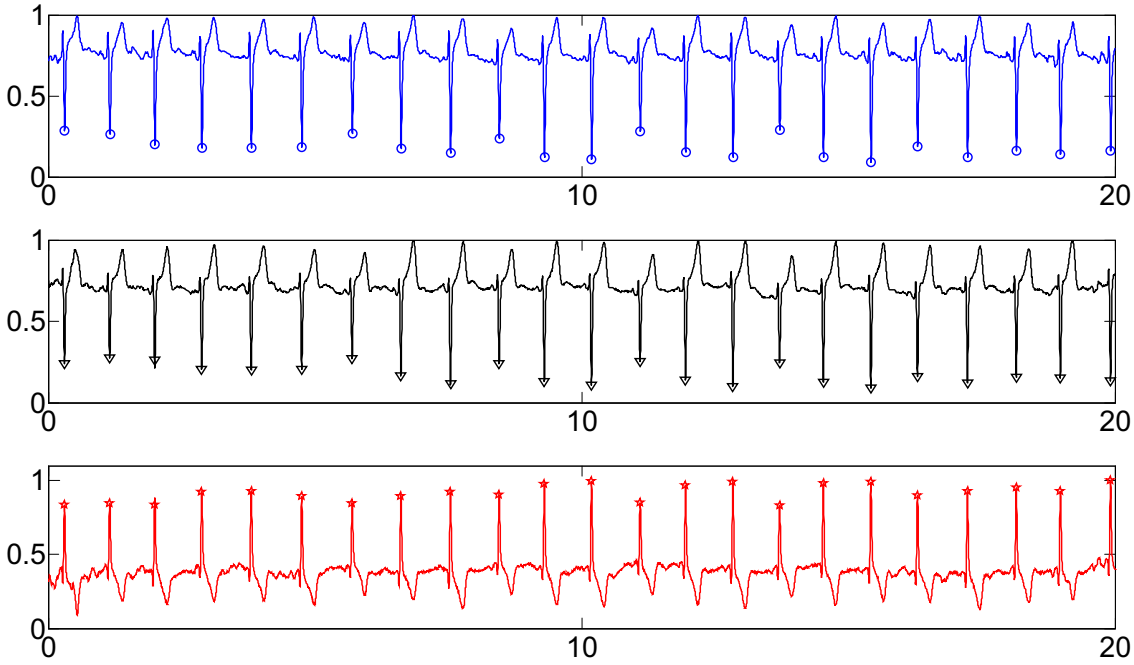

Figure 4.18 (top) The standard ECG signals of V_1, (center) The difference signal between V_1' and V_1, (bottom) The difference signal between V_1'' and V_1.

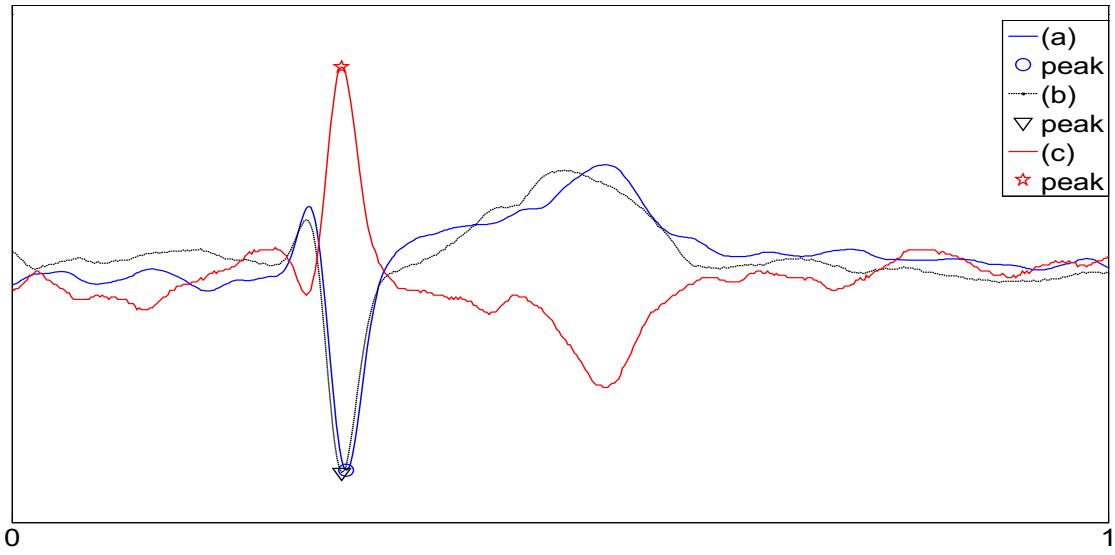

Figure 4.19 Detailed description of QRS loop of the standard ECG signal and signal differences. (a) The standard ECG signals of V_1, (b) The difference signal between V_1' and V_1, (bottom) The difference signal between V_1'' and V_1.

Heart rate is defined by the number of heartbeats within one minute, typically expressed as beats per minute (bpm). The measurement of heart rate is very important for its medicinal value to assist medical professionals to diagnose physical condition of human. The term of RR interval represents distance between two adjacent R waves that are used to assess the ventricular rate. The value of RR interval is the inverse of the heart rate. Heart rate can vary as the status of objective because the body needs to absorb oxygen into the blood and excrete carbon dioxide. RR interval is used to determine the pulse of the body because ECG method is more precise.

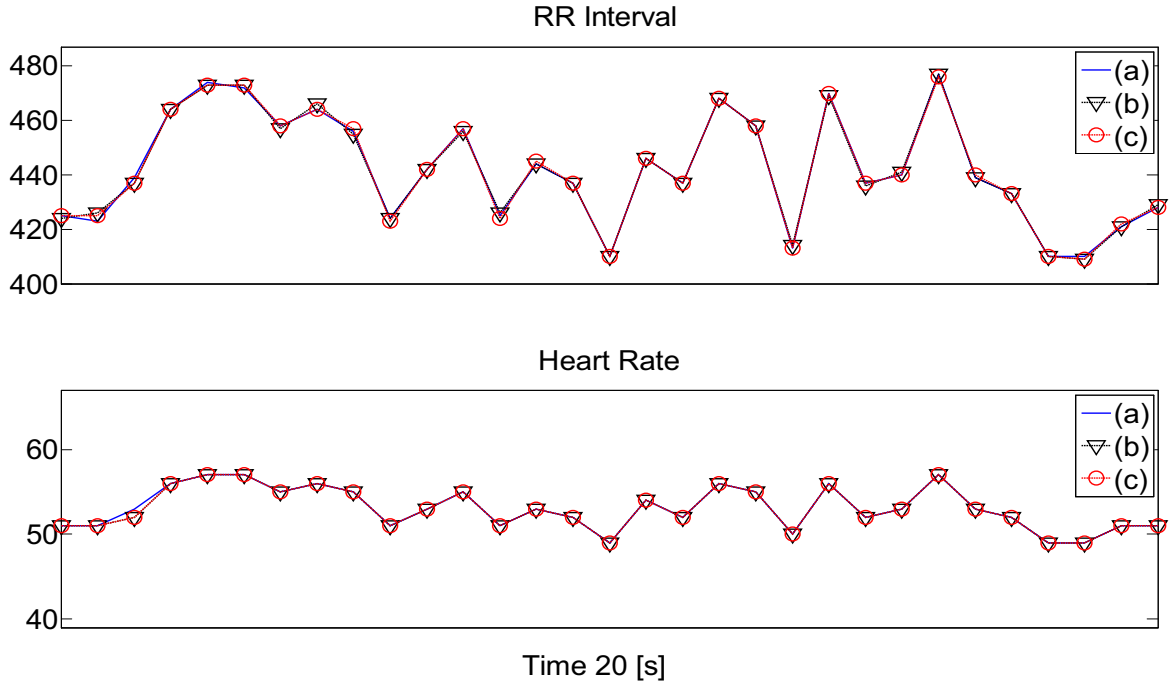

Figure 4.20 (top) RR interval, (bottom) Heart rate.

Learning from the experiment, the averaging scaling factor $\hat{\alpha}_{V_1'}$ is about 1.52. the scaling factor $\hat{\alpha}_{V_1'}$ is ratio of magnitude of V_1 and V_1' because the scaling factor $\hat{\alpha}_{V1}$ of every cardiac circle is adjusted to 1, the averaging scaling factor $\hat{\alpha}_{V_1''}$ is about 0.75. τ' is time-advance with a value of 2 ms and τ'' is time-delay with a value of 2ms. Estimated signal of V_1 from signal difference of V_1 and V_1' with the characteristic of V_1'

$$\hat{V}_1(i) = \hat{\alpha}_{V_1} * \left[\hat{V}_1(i-1) + V_{de}(i-2)\right] \quad i \in (3, N) \tag{4-102}$$

or estimated signal of V_1 from signal difference of V_1 and V_1'' with the characteristic of V_1''

$$\hat{V}_1(i) = \hat{\alpha}_{V_1} * \left[\hat{V}_1(i-1) - V_{de}(i-1)\right] \quad i \in (2, N) \tag{4-103}$$

The relative function can be defined as a dimensionless ratio of the energy of the reconstructed signal and the energy of original signal

$$RF = \frac{\sum_0^T (\hat{V}_{V1})^2}{\sum_0^T ((V_{V1})^2} \tag{4-104}$$

and also another similarity of the energy of reconstructed signal and the energy of original signal is also as a dimensionless ratio

$$SF = \frac{\sum_0^T (\hat{V}_{V1} V_{V1})}{\sum_0^T (\hat{V}_{V1})^2 \sum_0^T (V_{V1})^2} \tag{4-105}$$

More detailed descriptions are shown in Figure 4.22.

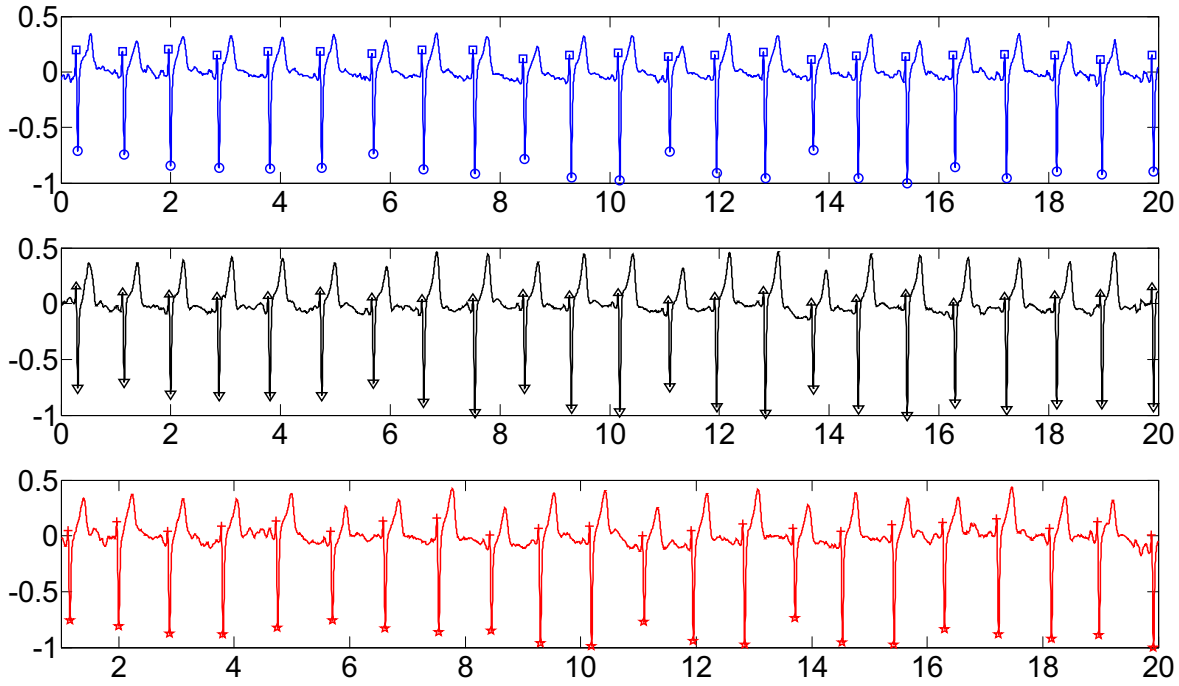

Figure 4.21 (top) The standard ECG signals of V_1, (center) The estimated signal $\widehat{V_1'}$ from the difference signal between V_1' and V_1, (bottom) The estimated signal $\widehat{V_1''}$ from the difference signal between V_1'' and V_1.

In general, the Q wave, R wave, and S wave with a succession appear in all normal QRS complex. But sometimes it is difficult to clearly identify these three components. As shown in Figure 4.22, it is difficult to determine the position and existence of Q wave. We use two terminologies to describe QRS complex, they are RS duration and RS amplitude. RS duration is the distance between R wave and S wave. RS amplitude is the magnitude of summation of R wave and S wave.

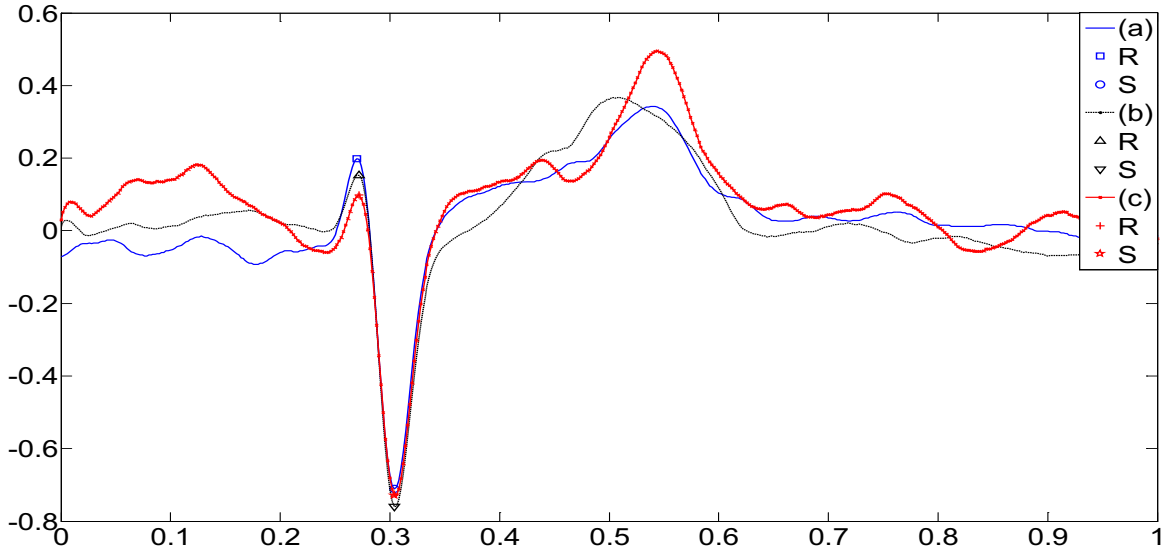

Figure 4.22 Detailed description of QRS loop of the standard ECG signal and its estimations. (a) The standard ECG signals of V_1, (b) The estimated signal $\widehat{V_1'}$, (c) The estimated signal $\widehat{V_1''}$.

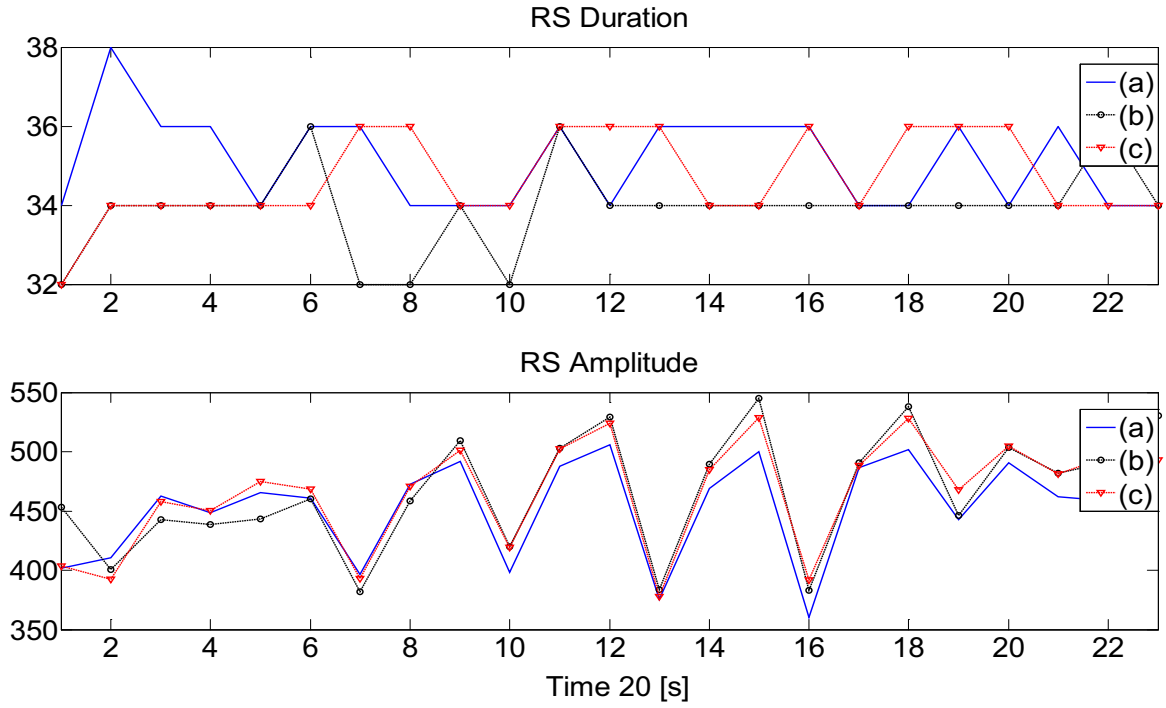

Figure 4.23 From the top to the bottom are the duration and amplitude of RS wave. (a) The standard ECG signals of V_1, (b) The estimated signal $\widehat{V_1'}$, (c) The estimated signal $\widehat{V_1''}$.

Table 4.2 Performance of estimation form signals difference around V_1

V_1	Heart Rate	RS Duration	RS Amplitude
1	2.8×10^{-4}	2.7×10^{-3}	3.5×10^{-3}
2	2.4×10^{-2}	1.5×10^{-2}	11.1×10^{-2}
3	3.0×10^{-4}	2.0×10^{-3}	1.8×10^{-3}
4	3.1×10^{-2}	2.0×10^{-2}	12.0×10^{-2}

4.4.5. Vector Lead Model of V_5

Ideally, the voltages of these electrodes are measured with a remote reference where the value is generally regarded as infinity. So the voltage difference between V_5 and $V_5^{'}$ can be presented as

$$V_{de} = V_{V_5} - V_{V_5} \tag{4-106}$$

Similarly the voltage difference between V_5 and $V_5^{''}$ can be presented as

$$V_{de} = V_{V_5} - V_{V_5} \tag{4-107}$$

The voltage difference $V_{de}^{'}$ is linear combinations of ECG signals at V_5 and ECG signals at $V_5^{'}$. The standard ECG signals of them are shown in Figure 4.25, furthermore modeled as be compared to the same reference model which is derived from the reference model of V_5. The ECG signals of V_5 also exhibit quasi-periodic and nearly quasi-periodic property as V_1.

The parameters of the estimated loop are obtained by minimizing the normalized Euclidean distance between the two loops where another is reference loop

$$\hat{Z}_{V_5} = \begin{bmatrix} \hat{X} \\ \hat{Y} \\ \hat{Z} \end{bmatrix} = \hat{\alpha}_{V_5} \hat{Q}_{V_5} Z_r J_\tau \tag{4-108}$$

and

$$V_{V_5} = 1.125\hat{X} + 0.127\hat{Y} - 0.086\hat{Z} \tag{4-109}$$

The observation of recorded ECG signals indicates that the morphology of these signals at three points located together are similar only difference on the amplitude. So

$$\hat{Z}_{V_5} = \hat{\alpha}_{V_5} \hat{Q}_{V_5} Z_r J_\tau \tag{4-110}$$

As the previous analysis of V_1, we can take the impact that the variance of rotation angles is to the magnitude of the signal attributed to scaling factor α. The expansion or contraction of the loop is controlled by the scaling factor α. So the above equation is rewritten as

$$\hat{Z}_{V_5} = \hat{\alpha}_{V_5} Z_r J_\tau \tag{4-111}$$

and

$$\hat{Z}_{V_5} = \hat{\alpha}_{V_5} Z_r J_\tau \tag{4-112}$$

Figure 4.24 shows the results of estimation form the reference loop. On the top three subplots, estimated ECG signals are indicated by dashed line and actual recorded ECG signals are indicated by solid line.

The characteristics of standard ECG signals recorded by the sensor 'A' are given in the above content. Now we discuss the information directly obtained from the signal difference of the sensor 'B' comparing with the standard signal V_5. It is cautioned that we do not detect exactly QRS complex in this procedure because the recorded signal is not standard ECG signal but signal difference. Figure 4.25 displays the result of the proposed method that detects the peak of QRS complex to clearly demonstrate how the algorithm works and its effectiveness to identify the position of QRS complexes. Following the same procedure as V_1, the results of the detection of QRS complex position are shown. More detailed descriptions are shown in Figure 4.26. RR interval and heartbeat are shown in Figure 4.27.

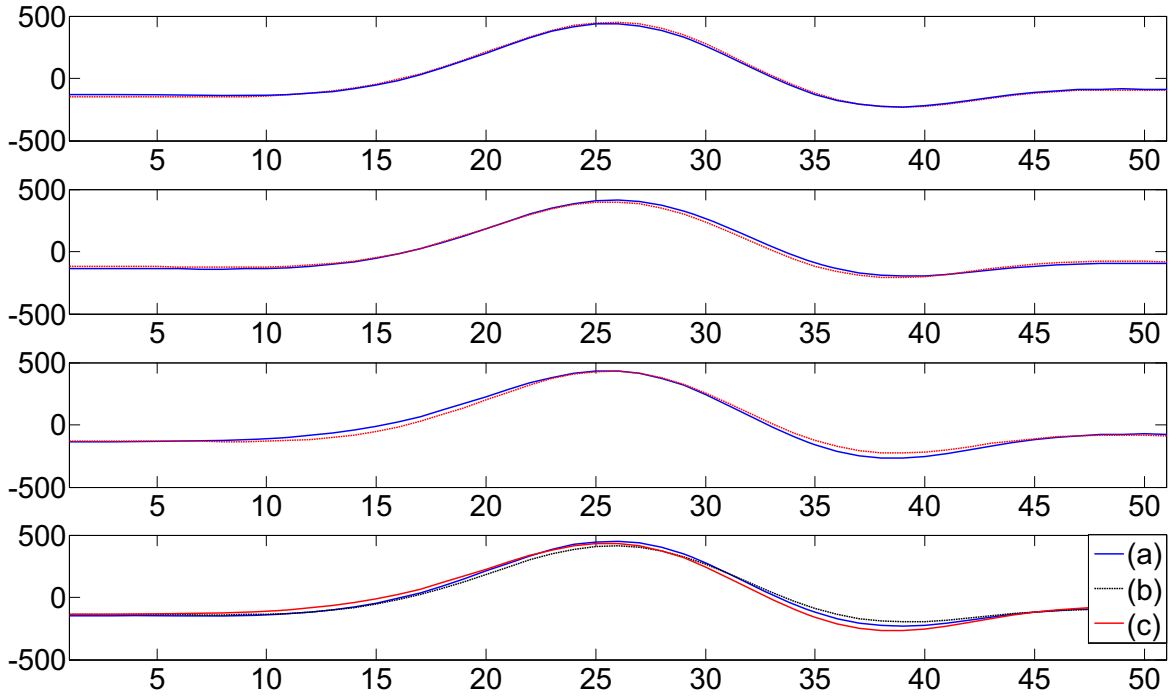

Figure 4.24 Morphologic variability shown of these three ECG signals. Estimated ECG signals are shown by dashed line and the actual recorded ECG signals are shown by solid line. On the bottom subplot, (a) the estimated ECG signals on different locations by the same reference loop.

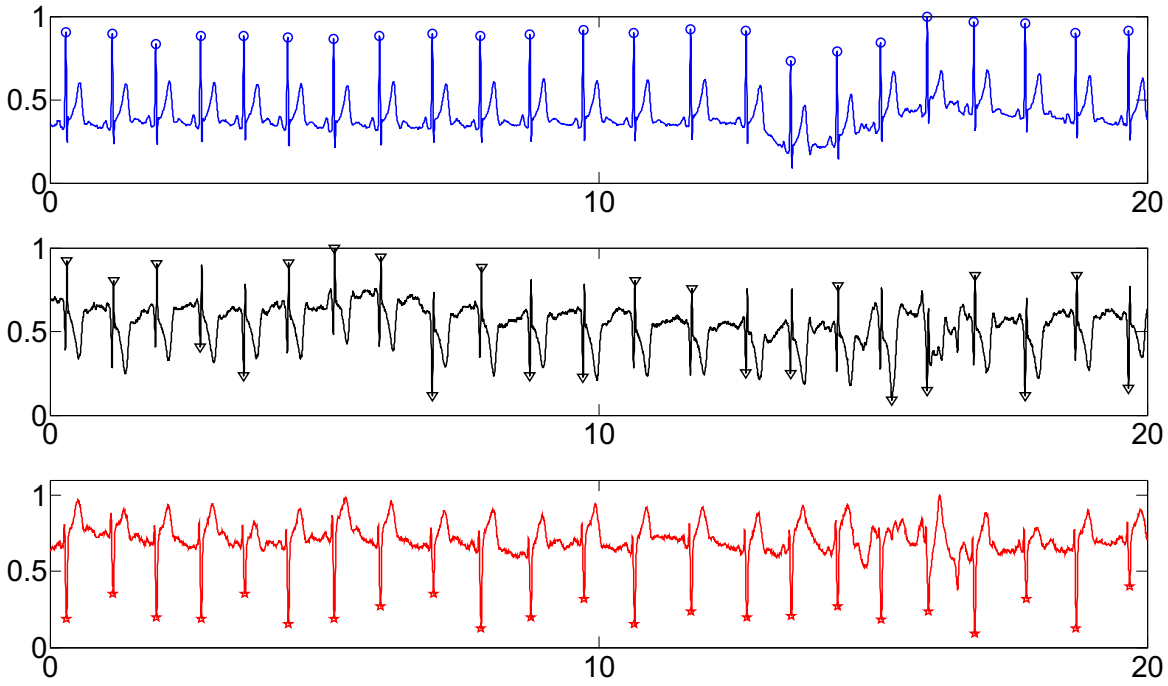

Figure 4.25 (top) The standard ECG signals of V_5, (center) The difference signal between V_1' and V_5, (bottom) The difference signal between V_5'' and V_5.

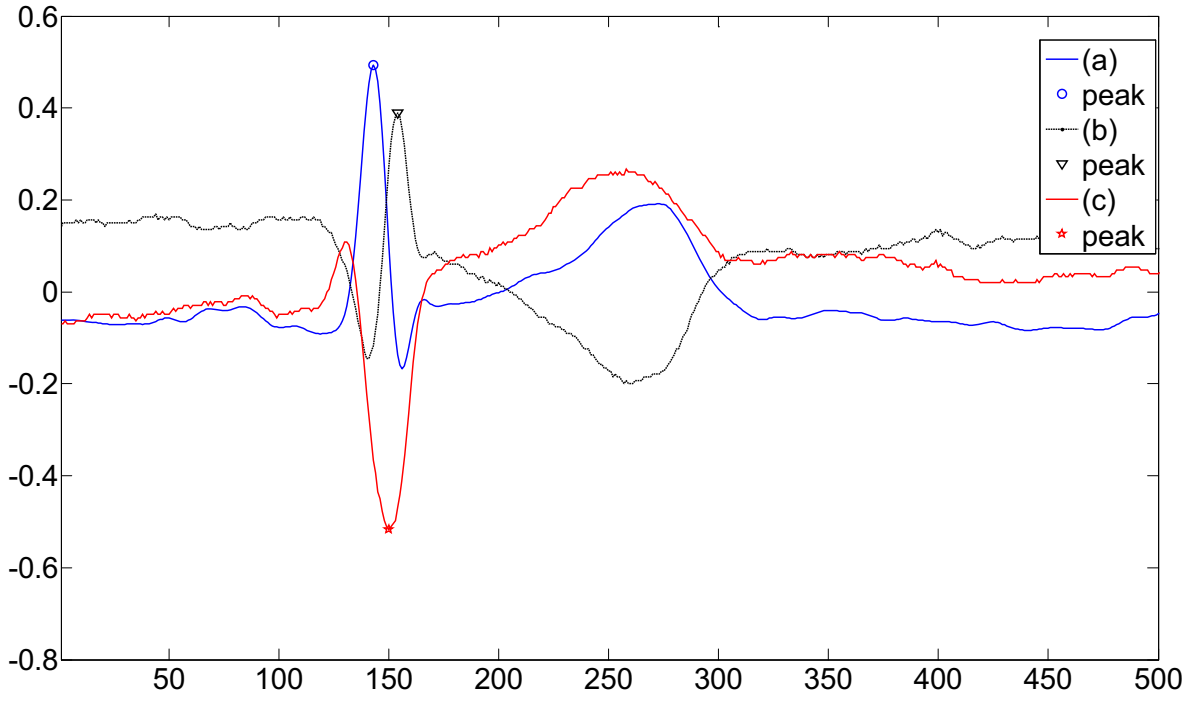

Figure 4.26 Detailed description of QRS loop of the standard ECG signal and signal differences. (a) The standard ECG signals of V_5, (b) The difference signal between V_5' and V_5, (bottom) The difference signal between V_5'' and V_5.

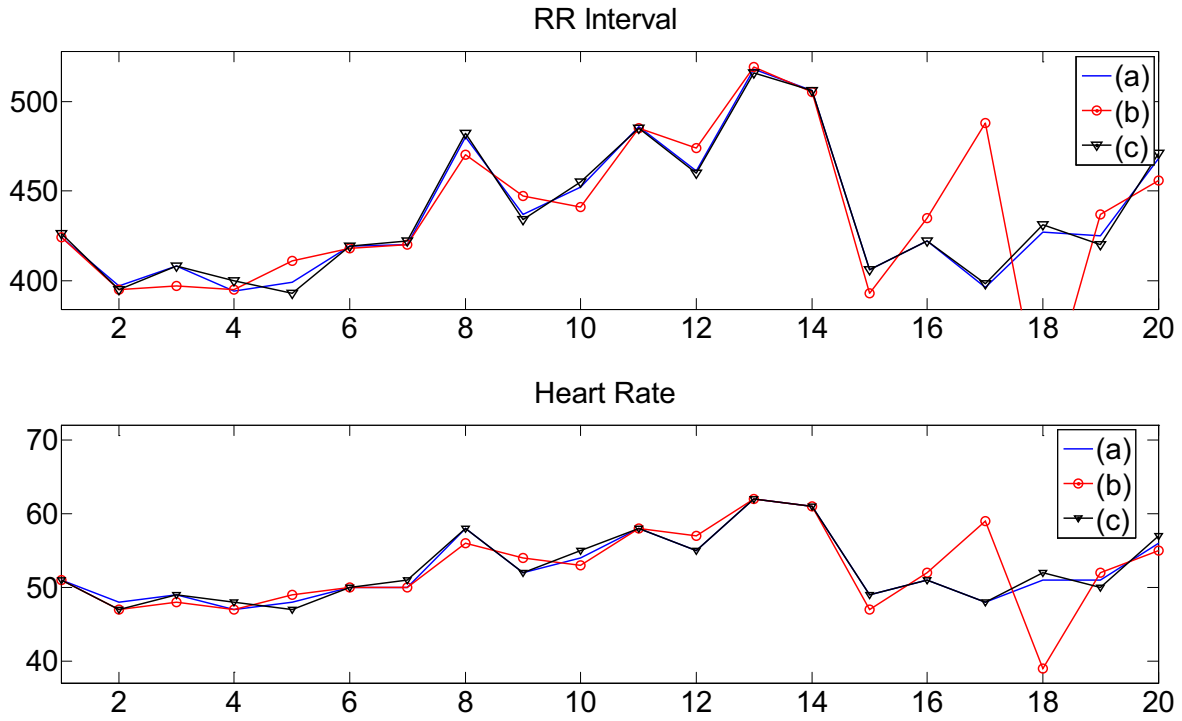

Figure 4.27 (top) RR interval, (bottom) Heart rate.

Learning from the experiment, the averaging scaling factor $\hat{\alpha}_{V_5'}$ is about 0.91. the scaling factor $\hat{\alpha}_{V_5'}$ is ratio of magnitude of V_5 and V_5' because the scaling factor $\hat{\alpha}_{V5}$ of every cardiac circle is adjusted to 1, the averaging scaling factor $\hat{\alpha}_{V_5''}$ is about 0.985. $\hat{\alpha}_{V_5''}$ is greater than $\hat{\alpha}_{V_5'}$ but less than 1 because V_5'' is closer to the heart than V_5'. The reason for scaling factor less than 1 is to estimate the signals of V_5' and V_5'' based on the reference loop of V_5. Actual recorded signal of V_5' has larger interference from the lead V_4, which does not confirm our assumption that the signal of adjacent point of V_5 associated only with lead V_5. The result shows the effect is not good because it does not consistent with the hypothetical model.

τ' is time-advance with a value of 1 ms and τ'' is time-delay with a value of 0 ms. Estimated signal of V_5 from signal difference of V_5 and V_5' with the characteristic of V_5'

$$\hat{V}_5(i) = \hat{\alpha}_{V_5} * \left[\hat{V}_5(i) + V_{de}(i-1)\right] \quad i \in (2, N) \tag{4-113}$$

$$\hat{V}_5(i) = \frac{V_{de}(i)}{\hat{\alpha}_{V_5} - 1} \quad i \in (1, N) \tag{4-114}$$

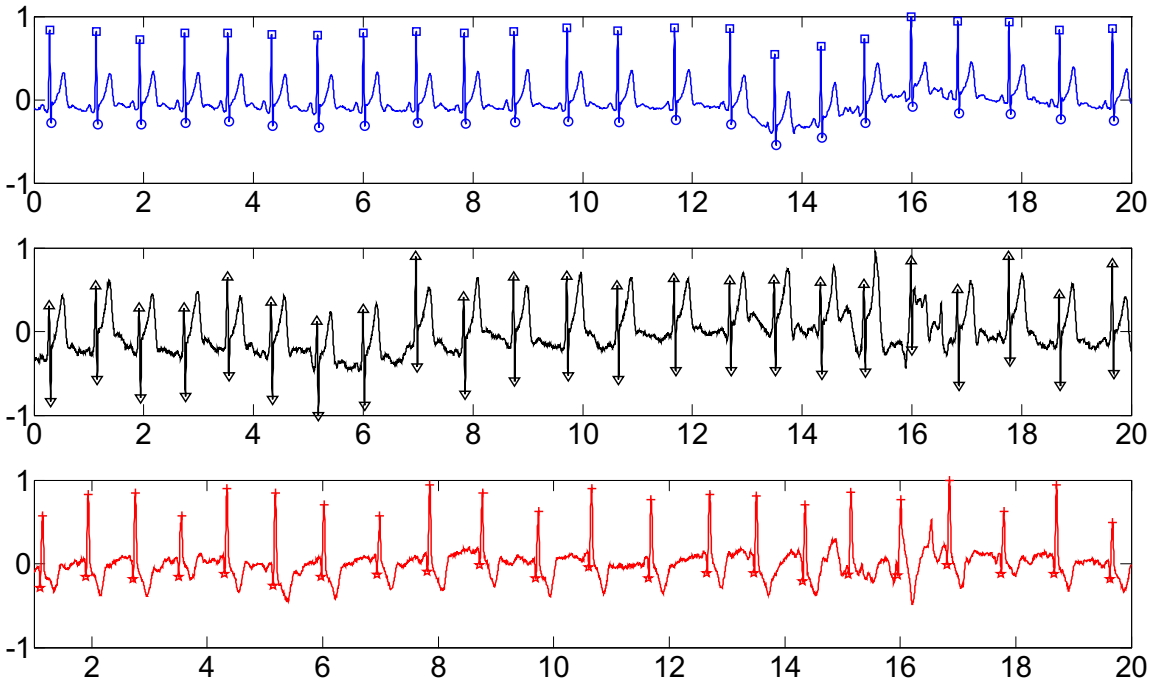

Figure 4.28 (top) The standard ECG signals of V_5, (center) The estimated signal $\widehat{V_5'}$ from the difference signal between V_5' and V_5, (bottom) The estimated signal $\widehat{V_5''}$ from the difference signal between V_5'' and V_5.

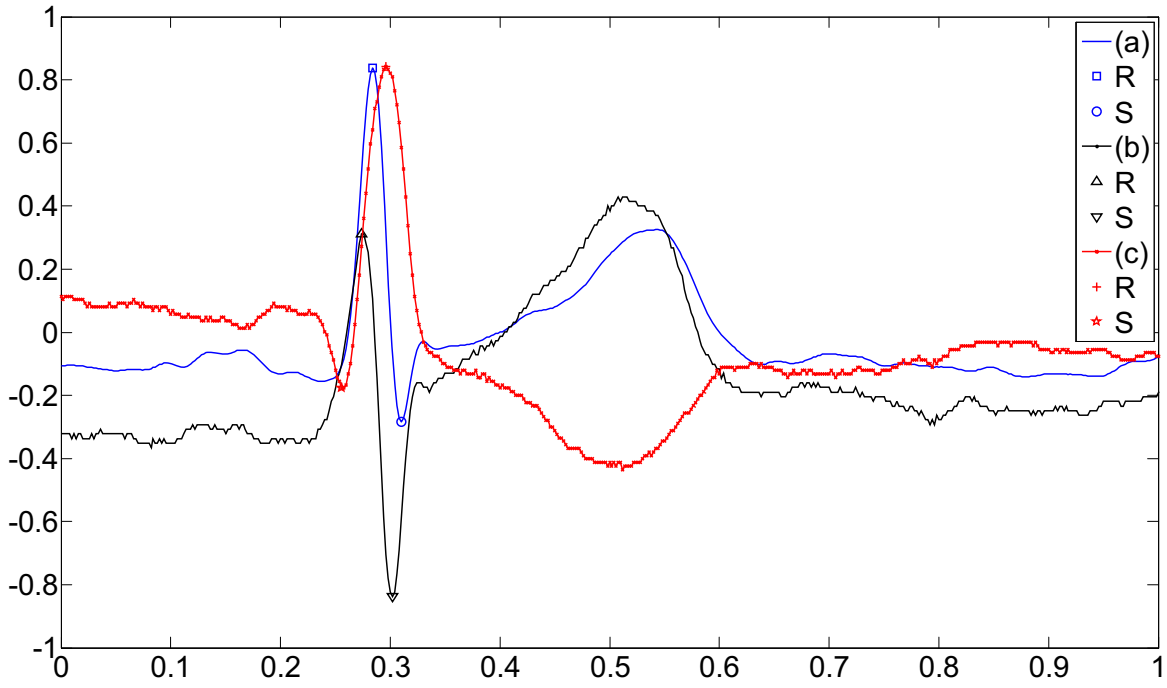

Figure 4.29 Detailed description of QRS loop of the standard ECG signal and its estimations. (a) The standard ECG signals of V_5, (b) The estimated signal $\widehat{V_5'}$, (c) The estimated signal $\widehat{V_5''}$.

More detailed descriptions are shown in Figure 4.29. RR interval and heartbeat are shown in Figure 4.30.

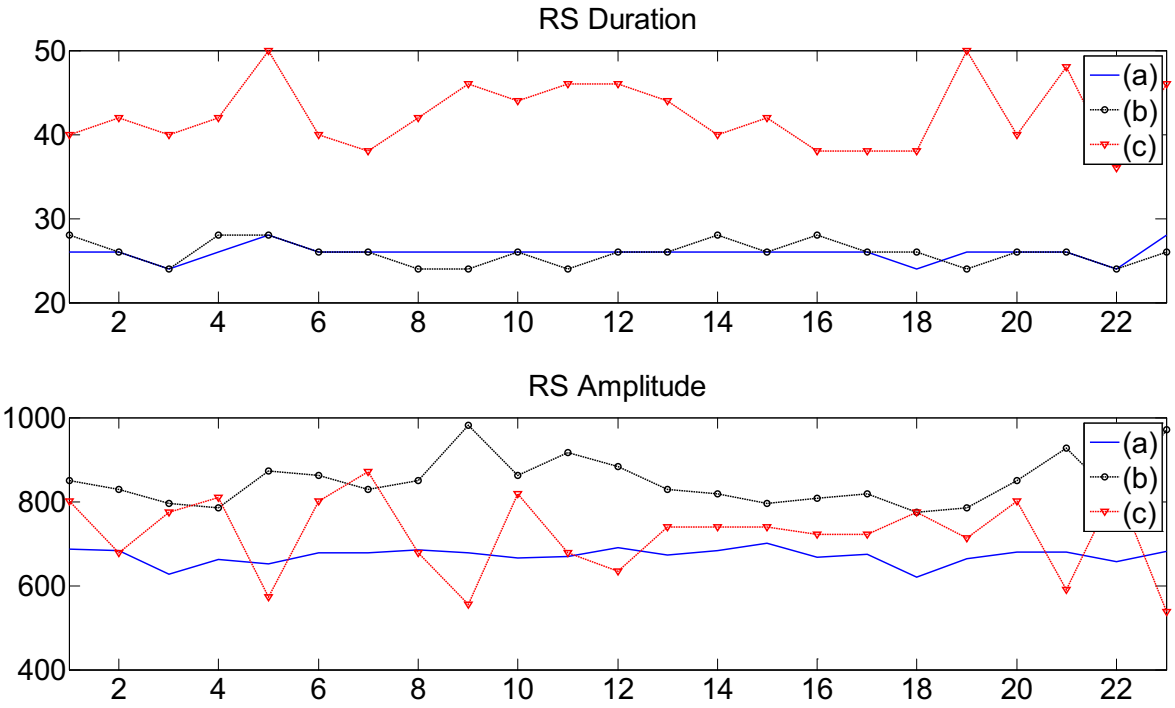

Figure 4.30 From the top to the bottom are the duration and amplitude of RS wave. (a) The standard ECG signals of V_5, (b) The estimated signal $\widehat{V_5'}$, (c) The estimated signal $\widehat{V_5''}$.

Table 4.3 Performance of estimation form signals difference around V_5

V_5	Heart Rate	RS Duration	RS Amplitude
1	4.6×10^{-2}	2.6×10^{-3}	6.7×10^{-2}
2	4.9×10^{-2}	5.1×10^{-3}	8.2×10^{-2}
3	9.4×10^{-2}	*	7.2×10^{-2}
4	5.3×10^{-2}	1.2×10^{-2}	8.4×10^{-2}

4.5. Conclusion

Figure 4.31 shows the projection of a VCG loop onto the orthogonal planes. It is obvious if the magnitude and direction of a resultant vector change throughout the cardiac cycle, then we can image that the tip of this vector will draw a three-dimensional path in space. The projections of three planar show the same conclusion. It can be explained by only the QRS loop because we mainly use the information and characteristic of QRS complex. But if we really need other information of ECG signal such as P and T loops, it is easy to derive based on the same principle. Figure 4.32 shows the projections of VCG loops of continuous several circles in space onto the three orthogonal planes. We not only draw the same conclusion as the above, but also summary the periodicity of signals.

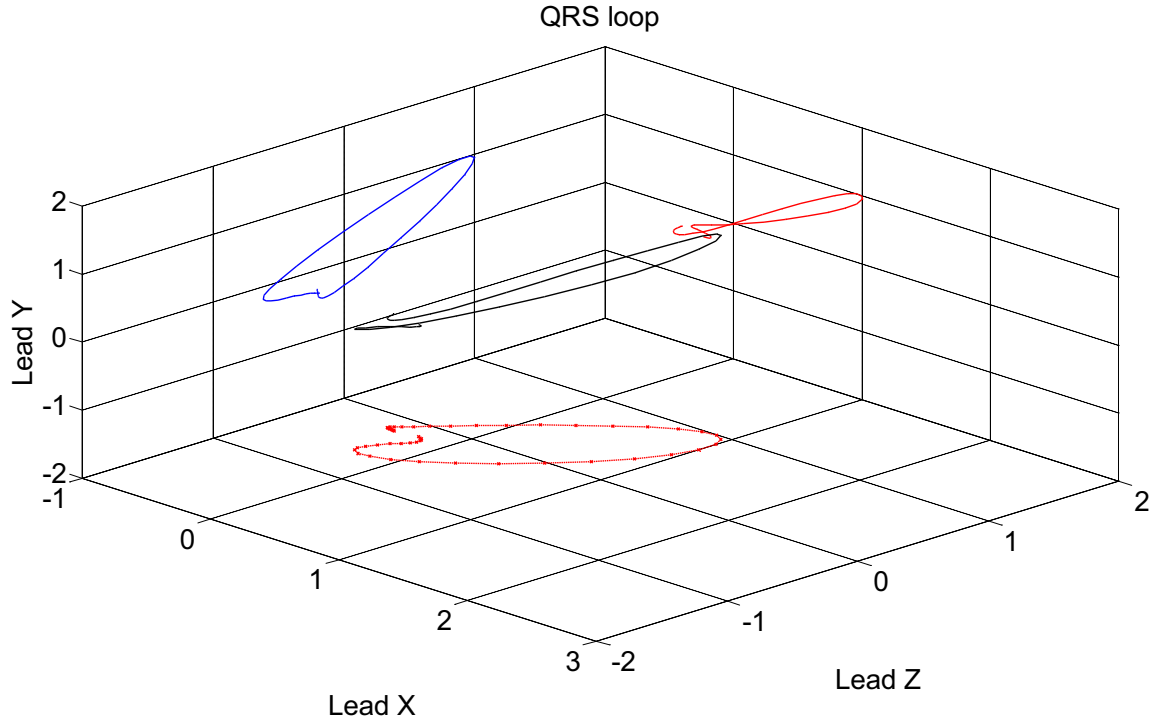

Figure 4.31 VCG loop of QRS complex. The QRS loop has been rotated to three singular planes where the components projected to the axes of the singular values in decreasing order.

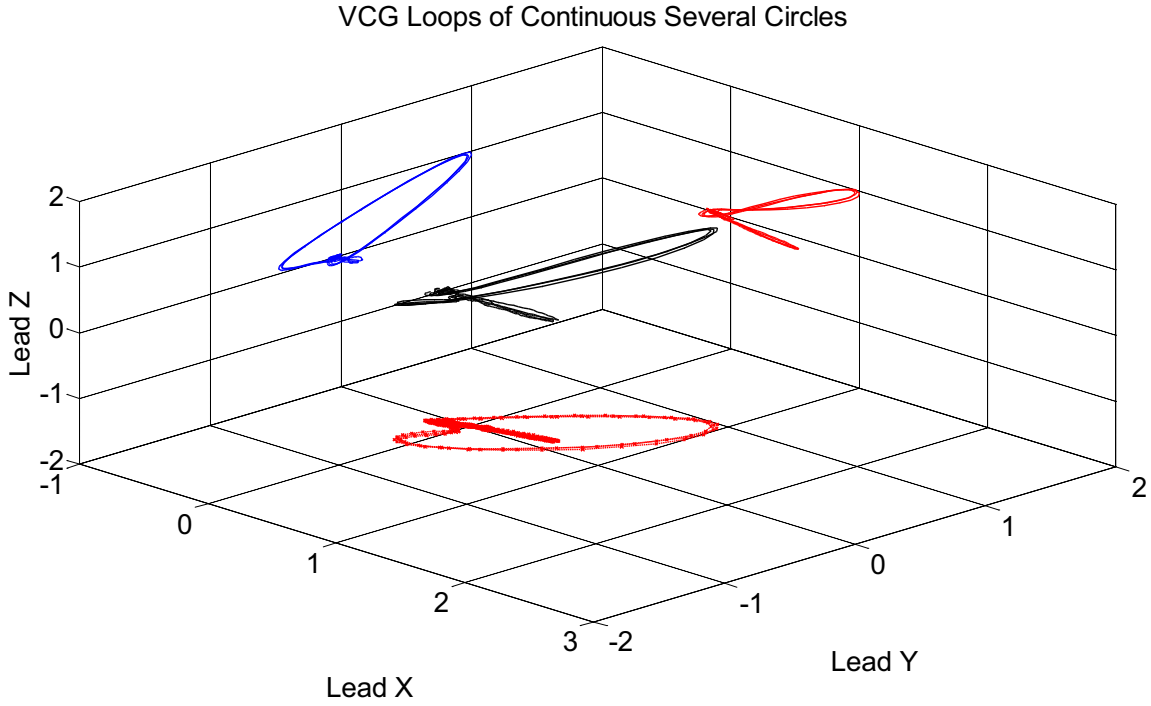

Figure 4.32 VCG loops of continuous several circles. The loops have been rotated to three singular planes where the components projected to the axes of the singular values in decreasing order.

Our present detector is dedicated to Cardiac arrhythmia monitoring application. Thus the work will focus on the processing of QRS complex (e.g. P and T waves are not processed).On

one hand, in monitoring applications, the estimated signal is only based on QRS VCG alignment. On the other hand, the information of P wave, T wave and other ingredients unrelated to estimation of heart rate and analysis of QRS complex can be ignored, as they do not influence the performance of the end result. We assume that the signal measured in the adjacent point of the standard location of electrode approximately has the same property. The rather likely signal is derived from signal difference of the adjacent point and standard point. The process is based on a well-known fact that adjacent circles of ECG signals have a deflection of morphology because various interferences cause that the heart's electrical axis shifts slightly. We use QRS-VCG loop alignment algorithm to quantity such shifts by estimating the rotation angles of loop alignment. The estimation of standard signal is based on the simple model of QRS loop. Various placement of electrode are investigated. We found the electrode placement have significant influence on performance. Lead vectors that are connected with one pair of electrodes are used to predict the voltage difference between two adjacent electrodes at an instant of time. The direction of lead vector is determined by a criterion that voltage difference of every pair of electrodes has a maximal value along lead vector. In the set of our experiments, one of the pair of electrodes is placed on the precordial leads V_1 to V_5, and another is place in the center of the heart through imagination. There is a virtual arrow pointing from the heart to precordial leads V_1 to V_5. Then the resultant vector flows along the virtual arrow and close to the heart, upward deflection occurs, whereas the resultant vector flows along the virtual arrow and away from the heart, downward deflection occurs. The result of Figure 4.18 shows that the recorded signal of V_1' has greater magnitude of QRS complex than on the location of V_1 because V_1' is closer to the heart than V_1. By the same token, the recorded signal of V_1'' has smaller magnitude of QRS complex than on the location of V_1 because V_1'' is farther to the heart than V_1. But another location of V_5 is special because V_1 is completely located in the side of the heart and V_5 does not. The location on the left of V_5 parallel to Y axis has the characteristic that it is closer to the left atrium but away from the right atrium. The location on the right of V_5 parallel to Y axis has the characteristic that it is farther away the left and the right atrium. Measurements of V_5 and its adjacent points are presented in Figure 4.25.

Chapter 5

Conclusion and Ongoing Work

The ubiquitous wireless sensor network allows us to implement pervasive cardiac care (PCC) by sensing and managing the nodes embedded in our daily living environment. To make successful deployment of PCC the cardiac monitoring device must be low cost, small size and long lifetime (e.g. 1 week) . By taking into account the specifications for the cardiac monitoring device, our objectives are largely achieved. By selecting the appropriate circuit topology, we ensure the desired parameters to be achieved. The use of Cadence software facilitates the simulations and the analysis of our circuit. The performance of the final design is compared between the theoretical expectation and the simulation one thanks to Cadence software.

The technologies of Wireless Sensor Networks (WSNs) enable to implement remote cardiac monitoring solution by adding a single tiny processing core with the sensor, and wireless access medium. A new concept of Compressed Sensing (CS) is introduced to recorded ECG signal because the storage of all the signals exceeds the capability of the device. The feasibility and performance of the compressed sensing in a wireless sensor node for remote cardiac monitoring has been assessed. The ECG signal is compressed with different compression ratios. Compressed measurements are processed and stored in the device. Notice that, it is solution great advantage if only the abnormal ECG signal compressed measurements are transmitted, because it can reduce significantly the energy consumption and the memory footprint and the diagnosis time. However invalidate compression ratio and failing a wireless delivery may lead the reconstructed signal be unrepresentative. Thus the balance between compression ratio and reconstruction performance is need to be found in a compressed sensing implementation. The obtained results indicate that the approach combined wireless sensor network and compressed sensing is very interesting for cardiac monitoring. The results obtained from the real-world experimentations show that with compression ratio around 50%, it enables to reduce system consumption and then increase its lifetime.

There can be no clear-cut distinction between standard signal and difference signal, yet some attempt has to be made to define the normality of the signal by the interpretation of the ECG in which the ECG pattern varies from standard ECG signal. Different kinds of electrode location may affect the precordial leads and therefore the accuracy of the recorded ECG. The study of chapter 4 was intended to evaluate the comparison between the standard and the modified ECG recordings using the difference signal. The standard ECG with the placement of the precordial lead electrodes and the modified ECG with the reference electrode placed not on the neck but the adjacent place were recorded and compared. ECG morphology recorded by adjacent locations of the ECG precordial lead electrodes is affected and therefore the accuracy of the current ECG criteria and algorithms. The work of chapter 4 is used to

prospectively evaluate and compare variability using standard and difference ECG using current proposed criteria. The heart rate, the amplitude of QRS complex and the duration of QRS complex deduced from difference signal are not significantly negative compared the standard ECG. The results assessed the effect of electrode location on the QRS complex recorded. Amplitude and morphology of a recorded ECG on the precordial lead can vary based on locations on the surface of the chest. Because the recorded ECG is a difference signal and affected by the distance between the precordial lead and the adjacent lead. However difference ECG signal is recorded from the same patient, it seems to eliminate the effect of the distortion factor in the difference ECG signal. In addition not prominent difference between observers is found, however the precision of the conclusion may be weakened because there are not enough observation sample in the study. Another place that we need further study is that the QRS amplitude and the duration of QRS complex may be significantly changed on the different locations compared to standard ECG. The QRS morphology is the important and first clue to the diagnosis of cardiologists. Therefore more researches should be carried out for more accurate evaluation of difference ECG signals compared to standard ECG ones.

Finally, I think that WSN having different type of sensors and multiple sinks enables to implement ambient computing dedicated to pervasive healthcare monitoring is an important and interesting research field.

Bibliography

[1] S. Arnon, D. Bhastekar, D. Kedar, *et al.*, "A comparative study of wireless communication network configurations for medical applications," *IEEE Wirel. Commun.,*vol. 10, pp. 56-61, 2003.

[2] H. Y. Zhou, "Wireless sensor network dedicated to remote continuous real-time cardiac arrythmias detection and diagnosis," *PhD Thesis*, Blaise Pascal University, Clermont-Ferrand, France, 2005.

[3] H. Sohn, C. R. Farrar, F. M. Hemez, *et al.*, "A review of structural health monitoring literature: 1996-2001," *Report*, Los Alamos National Laboratory, 2004.

[4] A. L. Liu, H. Hile, G. Borriello, *et al.*, "Informing the design of an automated wayfinding system for individuals with cognitive impairments," *Proc. 3rd Int'l Conf. Pervasive Computing Technologies for Healthcare,* IEEE CS Press, 2009.

[5] S. Patel, K. Lorincz, R. Hughes, *et al.*, "Monitoring motor fluctuations in patients with parkinson's disease using wearable sensors," *IEEE T. Inf. Technol. B.,* vol. 13, pp. 864-873, 2009.

[6] B. R. Chen, T. Buckley, R. Rednic, *et al.*, "MercuryLive: a web-enhanced platform for long-term high fidelity motion analysis," *7th Annual IEEE Communications Society Conf. on Sensor Mesh and Ad Hoc Communications and Networks (SECON)*, Boston, pp. 1-2, 2010.

[7] Y. Yu, V. K. Prasanna, and B. Krishnamachari, "Introduction to wireless sensor networks," in *Information processing and routing in Wireless Sensor Network*, World Scientific Publishing Company (Ed), pp. 1-21, 2006.

[8] T. Yang, Z. G. Li, and Y. C. Shi, "Study elderly care services by integration with the community health services in rural China," *General Report* (in Chinese), 2007.

[9] K. Hung and Y. Zhang, "Implementation of a wap-based telemedicine system for patient monitoring," *IEEE T. Inf. Technol. B.,* vol. 7, pp. 101-107, 2003.

[10] G. G. Mendoza and B. Q. Tran, "In-home wireless monitoring of physiological data for heart failure patients," *Proc. of. EMBS/BMES Conf.*, vol. 10, pp. 1849-1850, 2002.

[11] C. H. Salvador, M. P. Carrasco, M. A. G. d. Mingo, *et al.*, "Airmed-cardio: a GSM and internet services-based system for out-of-hospital follow-up of cardiac patients," *IEEE T. Inf. Technol. B.,* vol. 9, pp. 73-85, 2005.

[12] H. Y. Zhou and K. M. Hou, "Pervasive cardiac monitoring system for remote continuous heart care," *2010 4th Int. Conf. on Bioinformatics and Biomedical Engineering (iCBBE)*, Chengdu, 2010.

[13] S. Chatterjee and A. Miller, "Holter monitor," in *Biomedical instrumentation systems*, Cengage Learning (Ed), pp. 236-237, 2010.

[14] H. Y. Zhou, K. M. Hou, L. Gineste, *et al.*, "A new system dedicated to real-time cardiac arrhythmias tele-assistance and monitoring," *J. Univers. Comput. SCI,* vol. 12, pp. 30-44, 2006.

[15] Heart Center, in http://www.dukehealth.org/health_library/topic_centers/heart, Duke heart center.

[16] H. Y. Zhou, K. M. Hou, J. Ponsonnaille, *et al.*, "Real-time cardiac arrhythmia tele-Assistance and monitoring platform: RECATA," 3*rd Int. Conf. On Smart homes and health Telematic.*, pp. 99-106, 2005.

[17] H. Y. Zhou, K. M. Hou, J. Ponsonnaille, *et al.*, "Real-time arrhythmias tele-assistance and monitoring platform: RECAD," *Proc. of EMBC'05*, Shanghai, pp. 882, 2005.

[18] J. J. Bailey, A. S. Berson, A. J. Garson, *et al.*, "Recommendations for standardization and specifications in automated electrocardiography: bandwidth and digital signal processing," *Special report circulation,* vol. 81, pp. 730-739, 1990.
[19] R. M. Sullivan, W. W. Li, A. C. Kendig, *et al.*, "Diagnosis of arrhythmias with non-invasive tools," in *Management of cardiac arrhythmias*, Human Press (Ed), 2011.
[20] Texas-Instruments, "MSP430x13x, MSP430x14x signal microcontroller," 2000.
[21] B. Razavi, *Design of analog CMOS integrated circuits*. New York: McGraw-Hill (Ed), 1994.
[22] E. Bruun, "Feedback analysis of transimpedance operational amplifier circuits," *IEEE T. Circuits-I,* vol. 40, pp. 275-278, 1993.
[23] Mason, "Feedback theory - some properties of signal flow graphs," *Proc. IRE,* vol. 64, pp. 1144-1156, 1953.
[24] P. J. Hurst, S. H. Lewis, J. P. Keane, *et al.*, "Miller compensation using current buffers in fully differential CMOS two-stage operational amplifiers," *IEEE Trans. Circuits Syst. I,* vol. 51, pp. 275-285, 2004.
[25] A. Veeravalli, E. Sánchez-Sinencio, and J. Silva-Martínez, "Transconductance amplifier structures with very small transconductances: a comparative design approach," *IEEE J. Solid-S.t Circ.,* vol. 37, pp. 770-775, 2002.
[26] A. Veeravalli, E. Sánchez-Sinencio, and J. Silva-Martínez, "A CMOS transconductance amplifier architecture with wide tuning range for very low frequency applications," *IEEE J. Solid-St. Circ.,* vol. 37, pp. 776-781, 2002.
[27] S. Sols-Bustos, J. Silva-Martnez, and F. Maloberti, "A 60-dB dynamic-range CMOS sixth-order 2.4-Hz low-pass filter for medical applications," *IEEE J. Solid-St. Circ.,* vol. 47, pp. 1391-1398, 2000.
[28] R. L. Geiger and E. Sánchez-Sinencio, "Active filter design using operational transconductance amplifiers: a tutorial," *IEEE Circuits Devic.,* vol. 1, pp. 20-32, 1985.
[29] J. Wang, E. Sánchez-Sinencio, and F. Maloberi, "Very linear ramp-generators for high resolution ADC BIST and calibration," *43rd IEEE Midwest Symp. on Circuit and System*, vol. 2, pp. 908-911, 2000.
[30] I. A. Powell and W. J. Perold, "A switching logic digitizer for analog-to-digital conversion," *IEEE Trans. Applied Superconductivity,* vol. 17, pp. 3886-3896, 2007.
[31] H. Krad, "A dual-slope integration based analog-to-digital convertor," *American J. of Engineering and Applied Sciences,* vol. 2, pp. 743-749, 2009.
[32] H. P. Forghani-Zadeh and G. A. Rincón-Mora, "Low-power CMOS ramp generator circuit for DC-DC converters," *Journal of Low Power Electronics,* vol. 2, pp. 437-441, 2006.
[33] Y. H. Chee, J. M. Rabaey, and A. Niknejad, "Ultra low power transmitter for wireless sensor networks," *Report*, University of California, Berkeley, 2006.
[34] Atmel-Corporation, "Microcontroller with 128K bytes in-system programmable flash, Atmega 128, Atmega 128L," 2006.
[35] P. W. Macfarlane, A. V. Oosterom, O. Pahlm, *et al.*, *Comprehensive electrocardiology*, Springer (Ed), 2010.
[36] CardioSource, in http://www.cardiosource.org/, American College of Cardiology.
[37] K. A. Gatzoulis, M. D. Carlson, L. A. Bibl, *et al.*, "Time domain analysis of the signal averaged electrocardiogram in patients with a conduction defect or a bundle branch block," *Eur. Heart. J.,* vol. 16, pp. 1912-1919, 1995.

[38] M. S. Chavan, R. A. Aggarwala, and M. D. Uplane, "Suppression of baseline wander and power line interference in ECG using digital IIR filter," *Int. Journal of Circuits, Systems And Signal Proc.,* vol. 2, pp. 356-365, 2008.
[39] N. V. Thakor and J. G. Webster, "Design and evaluation of QRS and noise detectors for ambulatory e.c.g. monitors," *Med. Biol. Eng. Comput.,* vol. 20, pp. 709-714, 1982.
[40] J. Malmivuo and R. Plonsey, *Bioelectromagnetism - Principles and Applications of Bioelectric and Biomagnetic Fields*, Oxford University Press (Ed), 1995.
[41] "MIT-BIH arrhythmia database," in http://www.physionet.org/physiobank, Laboratories at Boston's Beth Israel Hospital (now the Beth Israel Deaconess Medical Center) and at MIT.
[42] M. C. Van, M. Sabble and D. Knockaert, "The clinical value of the ECG in noncardiac conditions," *Chest 2004*, vol. 125, pp.1561-1576, 2004.
[43] S. Kinlay, J. W. Leitch, A. Neil, *et al.*, "Cardiac event recorders yield more diagnoses and are more cost-effective than 48-hour Holter monitoring in patients with palpitations: a controlled clinical trial," *Annals of Internal Medicine*, vol. 124, pp. 16-20, 1996.
[44] K. Minami, H. Nakajima, and T. Toyoshima, "Real-time discrimination of ventricular tachyarrhythmia with Fourier-transform neural network," *IEEE Trans. Biomed. Eng.,* vol. 46, pp. 179-185, 1999.
[45] S. Evans, H. Hastings, and M. Bodenheimer, "Differentiation of beats of ventricular and sinus origin using a self-training neural network," *Pace Envtl. L. Rev.,* vol. 17, pp. 611–626, 1994.
[46] R. Clayton, A. Murray, and R. Campbell, "Recognition of ventricular fibrillation using neural networks," *Med. Biol. Eng. Comput.,* vol. 32, pp. 217-220, 1994.
[47] W. Zareba, A. J. Moss, and S. l. Cessie, "Dispersion of ventricular repolarization and arrhythmic cardiac death in coronary artery disease," *Am. J. Cardiol.,* vol. 74, pp. 550-553, 1994.
[48] B. U. Kohler, C. Hennig, and R. Orglmeister, "The principles of software QRS detection," *IEEE Eng. Med. Biol.,* vol. 21, pp. 42-57, 2002.
[49] G. M. Friesen, T. C. Jannett, M. A. Jadallah, *et al.*, "A comparison of the noise sensitivity of nine QRS detection algorithm," *IEEE T. Bio-Med. Eng.,* vol. 37, pp. 85, 1990.
[50] W. P. Holsinger, K. M. Kempner, and M. H. Miller, "A QRS preprocessor based on digital differentiation," *IEEE T. Bio-Med. Eng.,* vol. 18, pp. 212, 1971.
[51] M. L. Ahlstrom and W. J. Tompkins, "Automated high-speed analysis of Holter tapes with microcomputers," *IEEE T. Bio-Med. Eng.,* vol. 30, pp. 651, 1983.
[52] W. A. H. Engelse and C. Zeelenberg, "A single scan algorithm for QRS-detection and feature extraction," *Comput. Cardiol.,* vol. 6, pp. 37-42, 1979.
[53] P. S. Hamilton and W. J. Tompkins, "Quantitative investigation of QRS detection rules using the MIT/BIH arrhythmiac database," *IEEE T. Bio-Med. Eng.,* vol. 33, pp. 1157-1165, 1986.
[54] S. Suppappola and Y. Sun, "Nonlinear transforms of ECG signals for digital QRS detection: a quantitative analysis," *IEEE T. Bio-Med. Eng.,* vol. 41, pp. 397-400, 1994.
[55] Barro, S. Fernandez-Delgado, and J. A. M. Vila-Sobrino, "Classifying multichannel ECG patterns with an adaptive neural network," *IEEE Eng. Med. Biol.,* vol. 17, p. 45, 1998.
[56] Q. Xue, Y. H. Hu, and W. J. Tompkins, "Neural-network-based adaptive matched filtering for QRS detection," *IEEE T. Bio-Med. Eng.,* vol. 39, pp. 317-329, 1992.

[57] H. H. Huang, H. L. Chan, P. L. Lin*, et al.*, "Time-frequency spectral analysis of heart rate variability during induction of general anesthesia," *Brit. J. Anaesth. ,* vol. 79, pp. 754-758, 1997.

[58] F. Zhang and Y. Lian, "Effective ECG QRS detection based on multi-scale mathematical morphology filtering," *IEEE Trans. Biomed. Circuits Syst.*, vol.3, pp. 220-228, 2009.

[59] X. S. Zhang, Y. S. Zhu, and X. J. Zhang, "New approach to studies on ECG dynamics: extraction and analysis of QRS complex irregularity time series," *Med. Biol. Eng. Comput.,* vol. 35, pp. 467-474, 1997.

[60] H. Y. Zhou, K. M. Hou, J. Ponsonnaille*, et al.*, "Remote continuous cardiac arrhythmias detection and monitoring," *IOS Press,* pp. 112-120, 2004.

[61] E. J. Candès and M. B. Wakin, "An introduction to compressive sampling," *IEEE Signal Proc. Mag.,* vol. 25, pp. 21-30, 2008.

[62] R. G. Baraniuk, "Compressive sensing," *IEEE Signal Proc. Mag.,* vol. 24, pp. 118-120, 2007.

[63] P. K. Baheti and H. Garudadri, "An ultra low power pulse oximeter sensor based on compressed sensing," *IEEE Computer Society, Sixth Int. Workshop on Wearable and Implantable Body Sensor Networks*, pp. 144-148, 2009.

[64] R. Robucci, L. K. Chiu, J. Gray*, et al.*, "Compressive sensing on a CMOS separable transform image sensor," *IEEE Int. Conf. Acoustics, Speech, and Signal Processing*, 2008, pp. 5125-5128.

[65] S. Hong, "Direct spectrum sensing from compressed measurements," *Commu. Conf. 2010*, San Jose, CA, pp. 1187-1192, 2010.

[66] L. Senhadii, G. Carrault, J. J. Bellanger*, et al.*, "Comparing wavelet transforms for recognizing cardiac patterns," *IEEE Eng. Med. Biol. Mag.,* vol. 14, pp. 167-172, 1995.

[67] M. Unser, "A review of wavelet in biomedical applications," *P. IEEE,* vol. 84, pp. 626-638, 1996.

[68] L. Senhadji, J. J. Bellanger*,* G. Carrault, *et al.*, "Wavelet analysis of ECG signals," Proc. Int. Conf. IEEE EMBS, Philadelphia, pp. 811-812, 1990.

[69] I. C. Atkinson and F. Kamalabadi, "Basis selection for wavelet processing of sparse signals," *Signal Process.,* vol. 88, pp. 2340–2345, 2008.

[70] Y. C. Wang, Y. Y. Hsieh, and Y. C. Tseng, "Compression and storage schemes in a sensor network with spatial and temporal coding techniques," *IEEE Vehicular Technology conf.*, Singapore, pp. 148-152, 2008.

[71] Baraniuk, R.G.Cevher, M. F. V. Duarte*, et al.*, "Model-based compressive sensing," *IEEE T. Inform. Theory,* vol. 56, pp. 1982-2001, 2010.

[72] D. Needell, "Topics in compressed sensing," *PhD thesis,* University of California DAVIS, Davis, USA, 2009.

[73] D. L. Donoho, M. Elad, and V. Temlyakov, "Stable recovery of sparse overcomplete representations in the presence of noise," *IEEE Trans. Info. Theory,* vol. 52, pp. 6-18, 2006.

[74] J. Trzasko and A. Manduca, "Highly undersampled magnetic resonance image reconstruction via homotopic ℓ_0–minimization," *IEEE Trans. Med. Imaging,* vol. 28, pp. 106-121, 2009.

[75] G. H. Mohimani, M. Babaie-Zadeh, and C. Jutten, "A fast approach for overcomplete sparse decomposition based on smoothed ℓ_0 norm," *IEEE Trans. Signal Process.,* vol. 57, pp. 289-301, 2009.

[76] D. L. Donoho and Y. Tsaig, "Fast solution of ℓ_1 minimization problems when the solution may be sparse," *IEEE. T. Inform.,* pp. 4789-4812, 2008.
[77] S. Ji, Y. Xue, and L. Carin, "Bayesian compressive sensing," *IEEE. T. Signal. Proces.,* vol. 56, pp. 2346-2356, 2008.
[78] M. E. Tipping and A. C. Faul, "Fast marginal likelihood maximisation for sparse Bayesian models," *Proc. of the Ninth International Workshop on Artificial Intelligence and Statistics*, 2003.
[79] S. D. Babacan, R. Molina, and A. K. Katsaggelos, "Bayesian compressive sensing using Laplace priors," *IEEE T. Image. Process.,* vol. 19, pp. 53-63, 2010.
[80] M. Tipping, "Sparse Bayesian learning and the relevance vector machine," *J. Mach. Learn. Res.,* vol. 1, pp. 211-244, 2001.
[81] J. Haupt, R. Castro, R. Nowak*, et al.*, "Compressive sampling for signal classification," *Proc. 40th Asilomar Conf. on Signals, Systems, and Computers*, pp. 1430-1434, 2006.
[82] M. Mishali, Y. C. Eldar, and J. A. Tropp, "Efficient sampling of sparse wideband analog signals," *Electrical and Electronics Engineers in Israel,* pp. 290-294, 2008.
[83] E. Simonson, H. Horibe, N. Okamoto*, et al.*, "Effect of electrode displacement on orthogonal leads," *Proc. Long Island Jewish Hosp. Symposium, Vectorcardiography,* pp. 424, 1966.
[84] H. B. Williams, "On the cause of the phase difference frequently observed between homonymous peaks of the electrocardiogram," *Am. J. Physiol.,* vol. 35, pp. 292-300, 1914.
[85] E. FRANK, "An accurate, clinically practical system for spatial vectorcardiography," *Circ. J.,* vol. 13, pp. 737-739, 1956.
[86] M. B. Conover, *Understanding Electrocardiography*, Mosby (Ed), 2002.
[87] W. Einthoven, G. Fahr, A. Waart, "On the direction and manifest size of the variations of potential in the human heart and on the influence of the position of the heart on the form of the electrocardiogram," *Am. Heart J.,* vol. 40, pp. 163-211, 1950.
[88] F. N. Wilson, F. D. Johnston, A. G. MacLeod*, et al.*, "Electrocardiograms that represent the potential variations of a single electrode," *Am. Heart J.,* vol. 9, pp. 447-458 1934.
[89] E. Frank, "Determination of the electrical center of ventricular depolarization in the human heart," *Am. Heart J.,* vol. 9, pp. 670-692, 1955.
[90] J. A. K. Hyttinen, J. A. Malmivuo, and S. J. Walker, "Lead field of ECG leads calculated by a computer thorax model-an application of reciprocity," *Proc. 1993 Computers in Cardiology Meeting*, Imperial College, London, 1993.
[91] A. K. Liu, J. W. Belliveau, and A. M. Dale, "Spatiotemporal imaging of human brain activity using functional MRI constrained magnetoencephalography data: Monte Carlo simulations," *Proc. of the national academy of sciences of the united states of america,* vol. 95, pp. 8945-8950, 1998.
[92] G. Daniel, G. Lissa, D. M. Redondo*, et al.*, "Real-time 3D vectorcardiography: an application for didactic use," *J. of Phys.: Conf. Ser.*, vol. 90, pp. 1-6, 2007.
[93] G. Uijen, V. A. Oosterom, and V. R. Dam, "The relationship between the 12-lead standard ECG and the XYZ vector leads," *Proc. of 14th Int. Congress on Electrocardiography*, Berlin, 1998.
[94] J. L. Willems, "Common standards for quantitative electrocardiography," *J. Med. Eng. Technol.,* vol. 9, pp. 209-217, 1985.

[95] J. L. Willems, P. Arnaud, J. H. V. Bemmel*, et al.*, "Assessment of the performance of electrocardiographic computer programs with the use of a reference data base," *Circ. J.,* vol. 71, pp. 523-534, 1985.
[96] L. Edenbrandt, A. Houston, and P. W. Macfarlane, "Vectorcardiograms synthesized from 12 lead ECGs: a new method applied in healthy children," *Pediatr. Cardiol,* vol. 15, pp. 21-26, 1994.
[97] P. J. Strommer, J. O. Lekkala, and J. A. Malmivuo, "Accurate digital synthesiser for simulating vectorcardiogram," *Med. Biol. Eng. Comput.,* pp. 250-254, 1981.
[98] E. Frank, "The image surface of a homogeneous torso," *Am. Heart J.,* vol. 47, pp. 757-768, 1954.
[99] A. Kachenoura, F. Porée, A. I. Hernández*, et al.*, "Using intracardiac vectorcardiographic loop for surface ECG synthesis," *Special Issue of EURASIP Journal on Advances in Signal Processing,* pp. 1-8, 2008.
[100] G. D. Clifford, F. Azuaje, and P. E. McSharry, "Advanced methods and tools for ECG data analysis," in *QRS-VCG Loop Alignment EDR Algorithm*, Boston/London: Artech House (Ed), 2006.
[101] R. Bailón, L. Sörnmo, S. Member*, et al.*, "A robust method for ECG-based estimation of the respiratory frequency during stress testing," *IEEE Trans. Biomed. Eng.,* vol. 53, pp. 1273-1285, 2006.
[102] M. Åström, J. Garcia, P. Laguna*, et al.*, "Detection of body position changes using the surface electrocardiogram," *Med. Biol. Eng. Comput.,* vol. 41, pp. 164-171, 2003.
[103] M. Åström, E. C. Santos, L. Sörnmo*, et al.*, "Vectorcardiographic loop alignment and the measurement of morphologic beat-to-beat variability in noisy signals," *IEEE Trans. Biomed. Eng.,* vol. 47, pp. 497-506, 2000.
[104] L. Sörnmo, "Vectorcardiographic loop alignment and morphologic beat-to-beat variability," *IEEE Trans. Biomed. Eng.*, vol. 45, pp. 1401–1413, 1998.
[105] H. C. Burger and J. B. v. Milaan, "Heart vector and leads. I, II and III," *Br. Heart J.,* vol. 9, pp. 157-161, 1946.
[106] J. Pan and J. Willis, "A real-time QRS detection algorithm," *IEEE Trans. Biomed. Eng.,* vol. 32, pp. 230-236, 1985.